Multimaterial Nanoscale Printing via Charged Nanoparticle Deposition

Daniel Teal

Electrical Engineering and Computer Sciences
University of California, Berkeley

Technical Report No. UCB/EECS-2024-233
http://www2.eecs.berkeley.edu/Pubs/TechRpts/2024/EECS-2024-233.html

December 20, 2024

Multimaterial Nanoscale Printing via Charged Nanoparticle Deposition

By

Daniel Teal

A dissertation submitted in partial satisfaction of the

requirements for degree of

Doctor of Philosophy

in

Engineering — Electrical Engineering and Computer Sciences

in the

Graduate Division

of the

University of California, Berkeley

Committee in Charge:

Professor Kristofer S.J. Pister, Chair
Professor Clark T.-C. Nguyen
Professor Jeffrey Bokor
Professor Hartmut Häffner

Fall 2024

Multimaterial Nanoscale Printing via Charged Nanoparticle Deposition

Abstract

Multimaterial Nanoscale Printing via Charged Nanoparticle Deposition

by

Daniel Teal

Doctor of Philosophy in Engineering — Electrical Engineering and Computer Sciences

University of California, Berkeley

Professor Kristofer S.J. Pister, Chair

Microfabrication, the set of manufacturing techniques used to make computer chips, displays, MEMS, and other devices, is famously difficult, slow, and capital equipment heavy. In this dissertation we propose a much simpler path toward rapid prototyping of microfabricated devices by deposition of nanoparticles in vacuum.

We will discuss generation of nanoparticles of standard microfabrication materials such as metals, oxides, and semiconductors, as well as methods to manipulate these as aerosols in low-pressure gas, culminating in a demonstration of multimaterial printing. We will then describe electrical charging of nanoparticles and develop a new method to electrostatically focus and accelerate nanoparticles theoretically capable of printing with sub-1 µm resolution. Finally, we will detail the future work required to 3D print silicon transistors and conclude our new manufacturing process will likely be faster and cheaper than standard microfabrication for making small quantities of simple chips.

Dedicated to a kind and awesome future.

Acknowledgments

With the understanding that the acknowledgments section of a thesis is traditionally freed from the rigid constraints of academic formality:

I need to give huge thanks to **Kris**. You let me pursue this initially-uncertain project despite your wish I spent more time building cooler MEMS robots with traditional microfabrication; I still intend to build plenty of better robots via printing someday. You were simultaneously an excellent advisor, providing proof it's possible to be good at many things, kind to people, and kinda funny sometimes. You set a good example. I also need to give a shoutout to the rest of my thesis committee—**Clark**, **Jeff**, and **Hartmut**—for going along with it and letting me try something a bit unusual. I'm pretty happy with the result.

Thanks to everyone I met and lived with here at Berkeley. **Lydia**, it's nice to know somebody who knows what they want in life and is excellent at finding it. **Durham**, for successfully convincing me that more is possible then pushing me to discover it. **Kevin** and **Lars**, for being omnipresent around BSAC, willing to banter, and each good at your own thing. To all my group members, past and present, I appreciated working with you: **Hani** and **Craig**, for mentoring me in MEMS; **Mauricio** and **Alex** and **Nathan**, **Alexander** and **Dillon**, and now **Yichen** and **Daniel** (Lovell) and **Yu-Chi** and **Titan** and then **Amanda**. The same to **Anju**, **Micah**, and other Swarm Lab members. Thanks also to the BSAC staff, especially **Dalene**: you were always on top of things, available, helpful, and forgave me when I turned stuff in late. Then there's everyone I worked with to teach EE143 over the years. To all the TAs: **Niharika**, **Lars** (again), **Jason**, **Yejin**, **Judd**, **Hanuman**, **Adi**, **Jongho**, and **Reaz**: I appreciated working together; y'all are great. EE143 professors **Ali** and **Jeff** (again!), I had a good time. Plenty of my microfabrication knowledge comes from the Marvell NanoLab and its staff: **Bill**, **Ryan**, **Allison**, **Joanna**, **Sam**, **Danny**, **Anthony**, **Greg**, **Tariq**, **Daniel** (Martinez), **Dave**, and everyone else. Thanks for for showing me what a proper well-run fab looks like. I always enjoyed how organized and competent yet relaxed (like, decent work hours) y'all were; I will hold other organizations up to your standard (and if I complain about microfabrication, that's only the fault of physics; I get the impression Marvell's about the best a research fab can be). Thanks also to all my other Berkeley professors; I enjoy being able to find researchers working on just about anything.

Thank you to my family: **Mom** and **Dad**, for always being there: kind and simple background support is the best kind, and I cannot imagine anything better. To **Erin** and **Kristen** and **Robert** and **Mary** (and now **Jacob** and **Eleanor**), you're all the best. And to everyone else (of course including **Uncle John** and **Grandpa Teal**'s questions).

Thanks to everyone else from earlier times, friends and colleagues. To members and mentors from the UT Austin makerspace, the UT IEEE RAS club, and LASA Robotics: I still take the same approaches I learned with you to both engineering and life.

To researchers who worked on this and other problems in the past: thanks for your work (and then for publishing it!). Y'all did good, and I hope my work similarly inspires others. Being able to simply look up progress on most problems makes it possible to go so much further. I tried to reference prior work everywhere I could; apologies to anyone I missed.

Thanks to the diffuse group of authors and musicians and artists and engineers whose works of fiction and otherwise have kept me sane these past years then shown me what could be. If anything makes life worth living, it's what we choose to make from it.

And to everyone else: you make this world a better place. I rather enjoy it. (And if I omitted anyone, I'm sorry, that was unintentional. You're worthwhile.)

Financially, credit goes to the NSF Graduate Research Fellowship Program (GRFP) (grant DGE 1752814), which gave me the freedom to explore ideas eventually resulting in this dissertation, and to Kris, BSAC, and Berkeley for supporting me the rest of the way.

Minimal thanks to air. Oxygen especially. I love breathing, but I gotta admit this project would have been much easier if everything were in vacuum to begin with.

Finally: thanks to you, reader. I can't resist breaking the fourth wall in order to wish you luck with whatever you're trying to do. I hope you enjoy this show.

List of Symbols

The following are standard symbols used throughout this dissertation and listed here with their SI units for reference. Any symbol with a superscript arrow ($\vec{F}$) denotes a vector.

Dynamics	
t	time (s)
x	position (m)
r	radial position (m)
v	velocity ($\mathrm{m\,s^{-1}}$)
a	acceleration ($\mathrm{m\,s^{-1}}$)
L	distance (m)
$\vec{F}$	force (N)
$\vec{E}$	electric field ($\mathrm{N\,C^{-1}}$)

Constants	
k_B	Boltzmann constant ($\mathrm{J\,K^{-1}}$)
e	elementary charge (C)
ϵ_0	vacuum permittivity ($\mathrm{F\,m^{-1}}$)

Nanoparticle Parameters	
d_p	nanoparticle diameter (m)
m	nanoparticle mass (kg)
n	number of elementary charges (-)
q	nanoparticle charge ($q = ne$) (C)
β	viscous damping coefficient ($\mathrm{kg\,s^{-1}}$)
D	diffusion coefficient ($\mathrm{m^2/s}$)

Gas Parameters	
m_g	mass of single gas molecule (kg)
P	pressure (Pa) (we also use Torr)
T	temperature (K)
ℓ	mean free path (m)

Ion Traps	
R_T	quadrupole trap radius (m)
L_T	quadrupole trap length (m)
ω	trap angular frequency ($\mathrm{rad\,s^{-1}}$)
f	trap frequency ($2\pi f = \omega$) (Hz)
V_T	peak-to-peak AC amplitude (V)
U_T	trap potential energy (J)
$\widetilde{U}_T$	trap pseudopotential energy (J)

Nanoparticle Beams	
r_B	beam minimum radius (m)
d_B	beam minimum diameter (m)
A_B	beam minimum area ($\mathrm{m^2}$)
θ	beam half-angle (rad)
Ω	beam solid angle (sr)
v_a	particle axial speed ($\mathrm{m\,s^{-1}}$)
v_r	particle radial speed ($\mathrm{m\,s^{-1}}$)
Q	beam volumetric flux ($\mathrm{m^3/s}$)
N'	beam number flux (particles $\mathrm{s^{-1}}$)

Contents

Chapter 1

Introduction

Contemporary life is built on computer chips and displays, LEDs and solar cells, inkjet printers and cell phone RF filters. All these are made with the same set of fabrication tools, which we collectively call microfabrication. Microfabrication is notable for three reasons:

- it lets us build nanometer-scale multimaterial devices;
- it is often the *only* way to build these devices;
- it is very difficult, expensive, and time-consuming.

This last point is unfortunate. As we will show, it means R&D is slow and microfabrication is out of reach of most researchers and engineers. It is a testament to its importance that we've persisted with microfabrication long enough to build computers and the Internet—but how much more could be done if it were easier and accessible? We argue it is worthwhile to investigate new manufacturing methods that achieve similar results with fewer constraints.

In this dissertation, we'll describe our progress developing one such fabrication process[1]. It will not replace microfabrication in general but should be capable of creating some of the same devices while being easier, cheaper, and faster in limited circumstances.

What are these nanometer-scale multimaterial devices, and what is the challenge in making them? The prototypical device is a transistor, billions of which are contained in each computer CPU, but other exemplar devices include solar cells and LEDs. All these are nothing more than solid blocks of the right materials put together in the right configurations. Some silicon here, some aluminum there, some oxides between them. This is comparable to games like Minecraft: put particular materials in correct positions, and you have a transistor. The difficulty is that, in reality, this needs extreme precision and control.

For example, a simple MOSFET transistor might consist of at least four different materials: silicon with a small amount of boron, silicon with a small amount of phosphorus, silicon

[1]The impatient reader can skip to section 1.3 for details. In short: 3D printing nanoparticles.

dioxide (SiO_2, i.e., glass), and aluminum, placed together as in figure 1.1 [1][2]. In order for the transistor to work, the thin later of SiO_2 in the center (the "gate oxide") must be less than 100 nm thick (only several hundred atoms!), while the proportion of boron and phosphorus ("dopants") in silicon needs to be extremely precise with no contaminants[2]. Increasingly complex improvements (silicon crystal orientation, different gate oxide materials, etc.) raise performance. Other devices, like solar cells and LEDs, or MEMS[3] devices like inkjet printer nozzles and cellphone RF filters (which all have air gaps that allow miniature mechanical parts to move), have their own constraints. A solar cell, for example, is just a layer of this phosphorus-doped silicon on boron-doped silicon with metal electrodes on each side.

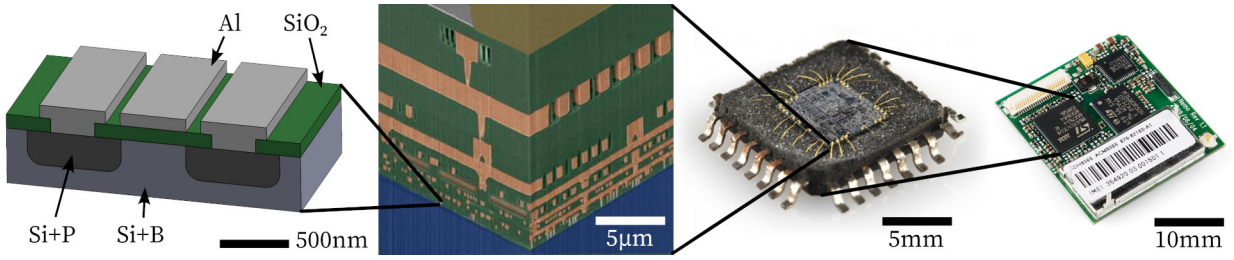

Figure 1.1: From left to right: a minimal transistor, tens of transistors in a cutaway view of a chip that contains millions, the chip in a standard integrated circuit package, and the result mounted to a printed circuit board. Right pictures from [3], [4].

Fortunately some of these constraints can often be relaxed slightly at the cost of reduced performance, but in general interesting devices always have the following requirements:

- **Multimaterial construction:** These devices consist of several different types of material, and each material must be very pure, sometimes to better than one non-silicon atom per billion silicon. Furthermore, the interfaces between two different materials needs to be near atomically perfect. The usual macroscopic approach of making two parts separately then attaching them leaves rough surfaces and dust and grease and is not good enough. Usual materials include metals (as electrical conductors), oxides (like SiO_2, often electrical insulators), and especially semiconductors (like silicon).
- **High resolution:** At least some parts of the more interesting devices need to be below 1 µm thick (human hair is 80 µm in diameter). Compare this to traditional macroscopic metal machining, where just the roughness of a smooth surface might be around 1 µm!

The combination of these two qualities—multimaterial capability and high resolution—is the main challenge that microfabrication solves and no other manufacturing method has yet reached. Achieving this will be our main challenge in this dissertation.

[2]Silicon has a density of about 5×10^{22} atoms per cubic centimeter. Common levels of purposely added dopants range anywhere from 1×10^{13} to 1×10^{20} atoms per cubic centimeter, and unwanted impurities must be below that (less than one unwanted atom per billion others). Electrical purity silicon is one of the most precise materials humans have ever produced and is far beyond, e.g., natural gemstones.

[3]Microelectromechanical systems (MEMS) are tiny gears, vibrating beams, and other mechanical parts made with microfabrication. Moving parts are made by etching away specific materials to leave air gaps and can then be moved around with electrostatics by applying a voltage via an attached electrical circuit.

1.1 Microfabrication is Hard

We now know what microfabrication has to do: it places metals, semiconductors, and oxides together with high resolution. But how does it work, and why is it so slow and difficult?

Microfabrication is a set of different tools combined in what was originally called the planar process, first conceptualized some 65 years ago [5][6]. Starting with a flat substrate—typically a silicon wafer—the substrate is passed through many steps, each performed by a different tool. Some steps deposit a thin layer of a new material across the entire surface, some add a layer of special material onto which a 2D pattern is drawn with light ("photolithography"), and some steps selectively etch some materials but not others. This process makes hundreds of copies in parallel on the same wafer, so a final step cuts this into individual rectangular chips, which are then packaged and attached to PCBs in larger devices [1][7][8].

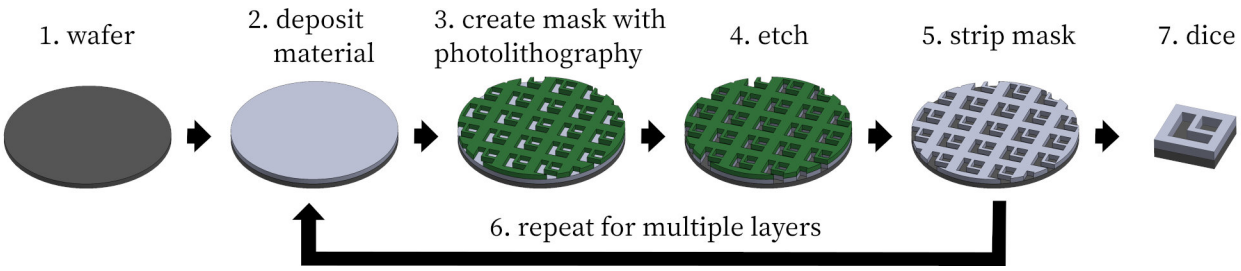

Figure 1.2: The steps of microfabrication. A silicon wafer has material deposited, a mask patterned, the material etched through the mask, and mask removed. These steps are repeated up to tens of times for multiple layers until the wafer is finally diced into complete chips. Each step requires its own precise piece of manufacturing equipment.

This planar microfabrication process can make multimaterial devices by depositing each material in a separate step. These thin-film deposition tools generally work by introducing into a vacuum chamber the wafer and a cloud of atoms, which condense into a solid film on the wafer surface, not unlike the everyday experience of water vapor condensing into fog on a cold mirror except the condensation might be metal. There are many variations[4], all of which can precisely control film thickness to the nanometer level, sometimes even with atomic precision (via ALD), and all result in pure materials due to the lack of contaminants in a vacuum. Thus our first requirement, multimaterial construction, is achieved.

In order to achieve the second requirement, high resolution, in addition to precisely controlling film thickness we also need to make 2D patterns across the wafer. This is achieved by photolithography, a process in which a layer of light-sensitive polymer photoresist is deposited on the wafer and a pattern of light, made with a patterned mask, is magnified and chemically changes this photoresist in exposed areas. The exposed photoresist can be etched away, and another etching process used to selectively remove material below those areas, after which the photoresist is removed. The resolution of this process is limited mainly by the

[4]Some variations include evaporation and sputtering, which are often described as physical vapor deposition processes, and chemical vapor deposition, in which the vapor reacts on the surface [1].

wavelength of light used and is easily sub-1 µm; 200 nm resolution is decades old technology while state-of-the-art extreme ultraviolet (EUV) photolithography tools approach 10 nm.

The result is impressively capable. Microfabrication makes not only small multimaterial transistors, but also arrays of many transistors spread across a chip—an integrated circuit (IC)—and easily mass produces them. Early ICs quickly superseded vacuum tubes in size and performance. As microfabrication (and especially photolithography resolution) improved, ICs contained more transistors, quickly increasing from several thousand in the early Intel 4004 microcontroller, to millions in the 1990s, to billions of transistors per chip today (or even trillions in terabyte memories). This rapid increase in capability, known as Moore's Law [6][9], allowed the rapid adoption of computers in every part of society[5]. Almost as an afterthought, the same microfabrication process is used to build solar cells, LCD displays, hard drives, DVDs, accelerometers, LEDs, microfluidic chips, and more.

That's how microfabrication works. Why do we emphasize its difficulty?

Briefly: it is too complex. A modern CPU might have 80 layers, each of which needs its own deposition, lithography, and etch steps, not to mention cleaning and metrology steps in between. This means a total of hundreds or thousands of individual steps, each of which is performed in a different piece of machinery. A wafer is moved back and forth between these pieces of equipment[6] in a process that takes days at minimum, but more often weeks to months, and the warehouse-sized factory ("fab") holding this equipment must be a cleanroom to minimize dust. Even worse: if a single step messes up, there is often no way to correct it but to start over from the beginning. Thus each tool needs to be precisely built to be as perfect as possible, which is naturally expensive. Simpler devices like MEMS often have fewer layers but the microfabrication process has to be customized to each device, making them almost equally challenging to build.

To convince the reader this is worth improving, we submit the following evidence:

- **2020 chip shortage, due to time constraints:** around 2020–2023, a combination of economic factors resulted in a significant mismatch between which chips were produced by microfabrication fabs and what customers required [11]. This affected many industries in which larger systems (e.g., cars) could not be built without a missing chip. These problems took years to resolve, despite significant financial incentive, because it takes that long for a fab to change the chips it makes or for new fabs to be built.
- **Inaccessibility, due to cost:** the minimum cost to make a single new custom chip, ordered from an existing fab, is typically at least tens of thousands of dollars[7]. Building even a minimal custom fab from used tooling is even more expensive. This limits chip design to large companies. Well-funded startups can only afford one or two tries to make a working chip, and this is even harder for researchers or hobbyists (who are also affected by the multi-month times required to make anything, including MEMS).

[5]As of 2024 we are running out of further iterative improvements to make to microfabrication, slowly leading arguably to the end of Moore's Law. The effect this will have on the industry is uncertain, although microfabrication and computers are definitely here to stay. We share some thoughts in chapter 7.

[6]Wafers often spend half their time en route between tools as a consequence of queueing theory [10].

[7]For simple chips; recent nodes can cost millions. For details and references, see section 7.2.1.

Thus, unlike fields such as robotics or metalwork, where cheap kits and tools are widely available to teach students, microfabrication has no ecosystem of slowly improving amateur talent. It remains a niche activity despite its massive importance.

- **Supply chain complexity, due to difficulty:** the semiconductor supply chain has become one of the most complex in the world [12], there are many possible points of failure in a fab, and keeping up with the state-of-the-art requires increasingly fragile, precise, and expensive microfabrication tools. The largest challenge in building a new fab is often not the economics, despite its multimillion (or billion) dollar cost, but the technical problem of setting up even a copy of an existing working fab [13].

These problems have inspired worldwide efforts such as the $52-billion-dollar 2022 US CHIPS Act [14], which tries to address each of these by improving existing microfabrication.

At this point, we believe it makes sense to recognize that since microfabrication is simultaneously important yet difficult, it is worthwhile to spend at least minimal effort investigating alternative fabrication processes not subject to the same time, cost, and difficulty limits[8]. While it is unlikely we will be able to compete with the half-century of intense technological effort that is microfabrication, an alternative can start small and might help in a subset of cases—what if we could iterate minimal designs in days instead of months? What if building a single bad transistor only needed a desktop tool, not a warehouse-sized fab? What if hobbyists could order simple custom chips as easily as PCBs today? Or will there never be another way to make a million-transistor computer? It seems likely alternatives can exist as there's no law of physics prohibiting construction far faster and with far more precision than microfabrication other than our skill in designing new ways to move atoms around [16][17]. Thus, in the grand academic tradition of asking difficult questions, we'll follow this thought and see if we get anywhere interesting.

So: in what ways other than the planar microfabrication process can we make high-resolution multimaterial devices, both transistors and beyond?

1.2 Existing Microfabrication Alternatives

The reason we continue to use microfabrication despite its difficulty is we have no alternative simultaneously capable of the multimaterial patterning and high resolution required to make useful devices. But partial alternatives certainly exist. Here we list a number of manufacturing methods[9] that can get close to microfabrication's resolution and material capabilities and, despite falling short of this particular goal, often find a niche for themselves.

[8] As the author, I admit a personal motivation: frustration with these limits of microfabrication while teaching Berkeley's EE143 microfabrication lab course or building MEMS devices [15] even in our excellent research fab. It's not fun to spend more time waiting for tools to finish then doing more useful research.

[9] The reader may be familiar with a distinction in macroscopic manufacturing tools between subtractive and additive processes: a subtractive process, like woodwork or CNC milling, begins with a block of material and removes mass to carve it to shape, while an additive process like welding or 3D printing adds material. Although this division breaks down for more complex methods, microfabrication is arguably a combination of repeated additive then subtractive cycles. The following processes, excepting FIB milling, are all additive (or "direct write" [18][19]) as this more easily satisfies the requirement to use multiple materials.

1.2.1 Inkjet Printing

Inkjet printing is perhaps the most well-known of all alternative manufacturing methods that pattern multiple materials with high resolution. Small liquid ink droplets are dispensed through a small (microfabricated!) nozzle via mechanical pressure or thermal expansion. Scanning the the dispensing head over a substrate while switching inks allows 2D multimaterial printing. Many nozzles can be operated in parallel for fast printing—at the upper end, 200×10^3 nozzles across 40 printheads, each at 80×10^3 drops per second per nozzle, gives 16 billion drops per second [20][21] . It is possible to layer inks to build 3D structures [22][23]. However, despite these abilities, inkjets still can't compete with microfabrication.

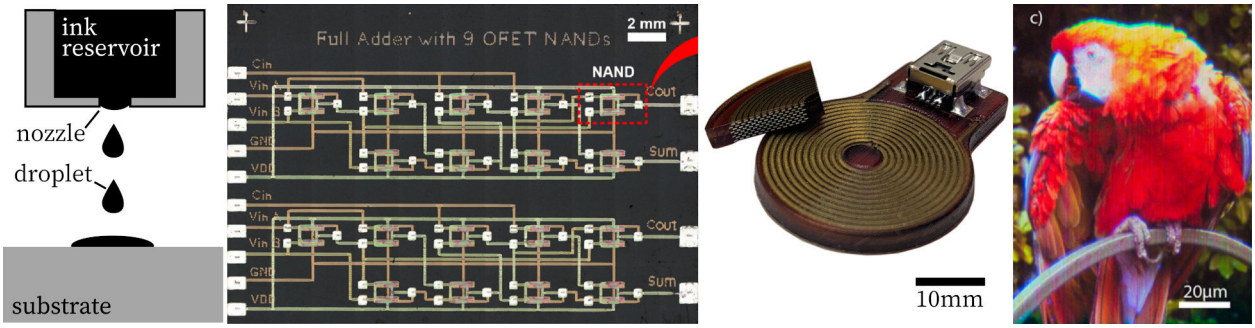

Figure 1.3: Left: the basic inkjet mechanism, in which liquid ink is expelled in droplets from a micron-scale nozzle by piezoelectric mechanical pressure or thermal expansion. Center left: an inkjet-printed full adder circuit [24]. Center right: printed thick insulating and conducting inks makes a 3D coil onto which a connector is soldered [23]. Right: EHD printing achieves 250 nm resolution [25].

A large limitation of inkjets is that they only work with liquid inks within a certain viscosity range. This prohibits the use of standard semiconductor materials—for example, silicon is only a liquid when molten above 1414 °C which is infeasible to work with[10]. Instead, inks are generally polymer-based in a liquid organic solvent that evaporates after printing. Conductive traces are possible by printing metal nanoparticles in liquid followed by sintering [26][27], but semiconductors are limited to low-performance complex polymers and metal oxides [24][28]. These material difficulties, compounded with reliability and accuracy issues, have limited the largest inkjet printed circuits to about 100 transistors [24][28].

Inkjets also have a low resolution limit: the method cannot print well with resolutions below about 20 µm (in printing industry terms, 1200 dots per inch). It is possible to use the spreading of droplets or chemical forces to achieve smaller features in one dimension [29]. Both resolution and viscosity limits can be improved by changing the deposition process to electrohydrodynamic jet (EHD) printing, where an electric field pulls a liquid into a sharp tip from which a smaller droplet is ejected [30]. This has been shown to reach 250 nm resolution [25][31] and is commercially available at 1 µm [32]. But materials must still start in a liquid phase and the reliability issues of clogged or spreading liquid inks are not improved.

[10]Most rocks are silicates, so molten silicon might be considered lava.

1.2.2 Resin 3D Printing and Two-Photon Lithography

Another category in high-resolution manufacturing is 3D printing methods that use liquid polymer resins specially formulated to be light-sensitive to harden to a solid upon exposure to the right wavelength. These can be solidified with a light pattern projected with conventional optics (not unlike photolithography), in which case the process is called stereolithography (SLA), or cured at the small focus of a laser, called two-photon lithography.

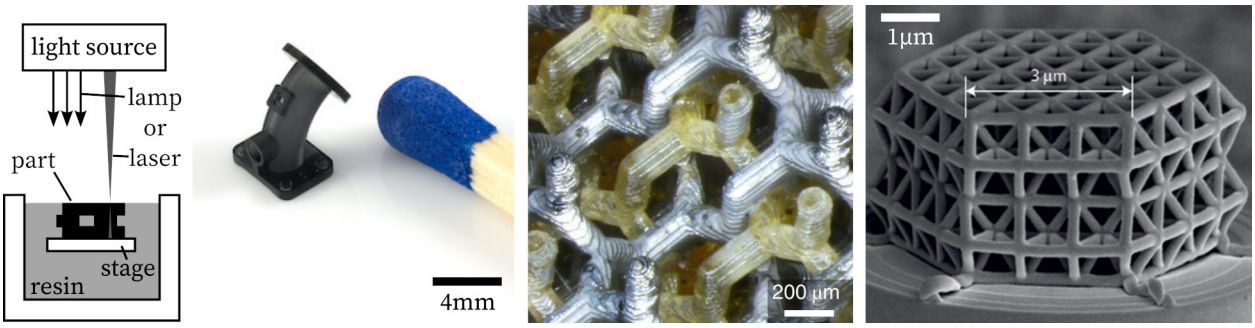

Figure 1.4: From left to right: resin printing techniques use focused light to create one layer of a 3D object at a time, a small tubing adapter made with SLA next to a matchstick [33], a multimaterial lattice printed by switching resin baths during an SLA print [34], and a significantly smaller lattice made with two-photon lithography [35].

These printers are usually only capable of printing a single material at once, and that material must be a light-sensitive polymer resin (a category even more restrictive than inkjet ink). There is some limited multimaterial capability: it is tricky but possible to change materials by moving the part under construction between multiple resin baths during the print. Postprocessing a print with electroless plating can make conductive traces [34], and piezoelectrics can be printed by embedding particles in the resin [36].

But these methods begin to approach interesting resolutions. While SLA 3D printing can only achieve perhaps 10 µm minimum features, two-photon lithography printers, which formulate their resin molecules to require absorption of two photons (not just one) to solidify allowing the intensity of a focal point of a laser to draw below the light diffraction limit, can regularly demonstrate almost 100 nm resolution [37]. This compares to photolithography (though not precise sub-100 nm thin film deposition methods).

The main strength of these resin printing processes is their 3D geometry capabilities, which can build photonic lenses [38] or MEMS actuators [39]. Microfabrication cannot make very complex 3D structures as that would require many photolithography layers which vastly increases fabrication time and cost[11]. However, the material limitations of resin printing are far too strict for broader applicability in electrical devices.

[11] Though this has been done in limited circumstances. See [40], which "3D prints" complex sub-millimeter metal mechanisms by microfabricating tens of layers of electroplated metal.

1.2.3 Aerosol Deposition and Cold Spray

Both inkjet and resin printing were limited primarily by their materials. There exists a different category of fabrication methods capable of printing more interesting metals and ceramics: small particles of material, either solids or liquid ink and from the nanometer to micrometer scale, are shot onto a surface in an air jet. This is vaguely similar to the sputtering or evaporation thin-film deposition methods of microfabrication, but faster, less controllable, and with some ability to draw patterns instead of uniformly coating a surface. Many varieties exist: cold spray [41], aerosol deposition [42], cluster beam deposition [43].

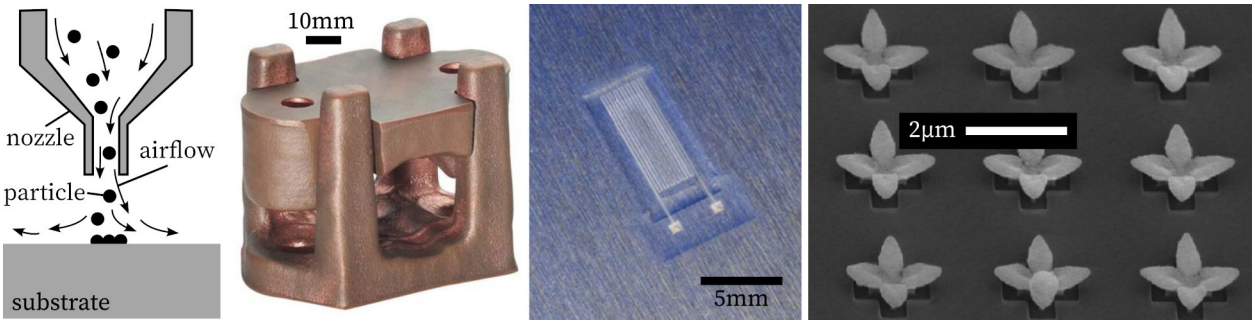

Figure 1.5: Left to right: a diagram of cold spray and aerosol deposition, which differ merely in scale, a copper cable clamp printed by cold spray [44], a silver and polymer strain gauge aerosol jet printed on aluminum [45], and 3 nm copper nanoparticles deposited into 3D shapes by an electric field formed by crosses in a microfabricated mask [46].

Material capabilities are very good and comparable with microfabrication [47]—cluster beam deposition has even been used as a microfabrication thin-film deposition tool [48][43]. It is possible to use liquid inks [49] or solid metals and ceramics which deform then form covalent bonds to the substrate (for details, see chapter 3) [50][51]. Multimaterial structures are easily made via serial deposition. Cold spray methods are used industrially [41] to produce hard ceramic coatings reaching over 90% of bulk properties and to 3D print large metal items [52][42][44]. Transparent ceramics and piezoelectrics are possible [42], and mixing particles gives material gradients [53]. Transistors have been aerosol jet printed with semiconducting inks [54][55][56][57], and depositing pure and doped silicon works [58][47][59].

The main limit of these methods is resolution [60], which requires extremely precise airflow. An aerodynamic lens is a particular fluid dynamic structure that focuses a given particle diameter [61]; sufficiently good control allows resolution down to ≈10 µm [62] but is ultimately limited by Brownian motion (section 4.2.1). Some promising experiments[12] use electric fields from charged masks to direct charged nanoparticles during deposition with sub-micron results [63][69][68], but this has not been explored fully or developed into a general printing method. As we will see shortly, the method proposed in this dissertation is essentially aerosol deposition with a better electrostatic focusing method bolted on top.

[12]These papers [46][63][64][65][66][67][68] were among the strongest a priori evidence that this dissertation's proposal could eventually work. [64] demonstrates minimum feature sizes as low as 35 nm!

1.2.4 Other Methods

Besides inkjet, resin printing, and aerosol deposition, there are many less common fabrication techniques still worth mentioning [70]. Some scale to higher resolutions than microfabrication with impressive capabilities, but all currently have some material or practicality limit that has prevented their use for semiconductor device manufacturing.

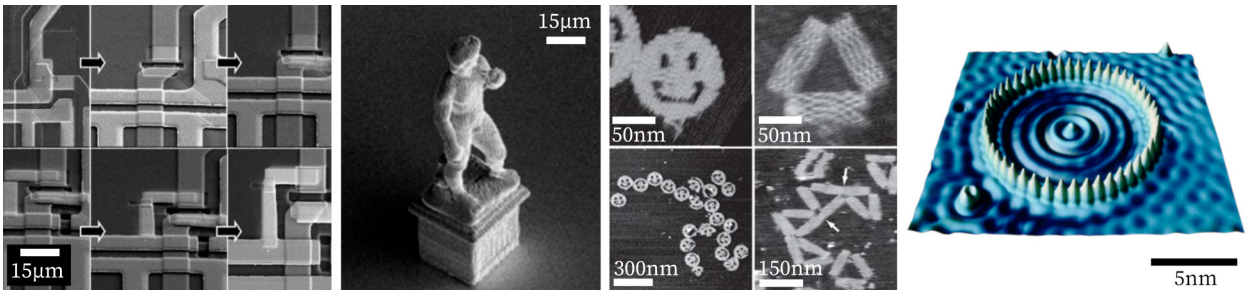

Figure 1.6: Left to right: circuit traces from tungsten and SiO_2 made with FIB [71], a statue electrochemically printed in copper [72], geometrical patterns made from assembled DNA molecules [73], and 48 iron atoms arranged on a copper surface via STM [74].

Focused beam tools: some methods electromagnetically focus a beam of electrons or atoms in vacuum, then use the narrow beam to interact with the surface of a material [75][76]. This includes scanning electron microscopes (SEMs), but the beam can locally initiate a chemical reaction with a surrounding gas to deposit material [77] as in focused electron (or ion) beam induced deposition (FEBID and FIBID)—or cure photoresist, in electron beam lithography. A focused ion beam (FIB) tool etches away material. These methods can reach sub-10 nm resolution but are very slow with limited material choices (e.g., no doped semiconductors). Combination "multibeam" FIB, FIBID, and SEM tools are used commercially to investigate, debug, and rewire small parts of microfabricated integrated circuits[13] [71][78][79]. Extensions of these methods have managed to deposit single atoms with sub-100 nm resolution [80]. All these are similar to what we propose; see section 6.5.4 for a detailed comparison.

Spatial atomic layer deposition (ALD): standard ALD, which creates films of atomically precise thickness by repeatedly layering certain gas precursor molecules, is common in microfabrication. By focusing these gases through a small nozzle scanned over a substrate it is possible to draw 2D patterns [81][82][83][84] (for CVD: [85][86]). However, the chemistry limits materials to what chemical precursors are available, and the nozzle resolution is a large 100 µm giving its atomically thin prints somewhat unwieldy large width-to-height ratios, making any devices simultaneously wider and slower to make than is practical[14].

Electrochemical printing: it is possible to deposit pure metals electrochemically [87] on a substrate submerged in a liquid bath through a small (microfabricated) nozzle with near 1 µm resolution [72][88]. Parallelism to print large objects is possible [89]. This method is restricted to metals capable of electrochemical deposition, i.e., no insulators or semiconductors.

[13] A FIB tool was likely used to make the chip cross-section in figure 1.1.

[14] It is possible that spatial ALD/CVD makes a good companion method to this dissertation's nanoparticle printing process, which should be generally more capable but worse at controlling film thickness.

Laser direct write: like focused beam tools, a laser can induce local material deposition [90]. Laser chemical vapor deposition (LCVD) directs a gas-to-solid reaction that can print metal [91] but is very slow. In laser induced forward transfer (LIFT), a thin film of material is suspended over a substrate where it (or a donor layer) is selectively hit by a focused laser to expand and fly off onto said substrate [92]. This can work with a broad range of materials including solid metals, but minimum resolution is typically limited to 1 to 20 µm.

DNA nanotechnology: in a dramatically different approach, it is possible to generate DNA strands that fold in liquid solution into nanoscale structures with near 1 nm resolution and atomic precision [93][94][73]. This makes millions of copies of the same structure, randomly arranged. Significant research is in progress, but there is not yet a reliable way to make electrical devices from these or connect them to even microfabricated circuitry.

Scanning probe lithography: in atomic force microscopy (AFM) and scanning tunneling microscopy (STM), a near atomically sharp tip is dragged over a surface with subatomic resolution to image it. This can instead be used for fabrication by selectively heating a substrate, transferring ink ("dip-pen lithography"), or even electrostatically pushing individual atoms [95][96][74]. These methods reach the highest resolution of anything discussed (comparable to or exceeding focused beam methods) and have been used to build parts of transistors [97], but are impractically slow and generally only capable of moving a single type of material at a time. Best used in combination with other methods.

1.3 Our Proposal: Nanoparticle Printing

We are now well-positioned to design a new fabrication method that avoids the limitations of existing methods to achieve the multimaterial high-resolution capabilities that semiconductor devices require.

In order to print standard materials—metals, semiconductors, and oxides—we'll use vacuum deposition similar to aerosol deposition or focused beam tools (or the physical and chemical vapor deposition processes used in microfabrication itself). Methods that operate with or in a liquid, like inkjet printing, two-photon lithography, and electrochemical printing, are too strongly restricted by chemical compatibility and material properties of their liquids. The ability to control the pressure, temperature, and composition of the environment around any part under construction is much more likely to provide in high-quality results than remaining in standard atmosphere or liquid.

To reach sufficiently high resolution, we'll ignore the small nozzle approaches of inkjet and electrochemical printing (which are limited to about 1 µm and can be unreliable due to clogged nozzles), focused light methods like photolithography and two-photon lithography (which are mostly diffraction-limited and constrain material properties), and gas jet focusing of aerosol deposition (which is limited to 10 µm by Brownian motion and inability to more precisely control fluid flow). We'll instead use the electrostatic focusing found in EHD printing and focused beam tools. This has no fundamental resolution limit as the electromagnetic field scales well below atomic level; the final theoretical resolution (which will be sub-1 µm) will come from other implementation details (chapter 6).

Specifically, we'll try to make the following idea work: begin with nanoparticles (clumps of atoms, as individual atoms would be too slow) of standard microfabrication materials, focus these electrostatically in vacuum, and impact them onto a substrate, where they should meld with the surface as in aerosol deposition methods. Switching between types of particles would allow multimaterial prints. If successful, nothing should prevent manipulation and printing of pure (and doped) semiconductor nanoparticles at very high resolutions.

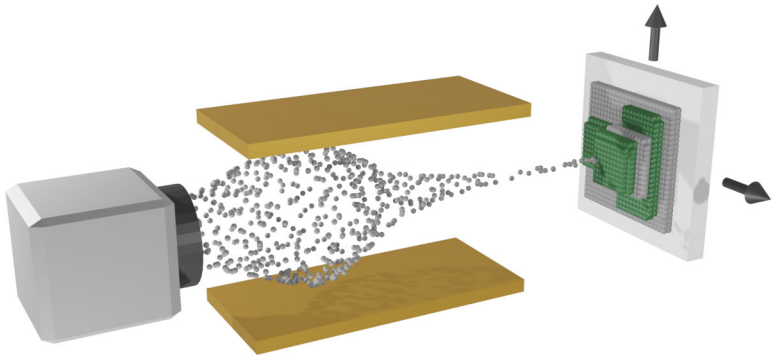

Figure 1.7: A cartoon of the basic idea: nanoparticles are generated (left), focused and accelerated in vacuum via electric fields between electrodes (gold, center), and finally shot onto a substrate, which is moved by a motorized XY stage in two dimensions to draw a pattern. Switching between types of nanoparticles would allow depositing different materials.

As we saw in the prior art, this idea is fundamentally similar to gas jet processes like cold spray, aerosol deposition, and cluster deposition, but we add electric fields to focus particles beyond the limits of fluid dynamics. It has been recognized that focusing resolution is the main limit to using aerosol deposition for nanoscale manufacturing [60], and several groups have previously proposed using electric fields for this [98][99][100][64][63], but none have figured out an ideal general solution. As we will see, this thesis develops a more capable electrostatic focusing mechanism that should achieve higher resolution. Our method is also similar to focused ion beam tools (see section 6.5.4) but uses nanoparticles instead of single atoms and at lower impact velocities.

In the rest of this dissertation, we'll discuss our progress engineering each part of this system. In chapter 2 we will see how to create nanoparticles in inert gas, and chapter 3 will theorize what needs to be done to print them. Some minimal low-resolution but multimaterial deposition is surprisingly straightforward with aerosols in chapter 4. To achieve higher resolution we describe the process of electrically charging nanoparticles in chapter 5 as a prerequisite for chapter 6, where we find electrostatic focusing mechanisms are common across particle accelerators and mass spectrometry then design our own with techniques theoretically capable of printing with sub-1 µm resolution. Finally, in chapter 7, we will summarize our results: although we didn't manage to demonstrate a complete system or print a transistor, we came close, showed partial success, and have a short roadmap toward a full demonstration with no major roadblocks. We'll show this printing process has the potential to be easier, cheaper, and faster than microfabrication for some limited applications, achieving our original goal.

Chapter 2

Nanoparticle Generation

The first step in printing nanoparticles is to, well, somehow obtain nanoparticles. We'll discuss what this means then detail our construction of two custom nanoparticle sources.

What is a nanoparticle? For our purposes, a nanoparticle is just a clump of atoms. Assume it is roughly spherical and we can define its size by its diameter, which we'll typically want to be between 5 nm and 50 nm or so (in the nanometer range, thus "nanoparticle"). We'll use nanoparticles of all the same type of atom: all silicon or all aluminum, perhaps, though sometimes we might use slightly doped silicon[1] or an oxide like SiO_2.

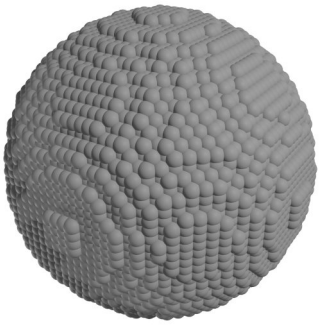

Figure 2.1: A cartoon representation of a simple example nanoparticle. Each gray sphere is an individual atom. This is about 42 atoms wide, or perhaps 10 nm in diameter, with about 40000 atoms in total. Note many inorganic nanoparticles are small enough that their crystal structure becomes monocrystalline or amorphous, not polycrystalline [101].

Nanoparticles are common [102]. Any aerosol, like smoke or fog, is simply small solid or liquid nano (or micro) particles moving around in a gas. Many more complex biological molecular structures, like viruses or organelles, could arguably be considered nanoparticles. For our purposes, however, we'll stick to spherical nanoparticles of a single solid material.

[1] This is important—it is why printing semiconductor devices with reliable doping should be possible.

Why do we want nanoparticles in particular? The trouble comes from our desire to place small bits of matter serially. We could try printing single atoms one at a time, but that would be slow[2]: even at a ridiculously fast 1 million atoms per second, even a tiny 100x100x1µm chip would take multiple years to print, not to mention this is overkill as we probably couldn't place those atoms with atomic resolution anyway. We could speed this up at the cost of spatial resolution by printing a cloud of several atoms hitting the same area at once[3]—but at this point we might as well use nanoparticles, which we'll see squish together on impact to give a similar result (see chapter 3) and print faster than atoms when charged (see section 6.5.3). On the other hand, if we printed even larger clumps of atoms (say, 10 µm diameter), we couldn't get the sub-1 µm resolution we need for semiconductor devices.

For reference, here are the approximate number of atoms in and total masses of nanoparticles of some particular diameters and materials, assuming the same densities as in bulk:

	Au (gold)	SiO_2 (glass)	Si (silicon)	Cu (copper)
atoms, 1 nm	31	42	26	44
atoms, 10 nm	30900	41700	26200	44500
atoms, 100 nm	30900000	41700000	26200000	44500000
mass, 1 nm	1.01×10^{-23} kg	1.39×10^{-24} kg	1.22×10^{-24} kg	4.69×10^{-24} kg
mass, 10 nm	1.01×10^{-20} kg	1.39×10^{-21} kg	1.22×10^{-21} kg	4.69×10^{-21} kg
mass, 100 nm	1.01×10^{-17} kg	1.39×10^{-18} kg	1.22×10^{-18} kg	4.69×10^{-18} kg

Table 2.1: Some example nanoparticle properties calculated with densities from [103].

2.1 Nanoparticle Generation Methods

Because nanoparticles are so prevalent, significant study has gone toward simple reliable ways of making them. Breaking down larger material by physical grinding or aerosolizing a liquid tends to make larger particles, but nanoparticles are small enough they can be grown from individual atoms sticking to each other under the right conditions.

The most common particle generation methods include:

- **Mechanical milling:** Large chunks of material are ground down into powder via mechanical action [104][105]. Resulting particles are larger than at least 100 nm as smaller particles melt together (elaborated on below). Can be used to alloy materials together (frequently used in metallurgy).
- **Atomization:** Also referred to as nebulization or aerosolization. Gas is blown through a liquid, making small droplets carried as an aerosol in the gas [106]. Used for aerosol deposition, paint guns, and air fresheners. It is also possible to atomize molten (liquid) metal, which is a common way to mass-produce metal powder in industry [107], or even

[2]This has kind of been done, excruciatingly slowly: see [80] or [74], and section 6.5.4.

[3]Microfabrication thin-film deposition processes like evaporation, sputtering, and CVD arguably deposit clouds of single atoms over an entire wafer (without patterning), in minutes to hours.

blow air through a metal powder instead of a liquid. All these result in fairly large particle sizes in the micrometer range.

- **Electrospray:** A high voltage can be used to draw a liquid out from a narrow nozzle (a "Taylor cone") and break it into droplets [108][109]. This can make liquid nanoparticles, but the liquid can also evaporate to leave molecular ions or nanoparticles that were already in the liquid solution [110][111][30][112]. Commonly used in mass spectrometry to remove molecules from a liquid solution. Slow compared to other methods[4].
- **Liquid nucleation:** One of most reliable ways of making particles truly in the nanometer size range. Atoms or molecules are dispersed in a liquid solution carefully engineered so these atoms nucleate and stick together to grow nanoparticles [113]. Commonly used in biomedical applications or research. Pre-grown nanoparticles in liquid are commercially available in many different materials [114].
- **Vapor nucleation:** Also called gas phase nucleation, vapor synthesis, or aerosol synthesis. Similar to liquid nucleation but in a gas. Commonly occurs in the atmosphere (for example, cloud formation) [115][116], and making metal particles is possible. Can even happen in microfabrication processes like CVD [117] or PVD [118].

Note several more methods exist to generate individual atoms as ions for focused ion beam sources (see chapter 5 and section 6.5.4), but these are generally too small and the production rate and efficiency too low for what we want.

Of all these methods, which do we choose? Vapor nucleation is the most promising.

Recall our materials need both very high material purity and dimensions below 100 nm. The need for high purity to sometimes better than one part per billion (see chapter 1) by itself rules out mechanical milling—which might contaminate particles with atoms worn off the milling apparatus by mechanical contact—or atomization, liquid synthesis, and electrospray methods, in which case the particle might be somewhat contaminated by the surrounding liquid. Vapor nucleation is a promising option because no atoms are involved save the material we want and a background gas, which can be chosen to be an inert noble gas (He, Ar, etc.) that should not react with the nanoparticles.

The nanoparticle size also matters significantly. Sufficiently small nanoparticles (below our approximate threshold of 1 µm or so, not entirely coincidentally) react very easily with their surroundings. Because of their size and geometry, a large fraction of their atoms are near their surface with freedom to move. The resulting surface energies are much higher than in bulk [119]. This also decreases the melting point of nanoparticles—in fact, nanoparticles often melt into to each other slightly at room temperature. The result is that nanoparticles packed together as a powder, like an everyday bag of flour[5], will tend to agglomerate until

[4]We briefly tried electrospray, without much success. Dr. Williams of [111] informed us producing up to 10k 100 nm particles per second is typical for use in charge detection mass spectrometry. That is a mass rate of $1 \times 10^{-3}\,\mathrm{mg\,h^{-1}}$, 3 orders of magnitude slower than our spark ablation and laser ablation sources.

[5]The reader may be familiar with dust explosions from clouds of flour or metal. These are a result of particle surface reactivity: an exothermic reaction with a surrounding gas, multiplied by the large surface area of a collection of particles, is a significant amount of energy. Dust explosions are often from more easily manufactured microparticles; nanoparticles, due to higher surface energies, would be worse.

their clumps reach at least micron size scales[6] [120]. In order to store nanoparticles, we'll need to either keep them in a liquid (which has contamination concerns, as noted previously) or levitate them in a gas. This last option best fits vapor nucleation.

2.1.1 Vapor Nucleation

This is how vapor nucleation creates nanoparticles [121][122][123][124]:

The material we want to make nanoparticles of is first vaporized into a cloud of its constituent atoms. This is easy enough to do by any of several methods: add enough energy and any solid or liquid will evaporate, sublimate, or otherwise break up into a gas or plasma.

As this cloud of atoms cools down, it loses thermodynamic stability (is supersaturated), at which point multiple effects occur at different rates: atoms condense and form clusters (another name for very small nanoparticles with mere tens of atoms), these clusters collide and coagulate into larger clusters (which coalesce into uniform crystalline structures), and some atoms evaporate off existing clusters to make them shrink again. These processes happen simultaneously at different rates. According to classical nucleation theory, which compares the growth of cluster surface area (increasing instability due to evaporation) vs. volume (increasing stability from bulk energy), clusters become stable and continue to grow above a critical diameter; below this they dissipate [43][125][126][127]. The result is a distribution of particle sizes (often lognormal [128][102]) around some nonzero mean value. Particles are mostly rather chunky polyhedra but are close enough to spherical for our purposes.

This can work in vacuum [47][43] but also in gas[7] (preferably an inert gas that does not react). This gas can modify the process by, e.g., adjusting the cooling rate or atom collision frequency. It is also possible this gas reacts with the nanoparticles to add an oxide layer or other coating, possibly making multimaterial nanoparticles [60][128], and trace contamination levels can be maintained below the limits required in microfabrication [129]. As we will see in chapter 4, using a gas medium also lets us conveniently move nanoparticles.

Many options exist to implement vapor nucleation [130][101]. The atom vapor can be generated by directly heating a solid [131], magnetron sputtering [132], electrical joule heating, or a laser, and the resulting cloud moved though assorted pressure differentials and geometries. Accurate quantitative analysis of nucleation is possible but somewhat involved [125], so for purposes of this work we'll start with trial and error based on existing literature results.

In order to develop our proposed nanoparticle printer, we began by building a spark ablation nanoparticle generator but eventually switched to laser ablation to improve consistency, material capability, and system compatibility.

[6] Selective laser sintering (SLS) 3D printing, which melts together layers of metal or plastic powder with a laser, is limited in resolution by its particle diameter, which cannot be below 1 µm for this reason [120]. If we successfully print nanoparticles, we will have turned this previously undesired effect to our advantage.

[7] This nucleation process also works in liquid—that's what aforementioned liquid nucleation is—and is closely related to how crystals grow in general.

2.2 Spark Ablation

As the first step in developing a nanoparticle printer, we built a spark ablation nanoparticle generator as a source with which to test nanoparticle manipulation and printing.

Spark ablation begins with repeated electrical spark discharges between two electrodes of the desired material. The large current of each spark through a small area on the surface of the electrodes results in localized joule heating, vaporizing that part of the electrodes, from which vapor nucleation proceeds. A background gas at significant pressure is required for the initial spark and can also carry the nanoparticles away to a point of use.

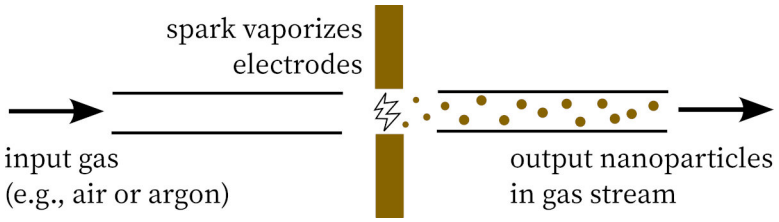

Figure 2.2: A minimal cartoon illustrating spark ablation nanoparticle generation. A spark locally heats and vaporizes two electrodes, the vapor from which condenses into nanoparticles which are pushed along in a gas flow.

This method was first introduced in 1988 [133] and has since seen wide use [134][128][68] with little change to its fundamental principles[8]. Its advantage is simplicity[9]: the only equipment required for a minimal system is several electrodes and tubing assembled with merely millimeter precision in atmosphere and a small high-voltage circuit. Metal nanoparticles are easy, and spark ablation has also been shown to make doped silicon nanoparticles [58]. Although the electrodes must be conductive so creating insulating nanoparticles directly is not possible, metal nanoparticles can be oxidized if the surrounding gas contains oxygen [128], giving us all the basic materials semiconductor devices need.

We constructed the system shown in figure 2.3. The spark discharge apparatus itself is held in an airtight KF-25 6-way cross vacuum fitting to allow control of pressure and gas movement. Two metal electrodes of the material we want to create nanoparticles out of and about 1 mm in diameter are held in miniature brass drill chucks, which are connected to custom vacuum feedthroughs built of stainless steel KF-25 fittings, copper wire, SLA 3D printed parts from Formlabs Durable resin [135], and Loctite Hysol 1C epoxy[10]. The electrodes are connected to external spark circuitry by alligator clips[11] on the feedthroughs. The electrodes can be

[8]Spark ablation generators are commercially available from [51] (a company founded by Dr. Schmidt-Ott of [133] and [128]). These off-the-shelf generators are well-engineered with optimized electrode geometry and improved circuitry but cost (quoted) $80k each. We chose to build our own for better system integration, to more easily handle multiple materials in the future, and to avoid dwarfing the rest of the nanoparticle printer cost as tabulated in section 7.2.1.

[9]Contrast this with cluster beam synthesis methods, which more conventionally heat metals to increase their vapor pressure and need a high vacuum [43], or laser ablation which needs a sufficiently capable laser.

[10]Which is compatible with high vacuum systems and cheaper than competing Torr Seal brand epoxy.

[11]Carefully monitored. Please do not use alligator clips for high voltages on a production system.

removed and replaced by unfastening the KF-25 clamps holding them to the 6-way cross and are adjusted until the gap between the electrodes is 1 mm to 2 mm[12]. We were thus able to change the electrode material to anything in a thin cylindrical form factor including off-the-shelf copper, steel, and gold wire[13], or even pieces of a shattered p-type silicon wafer fit into the chuck[14].

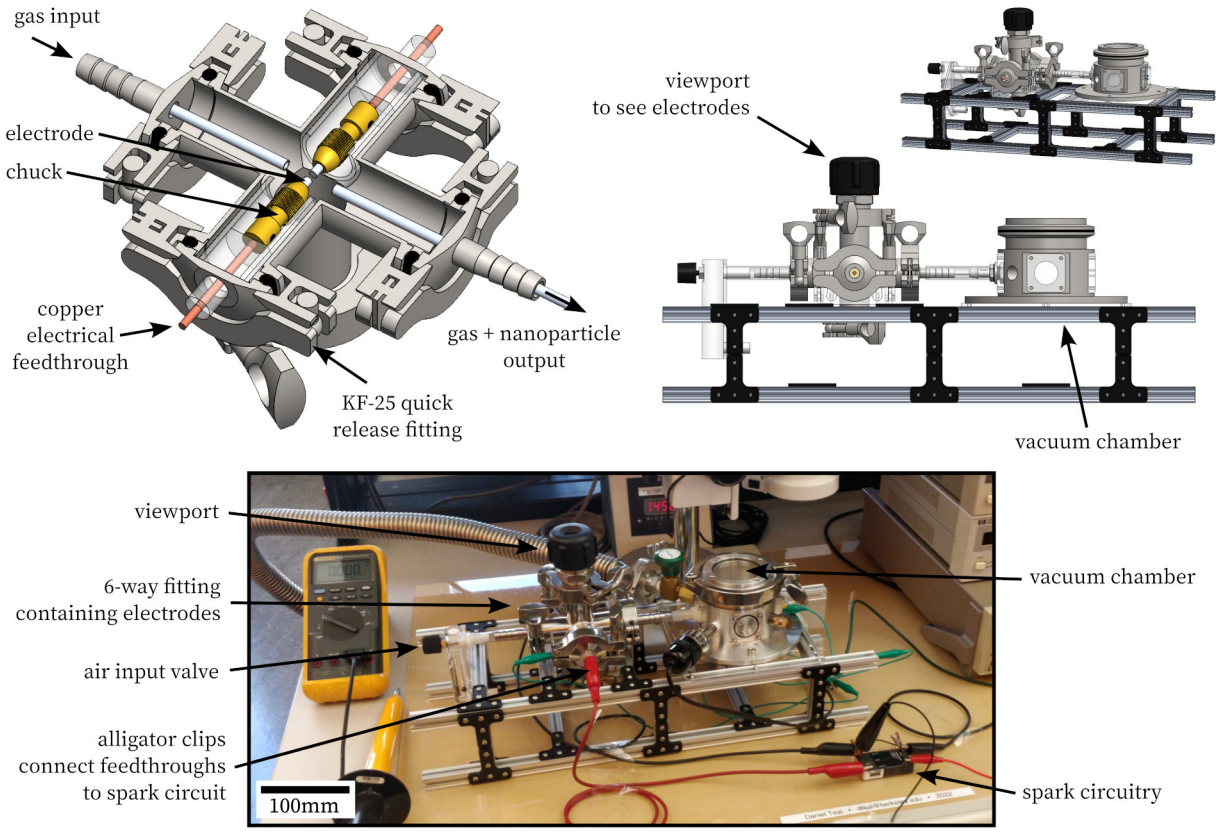

Figure 2.3: Spark ablation nanoparticle generation system. Top right: a CAD model cross-section showing the spark electrodes and tubing. Top left: CAD model of entire spark ablation test setup including input gas flowmeter/valve, generator, and secondary vacuum chamber. Bottom: physical implementation of the above system also including a small high-voltage spark circuit and a high voltage multimeter.

[12]While this worked, we recommend future engineers build a system to more easily finely adjust the distance between these electrodes, which is an important quantity in spark behavior.

[13]A 55 mm long 0.38 mm diameter 24K (0.9995 purity) gold wire was purchased from an eBay vendor for $29, equal to the raw material cost plus a significant markup. This demonstrates the extreme material efficiency possible in nanoparticle printing (elaborated on in section 7.2.3). A minimal microfabrication gold evaporation or sputtering target needs to be significantly larger and thus often costs $10k or more.

[14]Cylindrical silicon rods are available but much less common than flat wafers, especially in electrical semiconducting grades. This is another point in favor of laser ablation, which can use flat material targets.

Perpendicular to the electrodes are two aluminum tubes of 4 mm inner diameter, each about 1 cm from the electrode centerpoint. One tube about 150 mm long connects to a vacuum chamber continually pumped to a steady-state pressure of about 1 Torr (below 1% of atmospheric pressure, 760 Torr), while the other is about 100 mm long and connected to a needle valve (and rotameter for flow measurement) to atmosphere. Air is continually pulled at about $1\,\mathrm{L\,min^{-1}}$ through the needle valve, past the spark discharge electrodes—where it hopefully picks up nucleated nanoparticles from spark-generated vapor—and into the vacuum chamber. Note replacing air with argon would reduce oxidation, but in both cases our small nanoparticles should primarily follow the airflow rather than gravity (see chapter 4). We estimate the pressure of the air around the spark electrodes to be between 0.5 and 1 atmospheres. An ideal setup might increase this pressure up to several atmospheres of pressure, which results in higher breakdown voltage[15] and spark energy and thus more material vaporized and a higher nanoparticle generation rate [136].

The next step is to create sparks between the electrodes. A spark can be created by applying a high voltage that exceeds the breakdown voltage of the surrounding gas at its pressure and distance, which is given by Paschen's law as in figure 2.4. The resulting electron avalanche makes a conductive plasma pathway that short-circuits the electrodes, causing a large current and significant heat. The longer this current can be sustained, the larger the spark[16]. Repeat this process to continually generate nanoparticles.

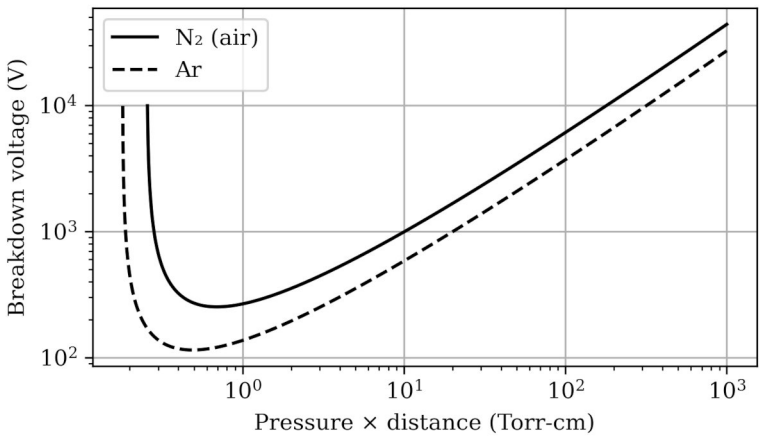

Figure 2.4: A graph of Paschen's law, which gives the voltage required to cause gas breakdown via electron avalanche (Townsend discharge) between two electrodes at a given pressure and distance (which are not independent). Curve data (from [137]) is approximate; these curves can vary significantly [138]. At high pressures, the lower gas mean free path requires a larger voltage to accelerate electrons to avalanche energies. At low pressures, there are too few stray electrons and gas atoms to produce an avalanche. Our spark discharge setup is slightly to the right of center. Note also there is never breakdown below a minimum of a couple hundred volts even if electrodes are very close together. This will be important in chapter 6.

[15]The dependency of spark behavior on pressure means the pressure cannot be varied solely to optimize nanoparticle nucleation. This is another downside of spark ablation that laser ablation does not share.

[16]This is a miniature lightning bolt.

We created these sparks with the circuit of figure 2.5. An XP Power FS20-12 2kV DC 5mA power supply was connected in parallel with a 47nF high voltage capacitor and the spark electrodes. The power supply slowly charged the capacitor until it exceeded the gas breakdown voltage, typically around 1.5 kV, at which point the full charge of the capacitor, around 50 mJ, was discharged in a spark. Increasing spark energy should increase vaporized material and, somewhat, particle size [136][134]. This process repeated at about 10 Hz to 20 Hz, with random fluctuations [136], rate limited by the power supply current. Nanoparticle production rate is proportional to frequency; the literature exceeds 150 Hz [136].

Safety note: high voltage is dangerous. The low kilovolt level and 50 mJ spark energy used here is enough to potentially cause electrical injuries. As safety measures, high voltage wires were placed safe distances apart to avoid breakdown in air between wires, the vacuum chamber was connected to earth ground, a bleeder resistor discharged the capacitor, and the system was completely disconnected when not in use.

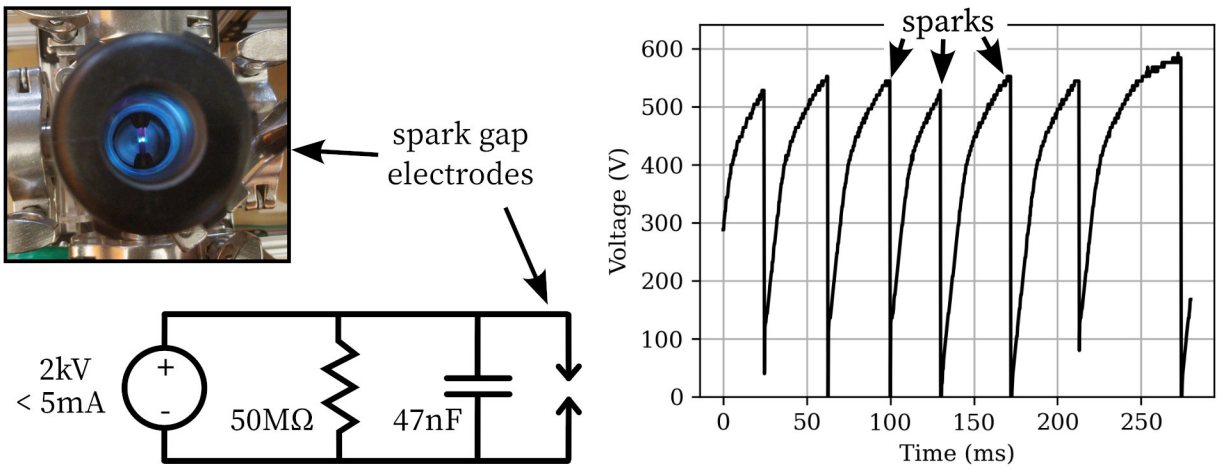

Figure 2.5: Top left: picture of a spark between electrodes seen through viewport. Bottom left: spark circuit diagram. Right: measured voltage across electrodes vs. time (albeit at a lower pressure and voltage than typical), showing multiple sparks with variable timing.

At this point we almost have all the hardware required to implement spark ablation except that we are missing a way to detect and measure the resulting nanoparticles to know whether it worked. This is nontrivial as each sub-100 nm particle is too small to be visible in the 1 µm diffraction-limited resolution of an optical microscope and even a cloud of nanoparticles in gas is still too diffuse to be seen. Instead, the standard tool for nanoparticle and aerosol detection and measurement is a differential mobility analyzer (DMA) from aerosol science [102]. A DMA takes as input a stream of nanoparticles in gas (precisely like we hope to make), electrically charges these nanoparticles (typically via radiation-based diffusion charging; see chapter 5), then detects an electric current from particles hitting a conductive plate (a

Faraday cup). Carefully deflecting particles with an electric field allows only a subset of particles with a particular air drag mobility coefficient to be detected, and scanning over these subsets produces a histogram of nanoparticle diameters. But although DMAs are widely used in the literature [136], we were not able to access one. This does not matter too much yet—this project's focus is on nanoparticle deposition and manipulation; the particles themselves can be characterized further in future work.

Instead, we chose to directly deposit nanoparticles on a surface where a sufficiently large deposit built up over time should be visible and perhaps measurable via optical or electron microscope. This is also a common practice in aerosol science, where it is called impaction [102] (and is also the principle behind aerosol deposition): nanoparticles are either caught in a gas-permeable filter or shot out of a nozzle where their inertia suffices to make them impact a surface (for more details, see chapter 4). We implemented these methods by adding a filter[17] or a 0.21 mm ID nozzle 1–3 mm from a substrate, respectively, to the setup vacuum chamber as shown in figure 2.6. After initial filter paper tests, we continued only with nozzle-based impaction to allow the use of many kinds of substrates.

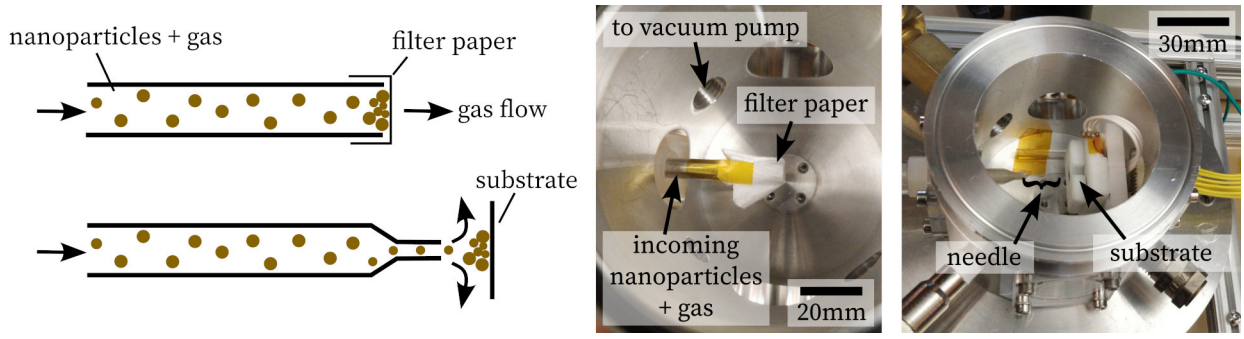

Figure 2.6: Left top and bottom: cartoons illustrating aerosol collection via filter or impaction, respectively. Center: nanoparticles moving through metal tubing from spark ablation generator into secondary vacuum chamber are captured by a filter attached to the open tube end. Right: the filter is replaced by a dispensing needle placed several millimeters from a substrate (that could be any flat surface but here is actually a custom XY stage).

We are finally ready to test nanoparticle generation. As pictured in figure 2.7, we began with copper electrodes and observed reliable deposits on filter paper, steel, and silicon after a deposition time of tens of seconds. Gold deposits well on steel but not glass, in which case it adheres to itself but flakes off the substrate. This is frequently seen in standard microfabrication due to gold's inability to oxidize; an adhesion layer of chromium or titanium is placed between SiO_2 and gold. All these are excellent signs: we successfully transferred material from electrodes to substrate and can conclude nanoparticle (or microparticle) generation is at least minimally functional.

[17] As filter paper we used Filtrete Ultra Allergen vacuum bags, which claim to trap 99% of airborne particles 1 µm or larger. For a more repeatable result, [58] chose Millipore Durapore 0.45 µm PVDF filters.

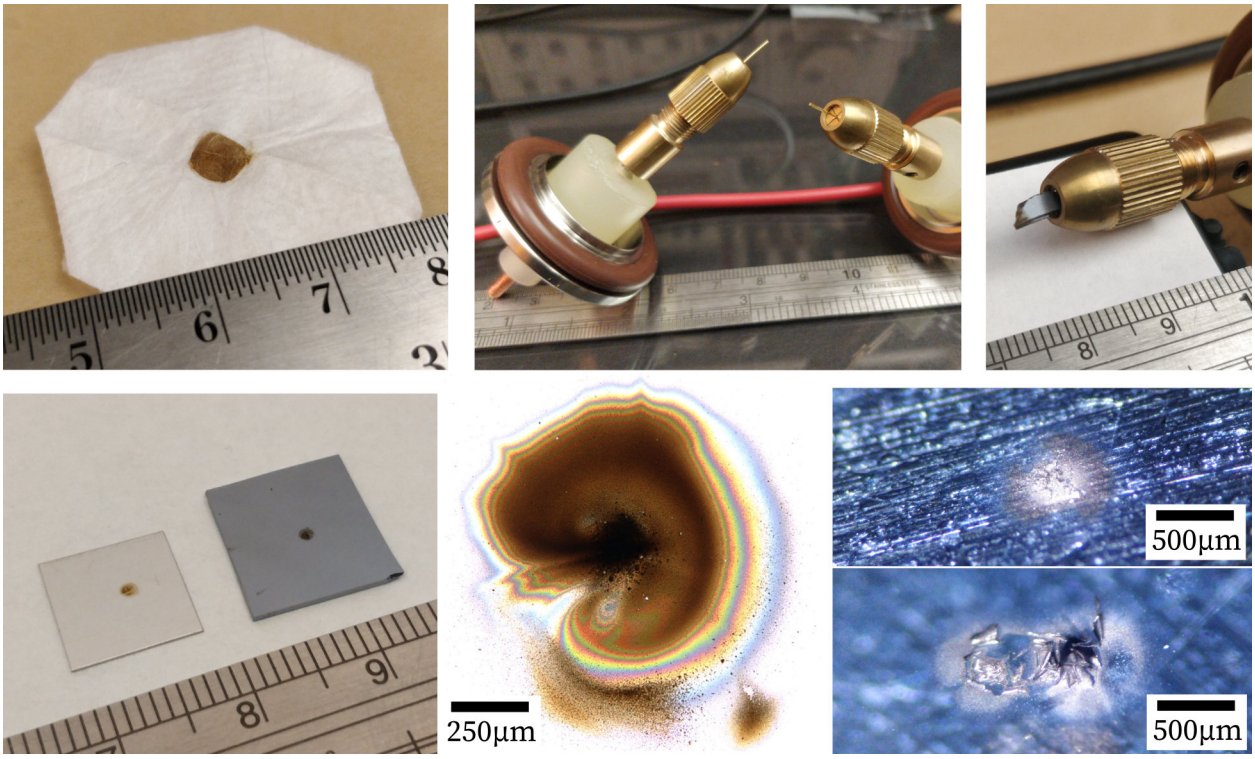

Figure 2.7: Spark ablation results. Clockwise from top left: copper deposited on filter paper. Gold wire electrodes mounted to chucks and feedthroughs. A silicon wafer shard as electrode. Gold deposited on steel (above) and glass (below); note the gold adheres to itself but not to the glass. A micrograph of a very large copper deposit on silicon demonstrating variation in particle diameter and airflow. Finally, copper on steel (left) and silicon (right).

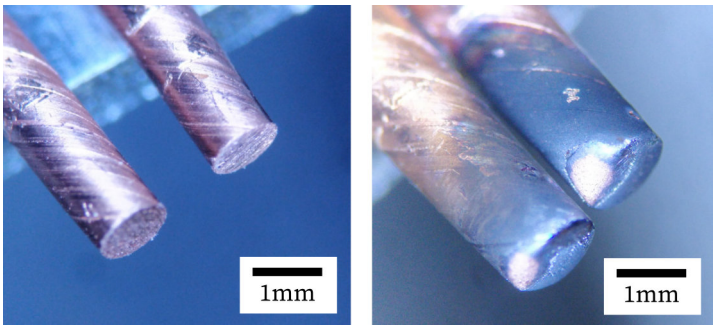

Figure 2.8: 1.3 mm diameter copper electrodes before (left) and after (right) being used as spark discharge electrodes. SEM EDS analysis suggests the black film may be carbon.

Now that we have a working spark ablation nanoparticle generator, we can perform at least some minimal characterization as previously noted before continuing to study nanoparticle movement in later chapters.

Rate measurement: we approximated the production rate by measuring copper electrodes (figure 2.8) before and after generating nanoparticles for 1 hour (spark rate 1 Hz to 5 Hz). We found a total mass loss of 0.6 mg, i.e., nanoparticles are made at 0.6 mg h^{-1} (if 10 nm, 3.5×10^{10} particles/s). The literature, using a better spark power supply capable of 100 Hz operation, reports anywhere from 1 to 30 mg h^{-1} [136]. This is a good sign we have successfully replicated the prior art. These are also convenient numbers for microfabrication: at only 0.6 mg h^{-1} a reasonably sized 10x10x0.01mm chip[18] could be printed in 15 hours.

Nanoparticle size: as stated earlier, the nanoparticle size distribution can be approximated by analysis of deposits. We impacted copper nanoparticles on a clean silicon wafer for 2 min to create the large deposit pictured in the bottom center of figure 2.7. Based on that image as well as the SEM[19] results shown in figure 2.9, it appears the majority of particles fell below $\approx$ 100 nm and formed a thick solid (and cracked) film; a minority of particles were 1 µm to 10 µm in diameter. This is excellent: we are generating sub-micron particles and future work should be able to characterize and control this further.

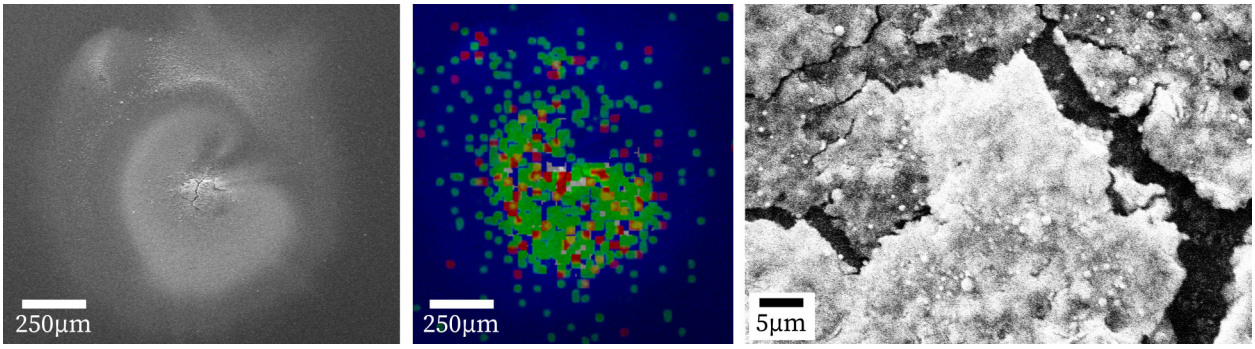

Figure 2.9: Left: SEM image of copper deposit on silicon. Observe the thick cracked film in the center and some larger particles near the top. Center: energy dispersive x-ray spectroscopy (EDS) image showing elemental composition. Blue is Si, green is O, red is Cu: apparently the copper is heavily oxidized (as expected due to our use of air; see section 4.3.3). Right: close-up SEM image of deposit center showing a cracked film presumably formed of agglomerated sub-100 nm particles plus several larger particles.

Although our spark ablation nanoparticle generation appears to be a success, the method has several problems. First, it cannot create insulating nanoparticles without inconvenient gas-phase oxidation reactions [128]. Second is its inconsistent generation rate: nanoparticles are generated in groups at each spark instead of in a continuous stream. Finally, the sparks creates very significant[20] electromagnetic interference (EMI). These limitations all have workarounds (conductive particles can be oxidized, particles can be buffered into a steady stream, and EMI can be shielded), but were enough to prompt us to experiment with a second vaporization method: laser ablation.

[18]This is typical. Chips made with the SkyWater SKY130 130 nm microfabrication process are 12 µm of transistors and wiring atop a silicon substrate [139], and most chips are several millimeters on a side.

[19]After testing the sample to ensure no particles would be released into the SEM chamber as required by its maintainers. We chose to minimize SEM usage for the rest of this dissertation over these concerns.

[20]We observed 9 V oscillations on a nearby 12 V DC lab power supply due to spark-generated EMI.

2.3 Laser Ablation

We implemented a laser ablation nanoparticle generator after finding the previously mentioned limits of spark ablation. This laser-based process is very similar. Instead of vaporizing electrodes with joule heating from a spark, material targets are instead vaporized by a laser; the rest of the apparatus can remain identical. Compared to spark ablation, EMI should be insignificant, the generation rate more constant, and material capabilities broader.

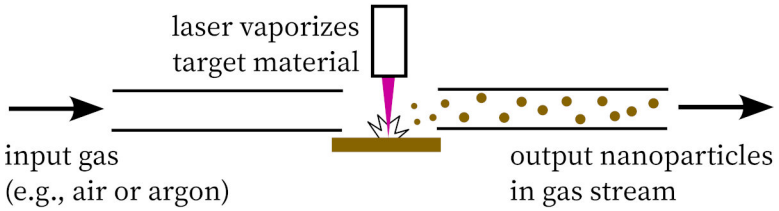

Figure 2.10: A simple cartoon illustrating laser ablation nanoparticle generation. A laser of the correct wavelength and intensity heats and vaporizes material, which condenses into nanoparticles which are pushed along in a gas flow.

This method is widely used with a variety of conducting, semiconducting, and (unlike spark ablation) insulating oxide materials [140] and has existed since at least 1981 [141][142]. The fundamental laser vaporization process is the same as used in laser cutting and machining [91] since 1962 [143]: a laser is absorbed in a material, generally via exciting electrons, and the energy is quickly coupled to the surrounding nuclei as heat[21]. If the incoming laser power is sufficiently larger than the rate at which heat is conducted and spread throughout the material, part of the material will become hot enough that it vaporizes. The material target can be a flat surface or a microparticle aerosol [147][148][149].

For our purposes, we need only that the laser (a) is of the correct wavelength to be quickly absorbed and (b) has peak intensity sufficient to heat material to vaporization. Metal machining most most commonly uses 1064 nm wavelength lasers [150], and higher intensities can be achieved by pulsing the laser (in nanoseconds or shorter) instead of a lower constant average power ("continuous wave"). The laser ablation source of [142] used a 1064 nm Nd:YAG pulsed laser (5ns and 10–30 mJ per pulse) to evaporate metals within a helium carrier gas at 1 to 2 atmospheres of pressure. Adjusting gas flow controlled nucleation conditions.

Historically, these lasers have been rather expensive (above $10k), but diode-pumped solid state (DPSS) lasers have recently become significantly cheaper and accessible. We acquired an xTool 1064 nm DPSS laser module designed for metal etching [151] with 2 W average optical power, 15 kW peak power, 20 kHz pulse rate, 7 ns pulse width, and 100 µJ per shot for less than $400 new. Its stock lenses produce a 30 µm diameter spot size with 20 mm throw and perhaps 1 mm depth of field. It is controlled by a standard 3.3 V PWM signal and 24 V power supply, making it easy to integrate into our own custom systems.

[21] There are minor variations to this basic physical process, e.g., a sufficiently intense and fast (femtosecond) laser can completely strip electrons via thermionic emission before they transfer heat elsewhere, and the remaining positively-charged nuclei undergo Coulomb explosion [144][145][146].

Safety note: high-intensity lasers are very dangerous as they can easily blind you. Above around 500 mW optical power (a class 4 laser), even scattered light can cause eye damage. The 1064 nm 2 W pulsed laser used in this work is easily in this category. To ensure safety, we built a full enclosure around the laser, added safety interlocks to only turn on the laser with the enclosure closed and software in the correct state, and ran it only when wearing high-quality laser safety glasses (ThorLabs LG10) rated to bring the worst-case intensity below maximum permissible exposure limits.

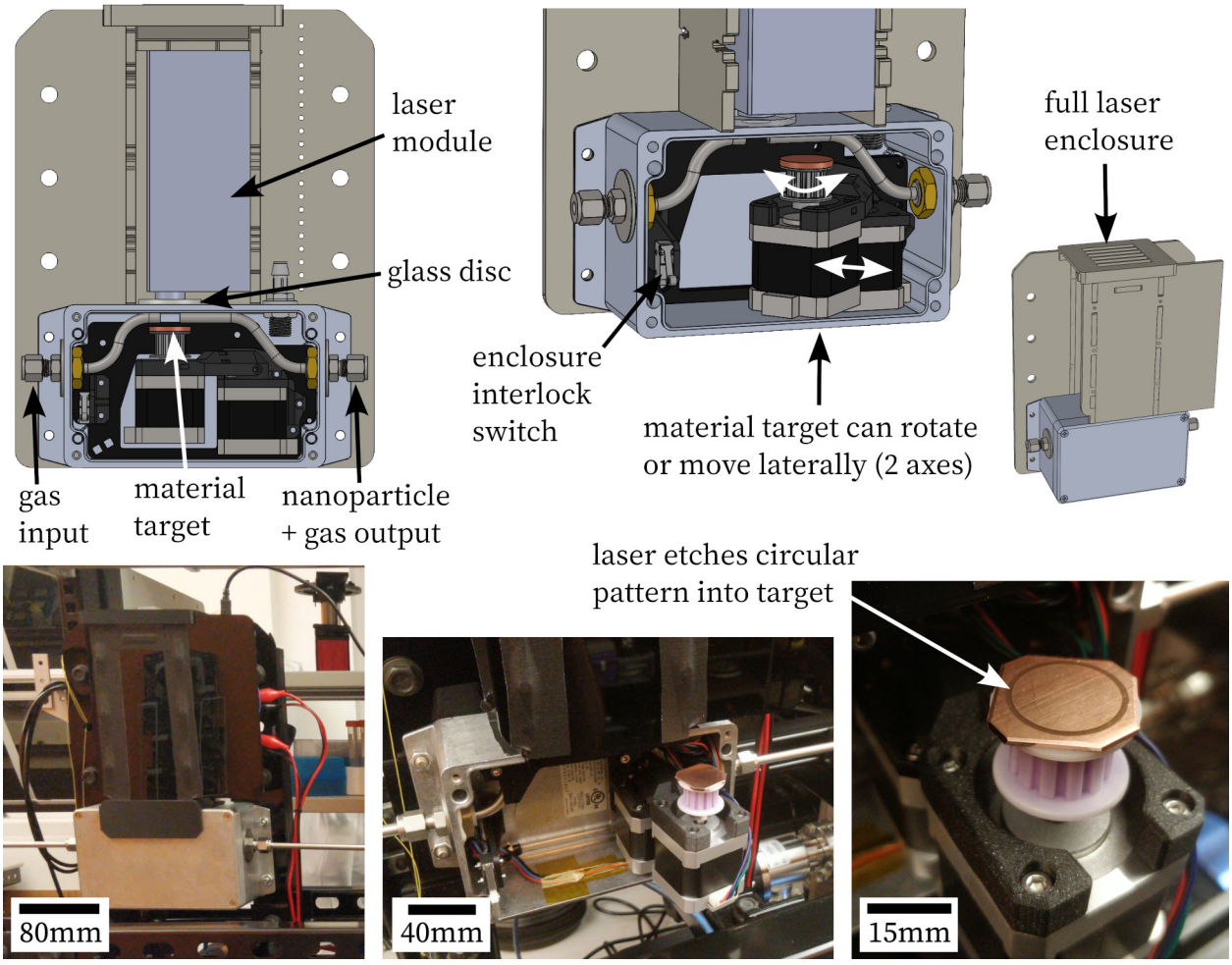

Figure 2.11: Top: CAD models of laser ablation nanoparticle generator, some with cover removed to show interior workings. Bottom left: assembled laser generator. Bottom center: material targets can easily be moved out of generator to be changed out with different materials. Bottom right: rotation causes the laser to etch a characteristic circular trace.

Similar to our spark ablation nanoparticle generator, we designed an airtight chamber with 4 mm ID gas tubing input and output. A 1064 nm-transparent borosilicate glass disc allows

the laser to enter the chamber and hit a material target in a 10 mm wide space between the tubing. All material targets are flat discs 10 mm to 25 mm in diameter which are easy to acquire. Because the laser is focused on a sub-1 mm^2 spot much smaller than the targets, it is typical to use some system to scan the laser across the target surface [142][140]. We built a motorized rotary two-axis scanning mechanism. The result is the system shown in figure 2.11. This was attached to a nanoparticle impaction setup similar to the spark ablation generator but with a larger vacuum chamber described in section 4.3.

As an initial experiment, we scanned the laser across a copper target at 0.3 $mm\,s^{-1}$ at 50% of its maximum power for a total time of 15 s, impacting the result onto glass. The result is shown in figure 2.12: this created a large 700 µm deposit implying copper nanoparticles were successfully generated, transported, and impacted. This speed is comparable to (if not faster than) our spark ablation nanoparticle generator results.

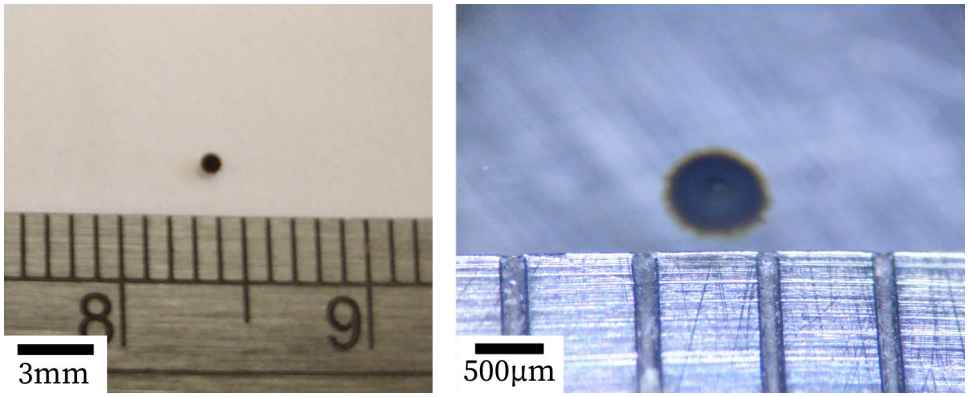

Figure 2.12: Left: copper deposited on a glass slide. Right: a close-up view showing the deposit may have 100 µm tall topography at its center.

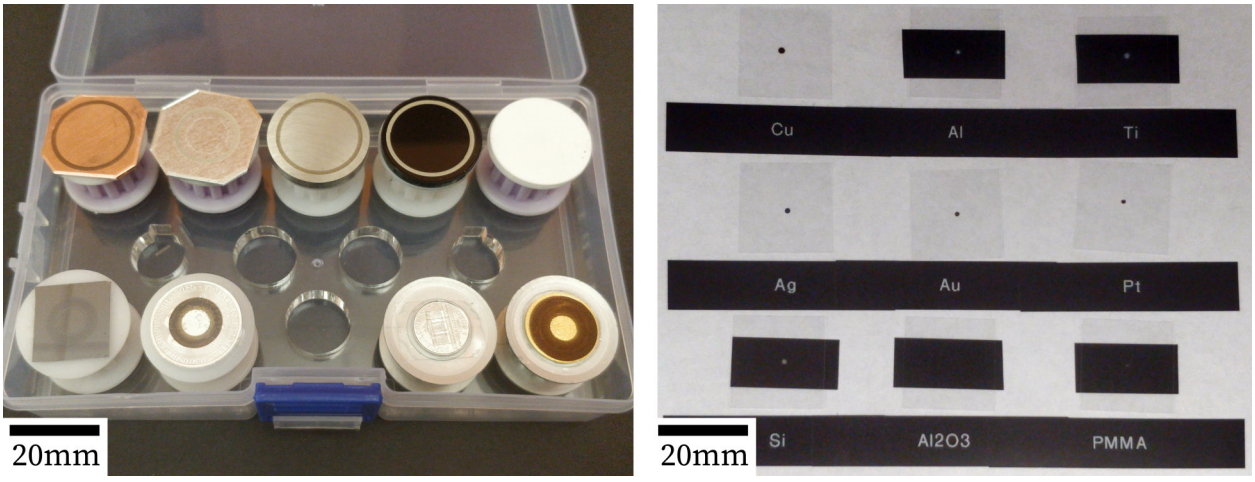

Figure 2.13: Left: material targets. Clockwise from top left: copper, aluminum, titanium, black acrylic (PMMA), alumina, gold, silver, platinum, silicon. Right: materials impacted onto glass slides. All materials work save for alumina. The PMMA deposit is barely visible.

Given our initial success with copper, we next tested a wide range of materials. Our generator was constructed to allow quick and easy material changes by swapping out the material target to any flat disc of diameter below 25 mm, letting us try the following: copper (101 alloy, 99.99% Cu, McMaster-Carr), aluminum (1100 alloy, > 99% Al, McMaster-Carr), titanium (99.995% Ti sputter target, ACI Alloys Inc), black acrylic (PMMA), alumina (96% Al_2O_3, remainder SiO_2), gold (2024 Armenia 1 gram gold 100 Dram Noah's Ark BU coin)[22], platinum (2024 Austria 1/25 oz platinum Philharmonic BU coin), silver (2024 Armenia 1/4 oz silver 100 Drams Noah's Ark coin), and silicon (boron p-doped wafer).

Each material was etched with the laser moving at $10\,\mathrm{mm\,s^{-1}}$ over the surface and at 50% maximum power. Gas flow rate was set to approximately $0.5\,\mathrm{L\,min^{-1}}$. Deposition was continued for 1 min for each sample onto a glass slide. The results are shown in figure 2.13: copper, silver, gold, and platinum produced dark deposits. Titanium, aluminum, and silicon produced white deposits. Alumina produced no visible deposit, and PMMA resulted in a very faint deposit with uncertain molecular structure. These are excellent initial results; it appears laser ablation nanoparticle generation works, and future characterization and improvement efforts can likely make a reliable convenient nanoparticle source.

We did attempt to quantify the nanoparticle production rate by measuring the mass change of both the material target and substrate during the material experiments of figure 2.13 but found no measurable difference above 0.1 mg over our 1 min deposition time[23]. This implies the generation rate is below $6\,\mathrm{mg\,h^{-1}}$, but the similarity of deposits to our spark ablation results suggests the generation rate is at least $0.6\,\mathrm{mg\,h^{-1}}$. This rate, between $0.6\,\mathrm{mg\,h^{-1}}$ to $6\,\mathrm{mg\,h^{-1}}$, is again reasonable for printing chips in hours.

2.4 Metrics and Improvements

We are now able to generate nanoparticles via either spark ablation or laser ablation and are ready to proceed with considering their deposition in chapter 3. However, we have only achieved the bare minimum. Although we can generate particles, we only have rough proxy measurements of their diameters and other properties. While this is fine for the moment—we thought it more important to confirm we can print nanoparticles before spending time refining the nanoparticle sources themselves—this characterization and refinement is an ideal target for future work.

An advanced nanoparticle printer might add the following:

Nanoparticle characterization: we would like to know the precise distribution of nanoparticle diameters as well as their shape, optionally using this to optimize the ablation and vapor nucleation processes—are the particles crystalline? Are they actually spherical or instead multiple smaller particles necking together? Are they oxidized? As mentioned earlier when

[22]Gold, silver, and platinum are most readily available in a flat cylindrical form factor as minted coins. We chose the cheapest coins commercially available of sufficiently large diameter. Costs were < $100 on average per metal, making this as affordable as spark ablation wire and again significantly cheaper than microfabrication material sources which typically have to be much larger.

[23]Longer deposition times were not attempted for fear of overheating the laser module.

we approximated particle sizes from SEM images, precise size distributions can be better measured via a differential mobility analyzer (DMA), a cascade impactor (which uses a combination of aerodynamic lenses and inertia to similarly select particles of a certain diameter [102]), or charge detection mass spectrometry [111]. Size as well as particle geometry can be determined to some extent by inspection of particles with a scanning or tunneling electron microscope (TEM) [149] or atomic force microscope (AFM) after deposition.

Nanoparticle size control: to make a very precise and repeatable manufacturing method, it would be preferable to control (and not just measure) the distribution of nanoparticle sizes—perhaps we want nanoparticles of exactly $5 \pm 0.5\,\text{nm}$. However, all discussed nanoparticle generation methods result in a wide distribution of particle diameters (say, a lognormal distribution [128][102] from 5 nm to 30 nm) and more precise control is notoriously difficult and may not be possible without using a process other than vapor nucleation. But there is an alternative: it is relatively straightforward[24] to sort particles by diameter in the same DMA or cascade impactor tools used for characterization, a similar but less precise virtual impactor [102], a time-of-flight filter based on mobility in gas [152], or a quadrupole mass filter as used in mass spectrometry and discussed in section 6.3.2 [132][153]. We can simply select the subset of nanoparticles of the correct diameter to print and recycle the rest.

Deposition efficiency: ideally 100% of the material vaporized from target electrodes is transformed into nanoparticles and deposited onto the substrate. That this is theoretically possible is a strong benefit of nanoparticle printing that is not possible in microfabrication, where a significant fraction of material (easily far above a majority, depending on how one calculates) goes to waste (see section 7.2.3). This efficiency can be quantified by measuring the mass of a target material and deposition substrate before and after moving material from the former to latter. One spark ablation paper in the literature [136] found a 22–38% efficiency, i.e., at least 62% of vaporized material was lost by deposition onto tubing sidewalls before being deposited as desired on the substrate, but noted this is mainly due to diffusion and can be reduced by increasing gas flow to minimize transfer time.

All these results and possibilities make us confident that precise reliable multimaterial nanoparticle sources are feasible and practical. With that determined, we are ready to consider what happens to nanoparticles after they are made: how we will deposit them and how this can be achieved by manipulating them with a combination of gas drag and electrostatic forces.

[24] The company [51] that sells a spark ablation generator also sells an aerosol-based particle size selector with claimed 0.1 nm diameter resolution for 1 nm to 10 nm particles.

Chapter 3

Deposition Theory

Now that we have nanoparticles, we can get to the fun part: printing.

More specifically, we need to consider what physical processes need to happen to attach these nanoparticles to the substrate or part under construction. Understanding this is a prerequisite for designing any printing mechanism. We'll review the physics and literature of similar nanoparticle deposition processes to find out what is possible and in what conditions (e.g., nanoparticle impact speeds). We'll then briefly discuss systems to move nanoparticles around and conclude we should focus on the gas/aerosol and electrostatic systems we later pursue in chapters 4, 5, and 6.

3.1 Deposition Review

When proposing our nanoparticle printing process in section 1.3, we wanted nanoparticles to hit the surface of a part under construction, then stick. What does that mean? How does that work? Most macroscopic things don't spontaneously stick together.

Roughly speaking, the materials we're interested in (metals, semiconductors, and oxides) consist of individual atoms bonded equally to all their neighbors; they are near-infinite 3D grids of atoms. Now suppose you were to take two pieces of the same metal with atomically flat surfaces and push these flat pieces together with no air or grease or other contaminants[1] in between. The atoms would line up, the electrons forming bonds would spread across the now-nonexistent gap, and the pieces would meld together into one as if they were never two separate parts [154]. In Feynman's words [155], "there is no way for the atoms to "know" that they are in different pieces". This process is often called cold welding[2].

In our case, we want to cold weld nanoparticles to larger surfaces, which turns out to be particularly effective due to high nanoparticle surface reactivity (as in chapter 2).

[1] Another common contaminant is an oxide layer from the surface reacting with atmospheric oxygen.

[2] Why don't we see this more often on the macroscale? It's extraordinarily difficult to make metal surfaces flat and clean enough, especially at large sizes. But galling on tight screw threads is in part cold welding, and spacecraft can experience cold welding between their metal parts in vacuum.

We'll begin by considering what happens when a nanoparticle hits a flat surface at some velocity. Sometimes the nanoparticle will deform and cold weld to the surface. This interaction has been widely studied in several research areas that approach the same problems from separate directions[3]. These methods mainly differ in particle size and impact velocity (or, equivalently, the kinetic energy per atom of the moving particle before impact).

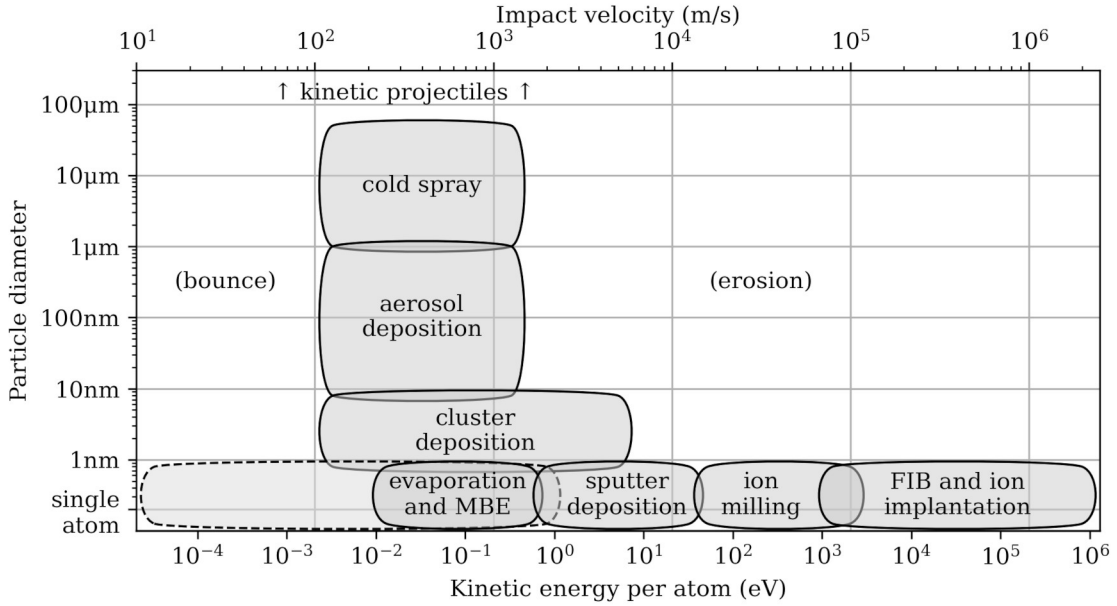

Figure 3.1: Assorted effects when nanoparticles hit surfaces, graphed by approximate particle sizes and impact velocities. Kinetic energy is computed as $\mathrm{KE} = \frac{1}{2}mv^2$ assuming particles consist of 40 amu atoms. Thermal energy k_BT at 25 °C is 26 meV. Single atomic bonds are 1 eV to 10 eV [103]. Inspired by similar graphs in [42] and [158]. See also figure 3.2.

Single atoms: suppose a single atom hits a surface [156]. This is a common part of many microfabrication thin-film physical vapor deposition (PVD) tools (which have many atoms impacting in parallel). If the atom was moving slowly, with some probability (the sticking coefficient) it will form temporary bonds then move around on the surface with thermal energy as an adatom. Eventually it may form a stronger bond. Many atoms make a thin film. This describes evaporation and molecular beam epitaxy (MBE) [118] but applies to any low-speed collision [159]. The structure zone model [160][161] notes a transition from porosity to small then large grains with substrate temperature, and film stress varies significantly [162]. If the incoming atom velocity and thus kinetic energy were greater than k_BT thermal energy or the ≈ 1 eV of chemical bonds, the extra energy is enough to modify film properties slightly [163]. This is also the regime sputter deposition tools typically operate in [164]. At even higher velocities, the incoming atom has enough kinetic energy to collide with many atoms in the substrate, sometimes making some fly off the surface ("sputter") so material is removed instead of added. This applies to ion milling, FIB, and ion implantation [75][1].

[3]For a broad overview, we can recommend the combination of [118], [156], [43], [42], and [157].

Clusters (1–10nm): the next smallest[4] particles, clusters[5], are clumps of several to several thousand atoms, that is, small nanoparticles with diameters up to tens of nanometers. These have a variety of behaviors similar to single atoms [43]. At low impact velocities, below about 0.1 eV per atom, these clusters merely bond as-is to the surface. Depositing multiple clusters can stack them without deformation, making a porous film. However, increasing the impact velocity and energy to 1 eV is enough to allow the clusters to deform and make solid films, which are good enough to form metallic ohmic contacts and PN junctions [171][172][47]. Varying process conditions can produce amorphous, nanocrystalline, and polycrystalline films [47] and, especially with a heated substrate, these clusters move around the surface similar to single adatoms (but surprisingly far: up to microns [171]) and form epitaxial films [173][174]. Higher velocities (10 eV per atom) begin to cause sputtering and erosion effects, and even faster speeds with small clusters still gives ion implantation[6].

Industrially, clusters in the erosion regime can be used to smooth microfabricated surfaces[7] in gas cluster ion beam (GCIB) processing [176][48][177]. Cluster deposition [125] is less common. It (specifically ionized cluster beam deposition, ICBD, from 1975 [178][47]) has been used commercially for DRAM contact hole filling [179] but, in general, the complexity of cluster sources [43] means it has no significant benefit over evaporation and sputtering for standard microfabrication (for our printing process, however, using larger particles than atoms is worthwhile to allow higher print speed in chapter 6).

Larger particles act progressively more macroscopically. Specifically:

Low-speed bounce (large particles below 100m/s): when a particle hits a surface at low speeds, it can bounce[8]. Below $\approx 100\,\mathrm{m\,s^{-1}}$, there is not enough kinetic or thermal energy available to reform bonds or bond the particle to the surface except for Van der Waals forces, so the particle elastically compresses slightly then rebounds, its inertia overcoming any minor surface attraction (unless it is so slow, perhaps below $5\,\mathrm{m\,s^{-1}}$ [157], that surface attraction dominates [102]) [157][158][181][182][183]. Single atoms can somewhat bounce: they adsorb then desorb from a surface (with sticking coefficient probability) [184].

Aerosol Deposition, Cold Spray (10nm–100μm): when particles larger than clusters hit a surface at intermediate velocities, typically $100\,\mathrm{m\,s^{-1}}$ to $1000\,\mathrm{m\,s^{-1}}$, they can undergo plastic deformation to conform to the surface while cold welding [42][185][41][52]. This works at room temperature (though more heat helps) with only a partial temperature increase (not necessarily to melting) at the collision point as kinetic energy is converted to heat [186]. There is both a material-dependent [187] minimum critical velocity (which can be predicted with solid mechanics as the onset of shear instability) and maximum velocity (notably a bit below the 1 eV per atom milestone) above which a particle fragments, does not fully adhere, and leaves an impact crater (hydrodynamic penetration) [186][188].

[4]Deposition of organic molecules exists as soft landing in mass spectrometry [165][166][167][168][169].

[5]Clusters were widely studied in the 1960s through 1990s for their interesting physics [170][43]. This research also led to vapor nucleation nanoparticle generation methods [142] and the C_{60} buckyball molecule.

[6]Molecular ion implantation used for shallow MOSFET doping is arguably a form of cluster deposition.

[7]EUV photolithography mirrors are smoothed with single argon atoms (ion beam figuring, IBF) [175].

[8]This is relevant for sub-1 µm tin droplets in EUV light sources [180].

Impacting these large particles over wide areas can produce thick solid films that exceed 95% of bulk density, are gas-tight, and have high optical transparency [185][42]. This is used in the semiconductor industry to apply nanocrystalline yttria coatings to semiconductor equipment plasma chambers [189] and to manufacture some sputtering targets. To clarify nomenclature: aerosol deposition and cold spray are so called because the main method to accelerate 10 nm–100 µm particles to impact speeds is as an aerosol in an air jet (see sections 3.3, 4.2.1). Cold spray is feasible at atmospheric pressures; the smaller particles of aerosol deposition have higher air drag and require partial vacuum for deposition (see section 4.2.1). Thermal spray methods are cold spray at high temperatures. Other names exist[9].

High-speed erosion (above 1000m/s): sufficiently fast particles have enough kinetic energy to vaporize a good bit of both themselves and the surface they impact. This is the hypervelocity regime [197]. Hypervelocity acceleration of micrometer-scale particles is useful for studying in-space micrometeoroid or cosmic dust impacts [198][199][157]. Particles above 1 mm and from low speeds to hypervelocity are common as kinetic projectiles.

3.2 Deposition Parameters

Given the above deposition regimes, what parameters should our proposed nanoparticle printer use? The literature suggests four properties are most important to control deposition: impact velocity, particle size, temperature, and material.

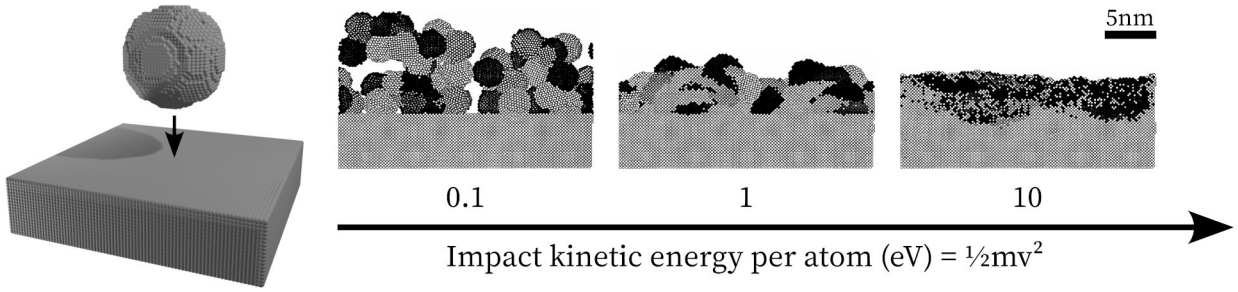

Figure 3.2: Left: what happens when a nanoparticle hits a surface? Right: depending on their initial velocity, particles can cohere, deform, and meld together (molecular dynamics simulations from [200]). This can be explained by noting that when a particle is at a given velocity, all its atoms have that same velocity, and the kinetic energy of each atom ($\frac{1}{2}mv^2$) turns into heat on impact and is available to reform the 1 eV to 10 eV chemical bonds between atoms. The total kinetic energy of the pre-impact particle is this multiplied by the (large) number of atoms. 1 eV per atom is equivalent to about 2000 m s^{-1}. See also figure 3.1.

Velocity: the most important parameter in any of these physical deposition processes is the speed at which nanoparticles impact a surface (for us, the substrate and part under construction). This is because deforming then bonding the particle to the surface requires

[9]Other names for air jet deposition include micro cold spray [190], hypersonic plasma particle deposition (HPPD) [191][59][192][193][194][60], vacuum kinetic spray [195], and nano-particle deposition system [196].

reforming chemical bonds, which needs energy, and the most convenient source is the kinetic energy of impact as in figure 3.2. According to figure 3.1, we probably want to choose impact velocities between $100\,\mathrm{m\,s^{-1}}$ and perhaps $3000\,\mathrm{m\,s^{-1}}$. Because the ideal velocity varies with material and particle size [188], we would ideally be able to precisely control the velocity within that window to fine-tune deposition conditions experimentally.

Particle size: as mentioned in chapter 2 (and later chapter 6), printing larger nanoparticles is faster than printing single atoms, and we'll also see in chapter 4 that larger particles are easier to focus to high resolutions. But there is a tradeoff: larger particles have more mass and are harder to accelerate to the required impact velocities, and, of course, we can't reach sub-100 nm printing resolution if the particles are larger than 100 nm in diameter. The best size range for our purposes—achieving high-quality materials with high resolution—is probably 1 nm to at most 50 nm, mostly within the cluster deposition regime that is known to be able to deposit films with high-quality electrical properties. This is also (not coincidentally) the size range the nanoparticle generators we built in chapter 2 are optimized for.

Temperature: kinetic energy is not the only source of energy for deforming and bonding particles; thermal energy can also help. At an absolute temperature T, atoms vibrate with energy on the order of $k_B T$ (where k_B is the Boltzmann constant). At room temperature $T = 298\,\mathrm{K} \approx 25\,^{\circ}\mathrm{C}$, $k_B T \approx 0.026\,\mathrm{eV}$, and at silicon's melting point of $T = 1687\,\mathrm{K}$ we have $k_B T = 0.15\,\mathrm{eV}$, sufficient to cause by itself the initial conglomeration in figure 3.2—which is why silicon becomes liquid there (but note this is still less than the kinetic energy velocity can deliver locally to the particle). Furthermore: both the substrate and particle can be heated. Heating the particle doesn't mean anything for a single atom but can provide significant energy with larger particles as in cold spray (giving thermal spray methods) [186][188][192]. This is why single atom methods like evaporation purely heat the substrate as described in the structure zone model [161]. What should we use? We'll ignore particle temperature, start with the substrate at room temperature[10], and can eventually add capability to heat up to the 500 °C used by Takagi for cluster epitaxy [47] (being aware that this might cause adatom movement of up to microns [171], potentially reducing print resolution).

Material: although velocities and other parameters vary with material [188], our material choices will mainly be determined by the requirements to build useful semiconductor devices as described in chapter 1: metals, semiconductors, and oxides. Fortunately, these all appear feasible with minimal variation. It might eventually be useful to also deposit polymers[11] as sacrificial release materials for MEMS devices, but we leave this for future work.

In conclusion: we suspect we need to move particles of 1 nm to 50 nm at velocities of $100\,\mathrm{m\,s^{-1}}$ to $3000\,\mathrm{m\,s^{-1}}$ and can eventually add temperature control. Varying parameters might allow printing assorted materials with a variety of crystal structures: amorphous, nanocrystalline, polycrystalline, and monocrystalline (epitaxial). This is exactly what we need to print our desired multimaterial nanoscale devices—if we can achieve these high nanoparticle velocities while simultaneously aiming the particles with high printing resolution.

[10] This will allow us to print on low-temperature substrates, like plastics.

[11] See PVD evaporation/MBE of organics [118] or mass spectrometry soft landing [165][166][167][168][169].

3.3 Manipulation Methods

According to section 3.2, we might be able to achieve the high-resolution multimaterial printing we want if we can shoot nanoparticles of 1 nm to 50 nm diameter at a substrate at well-controlled velocities somewhere between $100\,\mathrm{m\,s^{-1}}$ and $3000\,\mathrm{m\,s^{-1}}$, and with positioning accuracy below our final desired printing resolution, e.g., 1 µm.

But how can we do that? These are tiny particles (only tens of atoms wide), high speeds (supersonic), and high resolutions (accuracy within ten thousand atoms)!

Of the four fundamental forces—weak and strong, gravity, and electromagnetism—the weak and strong forces are irrelevant at these scales and gravity is far too small to be useful[12]. We need to use electromagnetism somehow. This includes long-range electrostatic and magnetic forces, photons, and matter interactions (since all matter is simply atomic nuclei and electrons held together by electromagnetism).

- **Matter interactions:** also called touching stuff. We could put some nanoparticles on the end of a robot arm then move it extremely fast. But as noted in chapter 2, we want to avoid having the nanoparticles contact anything else made of atoms before deposition to minimize the chance those atoms rub off and contaminate the particles, compromising the sub-part-per-billion atomic purity we require. It is difficult to have good enough control of chemistry to reliably do better. But there is a notable exception: many gases, especially the noble (inert) gases (helium, argon, etc.), are single atoms or molecules that can impact nanoparticles without reacting.
- **Photons (light):** it is possible to move nanoparticles with photon momentum (optical tweezers [201][202][203]), but simultaneously achieving velocity and resolution is tricky. We will use photons instead for electrical charging in chapter 5.
- **Electrostatics and magnetics:** an electrically charged nanoparticle will experience a force directly from electric or magnetic fields. This is promising. The nanoparticle can alternatively have a nonzero magnetic moment, but this is harder to control.

That leaves us two options: moving our nanoparticles (otherwise isolated in vacuum) either with gas atoms collisions somehow or with electrostatic forces. This conclusion is well-supported by the prior art[13] in section 3.1: aerosol deposition, cold spray, and some cluster methods [125] use gas to accelerate particles, while other cluster methods [47] and nanoparticle hypervelocity tests [198] use electrostatic acceleration. We also used gas already in our nanoparticle generators in chapter 2.

In chapter 4, we will discuss gas-based manipulation of nanoparticles and be able to demonstrate some minimal multimaterial printing. But it will prove insufficient to reach the full velocity and resolution we want, so we will turn to electrostatics in chapters 5 and 6.

[12] Any size particle falling a long 100 m distance in Earth-standard $9.8\,\mathrm{m/s^2}$ gravity in vacuum gains a total kinetic energy of only about 0.0004 eV per atom compared to the 1 eV we need.

[13] Evaporation and MBE instead use thermal energy to release atoms from a solid of the same material, but this neither scales up well to larger particles or allows efficient velocity control—the velocity distribution is Maxwell-Boltzmann [118] instead of the single value we want. Sputtering uses gas impacts.

Chapter 4

Aerosols and Printing

As proposed in chapter 3, we will try moving 1 nm to 50 nm diameter nanoparticles by having gas molecules collide with them, ideally accelerating the nanoparticles to precise high-speed velocities (up to $3000\,\mathrm{m\,s^{-1}}$) with high spatial resolution ($< 1\,\mu\mathrm{m}$). If we succeed, we can print them. How can we go about doing this? First consider how gas collisions work.

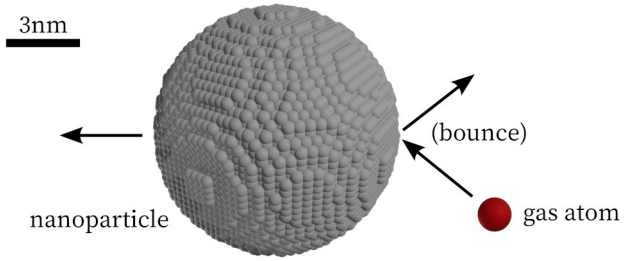

Figure 4.1: Cartoon of a single gas atom (or molecule) bouncing off the right side of a nanoparticle. This causes the nanoparticle to move slightly to the left.

By a gas, we mean a collection of individual atoms[1] moving around in what is otherwise a vacuum. When a single gas atom hits a nanoparticle, it acts like a nanoparticle hitting a large surface as in chapter 3. If the atom is unreactive and moving slower than perhaps $10 \times 10^4\,\mathrm{m\,s^{-1}} \approx 10\,\mathrm{eV}$ (often the case; larger velocities risk deforming or breaking the nanoparticle [204], so we'll avoid that), it will bounce off the nanoparticle and head in a different direction. Conservation of momentum dictates this acts like macroscopic collisions (just like billiard balls) and is at least partially elastic[2], so the nanoparticle will be pushed slightly away from the collision point. Repeat this many times (a nanoparticle is significantly heavier than a gas atom, so it takes a while), and the nanoparticle can be pushed in whatever direction we like. (The other relevant interaction is electrons can move between atom and nanoparticle, which is usually negligible but will matter in chapter 5.)

[1] A gas can be molecules like N_2, not just atoms, with little difference. We use "atom" for convenience.

[2] Although most collisions are specular (and elastic on average), the atom can temporarily adsorb (stick) to the nanoparticle giving a diffuse reflection [184][205], and some energy can also be lost or gained from vibrations (phonons) in the particle to bring it to mean gas temperature [206].

Unfortunately, we don't have a way to precisely shoot gas atoms at a nanoparticle to make it go exactly where we want[3]. Instead we'll allow millions of gas atoms to randomly hit each nanoparticle, and their average behavior will determine what happens. We will control the overall gas behavior—fluid dynamics[4]—to indirectly control the nanoparticles.

An aerosol is exactly this: a collection of nanoparticles in a gas. Aerosols are very common; examples include smoke, fog, steam, and clouds. Aerosol science [102], the study of aerosols, has produced useful results and tools like the differential mobility analyzer (DMA) mentioned in chapter 2. We'll quickly discuss gases in general then focus on aerosol-specific results.

4.1 Gas Physics

We will briefly review some basic gas behavior. Consider a large number of gas atoms inside an airtight chamber. The atoms move around, bouncing off the walls and each other just like they bounce off nanoparticles. This is the kinetic theory of gases, and statistical mechanics can be used to derive some useful average properties [102].

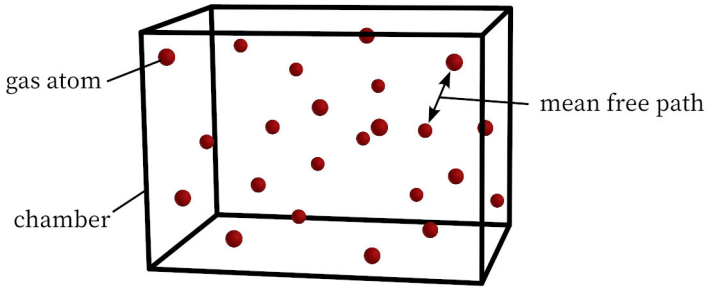

Figure 4.2: A 3D rectangular chamber holding gas atoms bouncing off the chamber walls and each other. The mean free path is related to the average distance between gas atoms.

As with nanoparticles, each collision between gas atoms and the surface is elastic on average[5], so at nonzero temperatures the gas atoms never stop moving even if their velocity might change on each bounce. The atoms' range of velocities is given by the Maxwell-Boltzmann distribution and is fairly broad (some atoms move slowly; other quickly). The average velocity increases with temperature and with smaller gas atoms. Standard air is just the particular gas consisting of about 78% N_2, 21% O_2, and some Ar, CO_2, and other trace elements, each part of which acts independently according to this same distribution.

[3]Atomic billiards! But collisions are only somewhat elastic on average; single shots might be unpredictable.

[4]In continuum mechanics, "fluid" refers to both gases and liquids since both continuously deform under applied shear stress and otherwise act similarly.

[5]Collisions equilibrate the temperature of the gas and chamber until this is the case; the atoms of the chamber surface vibrate according to their temperature and transfer energy to or from colliding gas atoms.

From the Maxwell-Boltzmann distribution we can derive that the average kinetic energy of the gas atoms (each moving in a random direction) at absolute temperature T is $\frac{1}{2}k_BT$ in each of the x, y, and z directions for a total of (again, in a random direction)

$$\frac{3}{2}k_BT \tag{4.1}$$

where $k_B = 1.381 \times 10^{-23}\,\mathrm{J\,K^{-1}} = 8.617 \times 10^{-5}\,\mathrm{eV\,K^{-1}}$ is the Boltzmann constant. At 25 °C, any gas atom has about 0.039 eV of kinetic energy. An argon gas atom, for example, would move on average (root mean square velocity[6]) at $431\,\mathrm{m\,s^{-1}}$. Nanoparticles will also randomly bounce around and eventually gain the same $\frac{3}{2}k_BT$ kinetic energy, but this applies to the entire particle (not its individual atoms), so a 10 nm nanoparticle would only move at $2\,\mathrm{m\,s^{-1}}$. This doesn't help us achieve the high velocities (up to $3000\,\mathrm{m\,s^{-1}}$) we want to accelerate nanoparticles to, and it might make positioning nanoparticles with sub-1 µm resolution difficult. We'll address this shortly as Brownian motion.

Also relevant is that gas atoms hitting a surface, whether it be part of the chamber sidewall or the side of a nanoparticle, apply a force. The average force (over time) per area is the pressure, which is often the best way to measure the number of gas atoms in the chamber. These are related by the ideal gas law

$$PV = Nk_BT \tag{4.2}$$

where P is the absolute pressure, V is the total volume of gas, and N is the total number of gas atoms. Normal Earth atmosphere is air at a pressure of about 101 325 Pa or 760 Torr[7]. Removing gas molecules from the chamber reduces the pressure; if below atmospheric we call it a vacuum. Pressure is always positive (achieving perfectly zero pressure is near-impossible), and for some applications (including ours; see sections 4.2.1 and 4.3.3) the difference in otherwise small pressures (say, 1 Torr and 1×10^{-7} Torr) can be significant.

The rate at which atoms hit a surface (creating a pressure) is the impingement rate

$$J = \frac{P}{\sqrt{2\pi m_g k_B T}} \tag{4.3}$$

where J (gas atom impacts per unit area per unit time) is the impingement rate and m_g is the mass of a gas atom. In standard 760 Torr atmosphere, the surface of a 10 nm diameter particle is hit by about 9×10^{11} gas atoms per second. This is an extremely large number.

A final important parameter is the distance between gas atoms[8]. It is often more convenient to use the average distance a gas atom travels before a collision with another gas atom. We call this the mean free path ℓ, calculated by

$$\ell = \frac{k_BT}{\sqrt{2}\pi d_g^2 P} \tag{4.4}$$

where d_g is the kinetic diameter of the gas atom, about 0.36 nm for Ar, N_2, and O_2 [103]. The mean free path of 760 Torr air is about 70 nm—larger than a 10 nm nanoparticle!

[6]Computed from $\frac{3}{2}k_BT = \mathrm{KE} = \frac{1}{2}mv^2$. The true (non-RMS) mean velocity is $\sqrt{\frac{8}{3\pi}} \approx 0.92$ of this value.

[7]Or 1.01 bar, 14.7 psi, or 1 atmosphere. Of all these units, torr are common in vacuum engineering.

[8]The mean spacing between gas atoms, about 3 nm in atmosphere, is smaller than the mean free path.

4.1.1 Nanoparticle Air Drag and Brownian Motion

Given how gases behave, we can now consider how they make nanoparticles move.

We'll consider the simple case where a nanoparticle with initial velocity v suddenly appears in the center of a chamber with gas otherwise in equilibrium at some pressure and temperature. This will take us surprisingly far. Note this is equivalent to the case where the nanoparticle has no initial velocity but the gas is moving with velocity $-v$ on average. It is only the relative velocity that is important.

If there are no gas atoms (zero pressure), the nanoparticle will of course move forever at velocity v. But in a gas, the nanoparticle collides with the gas atoms, transferring its kinetic energy to the gas until the gas temperature is raised and the system is at equilibrium. The nanoparticle is slowed down until it has the same relative velocity as the surrounding gas (plus its randomly-directed thermal motion from section 4.1). This is air drag[9]!

Air drag is the main interaction between a nanoparticle and a gas. As suggested in the introduction to this chapter, if we make gas atoms move somewhere on average, air drag will drag nanoparticles along (and if we move nanoparticles without moving the surrounding gas, those nanoparticles will quickly slow down). If we want to precisely move nanoparticles, we should quantitatively understand the effects of air drag as well as its interaction with the previously mentioned thermal (Brownian) motion.

Other nanoparticle-gas interactions besides drag include chemical reactions (unlikely with noble gases, common with oxygen) or exchanging electrons (important in chapter 5), and air drag itself has many subtle effects (e.g., thermophoresis). We will ignore these for now.

There are two ways to analyze drag: bottom-up statistical mechanics calculations accounting for how nanoparticles are randomly bumped around, or a top-down approximation[10] that treats the gas as a continuous viscous fluid. We'll start with the latter.

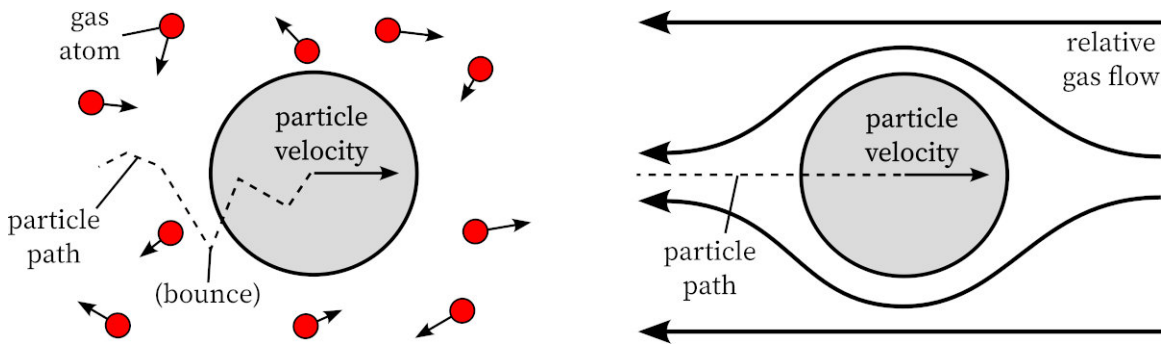

Figure 4.3: Two ways to analyze gas-particle drag. Left: a particle moving to the right experiences many collisions with gas atoms, each of which slightly redirects the particle course and, on average, slows it down. Right: as the number of gas atoms approaches infinity (a continuum), collisions are averaged out so a particle moving to the right (shown with gas streamlines moving to the left) has a straighter path but is still slowed down.

[9]Drag exists in all gases, not just air, but the term "air drag" is more common than "gas drag".
[10]Navier-Stokes can be derived from the kinetic theory of gases with Chapman-Enskog theory.

The reader may be familiar with Stokes' law, which says the force $\vec{F}$ due to drag on a sphere of diameter d_p moving at velocity $\vec{v}$ through a fluid of dynamic viscosity μ is

$$\vec{F} = -3\pi\mu\, d_p\vec{v}. \tag{4.5}$$

In other words, a particle moving relative to a gas experiences a force in the direction opposite its motion, proportional to its current (relative) velocity, vaguely similar to friction.

This equation is derived by assuming the surrounding gas is a continuum, then simplifying the incompressible Navier-Stokes equations at low speeds around a sphere with a no-slip boundary layer. The result is accurate[11] for large everyday objects.

However, this equation is often incorrect for nanoparticles since they are much smaller than the mean free path ℓ between air molecules (compare $\ell = 70\,\text{nm}$ in atmosphere to a 10 nm particle) so the no-slip boundary condition does not hold. In other words, the nanoparticle is so small the approximation that the gas is a smooth continuum breaks down. This is quantified by the Knudsen number $\text{Kn} = \frac{\ell}{d_p}$, the ratio of mean free path ℓ to particle diameter d_p. Kn can be thought of as the degree of non-continuous fluid behavior and in our case is much greater than 1, a region referred to as free molecular flow[12] [207].

It is sometimes possible to add a term to Stokes' law to compensate for small nanoparticle diameters. Specifically, the Stokes drag force is multiplied by $1/C$ defined by

$$C = 1 + \frac{2\ell}{d_p} \cdot (c_1 + c_2 e^{-c_3 \frac{d_p}{2\ell}}) \tag{4.6}$$

where c_1, c_2, and c_3 are empirical constants, approximately $c_1 = 1.17$, $c_2 = 0.52$, $c_3 = 0.78$ for air [102][205]. This is called the Cunningham-Millikan-Davies slip correction factor and has the distinction of being used in the Millikan oil drop experiment that demonstrated the existence of charge quantization [208]. The downside of this method is limited applicability due to the empirical fit (which assumes standard pressure and temperature air).

An alternate and more general method to compute the drag comes from a first principles analysis of hard sphere collisions. There are many minor variations to this method; see [205] for an excellent discussion. We will use the form (referred to as "Epstein's Law"):

$$\vec{F} = -\frac{8 + \pi\varphi}{12}\sqrt{\frac{2\pi m_g}{k_B T}} P d_p^2 \vec{v} = -\beta\vec{v}, \tag{4.7}$$

where $\vec{F}$ is the drag force, $\varphi \approx 0.9$ is a constant indicating the fraction of diffuse vs. specular collisions, m_g is the mass of each gas molecule, k_B and T are the Boltzmann constant and temperature, P is the gas pressure, d_p the particle diameter, and $\vec{v}$ the particle velocity. For convenience, we will sometimes abbreviate this as the viscous damping coefficient β.

[11] Stokes' law applies at low Reynolds numbers. Assuming continuum flow, a 10 nm particle at $3000\,\text{m}\,\text{s}^{-1}$ in 25 °C 760 Torr air has Reynolds number Re = 2, well below the Re ≈ 2000 onset of turbulence.

[12] "Free molecular flow" also refers to the point at which the mean free path is larger than the vacuum chamber holding the gas, which is not quite the case for most of our systems.

Advantages of Epstein's law include a clear relation to temperature, pressure, and gas molecular mass. The major downside is this only applies to the free molecular flow Kn $\gg 1$ regime, but this is satisfied for our nanoparticles in almost all cases[13]. Importantly, note the drag is directly proportional to velocity as in Stokes' law, just with a modified magnitude.

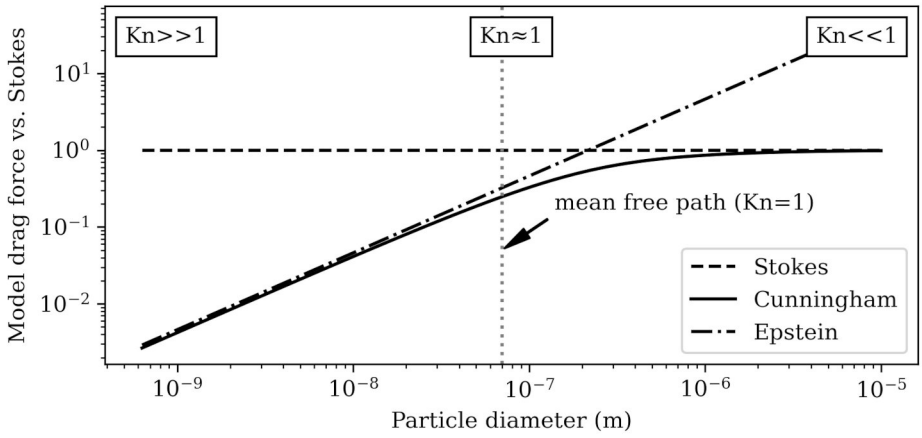

Figure 4.4: A comparison of Stokes, Cunningham, and Epstein drag models in 25 °C 760 Torr air, where the mean free path is about 70 nm. Air drag of nanoparticles larger than the mean free path (low Knudsen number) is modelled by Stokes drag, while Epstein drag is accurate for smaller particles. Cunningham drag interpolates between the two.

Minor model refinements exist for additional accuracy[14]. Small nanoparticles might require a lower Epstein φ parameter [184][205][213], and gas-particle temperature differentials might require additional corrections [206]. If particles were larger we might want to add secondary fluid continuum forces including the Basset force, gravity buoyancy, Magnus or Saffman lift due to particle rotation or shear flow; Saffman forces help model aerosol deposition [50]. For our smaller particles in large Knudsen numbers (and compared to the larger electrostatic forces in chapter 6), we will ignore these (unless particles are nonspherical [102]) [214].

One additional effect we cannot ignore is diffusion due to Brownian motion.

Earlier, we noted there were two ways of calculating drag. The first is the simple velocity-dependent force we just discussed, which we will refer to as viscous drag. The other method accounts for each individual collision of a gas atom with a nanoparticle.

Gas atoms hitting a nanoparticle cause it to have jagged motion: short straight-line movements changing directions upon each collision as shown in figure 4.3. With sufficiently many gas atoms, the force on the particle almost averages out to viscous drag—but not quite[15].

[13] A 10 nm diameter particle in 760 Torr atmosphere has Kn $\approx 7 \gg 1$, and Kn increases at lower pressures.
[14] See ion mobility spectrometry [209][210][211][212], which makes very precise nanoscale drag calculations.
[15] That gas collisions cause both drag and Brownian motion is the fluctuation-dissipation theorem.

The remaining motion is slow, random, and omnidirectional (though for a particle moving quickly, it is more noticeable perpendicular to the particle's primary direction of motion). This is called Brownian motion or diffusion[16] and is not accounted for in viscous drag. Given time, a particle will move arbitrarily far from the path we would otherwise predict.

Brownian diffusion is very significant for small particles [102] but can be tricky to analyze because of its large number of collisions and discrete nature. It does not have a single simple analytical formula like viscous drag. There are several ways of dealing with this:

- Computer simulation of random gas collisions is accurate and also replicates viscous drag but does not simplify analysis and is computationally expensive[17] [215][216][217].
- Average Brownian motion (ignoring motion with viscous drag) can be probabilistically but analytically approximated with Fick's laws of diffusion.
- Brownian motion gives particles $\frac{3}{2}k_BT$ mean kinetic energy. If a particle is trapped in a potential energy field, this can give us a probability distribution for its position.

We'll approximate particle motion as viscous drag plus independent Brownian movement (this is the Langevin equation [217]) given by one of the latter two approaches.

Using diffusion, a statistical mechanics analysis [102] can find that Brownian motion makes particles move an average (randomly oriented) distance[18] (beyond viscous drag) of

$$x_{\text{diffusion}} = \sqrt{4Dt} \tag{4.8}$$

where t is time and D is a diffusion coefficient computed by equating (the Stokes-Einstein-Sutherland relation) diffusion force from osmotic pressure to (Epstein) drag [102][205] as

$$D = \frac{12}{8+\pi\varphi} \cdot \frac{k_BT}{Pd_p^2} \cdot \sqrt{\frac{k_BT}{2\pi m_g}}. \tag{4.9}$$

	D (760 Torr)	D (1 Torr)	RMS Velocity
(single atom)	$4.0 \times 10^{-5}\,\text{m}^2/\text{s}$	$3.1 \times 10^{-2}\,\text{m}^2/\text{s}$	$431\,\text{m}\,\text{s}^{-1}$
1 nm	$5.2 \times 10^{-6}\,\text{m}^2/\text{s}$	$4.0 \times 10^{-3}\,\text{m}^2/\text{s}$	$69\,\text{m}\,\text{s}^{-1}$
10 nm	$5.2 \times 10^{-8}\,\text{m}^2/\text{s}$	$4.0 \times 10^{-5}\,\text{m}^2/\text{s}$	$2.2\,\text{m}\,\text{s}^{-1}$
100 nm	$5.2 \times 10^{-10}\,\text{m}^2/\text{s}$	$4.0 \times 10^{-7}\,\text{m}^2/\text{s}$	$0.07\,\text{m}\,\text{s}^{-1}$

Table 4.1: Some diffusion coefficients at 25 °C in air. Particles are of $5\,\text{g}/\text{cm}^3$ density or argon. Velocities due to thermal motion (in between Brownian collisions) shown for comparison.

In a 2D plane, a 10 nm nanoparticle diffuses 460 µm on average each second in atmosphere. It is clear this will be important when we attempt to achieve sub-1 µm resolution.

[16] "Brownian motion" generally refers to the random movement of a single particle and "diffusion" to the average behavior of a group. In this dissertation we will use both terms interchangeably.

[17] Recall we calculated a 10 nm particle has 9×10^{11} collisions per second in atmosphere.

[18] Specifically, the mean squared displacement is $2nDt$ where n is the dimension (1D, 2D, or 3D). Here we are mainly concerned about 2D particle motion perpendicular to the main direction of travel.

4.2 Aerosol Transport

We've established that nanoparticles are moved with a gas flow according to a viscous drag force (given by Epstein's law) with simultaneous diffusion (Brownian motion). These laws are enough to analyze particle motion in gas flow in tubing like we used in chapter 2.

First we'll establish how long a nanoparticle takes to react to a gas flow [102]. As suggested earlier, suppose a nanoparticle of mass m starts with velocity $\vec{v}_0$ relative to the surrounding gas (for example, it is moving $10\,\mathrm{m\,s^{-1}}$ while the gas is still, or the particle is still while the gas moves $10\,\mathrm{m\,s^{-1}}$ in the other direction). The particle follows Newton's second law while drag applies a force proportional to velocity by[19] viscous damping coefficient β giving

$$\vec{F} = m\vec{a} = -\beta\vec{v} \tag{4.10}$$

where, for Epstein drag (though our results apply to any velocity-proportional drag law),

$$\beta = \frac{8+\pi\varphi}{12}\sqrt{\frac{2\pi m_g}{k_B T}}Pd_p^2. \tag{4.11}$$

Solving for how the velocity evolves over time, we see this particle slows exponentially with a time constant (the relaxation time) $\tau = \frac{m}{\beta}$ until it reaches the gas velocity:

$$\vec{v}(t) = \vec{v}_0 e^{-\frac{\beta}{m}t} \tag{4.12}$$

In the time it takes to equilibrate velocity, the particle will travel a finite maximum distance $\vec{x}_{max}$, which is called [102] the stopping distance S:

$$\vec{x}(t) = \int_0^t \vec{v}_0 e^{-\frac{\beta}{m}t}dt = \vec{x}_{max} - \frac{m}{\beta}\vec{v}_0 e^{-\frac{\beta}{m}t} = \vec{x}_{max}\left[1 - e^{-\frac{\beta}{m}t}\right] \tag{4.13}$$

$$S = |\vec{x}_{max}| = |\frac{m}{\beta}\vec{v}_0| = |\tau\vec{v}_0| \tag{4.14}$$

That is, the gas will push the particle until the particle is moving at the same relative speed as the gas, and in this time (about 3τ) the particle will move a distance $S = |\tau\vec{v}_0|$.

	τ (760 Torr)	S (760 Torr)	τ (1 Torr)	S (1 Torr)
(single atom)	$6.5\times10^{-10}\,\mathrm{s}$	$6.5\times10^{-7}\,\mathrm{m}$	$5\times10^{-7}\,\mathrm{s}$	$0.0005\,\mathrm{m}$
1 nm	$3.3\times10^{-9}\,\mathrm{s}$	$3.3\times10^{-6}\,\mathrm{m}$	$2.5\times10^{-6}\,\mathrm{s}$	$0.0025\,\mathrm{m}$
10 nm	$3.3\times10^{-8}\,\mathrm{s}$	$3.3\times10^{-5}\,\mathrm{m}$	$2.5\times10^{-5}\,\mathrm{s}$	$0.025\,\mathrm{m}$
100 nm	$3.3\times10^{-7}\,\mathrm{s}$	$3.3\times10^{-4}\,\mathrm{m}$	$2.5\times10^{-4}\,\mathrm{s}$	$0.25\,\mathrm{m}$

Table 4.2: Example relaxation times and stopping distances in 25 °C air. Particles start at $|\vec{v}_0| = 1000\,\mathrm{m\,s^{-1}}$ and are of $5\,\mathrm{g/cm^3}$ density or argon.

We can see that even at high $1000\,\mathrm{m\,s^{-1}}$ initial velocities a particle will stop and match the gas flow movement within nanoseconds and micrometers in atmospheric pressure and can take microseconds and move millimeters in 1 Torr vacuum. Incidentally, this is one place where the precise vacuum pressure matters: if we want particles to travel multiple meters against the gas flow without an additional force[20], this would require a significantly lower

[19] Sometimes mechanical mobility $B = 1/\beta$ is used instead of β [102]. See electrical mobility in chapter 6.

[20] In chapter 6 we'll consider adding an additional electrostatic force.

vacuum below 1×10^{-3} Torr (in the high vacuum regime), even though both it and 1 Torr are close to zero compared to 760 Torr atmospheric pressure.

Let's consider particle motion through a series of chambers and pressure gradients, which illustrates a number of important and useful effects.

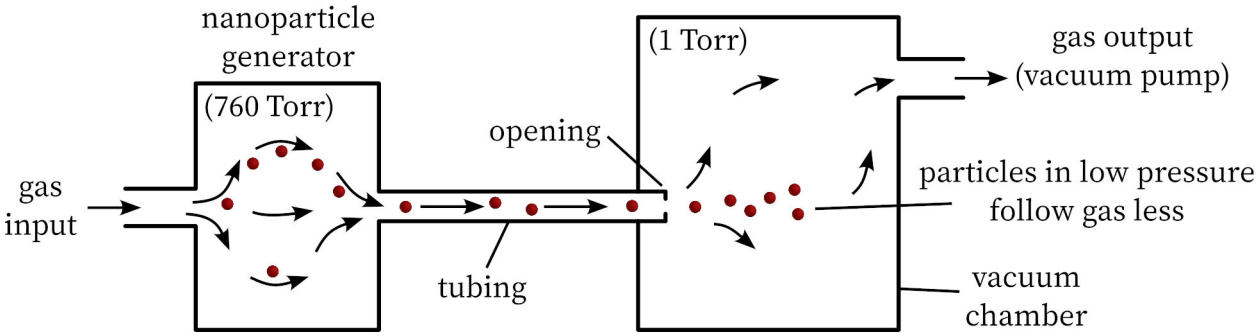

Figure 4.5: Gas (black arrows) flows into a left chamber (perhaps a nanoparticle generator), through tubing and a narrow opening into a right (vacuum) chamber at significantly lower pressure, and out into a pump. Nanoparticles (red circles) follow the gas as soon as they are created but start to deviate from gas streamlines in the low-pressure vacuum chamber.

Gas flow and pressure gradient: Before considering nanoparticle motion, note how the gas moves through this system. Gas is continually added on the left, removed from the right, and flows as one might intuitively expect[21]. The two chambers are each mostly at constant pressure, but the pressure can drop through the thin tube connecting them (in vacuum engineering, this is quantified as the conductance[22] [207]), and especially across the small opening into the right vacuum chamber. This leaves the chambers at different pressures (gas flow is driven by pressure gradients). We will assume gas flow is independent of particles (which are sufficiently small and sparse).

Flow into vacuum chamber: It is worth elaborating on how the right vacuum chamber is at low pressure at steady state even though gas is flowing into it. This is a differentially pumped vacuum system[23]. Similar setups are common in semiconductor process equipment to keep process gas at a specific pressure or in scanning electron microscope electron guns. In mass spectrometers these move analytes from high pressure to vacuum, and the opening is referred to as a skimmer[24] [219][220][221]. The small opening can be engineered (e.g., as an orifice plate or de Laval nozzle) to create a large pressure differential and often operates in the choked flow regime [207].

Particle motion: Due to short relaxation times and stopping distances as in table 4.2, particles almost exactly follow gas streamlines to move from the left chamber (where they

[21] A full treatment of fluid dynamics is out of scope of this dissertation.

[22] Conductance allows simple analysis of vacuum systems in free molecular flow. It acts similar to networks of electrical or thermal conductivities.

[23] A larger differentially pumped system might have separate vacuum pumps for each chamber.

[24] Skimmers have variations from simple to complex. For example, an ion funnel [218] uses ponderomotive force to guide charged particles toward an orifice, similar to the quadrupole we will investigate in chapter 6.

were perhaps created by vapor nucleation), through the tubing, and into the right. Once in the right chamber, however, their stopping distance is long enough that they start to break away from streamlines due to inertia; the lower the pressure the larger this effect. If they hit a chamber wall or surface, assume they stop moving. We will want to deposit particles on surfaces, but if any make it to the vacuum pump they can be caught by a filter.

Particles in tubing: Besides air drag, particles in flow through a narrow tube experience three major effects: Brownian diffusion (as previously discussed), thermophoresis, and electrostatic forces. Diffusion causes nanoparticles to move throughout the tube and possibly stick to the tube sidewall [102]. Thermophoresis, the effect that gas atoms near a hot surface have higher kinetic energy, can cause nanoparticles to move away from the tube wall if the tube is warmer than the gas flow or toward it if cooler [222][102][126][223]. Finally, charged particles will be attracted to electrically conductive tubing walls via image charge or possibly to charge built up on electrically insulating tubing [224][225]. We typically want particles to move through tubes like this without being lost by sticking to their walls, so we might choose to use large tube diameters, maximize gas speed to minimize residence time, or heat the tubes to induce thermophoretic force [126].

Gravity: So far we have ignored the effect of gravity on particle motion, and we can justify continuing to do so. Equating the force from $g = 9.8\,\mathrm{m/s^2}$ Earth gravity to air drag in atmosphere gives a 10 nm particle a terminal velocity $v = \tau \cdot g$ of only $3 \times 10^{-7}\,\mathrm{m\,s^{-1}}$ compared to the much larger[25] $4.6 \times 10^{-4}\,\mathrm{m}$ diffusion in 1 s we computed in section 4.1.1.

All that suffices to understand basic particle motion in a gas. In order to achieve our goal of printing particles on a surface at $100\,\mathrm{m\,s^{-1}}$ to $3000\,\mathrm{m\,s^{-1}}$ with sub-1 µm resolution, we'll need to carefully consider the motion of gas and nanoparticles through velocity-increasing nozzles and around surfaces.

4.2.1 Nozzles and Why We Want Vacuum

Consider what is required to print particles onto a surface via aerosol manipulation. When a gas flow is aimed at the surface, it breaks and turns to either side. If particles follow the gas streamlines exactly, as happens at high pressures (due to low stopping distances), they will be blown off to the side and will not reach the surface[26]. In order to print particles, we need their stopping distance to be long enough that they can diverge from the gas streamlines and instead travel straight onto the surface via inertia. This is done by making the gas pressure above the substrate be low: a partial vacuum[27].

We then need to design the gas flow to focus particles to a narrow area (our sub-1 µm resolution) and high speed (we want $100\,\mathrm{m\,s^{-1}}$ to $3000\,\mathrm{m\,s^{-1}}$). This is the job of a nozzle.

[25] This is subtly misleading because diffusion increases with square root of time, but the conclusion holds.
[26] Except maybe through Brownian diffusion, which is very imprecise.
[27] This won't be high vacuum because we're continually adding gas into the area.

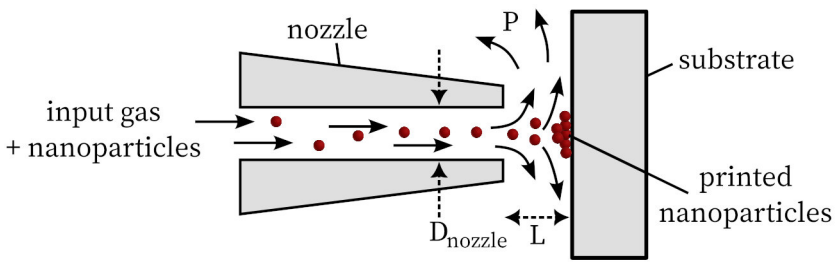

Figure 4.6: In order for nanoparticles (red circles) to be printed onto a surface, they can be accelerated and focused within a nozzle, but once exiting the nozzle they must continue to travel straight to reach the surface despite gas streamlines (black arrows) turning to the side, which can be achieved by making pressure P low. The distance L between nozzle and substrate is often comparable to nozzle diameter D_{nozzle}. Also, Brownian diffusion causes particles to spread out from the centerline anyway, decreasing resolution.

We can approximate what the pressure P above the surface must be even before knowing more specifics of the gas airflow. Particles travel a distance L between nozzle and substrate, and L must be nonzero and often greater than nozzle diameter D_{nozzle} so the gas has somewhere to go. D_{nozzle} is limited by manufacturing and flow rate concerns to be larger than 0.1 mm to 1 mm, so assume $L \geq 1\,\text{mm}$. We know the particle stopping distance S has to be significantly larger than this, i.e., $S > L$ (preferably $S \gg L$ because we want particles to have nonzero velocity upon impact). This dimensionless quantity S/L is called the Stokes number [102]. According to table 4.2, particles above 1 µm diameter might have $S > L$ in 760 Torr atmosphere, but below 100 nm a lower pressure closer to 1 Torr is required. This explains the divide between cold spray and aerosol deposition we saw in chapter 3: cold spray uses large particles so it works at atmospheric pressures, but aerosol deposition needs vacuum; its literature reports pressures of 0.1 Torr to 10 Torr[28] [185]. Even lower pressures are counterproductive as they require bringing the gas closer to the free molecular flow regime even upstream of the nozzle, limiting focusing drag force and increasing diffusion.

How much particle focusing and acceleration is possible? We want high resolution ($< 1\,\mu\text{m}$) and high speeds ($100\,\text{m}\,\text{s}^{-1}$ to $3000\,\text{m}\,\text{s}^{-1}$). The literature has several nozzle geometries:

Aerosol impactors: at its most basic, a nozzle can be just a narrow cylinder through which particles travel as in figure 4.6. Printing resolution is larger than the nozzle diameter D_{nozzle} (generally $> 100\,\mu\text{m}$) due to gas drag and Brownian diffusion. Velocities are limited by choked flow to about sound speed ($< 400\,\text{m}\,\text{s}^{-1}$). This simple mechanism finds use in the aerosol (cascade) impactors (as mentioned and used in chapter 2) that aim to efficiently collect nanoparticles on a substrate for later analysis with no need for high resolution or velocity [102][226][227][228]. Mass spectrometer interfaces are similar sans substrate [219]. These were briefly applied as "gas deposition", a precursor to aerosol deposition [229][230].

Converging-diverging (de Laval) nozzles: Initial work in the 1980s [231][232][233] found that in a converging-diverging nozzle[29], nanoparticles are given inertia to move toward the

[28] This pressure range is why we used 760 Torr and 1 Torr as example pressures throughout this chapter.
[29] These de Laval nozzles are also found on rocket engines.

nozzle center as the gas flow through the nozzle converges, and as the flow diverges (often at lower pressure) the drag force pulls particles away from the center. Proper nozzle design balancing these forces with particle inertia can result in focusing particles in the gas flow into a beam significantly more narrow (100x in theory) than the mechanical diameter of the nozzle, so a 100 µm nozzle, about the smallest feasible to build, can print with down to 1 µm theoretical resolution (ignoring Brownian motion). These nozzles are now ubiquitous in cold spray and aerosol deposition [234]. The gas velocity through these nozzles can be somewhat supersonic (in practice, below about $1000\,\mathrm{m\,s^{-1}}$ [59]); particle impact speed is somewhat lower than this (often $< 700\,\mathrm{m\,s^{-1}}$) [235] after particles slow down as they cross gas streamlines (bow shock, in supersonic nozzle flow [236][237]) between the nozzle and substrate [238]. Also, focusing depends strongly on particle diameter [236][237][239].

Sheath gas and collimation: Modifications can be made to converging-diverging nozzles, e.g., gas relief channels can reduce pressure for higher impact speeds [235], a stream of gas with particles can be surrounded by a sheath gas stream and the result compacted in a nozzle [240][239], or a collimating section can be added [241]. These latter methods can provide additional focusing and also help increase pressure upstream of a nozzle to maintain choked flow for high speeds. Some setups achieve experimental 10 µm to 20 µm printing resolution (the best demonstrated with aerosols to our knowledge) and 2 µm theoretically (neglecting Brownian motion), but with only $100\,\mathrm{m\,s^{-1}}$ velocity [239][241][242][240].

Aerodynamic lenses: Serially stacking converging-diverging nozzles (which can be as simple as a single orifice each) can better focus nanoparticles: this is called an aerodynamic lens [214][243][244][245][246][247]. A calculator exists for easy design [61][248]. Though smaller particles are harder to focus due to their lower inertia and higher diffusion, aerodynamic lenses provide a design framework that has been used to focus particles as small as 1 nm to 10 nm [244][125], though focusing resolutions are generally > 100 µm, velocities are usually $< 100\,\mathrm{m\,s^{-1}}$, and many particles are lost by adhesion to the lens sides. Deposition works [249], but the end of such a lens often opens into high vacuum to create particle beams for mass spectrometry or spectroscopy. [214] gives an expression for particle beam broadening due to the initial angular spread from Brownian motion when entering high vacuum.

We can see these aerosol nozzle particle focusing methods can approach the printing velocities and resolutions we want but cannot quite reach them. They are somewhat further suboptimal for deposition as discussed in chapter 3 for the following reasons:

- Velocity limits: gas flows are generally limited to slightly-supersonic $< 1000\,\mathrm{m\,s^{-1}}$, and particle speeds are somewhat slower than this. Though aerosol deposition and cold spray reach the $100\,\mathrm{m\,s^{-1}}$ to $500\,\mathrm{m\,s^{-1}}$ minimum speeds required for deposition, the higher velocities ($3000\,\mathrm{m\,s^{-1}}$) we hypothesized may be useful do not seem feasible.
- Resolution limits: the highest printing resolution experimentally demonstrated to date is only 10 µm [241] (for > 500 nm particles; smaller is harder) and it is not clear whether better is possible. Below we give another argument that sub-1 µm resolutions are unlikely due to Brownian diffusion.
- There is significant gas flow around the part under construction, which may damage fragile printed objects or be affected by substrates heated for epitaxy.

As a final argument that further development of aerosol-based focusing is unlikely to lead to our desired printing resolution, consider limits due to Brownian diffusion. In the setup of figure 4.6, suppose particles are perfectly focused into a tight beam ($< 10\,\text{nm}$ diameter) within a nozzle then leave at a maximum $1000\,\text{m}\,\text{s}^{-1}$ and travel a minimum 1 mm distance to the substrate (again, the surrounding gas pressure must be sufficiently low for the particle to make it to the substrate). In the 1 µs of travel time, we can approximate how far particles can diffuse perpendicular to their direction of travel using equation 4.8; twice this is the minimum particle placement resolution. The printing resolution is limited both by diffusion/placement and by particle size (1 µm particles cannot print a line $< 1\,\mu\text{m}$ wide).

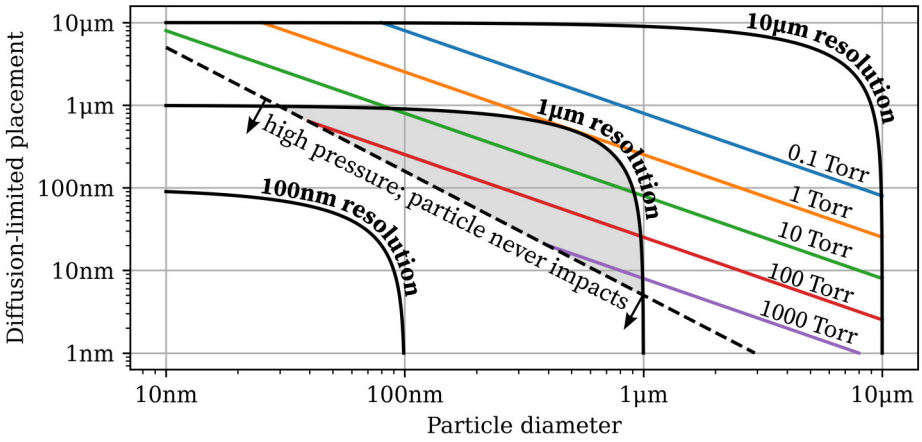

Figure 4.7: A rough model of aerosol printing resolution limits as described above. Achieving a given resolution (100 nm, 1 µm, 10 nm) requires both a small particle size and low Brownian diffusion, but increasing the pressure to minimize diffusion eventually means the particle stopping distance is too short and it never hits the substrate. There is only a small region (shaded light gray) where 1 µm printing may be possible; 100 nm never is, and unfortunately this requires large ($> 100\,\text{nm}$) particles less likely to make high-quality electronic thin films. It makes sense that the literature's best printing resolutions are just under 10 µm.

We can conclude that aerosol nanoparticle manipulation is close but insufficient; it can neither focus nor accelerate particles as much as we would like to make interesting devices.

In order to achieve higher velocities and resolutions, we will have to consider methods not limited by Brownian diffusion, i.e., electrostatic forces in vacuum (as a limit, recall single-atom focused beam methods can achieve sub-10 nm resolution and $> 1 \times 10^4\,\text{m}\,\text{s}^{-1}$). It is worth dedicating our effort (chapters 5, 6) to investigating these instead of pure aerosols.

However, aerosol manipulation is still useful. It is convenient for moving nanoparticles around before printing (we used it already in chapter 2) and might be used for bringing nanoparticles into vacuum in a controlled way before further electrostatic manipulation. Furthermore, aerosol focusing will let us test multimaterial deposition albeit with low impact speeds and bad resolution. We'll try that now.

4.3 Experimental Implementation

Although aerosol deposition cannot by itself reach the full range of deposition velocities and high resolutions we want, it can print nanoparticles with the minimum $100\,\mathrm{m\,s^{-1}}$ to $500\,\mathrm{m\,s^{-1}}$ velocity required for minimal particle-substrate adhesion and with sub-1 mm (not sub-1 µm) resolution. We constructed such a system to demonstrate multimaterial printing with the nanoparticle sources we built in chapter 2. Because the system includes moving nanoparticles into a vacuum chamber, it is also an excellent starting point to build a future electrostatic focusing and acceleration apparatus as described in chapters 5 and 6.

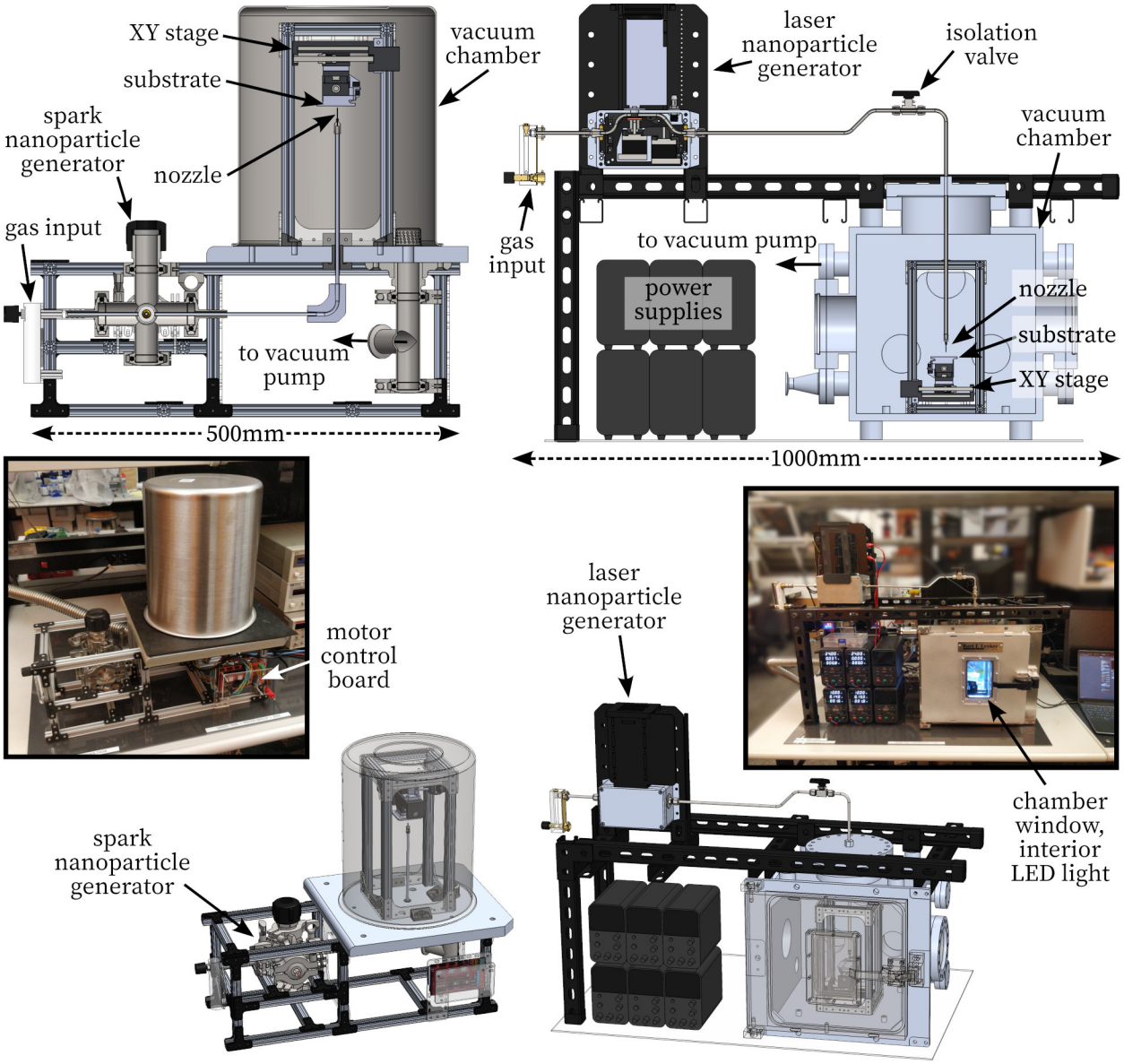

Figure 4.8: Two versions of the same system. Left: first version with spark ablation nanoparticle generator. Right: second version with larger chamber and laser nanoparticle generator.

Safety note: vacuum chambers are generally safe except for minor implosion concerns. Placed in standard atmosphere, a 300 mm cube vacuum chamber has a pressure differential of one atmosphere (101 kPa or 760 Torr) giving a potential energy of 2.7 kJ that can be suddenly released. This risk is easily minimized by sufficiently robust construction. This is also significantly safer than pressure vessels (like gas cylinders or common workshop air compressors): even the best vacuum chamber has a pressure differential of at most one atmosphere, but pressure vessels can be pressurized to potentially tens or hundreds of times atmospheric pressure with proportional stored energy.

We actually made two iterations of the same system. The first was built around the spark ablation nanoparticle generator from chapter 2. This system was replaced with the second which instead used the the laser ablation nanoparticle generator and also added a larger, higher-quality vacuum chamber. The systems otherwise worked similarly.

Both systems were constructed with a vacuum chamber as required for printing nanoparticles (see section 4.2.1). The first system used a custom[30] cylindrical chamber (220 mm diameter by 270 mm tall); the second had a commercially-built[31] high-vacuum-capable chamber with a 300 mm cubical interior. Both were pumped with an 160 L min^{-1} Edwards RV8 rotary vane vacuum pump and monitored by an Edwards APG-M-NW16 Pirani vacuum gauge. The chambers could both reach a base pressure of under 5×10^{-2} Torr within a couple minutes as expected. Progressively lower vacuum levels need progressively better hardware (see [207]). In our case, we needed only 1 Torr pressure, well within the low vacuum range that only requires a single pumping stage, and only used air (any semiconductor process gas, for example, would need much more attention paid to safe usage, venting, and exhaust). This meant we were able to take shortcuts for the first chamber: wire feedthroughs were custom made with laser-cut acrylic[32] bolted with o-rings to the aluminum baseplate, for example. The second chamber was made with significantly more care including CF flanges and commercial electrical feedthroughs and should be capable of reaching high vacuum ($< 1 \times 10^{-5}$ Torr) if a second pumping stage (e.g., turbopump) were later added.

After leaving the nanoparticle generators, aerosols were moved through standard 1/4 inch (4.6 mm ID) stainless steel instrumentation tubing connected with compression and VCR face seal fittings, eventually reaching the nozzle, a 20 mm long 0.21 mm ID (27 gauge) steel dispensing needle inside the vacuum chamber positioned 1 mm to 3 mm from the substrate. Total flow distance from the nanoparticle generator to nozzle was 380 mm or 800 mm for the two system versions, respectively. During operation, an input gas valve was adjusted to allow about 0.5 standard liter per minute gas flow (air) through the nanoparticle generators to each chamber. When entering the vacuum chamber through the nozzle and with our vacuum pump, this gas flow resulted in steady state chamber pressures of 0.5 Torr to 1 Torr. Based on the choked flow assumption and similarity to mass spectrometer inlet capillaries [219][220], we estimate nozzle gas (and particle) exit velocities were 100 m s^{-1} to 350 m s^{-1}.

[30] An epoxy degassing pot on top of a custom aluminum faceplate with a neoprene rubber gasket.

[31] From the Kurt J. Lesker Company. This chamber was bought cheap at auction; new it is worth >$10k.

[32] With wires through holes sealed with (sometimes) hot glue. Don't do that on better vacuum systems.

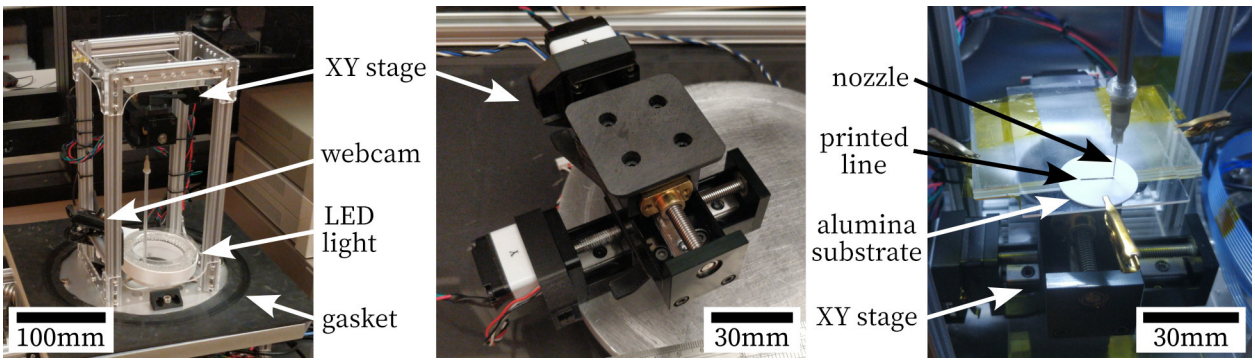

Figure 4.9: Left: first version with vacuum chamber cover removed to show XY stage, nozzle, webcam, and light. Center: custom XY stage. Right: inside of second version while printing the gold line from section 4.3.3 on an alumina substrate clamped to the XY stage.

Besides the large vacuum chambers, the largest addition to these systems beyond the basic impaction setup we used in chapter 2 was a motorized XY stage able to move the substrate (clamped on top of the stage) with respect to the nozzle in order to print 2D patterns. It is preferable to move the small and light substrate while keeping the nozzle, which is connected to rigid tubing, fixed in place[33]. Small vacuum-compatible XY stages with nanometer precision are commercially available[34]. We built our own stage from stepper motor linear slide modules, open loop stepper motor drivers, and open source 3D printer control software. This XY stage could move about 40 by 40 mm with estimated 10 µm repeatability. Besides the stage, we also added a USB webcam camera and LED light inside the vacuum chambers to observe the printing process. None of the XY stage, webcam, or light needed special care to survive the vacuum[35].

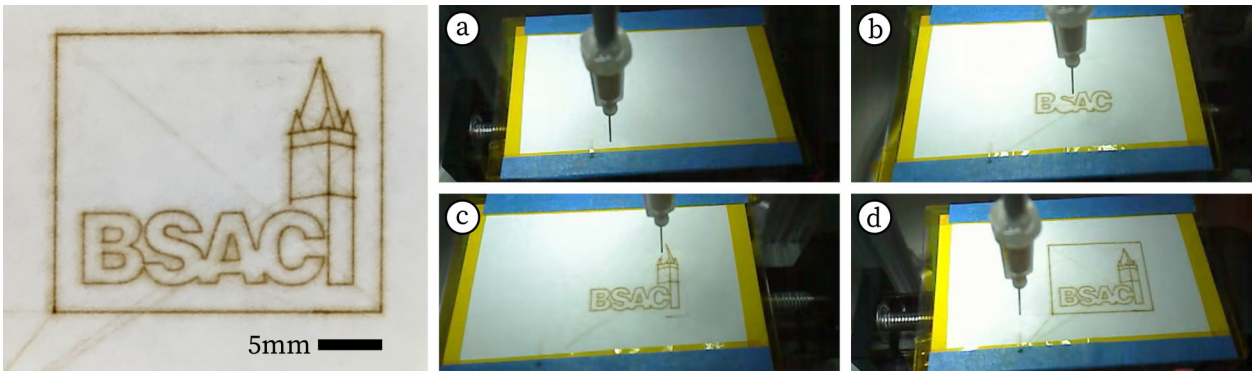

Figure 4.10: Left: BSAC logo in copper on paper, printed in 45 min. Right: the printing process at (a) 0 min, (b) 15 min, (c) 30 min, (d) 45 min.

[33]The electrostatic focusing system of chapter 6 replaces the nozzle and is larger and heavier. But then, given charged particles, we might additionally deflect particles electrostatically in XY (like scanning electron microscopy) for fast small motion. A mechanical XY stage is still necessary for long-distance movement.

[34]Piezo motor or voice coil stages with optical feedback are >$5k from [250][251][252].

[35]This worked because (a) we used no harmful process gases and (b) we did not need high vacuum which offgassing or virtual leaks from these parts might prohibit. We also found no heat dissipation problems.

As an initial test, we printed the logo of the Berkeley Sensor and Actuator Center (BSAC) with copper nanoparticles on paper. Using the deposition conditions outlined above with the spark ablation nanoparticle generator and moving the XY stage created the successful result shown in figure 4.10. The stage was moved at $0.1\,\mathrm{mm\,s^{-1}}$ below the nozzle; at this speed, the total print took 45 min to complete. This could be sped up significantly by increasing the nanoparticle flow rate or printing thinner lines. The printed lines had a dense inner portion about 160 µm wide and a fainter 400 µm outer portion, respectively thinner and thicker than the 0.21 mm nozzle. Nanoparticles were continually generated, so in order to print disconnected patterns (the "B" and rectangular border, for example), the stage was moved at a faster $1\,\mathrm{mm\,s^{-1}}$ between these thereby creating only faint (diagonal) lines[36].

It is interesting to note standard microfabrication cannot replicate this. Specifically, microfabrication cannot deposit a metal shape on paper substrates[37] because the paper would not survive the wet chemical photoresist developing and removal steps required to pattern the metal, not to mention whatever process is used for etching.

4.3.1 Multimaterial Printing

As emphasized in chapter 1, semiconductor devices are made of multiple electronics-grade materials, and one of the most interesting possibilities of a nanoparticle printer is the ability to pattern multiple such materials in a single tool.

We already demonstrated generation of nanoparticles from 8 different materials and printing on glass, steel, and silicon in chapter 2. We have also printed copper on paper. What remains to be shown is that multiple materials can be added to the same part[38].

To prove this is possible, we printed lines of copper, silver, gold, and silicon (in that order) on an alumina substrate. Specifically, we began with a 25 mm diameter alumina disk (96% Al_2O_3, remainder SiO_2) then deposited one material at a time, moving the substrate at $0.1\,\mathrm{mm\,s^{-1}}$ for 2.5 min each with the same parameters used previously, to create 15 mm long lines. After each line, the laser nanoparticle generator was stopped, opened, and had its material target changed out, all while the substrate remained at vacuum.

The successful result is shown in figure 4.11. All lines were about 500 µm wide; more detailed geometry measurements are shown in section 4.3.2. This is significantly wider than the 0.21 mm nozzle. Interestingly, each material demonstrated subtly different behavior despite being deposited in the exact same conditions (including laser nanoparticle parameters, gas flow rate, and print speeds). Copper and silver stuck to the substrate and printed well-defined clean lines. The gold adhered to both itself and copper and silver lines beneath but not to the substrate, resulting in a film that flaked off (especially when blown away by gas escaping the nozzle). As briefly noted in chapter 2, the poor adhesion of gold to alumina is due to its inability to oxidize. This is a known effect in microfabrication solved by depositing gold films instead on an intermediate Cr or Ti film as an adhesion layer. The printed silicon, finally, produced a thin yet tall ridge (see section 4.3.2).

[36] In future work this could be replaced with a proper beam blanking mechanism.

[37] Except maybe with a shadow mask, which has other drawbacks. See elaboration on this in section 4.3.1.

[38] Given a functional printer this might seem trivial. It somewhat is—that's why printers are interesting.

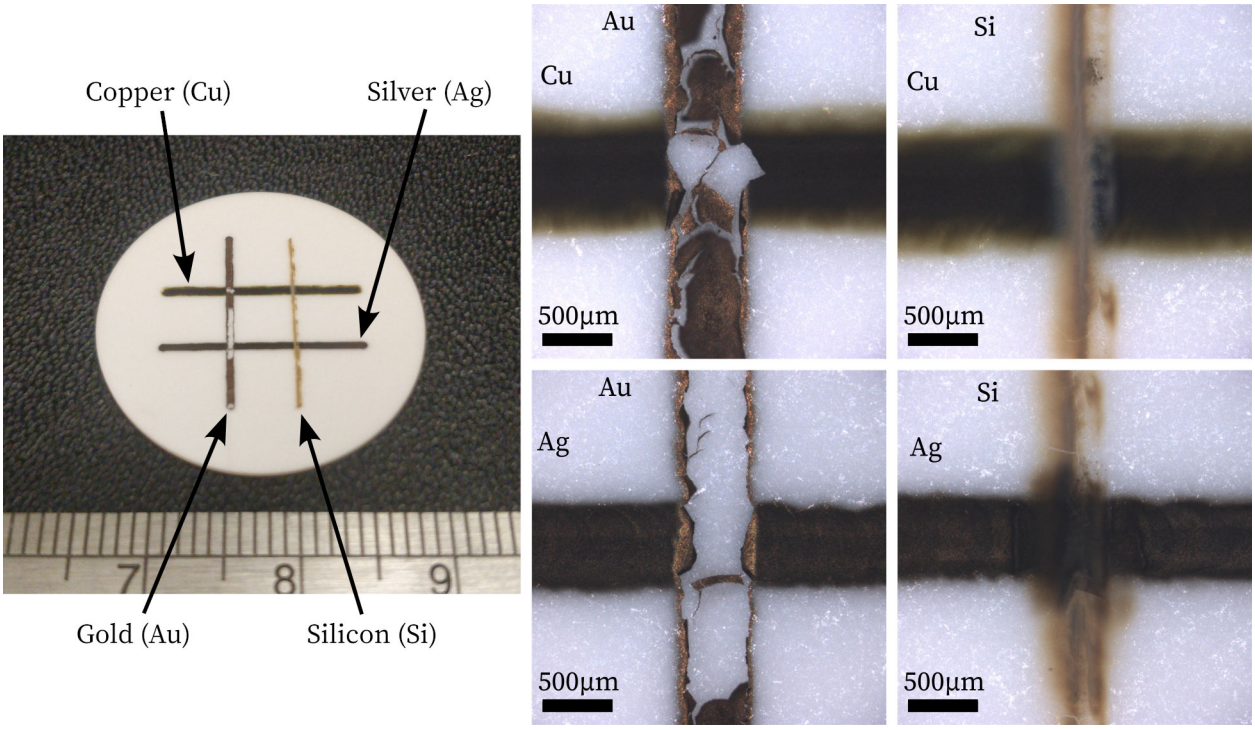

Figure 4.11: Left: copper, silver, gold, and silicon lines printed (in that order) on an alumina disk. Right: clockwise from top left, the intersection of Cu/Au, Cu/Si, Ag/Si, and Ag/Au.

Despite this result, more work remains to produce a working multimaterial semiconductor device (for example, a diode); we have yet to reliably print even simple conductors besides gold. We believe this is solvable: we discuss the major roadblock, oxidation, in section 4.3.3. The other problem is low film quality: as hypothesized in section 4.3.2, these lines are porous with sub-bulk qualities. The way to fix that (see chapter 3) is to print with higher particle impact velocities using something better than aerosol deposition.

But we have still shown another feat microfabrication cannot replicate: this simple pattern was printed in 10 min, but it would have taken microfabrication many hours to make this because each different material requires its own deposition, lithography, and etch steps.

For completeness, there is one microfabrication technique that can achieve similar results: stencil lithography [253][254], where a thin membrane with holes (a shadow mask) is placed in between an evaporator material source and a substrate in high vacuum[39]. The mask can be moved to change where material is deposited [255]; switching materials allows multimaterial deposition. Sub-100 nm patterning has been achieved. However, deposition rates are slow ($1\,\mathrm{nm\,s^{-1}}$), so patterning large arbitrary custom structures takes unreasonably long, and the stencil can become clogged over time. As a result, this is used only for occasional nanoscale research tasks. Nanoparticle printing, though it has yet to achieve the same printing resolutions, has neither of these limits and should be better suited to general applications.

[39]This can be modeled as apertures subject to the emittance theorem (see chapter 6).

4.3.2 3D Printing

Up until now, we have only discussed printing in 2D[40]. Theoretically a nanoparticle printer can easily extend this to 3D: simply print multiple 2D patterns on top of one another[41]. Doing this requires each layer to be thick but might allow printing MEMS.

We can get some preliminary evidence that printing thick layers is possible. We used a 3D laser confocal microscope to measure the cross-section of the Cu, Ag, Au, and Si lines we printed in section 4.3.1 with results shown in figure 4.12. These lines were about 500 µm wide and 10 µm tall with the exception of silicon that formed a 50 µm high peak.

We can also use these cross-sections to estimate the volume of the printed lines and, from there, the rate at which material was deposited. The volumes of these 15 mm long lines are, for Cu, Ag, Au, and Si, 0.033 mm^3, 0.039 mm^3, 0.053 mm^3, and 0.095 mm^3. Since each was printed in 150 s, this gives possibly unrealistically high mass deposition rates of 7.1 $mg\,h^{-1}$, 9.9 $mg\,h^{-1}$, 25 $mg\,h^{-1}$, and 5.3 $mg\,h^{-1}$. In chapter 2, we estimated the laser ablation nanoparticle generation rate at only 0.6 $mg\,h^{-1}$ to 6 $mg\,h^{-1}$. We can conclude that a large fraction of material was successfully transferred as nanoparticles from material target to substrate (i.e., high efficiency) and these lines are probably porous with lower density than bulk, as expected from low particle impact velocities (see chapter 3).

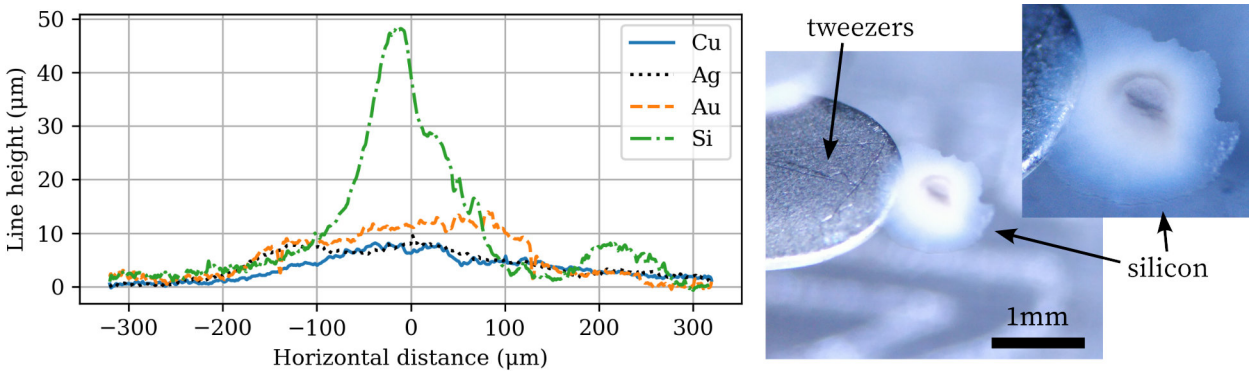

Figure 4.12: Left: height profiles of the lines printed in figure 4.11 showing 3D geometry. Right: a 3D conical silicon deposit in midair stuck to tweezers.

These deposits may be thick enough for 3D printing, but we can do better: focusing the same nanoparticles to a smaller area (and with higher impact velocities) as we eventually hope to do should produce thinner yet taller lines. It might also improve the rough surface (which is likely due in part to forces from impacting gas).

Also, in a separate experiment while printing silicon on glass, we noticed a large silicon deposit detached from its glass substrate (see figure 4.12). It stuck to a pair of tweezers used to pick it up, technically becoming a freestanding structure. This supports the hypothesis that nanoparticle-printed structures are sufficiently solid to form 3D shapes.

[40] Aside from mentions of aerosol 3D printing in chapter 1, which remain promising.

[41] Overhanging geometry can be made by printing then later etching away a sacrificial support material.

4.3.3 Conductors and Oxidation Problems

We can print multiple materials, but we should also show they still exhibit the electrical behavior necessary to make semiconductor devices. A good first step is confirming expected conductors (and semiconductors) are electrically conductive and insulators are not.

We confirmed printed gold is conductive. We deposited another 15 mm gold line on alumina (an insulator) with the same parameters as in section 4.3.1. As previously noted, the gold formed a solid film that flaked off due to poor adhesion to the alumina substrate, but it was still sufficiently solid to confirm conductivity. On a probe station, we positioned two micromanipulator probes about 100 µm apart atop one gold flake and measured a resistance of about 4 Ω fluctuating slightly with time (and removing the probes left visible scratches). This is conductive; we attribute the somewhat high[42] resistance and fluctuations to the hypothesized porous structure and resulting minor local joule heating. This should be fixed by creating a more solid film by increasing particle impact velocity as in chapter 3.

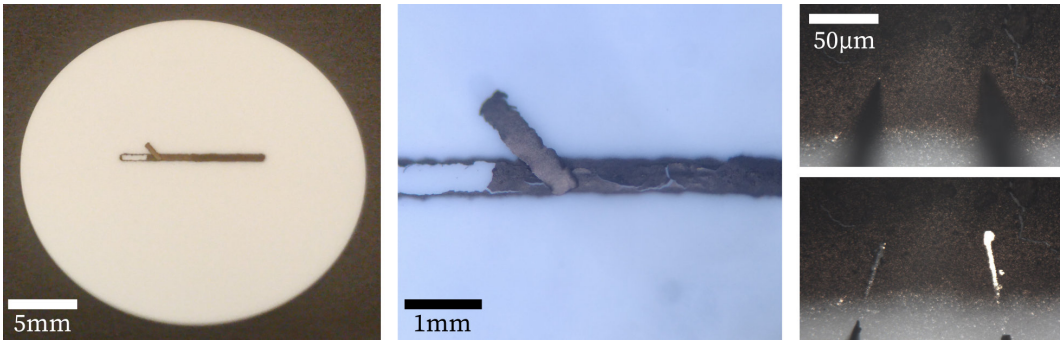

Figure 4.13: Left: gold line printed on alumina. Center: gold flakes off substrate. Right top: two probe tips on edge of gold line. Right bottom: visible scratches with probes removed.

However, repeating this with copper gave no measurable conductivity. It seems metals (and Si) other than gold are not conductive when they should be. This is problematic.

The problem is almost certainly oxidation: oxygen molecules that hit a surface will often react with the exposed atoms[43] to form an oxide that happens to be an electrical insulator. Copper becomes[44] CuO or Cu_2O, aluminum becomes Al_2O_3, silicon becomes[45] SiO_2. The gas flowing through our system was air, which contains much more than enough oxygen to oxidize the surface of nanoparticles nearly as soon as they are created, so the final printed material might be mostly insulating oxides with, at best, small isolated pockets of conductive metal that were incompletely oxidized. Gold is the exception as it is the only metal without a thermodynamically stable oxide. Oxidation is why welding needs inert gas, soldering needs flux, and why iron rusts[46]. The oxidation hypothesis is further supported by our EDS image of printed copper in chapter 2 which found significant oxygen.

[42] A solid 100 by 100 by 5 µm gold film should have 0.0049 Ω resistance.
[43] Sometimes oxygen can also diffuse through a material to oxidize more atoms underneath.
[44] Copper oxides are P-type semiconductors, but it is hard for us to take advantage of that right now.
[45] This is useful in microfabrication to purposely grow thin films of SiO_2 on silicon [1].
[46] Rust is just iron's oxide, but it happens to expand and become mechanically unstable when grown.

In other words: if our experiments were repeated but all oxygen were magically removed from the surrounding air, everything would still work and our printed copper, silver, and other metals would be conductive, and the silicon would likely be properly semiconducting. If not for oxygen, we might have printed diodes and transistors by now.

The best solution[47] to the oxidation problem is exactly this: to remove oxygen (and water vapor, which contains oxygen and can act similarly) from the chamber. Perfect removal is near-impossible, so we should ask exactly how much oxygen our process can tolerate.

We would like nanoparticles to remain (at least mostly) oxide free from their creation until they are printed[48] and covered with another layer of particles. Suppose this takes several seconds. Using equation 4.3 we can calculate it takes about 1 s for oxygen at a partial pressure of 1×10^{-6} Torr to completely cover a surface; this is a good minimum pressure target to aim for though lower is of course preferable.

Reaching oxygen pressures below 1×10^{-6} Torr is well within vacuum technology capabilities and is commonly used in microfabrication evaporation for this same reason [118]. This falls within the high vacuum regime (8×10^{-5} Torr to 8×10^{-9} Torr [207]); the typical approach is to bring a sufficiently good vacuum chamber down to a full vacuum (no gases including oxygen) then optionally backfill it with some other non-oxygen gas if desired (as used in sputtering [118]). What makes things a little more difficult is we need near-atmospheric pressure for the nanoparticle generators; those sections of our system need gas with part-per-billion oxygen levels. Argon is sold with part-per-million oxygen impurities but can be further filtered before flowing into a gas chamber to reach these low levels [58]. All this does require significant attention paid to chamber materials, cleanliness, and vacuum pump stages, but it may be worthwhile: another benefit of high vacuum is a large gas mean free path with negligible Brownian motion, and we may be able to take advantage of this to achieve high precision as discussed in chapter 6.

It is also useful to monitor oxygen and water vapor levels to confirm the desired low oxygen pressures are reached. Monitoring methods include [257] electrochemical sensors, optical sensing (spectrometry) [149], and residual gas analyzers [207].

Unfortunately we were unable to obtain a sufficiently good vacuum system within the time and budget constraints for this dissertation[49], so we will have to postpone printing non-gold conductors and semiconductors to future work.

However: we can still conclude multimaterial nanoparticle printing, the first half of what we need to create a better device fabrication technology, seems feasible. Since were not able to reach the second half—high particle resolutions and impact velocities—with aerosols, as proposed in 3 we will now consider electrostatic manipulation of nanoparticles to further refine their movement.

[47] An alternative solution is to make the gas actively reducing (often "forming gas", a 5% H / 95% N_2 mixture) to counteract oxide growth, but this might create other problems.

[48] Interestingly, the impact and deformation of the larger particles of cold spray can break through their surface oxide coating, allowing printing metals in atmosphere. This doesn't work on our smaller scales [256].

[49] We did briefly try using 1ppm nitrogen gas flow instead of air, but we saw no benefit as expected as the resulting 1×10^{-3} Torr oxygen partial pressure in the nanoparticle generator remained too high.

Chapter 5

Nanoparticle Charging

So far we have created nanoparticles, moved them in a low-pressure gas, and achieved some limited multimaterial printing success, but also found we need additional control over nanoparticle motion if we want to print truly small or high-quality structures. That control will come from electrostatic manipulation in chapter 6, but in order to move nanoparticles with electric fields, we must first electrically charge the nanoparticles.

That is, we must somehow add or remove electrons from each nanoparticle without affecting the positively-charged atomic nuclei thus leaving the particle with a negative or positive charge, respectively—and we need to do this while the particles remain suspended in midair to avoid compromising their material purity. This is nontrivial.

5.1 Charging Methods

Fortunately for us, plenty of nanoparticle charging prior art exists in the academic literature. Aerosol studies often charge nano- to micron-scale particles as the first step in measuring, collecting, or otherwise manipulating them. Charging (albeit for single atoms and molecules) is also fundamental to mass spectrometry, focused ion beam tools, and trapped-ion quantum computing. Charging methods include (but are not limited to) [102][76]:

- **Diffusion charging:** Suppose particles are in a gas and some gas molecules are ionized (unipolar, i.e., either positive or negative, not both). When an ionized molecule collides with a particle via Brownian motion, an electric charge is sometimes transferred. Repeated collisions can build up a large charge. If the gas has both positive and negative ions (a bipolar distribution), this can instead discharge.
- **Field charging:** This is diffusion charging in the presence of a uniform electric field, which more efficiently charges larger particles due to electric field distortions around the particles. Diffusion and field charging are often combined.
- **Corona, flame, radioactive, and photoelectric charging:** These are all methods to charge the gases that then charge particles via diffusion and field charging. Corona

charging uses high voltage breakdown of the gas, flame charging uses thermionic emission via the high temperature of a flame, radioactive charging uses an α or β source, and photoelectric charging uses the photoelectric effect.

- **Photoelectric charging:** Photoelectric charging can directly charge nanoparticles without diffusion or field charging as an intermediary [258]. Photons of sufficient energy (often UV or x-ray) hit a surface, are absorbed by electrons, and give them sufficient kinetic energy to leave the particle. This is the dominant mechanism for charging dust around a star or in the interstellar medium [259].
- **Electron impact ionization:** Bombarding nanoparticles with electrons can give them a negative charge or, via secondary electron emission, a positive charge [260][261]. Used in mass spectrometry for charging molecules; has been used for cluster beam deposition [178][47]. Requires high vacuum for the electron mean free path to be sufficiently long. Important in lunar dust behavior along with photoelectric charging [262].
- **Electrospray ionization:** A way to simultaneously generate and charge nanoparticles using a liquid medium (see also its description in chapter 2). Used as a mass spectrometry ion source or a liquid metal ion source (LMIS) for focused ion beam tools [76][108][109]. It is possible to charge nanoparticles [112], but we will ignore this as the process is messy, material-dependent, and might compromise material purity.
- **Field and thermionic emission:** More a fundamental physical effect than a charging method. Electrons are pulled from a material surface with a sufficiently strong electric field (field emission) or break away with sufficiently high kinetic energy from high temperature (thermionic emission). Commonly used for, e.g., electron microscopes. Is used for electron impact ionization. Sometimes flame charging makes nanoparticles emit electrons via thermionic emission in addition to field and diffusion charging. Field emission is also responsible for charging limits as described later.
- **Spark ablation:** The same spark ablation process used to generate nanoparticles can also allow some to end up with a charge due to the large ion concentration in the spark arc, not dissimilar from corona charging. The resulting nanoparticles have a distribution of positive, negative, and neutral charges [128].

All these methods have different capabilities. They result in different charge distributions (some percentage of nanoparticles are positively charged, neutral, and negative) and have different efficacies on nanoparticles of different diameters (e.g., field charging is more effective for larger particles). Many nanoparticle charging applications, such as mass spectrometry or the differential mobility analyzer (DMA) previously mentioned as a way to sort nanoparticle diameters, prefer methods that more reliably give a single electrical charge to all sizes of nanoparticles. This makes it easy to sort nanoparticles based on mass-to-charge ratio.

What qualities do we want from a charging method? As we will see later, we prefer nanoparticles to have as high a charge as possible, and we would also like to ensure all nanoparticles (instead of only a small fraction) are charged. To choose a method, we should first discuss maximum charge limits.

5.1.1 Charging Limits

There is a limit to how much charge can be put on a nanoparticle. If the negative charge is increased by adding electrons, the nanoparticle can have such a negative charge that any additional added electrons are spontaneously repelled. Likewise, if electrons are removed to leave a positive charge, there is a point at which repulsion between the positively charged nuclei is sufficient to break up the nanoparticle. This limit can be approximated [102] by comparing the surface electric field strength E_s needed to remove an electron (i.e., field emission) or nucleus to the field present on the surface of a charged particle of diameter d_p from Gauss's law $E_s = (ne)/(\pi\epsilon_0 d_p^2)$, where n is the number of elementary charges on the particle, $e \approx 1.60 \times 10^{-19}\,\mathrm{C}$ is the elementary charge, and $\epsilon_0 \approx 8.85 \times 10^{-12}\,\mathrm{F\,m^{-1}}$ is the permittivity of vacuum. This maximum number of charges n is

$$n \leq \frac{\pi\epsilon_0 E_s d_p^2}{e}. \tag{5.1}$$

The precise value of E_s, often modeled with Fowler-Nordheim theory, is heavily dependent on the surface. For a rough estimate, Hinds [102] suggests $E_s \approx 9.0 \times 10^8\,\mathrm{V\,m^{-1}}$ and $E_s \approx 2.1 \times 10^{10}\,\mathrm{V\,m^{-1}}$ for electron and nucleus emission, respectively.

There are limits for the diffusion and field charging methods mentioned above: a charged nanoparticle will electrostatically repel similarly charged gas molecules, reducing the likelihood of further charging[102]. All these charge limits can be quantitatively graphed:

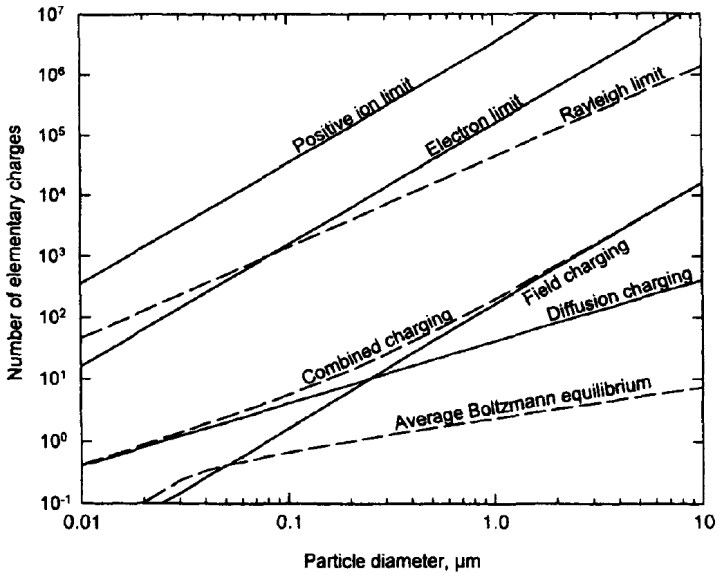

Figure 5.1: The limits to nanoparticle charging, from [102]. Above the positive ion limit, removing additional electrons will cause a nanoparticle to break apart via repulsion between positive nuclei; above the electron limit, adding more electrons is impossible as any new electrons are spontaneously repelled due to excess negative charge. The Rayleigh limit is the point at which liquid droplets break up overcoming surface tension. Contrast these with the much lower maximum charging limits achieved by field and diffusion charging or the average charge achieved in standard atmosphere due to background radiation.

For our desired nanoparticle diameters of approximately 5 to 50 nm, we see that positive charge is limited to hundreds of unit charges and negative charge sometimes to the low tens: if we positively charge nanoparticles, we can fit a higher net charge. But also note that field and diffusion charging may struggle to add even a single charge to a sufficiently small nanoparticle, far from the theoretical maximum.

The best nanoparticle charging method for us is likely photoelectric charging. It is theoretically able to charge particles to their maximum limits, unlike diffusion and field charging, and is much more capable at charging sub-100 nm diameter nanoparticles. It also results in a positive charge which has a higher maximum charge limit than negative charging, giving an advantage over electron impact ionization. Finally, it may be the simplest to implement in whatever printing system we build because it depends little on the nanoparticle material, gas, or ambient electric field: arbitrarily high photon densities have negligible effect on electrostatic nanoparticle movement, unlike the high densities of gas ions or electron densities needed for other charging methods.

5.2 Photoelectric Charging

How does photoelectric charging work, in detail, and how do we implement it? The fundamental idea is the photoelectric effect: when a photon arrives at the surface of a material, it can be absorbed by an electron which converts that photon into energy (kinetic and potential). If this step change in energy is sufficiently high, the electron might escape the surface of the material. Famously[1], this requires each individual photon to have sufficient energy[2]. Increasing the number of photons (the intensity) will not affect the photoelectric effect; it will merely be able to move more electrons at the same time.

Simply put: if we shine light of sufficiently high energy (low wavelength) photons at nanoparticles, electrons should jump off, leaving the nanoparticle positively charged.

How much energy does it take to remove an electron from a nanoparticle? First consider some edge cases. The energy required to remove an electron from a (neutral) atom is customarily termed the ionization energy, while the energy to remove an electron from an infinitely large surface of some material is called the work function Φ. The ionization energy is typically higher than the work function. The energy required to remove an electron from a (neutral) nanoparticle of intermediate diameter is somewhere between these. Furthermore, as soon as one electron is removed from a nanoparticle, the particle will have a positive charge, making it more difficult to remove the next electron, and so on.

This energy can be approximated in the same way as we previously computed the maximum charge limit in equation 5.1, but more care is required to match empirical data [264][265]. Specifically, the energy is well-modeled by the bulk work function, plus the energy required to move an electron from a spherical particle with a given charge, plus a correction to the original work function due to image forces on a sphere instead of a plane. This energy to remove the n^{th} electron from an initially neutral nanoparticle of diameter d_p is:

[1] This won Einstein the 1921 Nobel Prize in Physics.

[2] Usually. Sometimes lower-energy photons can combine to ionize material (multiphoton ionization) [263].

$$E(n) \approx \Phi + n\frac{e^2}{\pi\epsilon_0 d_p} - \frac{5}{8}\frac{e^2}{\pi\epsilon_0 d_p}. \tag{5.2}$$

To more easily visualize the implications of equation 5.2, we can generate a table of the excess energy beyond the work function required to charge a nanoparticle a given amount.

n	1 nm	2 nm	5 nm	10 nm	20 nm	50 nm	100 nm	∞
1	1.08	0.54	0.22	0.11	0.05	0.02	0.01	0
2	3.96	1.98	0.79	0.40	0.20	0.08	0.04	0
3	6.84	3.42	1.37	0.68	0.34	0.14	0.07	0
4	-	4.86	1.94	0.97	0.49	0.19	0.10	0
5	-	6.30	2.52	1.26	0.63	0.25	0.13	0
7	-	9.18	3.67	1.84	0.92	0.37	0.18	0
10	-	13.50	5.40	2.70	1.35	0.54	0.27	0
30	-	-	16.92	8.46	4.23	1.69	0.85	0
100	-	-	-	28.62	14.31	5.72	2.86	0

Table 5.1: The additional energy (measured in eV) beyond the work function Φ required to remove the n^{th} electron from a spherical particle of the given diameter according to equation 5.2. Sufficiently small particles have a maximum charge as previously noted with equation 5.1. The rightmost column labelled "∞" shows the limit as the particle diameter approaches infinity, i.e., it becomes the infinite surface used to define the work function, and is zero by definition. As an example of using this table, a 10 nm diameter nanoparticle of work function 5 eV would require photons of at least $5 + 0.40 = 5.4$ eV to reach a charge of +2.

Material	Work Function	Ionization Energy
Al	4.3 eV	6.0 eV
Si	4.7 eV	8.2 eV
Ti	4.3 eV	6.8 eV
Cr	4.5 eV	6.8 eV
Fe	4.8 eV	7.9 eV
Ni	5.1 eV	7.6 eV
Cu	4.7 eV	7.7 eV
Ge	5.0 eV	7.9 eV
Ag	4.3 eV	7.6 eV
Pt	5.6 eV	9.0 eV
Au	5.3 eV	9.2 eV

Table 5.2: The approximate work functions and first ionization energies of some assorted materials [103]. Work functions vary with crystal orientation; average values are used here. Note that ionization energy is not defined for compound materials such as SiO_2.

Work functions themselves are material-dependent and typically determined empirically. Some are listed in table 5.2 for reference along with ionization energies.

For any given material, we can condense the information from equations 5.1 and 5.2 and table 5.2 into a single graph as shown in the figure below for copper. This sort of plot makes it clear that charging will be most reliable with photon energies significantly higher than the work function, perhaps around 10 eV.

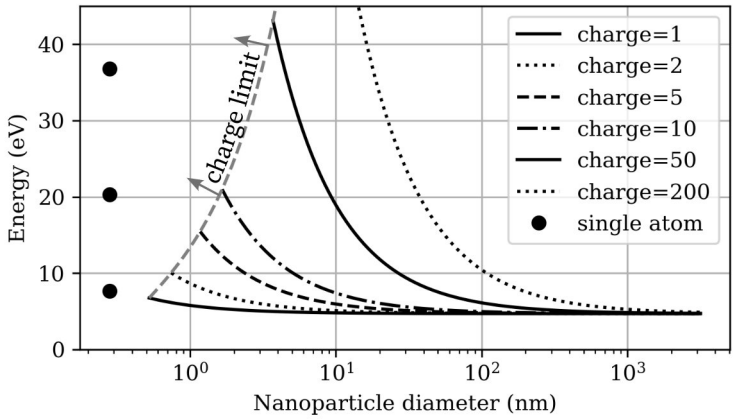

Figure 5.2: A graph of the energy required to positively charge a copper nanoparticle vs. its diameter, created from equations 5.1 and 5.2 and table 5.2. We see that smaller particles require more energy to reach a given charge and also have a lower maximum charge limit (above which a particle will break apart). The first three ionization energies of a single copper atom are shown on the left for comparison. The regime between the single atom and our models is not entirely empty but is complex due to quantum effects; atomic cluster studies report that energies fluctuate with single digit numbers of atoms [142][266][170].

5.2.1 Photoelectric Quantum Yield

There is another relevant factor we have not yet considered: how many photons are required to charge a nanoparticle? We can assume each photon results in at most one emitted electron (so a +10 charge requires at least ten photons), but not all photons impacting a surface succeed. The fraction of photons that successfully remove an electron is called the photoelectric quantum yield, and this also varies with nanoparticle diameter—fortunately in our favor, in that smaller nanoparticles are easier to charge [259][267][265]. The photoelectric quantum yield is another complex material-dependent property, but approximate typical values might be [259] on the order of 0.5 for 1 nm diameter nanoparticles (i.e., 50% of photons result in an emitted electron), 0.1 for 10 nm, and 0.01 in diameters above 100 nm, though efficiencies can easily be lower, e.g., 0.001 is not uncommon. Higher energy photons tend to give higher yields, which suggests it may be more efficient to choose photons with energies above the minimums previously calculated.

5.3 Photoelectric Engineering Considerations

We now know the minimum photon energy required to charge our nanoparticles. From figure 5.2, we want 5 eV to 20 eV, where the higher end of the range is preferable to reach higher charge and increase quantum yield. How can we build a charging system out of this?

5.3.1 Light Sources

The first step in nanoparticle photoelectric charging is to generate the light used to do so. Light is more commonly classified by wavelength than energy per photon, so recall that a photon of a particular wavelength has a fixed energy given by the relation

$$E = \frac{hc}{\lambda} \tag{5.3}$$

where E is the photon energy, $h = 4.14 \times 10^{-15}\,\mathrm{eV\,s}$ is Planck's constant, $c = 3.0 \times 10^{8}\,\mathrm{m\,s^{-1}}$ is the speed of light, and λ is the photon wavelength. Our desired 5 eV to 20 eV light sources have wavelengths 248 nm to 62 nm (with lower wavelengths preferred). Visible light is 400 nm to 700 nm; we are well past this into ultraviolet (UV) light. UV is often divided into the approximate categories [268] UVA (400 nm to 315 nm), UVB (315 nm to 280 nm), UVC (280 nm to 200 nm), and vacuum UV (VUV) (200 nm to 10 nm)[3] [269].

Photon energy	Wavelength	Notes and availability
1.8 eV	700 nm	(end of infrared light regime)
3.1 eV to 1.8 eV	400 nm to 700 nm	(visible light)
3.40eV	365nm	mercury arc lamp (i-line)
4.03eV	308nm	XeCl excimer lamp
4.88eV	254nm	mercury arc lamp
5.00eV	248nm	KrF excimer laser
5.28eV	235nm	lowest wavelength available UV LEDs
5.58eV	222nm	KrCl excimer lamp
6.42eV	193nm	ArF excimer laser
6.70eV	185nm	mercury arc lamp
7.21 eV	172 nm	Xe_2 excimer lamp
7.75 eV to 3.10 eV	160 nm to 400 nm	deuterium arc lamp
9.84 eV	126 nm	Ar_2 excimer lamp
10.2 eV	122 nm	H spectrum peak (Lyman-alpha)
21.2 eV	58 nm	He gas discharge lamp (He I peak)
40.8 eV	30 nm	He gas discharge lamp (He II peak)
124 eV	10 nm	(end of UV and start of x-ray regime)

Table 5.3: Some notable UV light sources sorted by wavelength.

[3]This includes the extreme ultraviolet (EUV) range in 13.5 nm EUV lithography. Other common photolithography wavelengths are 365 nm (mercury lamps), 248 nm, and 193 nm (KrF and ArF excimer lasers).

There are limited known good ways to generate UV light in the range we want, and many are fixed to certain UV wavelengths; some are shown in table 5.3. An additional difficulty (and the reason the vacuum UV range is so-called) is that below 100 nm wavelengths (above 10 eV) there is no solid material transparent to these wavelengths that can be used as a window, so lower wavelengths must both be generated and used within vacuum chambers[4] [270]. Specifically, the best SiO_2 glass (crystalline quartz) is transparent down to at most 142 nm; materials such as LiF and MgF_2 reach 100 nm to 110 nm [271].

Gas-based lamps are the most common of UV light sources [269]. In gas discharge lamps (also called arc lamps), a low-pressure gas is electrically ionized into a plasma that emits a gas-dependent spectrum of light. This includes mercury arc lamps, the most historically prevalent UV source, which has a spectrum including peaks at (among others) 365 nm, 254 nm, and 185 nm. Also notable are H and He lamps. He gas discharge lamps are used for UV photoelectron spectroscopy [272]; broad-spectrum deuterium arc lamps for UV-vis spectroscopy. The 13.5 nm source for EUV lithography is made with a tin plasma gas [273]. An improvement over gas discharge lamps are excimer lamps [274][275], which drive particular gases in particular excitation states to produce mostly monochromatic light [276]. Excimer lamps are mechanically simple and robust [277]. Particularly common are Xe_2 excimer lamps at 172 nm that balance low wavelength with the ability to use cheap glass windows.

Excimer lasers output in the UV range [273]. These use similar principles to gas lamps with high power focused output at the cost of complexity and efficiency. They are available in (mostly) fixed wavelengths, the most common of which are the 248 nm KrF and 193 nm ArF lasers used for photolithography, pulsed laser deposition [146], and medical purposes. It is also possible to use nonlinear optics to convert frequencies of other lasers to UV, e.g., to generate 118 nm from tripling the 355 nm third harmonic of an Nd:YAG laser [278].

LEDs are solid state and can be made to emit UV light [279][280][268]. These are currently popular for UV curing, sterilization, gas analysis, and more in the UVA–UVC range. However, current UV LEDs are limited (and an active research area): efficiency drops with lower wavelength, and the current lowest wavelength research LEDs are about 230 nm. 235 nm is commercially available [281]. These are not suitable for our wavelength requirements.

Synchrotron light sources achieve high energies (e.g., 5 eV to 30 eV or 40 nm to 250 nm) within a tunable precise wavelength band (millielectronvolts) [270][282][283]. Photon intensities are much higher than what can be achieved by filtering a broad-spectrum gas UV lamp to that wavelength band but total power is somewhat low in absolute terms. These are useful for photoionization and photodissociation chemical studies but are large and expensive. We do not need their wavelength resolution or tunability.

Of all these methods, gas-based excimer lamps may be our best option: they combine high energy (low wavelength), high output, high efficiency (both in light generation and in that their spectrum is narrow), simplicity, and relatively low cost. The 172 nm wavelength seems particularly promising except for its somewhat low 7.21 eV energy, which would limit us to single-digit charges for particles below 10 nm according to figure 5.2.

[4]Fortunately, we happen to be moving nanoparticles specifically within a vacuum chamber.

5.3.2 Light Intensity

We now know what wavelengths of light will work, but how much of it do we need? To reach a charge of n, each nanoparticle will need to be hit by at least n photons but needs more if the photoelectric quantum yield ϕ, the fraction of photons that result in an emitted electron, is low. With $\phi = 0.1$, a nanoparticle charge of +10 would require 100 photons. Also note that, as will be discussed later with ion optics, we want nanoparticle charge to be as high as possible and some variation in the number of charges per particle is acceptable.

Suppose nanoparticles of diameter d_p move at velocity v across an distance of length L over which UV light of sufficiently low wavelength shines at some irradiance (photons per area) J_e, some fraction of which ϕ are absorbed and result in an electron emission.

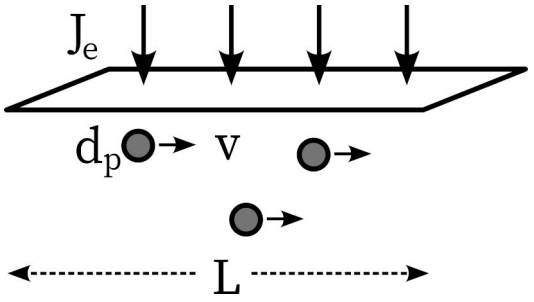

Figure 5.3: Nanoparticles of diameter d_p moving at velocity v through a region of length L into which UV light shines at intensity J_e.

Then the resulting positive charge n of each particle is approximately

$$n = \frac{\pi d_p^2 L \phi J_e}{4v}. \tag{5.4}$$

If we want a charge $n \geq 10$ with $d_p = 10\,\text{nm}$, $L = 100\,\text{mm}$, $\phi = 0.1$, and $v = 100\,\text{m}\,\text{s}^{-1}$, we find $J_e = 1.27 \times 10^{21}$ photons/m^{2}s. At a wavelength of 172 nm, $J_e = 1470\,\text{W/m}^2 = 147\,\text{mW/cm}^2$. This is somewhat high but feasible to achieve, especially over a small area. 172 nm Xe_2 excimer lamps are commercially available with irradiance above $100\,\text{mW/cm}^2$ (before focusing) [277][284]. Recent promising work in microfabricated flat microcavity plasma lamps can achieve higher intensities in smaller form factors with over 20% efficiency [285].

5.3.3 Charge Loss Mechanisms

Once nanoparticles are charged, there are several ways they might become discharged or lost that we should be aware of. First, as discussed in 4, charged particles moving in gas through narrow tubing have a greater attraction to its sidewalls (where they can stick and thus be lost) via image charges or adsorbed charges. Second, field and diffusion charging mechanisms can also discharge particles by transferring their charge to gas (in our case, by electrons moving from gas atoms to nanoparticles when they collide) [286][287]. Finally, a related effect is that sufficiently high-energy UV light [288] or electrons [289] can be absorbed by and ionize gas atoms instead of nanoparticles (the first ionization energies of Ar and N_2 are 15.8 eV and 15.6 eV [103]; interestingly, Ar^- is unstable—its electron affinity is negative).

5.4 Experimental Tests

We now know roughly how to charge nanoparticles in theory: shine a sufficiently strong UV lamp at them. Furthermore, the literature confirms this works experimentally: many groups have successfully built similar nanoparticle photoelectric chargers for studying common aerosols [286][258][290], fundamental nanoparticle photoemission tests [291][267], and mass spectrometry ion sources [292][293].

We attempted to build our own photoelectric nanoparticle charger. Unfortunately we were unsuccessful, but we ran several partial experiments with useful lessons that can be applied in future work. Building a charger continues to seem feasible.

Safety note: UV light is invisible and harmful to humans, capable of causing eye damage and long-term skin cancer (though diffuse UV lamps are less dangerous than a laser, which concentrates power). There is some evidence the human maximum permissible exposure limit to 200 nm to 222 nm light might be larger than at longer UV wavelengths [294], but for safety we considered the worst-case UV scenario. The UV lamp was operated away from skin, usually in a closed container, and while also wearing UV-blocking safety glasses (ThorLabs LG10, which also block 1064 nm laser light in chapter 2).

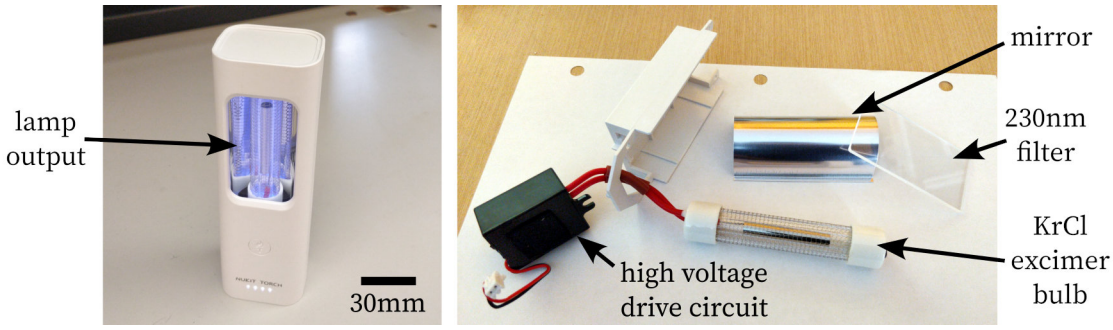

Figure 5.4: Left: UV lamp, operating (imaged safely with a camera). Although its 222 nm light is invisible, its output spectrum also contains some visible violet light. Right: the important optical components inside the lamp (its original control board excluded). The drive circuit converts low voltage DC to high voltage to drive the lamp bulb, whose output is partially reflected out of the lamp with a mirror then filtered to block UV above 230 nm.

The most important part of a photoelectric nanoparticle charger is its UV lamp. Although we predicted good results with a 172 nm lamp with over 100 mW/cm^2 power and noted in section 5.3.2 that these capabilities are commercially available, the best UV source we were able to obtain[5] was a $100 222 nm KrCl excimer lamp [295] meant for disinfection purposes with a reported UV optical power output of 0.12 mW/cm^2 (with 90% of this between 214 nm to 226 nm) at a 5 cm distance from the lamp (or 0.0107 mW/cm^2 at 20 cm). We confirmed

[5]This lamp was affordable compared to other sub-230 nm lamps, well-constructed, and easy to work with.

these specifications by measuring current generated in a UV photodiode (SD008-2171-112, Advanced Photonix) sensitive to 220 nm to 280 nm with a 0.019 A W^{-1} response at 222 nm and a 0.076 mm^2 active area. Placing the diode 5 cm from the lamp generated 15 nA from which we calculated an intensity of 1.04 mW/cm^2, about 10x higher than specified (this error is likely due to our poor-quality uncalibrated measurement setup, but, if correct, the higher intensity would be helpful for our purposes). We will conclude the lamp outputs about 1×10^{18} photons/m^2s to 1×10^{19} photons/m^2s at 5 cm.

To demonstrate nanoparticle charging, we chose to take our existing aerosol deposition setup from chapter 4 and, between generating nanoparticles and impacting them, charge the nanoparticles by flowing them through a 7 mm ID UV-transparent glass tube (quartz; we measured over 50% transmittance at 222 nm via photodiode) while irradiating them with our UV lamp. This general strategy appears to work in the photoelectric nanoparticle charger literature [258]. To detect nanoparticle charge, we deposited the nanoparticles onto an electrically isolated but conductive steel substrate attached to a Keithley 487 picoammeter (i.e., we built a Faraday cup).

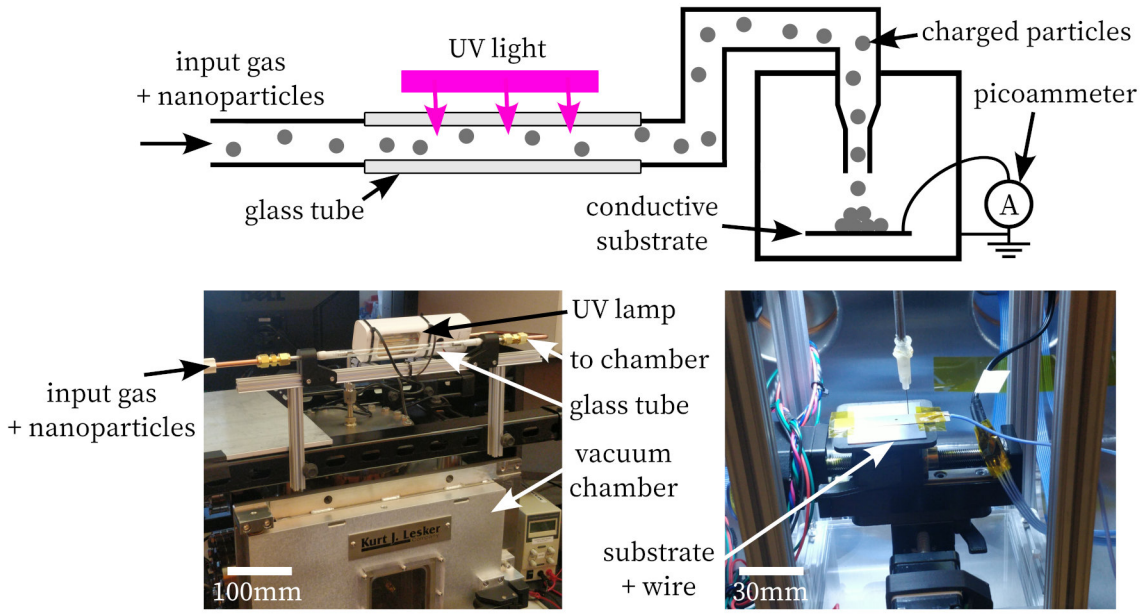

Figure 5.5: Top: cartoon of charging experimental setup built into chapter 4 apparatus. Nanoparticles are charged by UV light then deposited onto a conductive substrate where their charge creates a current detected by a picoammeter. Bottom: pictures of implementation. The UV lamp was covered for safety (not shown) while in operation.

Although this setup was crude, we calculated it might work. According to tables 5.1 and 5.2, 222 nm light (5.58 eV) should charge 10 nm copper particles up to +3. The nanoparticles travel 80 mm through UV light of our calculated lamp intensity (1×10^{18} photons/m^2s to 1×10^{19} photons/m^2s). Nanoparticle velocity was determined by gas flow speed, which, assuming the flow conditions as chapter 4, is likely about 1 m s^{-1} through the 7 mm diameter

glass tube. Assuming 10 nm diameter particles with a photoelectric quantum yield of $\phi = 0.1$, equation 5.4 suggests each particle (depending on lamp intensity) obtains a charge of 0.6 to 6, i.e., at least one charge per particle on average.

To compute the rate at which nanoparticles deposit charge, assume from chapter 2 we produce particles at $0.6\,\mathrm{mg\,h^{-1}}$. Assuming 10 nm diameter copper particles, this is 3.5×10^{10} particles/s. Assume 90% are lost in the system for assorted reasons, so a net total of 3.5×10^{9} particles/s are generated, sent through tubing, and deposited. At one charge per particle, the charge deposition rate should be 3.5×10^{9} charges/s or 0.6 nA.

We ran the experiment with copper nanoparticles and observed particles depositing on the substrate, but we measured an average charge deposition of (0.00 ± 0.01) nA (controlling for presence of UV light and signal noise). Noise limits only let us measure down to 0.01 nA, less than two orders of magnitude below our expected 0.6 nA signal. That is: we are confident particles moved through the UV charger and deposited on the substrate with whatever electric charge they possessed, but we observed no current meaning we remain unsure whether they were charged or not.

We hypothesize that particles were successfully charged when hit with a photon but a range of factors lowered the resulting signal below the range we were able to detect:

- Perhaps charging was successful but the increased charge increased particle loss sticking to tubing walls between charging and deposition. A more careful reading of the existing literature [258] reveals charged particles are often collected quickly after charging.
- From chapter 2, the particles have a range of diameters; they are not uniformly 10 nm. If the average particle size is larger but charge per particle is constant, the deposited current decreases. Smaller particles might not be charged with our 222 nm light.
- Diffusion (dis)charging—gas atom collisions—may have reduced charge per particle.
- The photoelectric quantum yield might have been less than the assumed 0.1.
- Because particles were insulators, their charge might not have transferred to the substrate (Faraday cup). Solving the oxidation problem as outlined in chapter 4 would fix this. We used copper nanoparticles due to their low work function; gold nanoparticles do not oxidize but have a higher work function (see table 5.2).

Any of these could easily have decreased the signal by an order of magnitude; all together, we are not surprised our signal was not above the 0.01 nA we could measure.

This suggests useful steps to build and successfully demonstrate a working nanoparticle generator in future work. Increasing UV lamp energy and intensity can increase charge per particle, using non-oxidizing conditions might deposit charge reliably, collecting particles quickly minimizes losses, and increasing measurement resolution is also helpful.

Finally, as a separate test, we tried operating the UV lamp inside the vacuum chamber. This might be useful in the future for charging nanoparticles in vacuum to minimize gas interactions. Unfortunately, as shown in figure 5.6, at pressures below 10 Torr the lamp stopped working; its light output changed. Further experimentation suggested an amusing

reason: the lamp construction consisted of a low-pressure KrCl gas in a sealed glass tube with metal electrodes on each side (i.e., both outside the tube and touching atmosphere). In standard operation, a high voltage AC potential between these electrodes capacitively couples to the gas inside to drive a plasma: this is a dielectric barrier discharge lamp [277]. However, when the surrounding atmosphere reached sufficiently low pressures, the lamp drive electrodes instead coupled to this atmosphere to make a gas discharge plasma from this surrounding gas (in our case, air) instead of the desired KrCl. Fixing this problem is straightforward but requires a different lamp geometry[6].

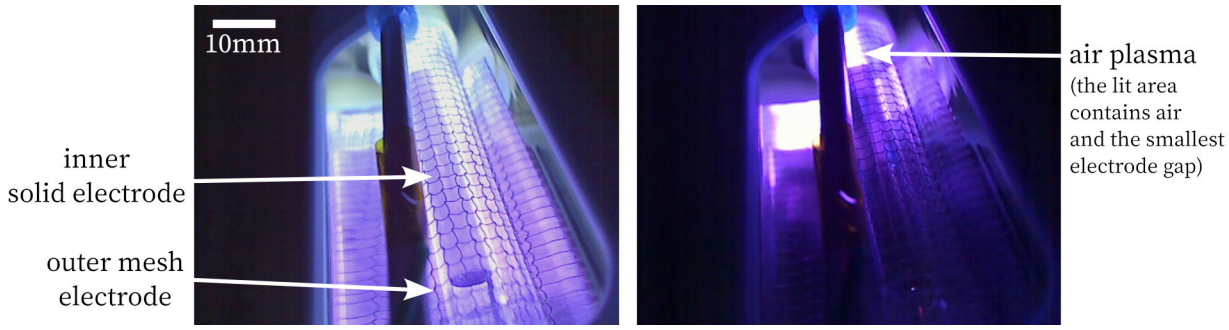

Figure 5.6: Left: close-up picture of the UV lamp bulb in normal operation. The lamp tube is a double-walled hollow cylinder; low-pressure Kr and Cl gas is contained between the walls. There is a mesh electrode around the outside cylinder and a solid electrode in the center area (also at atmospheric pressure). Right: at low exterior pressures, the indicated small cylindrical area (the closest distance between outer and inner electrodes at exterior pressures) becomes an excited air (nitrogen and oxygen) plasma. The color has changed due to different plasma composition.

In conclusion, we understood the theory behind charging nanoparticles but were not able to convincingly demonstrate this in experiment. However, we believe we understand our failure and can modify our apparatus to work in the future; problems included inability to obtain a sufficiently bright UV lamp, insufficient measurement resolution, and poor setup. The literature [258] still provides a convincing existence proof that a charger is possible.

We are now ready to continue our journey to figure out how to manipulate and focus nanoparticles with electric fields in chapter 6, though our current lack of charged particles to experiment with means we will have to continue in theory only.

[6]We were not able to fit the construction of a custom deep-UV lamp within our project's scope.

Chapter 6

Electrostatic Manipulation

We are finally ready to discuss the final step required for nanoparticle printing: using electric fields to move the particles. The approaches of previous chapters were not sufficiently precise or fast to build a good nanoparticle printer, but electrostatics can do better. Furthermore, contemplating this will let us write down quantitative theoretical limits on how good and fast nanoparticle printing can ever possibly be[1]. We will have some success.

Recall that chapter 3 concluded printing semiconductor devices requires shooting particles of 1 nm to 50 nm diameter at a substrate at well-controlled velocities somewhere between $100\,\mathrm{m\,s^{-1}}$ and $3000\,\mathrm{m\,s^{-1}}$ and with positioning accuracy below our final desired printing resolution, perhaps 1 µm. (Afterward, all we have to do is move the substrate back and forth on an XY stage while switching materials to have a multimaterial nanoscale printer, and these last parts are—relatively—easy, as demonstrated in chapter 4.) Furthermore, we argued the two feasible methods to do this are manipulating the nanoparticles with gas molecules or with electric fields.

We considered the first nanoparticle manipulation approach, colliding nanoparticles with gas atoms, in chapter 4. Although we found these aerosol methods were capable of conveniently transporting particles in several ways (and we were able to successfully print some basic multimaterial structures with them), theoretical limits from Brownian motion meant this would never be able to focus nanoparticles to achieve printing resolutions below 1 µm (in practice, 10 µm, and only for larger particles). These methods also had poor control over nanoparticle impact velocity. Achieving convenient semiconductor device manufacturing as contemplated in chapter 1 requires something better, and the only remaining possibility is electrostatic manipulation.

Thus, in this chapter, we investigate moving nanoparticles with electric fields. We will assume nanoparticles have a fixed electric charge (perhaps $1e$ to $100e$) according to our methods in chapter 5, then design electric fields to move them to our desired positions and velocities. Since we were unable to implement nanoparticle charging in chapter 5, we will run computer simulations instead of physical experiments, which we leave to future work.

[1]The superlative language in this chapter introduction may not be perfectly justified, but we think our arguments (see, for example, section 6.5.3) are sufficiently solid to excuse our use of the literary device.

6.1 The Focusing Problem

The one problem we haven't solved yet is how to deliver nanoparticles to a very small area. We have solutions for everything else (nanoparticle generation, large-scale manipulation, and charging), so let's simplify this last problem as far as possible.

Suppose we take our printer from chapter 4, add a photoelectric charger from chapter 5, and deliver charged nanoparticles into a vacuum chamber. The chamber would be at our choice of gas pressure, possibly down to high vacuum if desired[2].

We now have what appears to be a simple physics problem: charged particles start with random position, speed, and direction in a circular area 100 µm to 1000 µm wide (depending on aerosol nozzle qualities). We want to move as many particles as possible into a much smaller area, printing them onto a substrate within 1 µm or better. How can we do this?

The answer—the rest of this chapter—turns out to be surprisingly complex and nuanced.

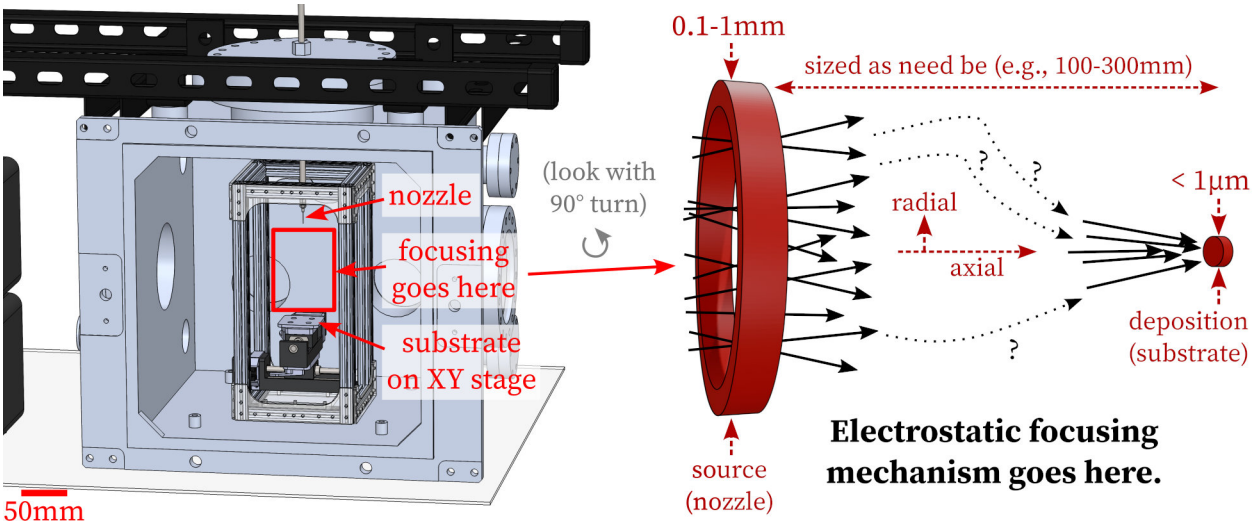

Figure 6.1: Left: starting with an aerosol printer as built in chapter 4, move the nozzle away from the substrate and there is room to add an electrostatic mechanism to focus particles. Right: an annotated cartoon of how this mechanism has to work (drawn turned 90 degrees). A wide beam of particles needs to be focused to a smaller area. Call the direction of movement from source to substrate "axial" and the perpendicular direction(s) "radial".

To analyze this problem, we will assume[3] particles mostly travel forward in a single direction (they won't stop or travel sideways very much, for example), which forms a nanoparticle beam (that particles travel close to the average beam position is called the paraxial approximation). Name the direction from nanoparticle source to substrate the axial direction, and movement perpendicular to that the radial[4] direction (a cylindrical coordinate system). A particle with

[2]Nanoparticles can be moved to high vacuum with a skimmer as briefly mentioned in chapter 4.

[3]We will justify this assumption in many cases in section 6.3.1, but we will also actually find reasonable circumstances where particles travel backward for a short while in section 6.4.2.

[4]Sometimes "transverse" is used instead of radial and "longitudinal" instead of axial [296].

a radial position of zero is centered on the beam axis; our particles start with random radial positions in 0 µm to 500 µm and need to end with positions less than 0.5 µm—100x to 1000x smaller! We also want particles to end up with a high and well-controlled axial velocity.

For later reference, record the starting and ending conditions we want:

	Start (exit nozzle)	End (deposit)
Beam diameter	0.1 mm to 1 mm	< 0.001 mm ($< 1/100$th input)
Axial velocity	$\pm 50\%$ in $100\,\mathrm{m\,s^{-1}}$ to $300\,\mathrm{m\,s^{-1}}$	$\pm 10\%$ in $100\,\mathrm{m\,s^{-1}}$ to $3000\,\mathrm{m\,s^{-1}}$
Particle diameter	$\pm 50\%$ in 1 nm to 50 nm	(no change)
Particle charge	± 2 in 1 e to 100 e	(no change)

Table 6.1: Particle input and desired output conditions. We will add additional constraints (emittance) later in table 6.3. The beam diameter is double the maximum radial position of any particle. We can choose mean values for speed, diameter, and charge inside the given range, at which point the tolerance represents variance around that mean. Particle charges are integer multiples of the elementary charge e. Tolerances are approximate.

All these parameters vary, and the combined wide parameter range is the primary reason focusing is so difficult: the same mechanism that focuses a +3 charge 20 nm particle moving at $300\,\mathrm{m\,s^{-1}}$ is unlikely to also focus a +1 5 nm particle at $100\,\mathrm{m\,s^{-1}}$ by the same amount. Initial particle speed is determined by aerosol nozzle (chapter 4) and is dependent on particle size. As in chapter 2, particle generation results in a broad size distribution (perhaps a 500% spread in diameters, almost an order of magnitude—e.g., 5 nm to 25 nm), though we can select a narrow slice of this via filtration (at the expense of lower throughput). We assume a 50% variation is a good compromise between consistency and nanoparticle generation rate, but note particle mass scales with the cube of the diameter, so 50% diameter variance is a 350% mass variance! Finally, particle charge is somewhat controllable as discussed in chapter 5 but may vary (different diameters give different photoionization thresholds, etc).

6.2 Electrostatic Nanoparticle Movement

To analyze particle movement, we will begin by reviewing basic electrostatic forces. The fundamental law governing charged particle movement is the Lorentz force, which states a particle with charge q and velocity vector $\vec{v}$ in an electric field $\vec{E}$ and magnetic field $\vec{B}$ experiences the force $\vec{F} = q(\vec{E} + \vec{v} \times \vec{B})$. We also have Newton's second law, of course, with $\vec{F} = m\vec{a}$ for particle mass m and acceleration $\vec{a}$. Together, these laws completely determine how a particle moves inside a given time-varying electromagnetic field[5]. Assume for now the particles and fields are inside a perfect vacuum. Applying a voltage across two conductive electrodes makes an electric field $\vec{E}$ in the empty space between them.

To simplify calculations we make several assumptions. First, assume each particle is merely

[5]To a good first approximation. This ignores relativistic effects and emitted radiation (cyclotron or bremsstrahlung/braking), for example, but the effect on our particular calculations will be negligible.

a point mass and charge[6]. Second, ignore magnetic fields—since particles are relatively slow, the force from electric fields will be much greater[7]. Finally, assume electrode electric fields are quasielectrostatic, i.e., depend only on electrode voltages at that instant[8], and are unaffected by the particles (image charge effects). Thus the force on each particle is merely

$$\vec{F} \approx q \cdot \vec{E} \tag{6.1}$$

(that is, a particle in an electric field experiences a force in the direction of the field, scaling with charge and field strength), and now we can proceed with straightforward calculations.

A basic demonstration of electrostatic movement is as follows. In a perfect vacuum, add two conductive pieces of metal ("electrodes") and apply a constant voltage between them. This creates an electric field in the space in between and around the electrodes. The strength of the field is approximately the voltage divided by distance (measured in volts per meter). Now put a particle of nonzero charge q in midair between these electrodes (if the particle has no charge, nothing happens). The particle will be pushed with force $\vec{F} = q \cdot \vec{E}$, and its trajectory can be determined by $\vec{F} = m\vec{a}$ (we use vector notation $\vec{v}$ for any 3D vector).

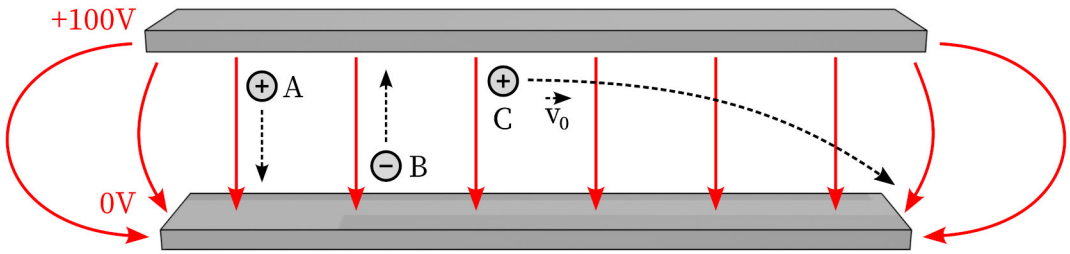

Figure 6.2: An electric field (red arrows, conventionally drawn from high to low potential, which we call the direction of the field) is created between electrodes, in this case by applying a 100 V potential difference. Note the field curves at electrode edges. Positively charged particle A is pushed in the field direction (from chapter 5, our particles will generally have a positive charge). Particle B has a negative charge, so it is pushed in the opposite direction. Positively charged particle C has initial velocity $\vec{v}_0$ and continues in that direction but is also pushed down like particle A, resulting in a parabolic trajectory.

These basic ideas are enough to start considering what it takes to achieve particle movement to solve our focusing problem of section 6.1: how can we focus a beam of particles?

[6]This is valid as the nanoparticle diameter is much smaller than any other system dimension. We assume also negligible effects from magnetic moments, which is reasonable given we use no magnetic fields.

[7]A 1000m/s particle in a reasonably large 100 mT field experiences a force equivalent to a single charge in a 100 V m^{-1} electric field, but most fields in this work are orders of magnitude greater, perhaps 100 V cm^{-1} = 10 kV m^{-1} or more. SEMs and particle accelerators have much higher particle velocities resulting in larger magnetic Lorentz forces and therefore make more use of magnetic fields instead of electric fields.

[8]This is valid because we use no magnetic fields and also because the frequencies at which electric fields change will be below 1 MHz with wavelengths (300 m) far greater than the size of the system or nanoparticle travel path. This will simplify electric field calculations.

6.3 Radial Focusing

Now that we have a way to create electric fields and analyze their effects on particle motion, it is time to turn to solving the particle movement challenge presented in section 6.1 and table 6.1. We can divide this problem into two parts:

- We need to focus particles in the radial direction, from a broad beam over 100 µm wide to a much more narrow beam less than 1 µm wide. This gives high printing resolution.
- Simultaneously, we want to adjust particle velocities in the axial direction so the impact velocity is well-controlled and within the $100\,\mathrm{m\,s^{-1}}$ to $3000\,\mathrm{m\,s^{-1}}$ range.

It will turn out the final solutions for these two subproblems are somewhat independent, so we will address them one at a time. Radial focusing is more difficult; we will start there.

As an illustrative partial solution, consider a broad beam of positively-charged nanoparticles we would like to print on a substrate as in figure 6.3. If the substrate is at a known voltage and a ring-shaped high voltage electrode is set just above, an electric field will be formed that pushes particles inward radially (in addition to some axial acceleration) to move through the hole in the high-voltage electrode before impacting the substrate. The final printed deposit is smaller than the original beam diameter; the particles are focused. This setup also has some significant drawbacks, but we can use it to introduce some important ideas.

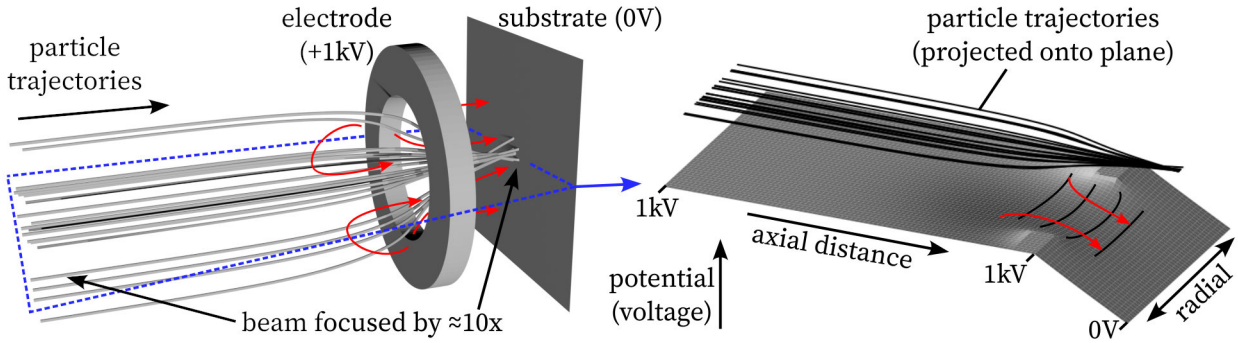

Figure 6.3: Left: 3D computer simulation of a beam of nanoparticles deflected inward by an electric field (red arrows) to impact a smaller area on the substrate. Right: the electric field in a 2D plane (blue) can also be visualized as a potential energy surface (height measured in volts) that particles travel through, with 2D projections of particle paths above.

The first idea is we can use computer simulation to calculate the exact shape of the electric field and resulting particle motion. Although we also use hand calculations and intuition to make some approximate broad statements and check the simulation (e.g., comparing the magnitudes of particle kinetic energy and electric potential can suggest how much focusing happens), the full field shape is complex. The specific software we use is SIMION 8.2[9] [297].

[9]SIMION [297] is industry-standard software for simulating particles in electric fields to design ion optics. Fields are computed by solving the Laplace equation via a finite difference method, then particle trajectories are found by integrating $\vec{F} = m\vec{a}$ over time. (We also use Python [298] and Blender [299] to display results.)

Second, instead of visualizing the electric field as arrows, we can draw an electric potential surface as shown in the right of figure 6.3. We take a 2D cross-section of the 3D geometry and graph the potential at each point on it. Higher potential is higher voltage; electric field lines point downhill. Particles move in this potential like how large objects would fall down a slope due to gravity. These plots are more exact and easier to draw than arrows.

Now: this radial focusing method partially works; what are the downsides?

One primary drawback is the need for substrate charge. The method has actually already been used to good effect in the literature to print structures from nanoparticle aerosols [46][63][300][69][68] (also cited in chapter 1) or electrohydrodynamic jets [30][301][302][303]. But the substrate must be at a known voltage or charge[10], which conflicts with our desire to print arbitrary geometry with both conductors and insulators (for transistors, for example), which change the field shape (section 6.5.2). We'd like to focus particles without relying on the substrate's electrical properties, so we need a different method.

Other important flaws are that focusing requires very low particle axial velocities or very high voltages, and there is a fundamental minimum to how much focusing is possible—we would never be able to fit the entire 0.1 mm incoming beam of table 6.1 into a sub-1 µm spot. These limits are the same as for Einzel lenses, which we will discuss in the next section.

6.3.1 Ion Optics, Einzel Lenses, and Emittance Limits

We still need to figure out how to focus particles radially, but we now have the additional constraint that the focusing mechanism shouldn't include the substrate as an electrode. This makes things harder. Fortunately, significant prior art exists, and there is a beautifully simple expression (emittance) that tells us what we need to do.

Ion optics (or charged particle optics, or electron optics) is the study of moving electrically charged particles (electrons or atomic ions) with electric and magnetic fields in vacuum [296][304][305]. The name comes from certain behavior analogous to light ray optics. Ion optics sees use in in scanning electron microscopes, particle accelerators[11], mass spectrometers, trapped ion quantum computing, cathode ray tube displays, and focused ion beam tools (see section 6.5.4), among others (see appendix A). The field is mature, and the focusing problem as laid out in section 6.1 is very familiar—it is almost identical to concerns in SEMs and FIBs except that the use of large nanoparticles is uncommon. Ion optics has a simple (partial) solution to the focusing problem: the Einzel lens [305][306].

An Einzel lens focuses a beam of charged particles. The beam travels through the lens and is made to converge, just like a converging optical lens does for light [306]. The Einzel lens itself consists of three ring electrodes with the center ring at a different voltage from the other two; the particle beam travels through the holes in the rings. Particles are slowed down by the first pair, slightly change direction depending on their distance from the beam axis, then are sped up to their original velocity (and energy) by the second pair. To a first-order approximation, the direction change is proportional to radial position.

[10] Attracting particles to a charged pattern is xerography; this is how paper laser printers work.

[11] SEMs and particle accelerators can use magnetic instead of electric fields due to higher particle velocities.

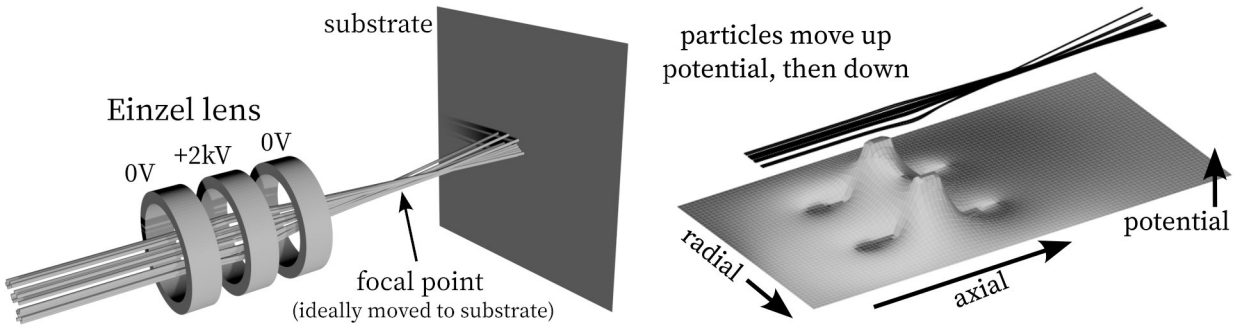

Figure 6.4: Einzel lens simulation in the same style as figure 6.3. Left: 3D render of lens and particle trajectories. Right: the potential energy field of the lens. The particles don't meet exactly at the focal point (the beam diameter is nonzero) due to some variation in incoming particle mass, velocity, and nonzero incoming angle.

In order to focus a beam, the height of the Einzel lens potential surface (its voltage times particle charge) must be close to the incoming kinetic energy of the particles. If the lens energy is low, particles are focused more gradually (the focal point is further away); if too high, the particles are reflected backward.

This is the first indication an Einzel lens is not the right tool for us. Our nanoparticles have a wide range of masses and thus kinetic energies (possibly 350% variation; see table 6.1). Thus different particles will be focused significantly differently or not at all (more correctly, particles with a different mass-to-charge ratio will be focused differently; with the laws $\vec{F} = q\vec{E} = m\vec{a}$, we have $\vec{a} = (q/m)\vec{E}$ so the ratio is the only determinant of particle trajectory). This is an extreme case of chromatic aberration[12]. A second related problem is large fast particles need unrealistically high voltages to focus.

Diameter	$100\,\mathrm{m\,s^{-1}}$	$300\,\mathrm{m\,s^{-1}}$	$1000\,\mathrm{m\,s^{-1}}$	$3000\,\mathrm{m\,s^{-1}}$
1 nm	0.146 eV	1.32 eV	14.6 eV	1.32×10^2 eV
10 nm	1.46×10^2 eV	1.32×10^3 eV	1.46×10^4 eV	1.32×10^5 eV
100 nm	1.46×10^5 eV	1.32×10^6 eV	1.46×10^7 eV	1.32×10^8 eV

Table 6.2: The kinetic energies (total, not per atom as in chapter 3) of assorted copper nanoparticles at different velocities, in electronvolts. A $1000\,\mathrm{m\,s^{-1}}$ 10 nm particle with a single charge needs an Einzel lens voltage of up to 14 600 V to be focused. Note this requires high vacuum; it would cause Paschen breakdown (see figure 2.4) at higher pressures.

If we were to filter particles even more to reduce variation in diameter and thus energy, and only use smaller particles at low speeds, this might start to work; there already exist several papers studying Einzel lenses to focus nanoparticles for deposition [308][309][99][100]. But there is another reason Einzel lenses are insufficient for what we want to do.

[12]In ion optics, chromatic aberration primarily refers to focusing imperfections due to a spread in particle kinetic energies. Reducing chromatic aberration is possible in only limited cases [307]. Spherical aberration is imperfect focusing due to lens shape, separate from the more fundamental emittance limits we will discuss soon. Astigmatism is deformation of the beam radial symmetry; we neglect it here. See [305] for more.

Einzel lenses have a second fundamental limit: emittance. Perfect focusing is impossible.

The emittance limit actually applies to virtually all ion optics, including our first radial focusing method in section 6.3, and even if all particles were the same diameter with the same charge and velocity (so there is no chromatic aberration).

The limit goes like this. Any beam of nanoparticles spreads out at some nonzero angle and at its narrowest point has some nonzero diameter—a beam is never perfectly collimated or focused. We can define a quantity called the beam "emittance" equal to the beam diameter times the spread angle at some point. It turns out this is a conserved quantity: no matter how we bend and focus the beam, the emittance will never decrease (but it can increase). If we want to focus the beam by decreasing its diameter, the beam angle must increase to compensate—and basic geometry limits the half-angle to 90°.

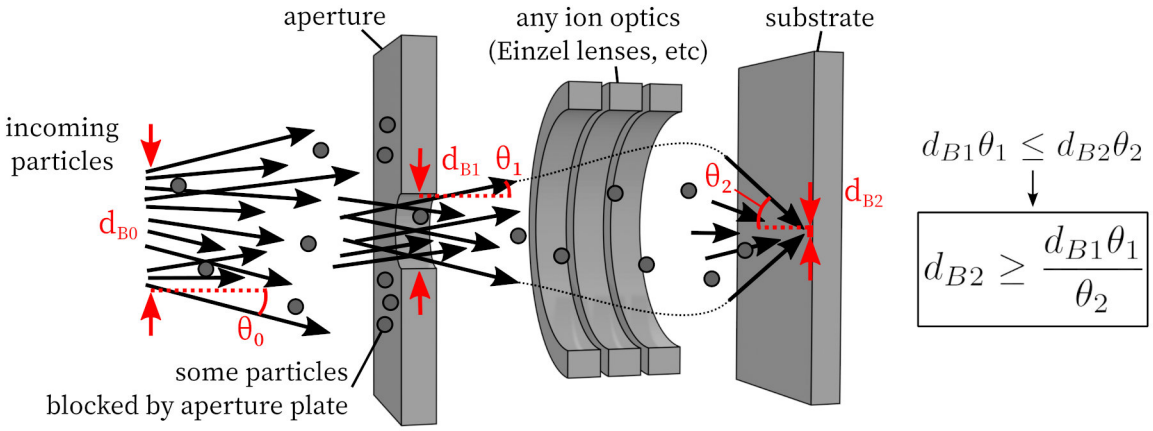

Figure 6.5: Cross-section cartoon of theoretical focusing limits due to emittance. Any beam of particles has nonzero half-angle θ_0 and at its narrowest some nonzero diameter d_{B0}. The diameter-angle product $d_{B0}\theta_0$ is the emittance. In an energy-conserving system (like particles moving in electrostatic fields in vacuum), the only way to reduce emittance is by removing some of the beam, e.g., with an aperture, giving a beam with a different diameter d_{B1} and angle θ_1 (though brightness will decrease). Focusing the beam while keeping all particles will at best preserve emittance giving $d_{B1}\theta_1 = d_{B2}\theta_2$, and $\theta_2 < 90°$ limits how small d_{B2} can be. (Also, the diameters and angles can be replaced with areas A_B and solid angles Ω.)

This theorem is well-known in ion optics (with minor variations; for a better discussion see [296]). Stated with a bit more precision: consider the movement of ions in a perfect vacuum through a non-time-varying electric field (potential). It can be shown the Lorentz force in this case is conservative, i.e., particle energy is shifted between kinetic and potential but always remains constant. Now consider a group of particles, each with their own initial positions and velocities. According to Liouville's theorem from Hamiltonian mechanics, the density of this group in phase space is constant, so if particles start and end at the same potential they end with an equally large group of positions and velocities. Alternatively: the system is time-reversible (could be run backward), so there is no case where two particles with different initial conditions end up in the same final position.

There are several mostly-equivalent ways to define emittance[13]. In figure 6.5 we define the minimum diameter[14] d_B of a beam and the half-angle θ it spreads out at; $d_B\theta$ is constant. Note θ is approximately the ratio of radial to axial velocity (when θ is small, i.e., the paraxial approximation). Instead of $d_B\theta$, we can also use the minimum beam area $A_B = \pi d_B^2/4$ and the solid angle $\Omega \approx \pi\theta^2$ and conserve $A_B\Omega$, but the 2D version remains simplest to use.

$$d_{B1}\theta_1 \leq d_{B2}\theta_2 \quad \text{or} \quad A_{B1}\Omega_1 \leq A_{B2}\Omega_2 \tag{6.2}$$

Again, emittance cannot decrease, given the theorem's assumptions, though it can increase via nonlinearity or focusing imperfection[15]. This is unfortunate as we want both small diameter and small angle (for more reliable impact and larger depth of field), i.e., we want small emittance. But there are minor loopholes.

One main way to decrease emittance in a vacuum is physically removing some of the beam, maybe by blocking it with an aperture (a hole in a flat plate). The remaining beam can have lower emittance but contains fewer particles (in our case, this would make printing slower). To account for this, define the volumetric flux Q (the total volume of nanoparticles moving in the beam per second) (units m^3/s), and define the volumetric brightness $Q/(A_B \cdot \Omega)$. This volumetric brightness[16] is conserved even through an aperture.

The other way to decrease emittance is accelerating particles to a higher axial velocity, which stretches out the beam to give a smaller solid angle while keeping area constant. Particles must start and end at different potentials. This is called an "immersion lens" for analogies to light optics; a basic Einzel lens is not one as its start and end potentials are identical. Increasing axial velocity v_a while preserving radial velocity v_r reduces angle θ approximately linearly (and Ω scales with $1/v_a^2$), so $v_a\theta$ or $v_a^2\Omega$ is conserved[17].

These quantities are the main figures of merit for a particle beam: the minimum beam area A_B (or diameter d_B), solid angle Ω (or half-angle θ), axial velocity v_a (note radial velocity v_r satisfies $\theta \approx v_r/v_a$ and $\Omega \approx \pi(v_r/v_a)^2$), and volumetric flux Q. We can write these together as the "reduced volumetric brightness", which is conserved similar to emittance:

$$\frac{Q_1}{v_{a1}^2 A_{B1}\Omega_1} \geq \frac{Q_2}{v_{a2}^2 A_{B2}\Omega_2}. \tag{6.3}$$

This is enough to understand how much focusing is theoretically possible[18].

(Incidentally, the same theorems can apply near-identically in light optics [314][315], specifically linear optical systems. For a given beam of light, define the "étendue" $G = n^2 A\Omega$ (units m^2sr) for area A, solid angle Ω, and index of refraction n, then also define the "radiance" $L = \Phi/(A\Omega)$ (units W/m^2sr) using radiant power Φ (units W). Combine these together as "basic radiance" $L/n^2 = \Phi/G = \Phi/(n^2 A\Omega)$ (units W/m^2sr). Basic radiance is conserved

[13]Accelerator physics in particular uses more complex but precise definitions [296][310].
[14]Sometimes the minimum diameter is called the size of a virtual source.
[15]Aberrations preserve emittance but can deform it so much it acts increased for practical purposes [296].
[16]Ion and electron beam systems measure flux as a current and call the result "brightness" [311][304][296].
[17]Ion beam systems define "reduced brightness" with voltage V instead of squared axial velocity v_a^2 [312].
[18]It is possible to refine this limit slightly with spherical and chromatic aberration calculations [313].

analogous to equation 6.3. In 2D cross-section using the half-angle $\theta \approx \sqrt{\Omega/\pi}$, one can also define the numerical aperture NA $\propto n\theta$ and lens f-number $N \propto 1/\theta$. Immersion microscopy is moving light into a medium of higher refractive index n. Synchrotron brilliance is radiance per wavelength. All this describes focusing limits to light[19].)

To apply emittance limits to our focusing problem, first rewrite table 6.1 to list all conditions including relevant parameters we did not previously consider:

	Start (exit nozzle)	End (deposit)
Beam minimum diameter d_B	0.1 mm to 1 mm	< 0.001 mm
Beam half-angle θ	$\approx 5°$ (90 mrad)	$< 30°$ (520 mrad)
Axial velocity v_a	$\pm 50\%$ in 100–300 $\mathrm{m\,s^{-1}}$	$\pm 10\%$ in 100–3000 $\mathrm{m\,s^{-1}}$
Particle diameter d_p	$\pm 50\%$ in 1–50 nm	(no change)
Particle charge q	± 2 in 1 e to 100 e	(no change)
Volumetric flux Q	1×10^4 to 1×10^6 $\mu\mathrm{m}^3/\mathrm{s}$	(no change)

Table 6.3: Approximate particle input and desired output conditions. This is the same as table 6.1 but we also specify the beam half-angle and clarify the diameter is the minimum anywhere along the beam at that angle. The 5° initial half-angle is based on our results from chapter 4. Volumetric flux is the range chapter 2 indicated is feasible.

We can now use equation 6.3 (which includes equation 6.2) to easily calculate whether ion optics can achieve the focusing we want. For example: unrealistically assuming no chromatic aberration for the moment, we can focus the beam to a minimum diameter of

$$d_{B2} = \frac{d_{B1}\theta_1}{\theta_2} = \frac{0.1\,\mathrm{mm} \cdot 5°}{30°} = 16\,\mu\mathrm{m}. \tag{6.4}$$

That's not great; we want resolution over an order of magnitude better. This doesn't improve much on aerosol focusing (though it should handle small particles better), and chromatic aberration from the spread of particle sizes and charges would significantly reduce the benefit as previously noted. We would get some additional improvement from increasing particle velocity, but our only way to do that is electrostatic acceleration, suffering from the same chromatic aberration flaws as lenses (see section 6.4.1).

We could also use an aperture to reduce the diameter by another 10x at the cost of reduced volumetric flux. Since beam area scales with diameter squared, that would leave approximately $1/10^2 = 1/100$ of the original flux, reducing print speed by orders of magnitude (see section 6.5.3). This might also run into clogging issues—such a small aperture is microscale, making this essentially stencil lithography as briefly mentioned in chapter 4.

[19]The reader may know that a magnifying glass on Earth can focus sunlight to start a fire [314]. Radiance and étendue calculations show this can also work with starlight (albeit with a 10 km wide lens), but not moonlight. When a sunbeam bounces off the moon, it reflects in a diffuse (Lambertian) way, spreading over an entire hemisphere and only partially reaching Earth. The resulting étendue of moonlight is about 1×10^5 times larger and even an infinitely large lens would fail to achieve sufficient intensity. A solution is to make the moon surface a mirror (avoiding étendue change).

At this point we see ion optics may be close to achieving our 1 µm resolution—and we can maybe get there if we're willing to accept impractical particle filtering and slow print speed constraints—but we're uncertain how feasible the result will be. Can we do even better?

There is one final loophole [316] in the emittance theorem: breaking the premise that particle motion is conservative. We can add a force other than time-invariant electrostatic fields.

6.3.2 Damping and Quadrupole Ion Traps

We just deduced time-invariant electrostatic fields by themselves are not quite good enough. If we want to focus particles radially with sub-1 µm resolution, we need to actively add or remove energy from each nanoparticle to get around the emittance theorem.

One (impractical) approach is to change the electric fields with feedback. For example, if we were able to somehow track the position of a nanoparticle, we could adjust the electric fields around it in real time (by changing electrode voltages) to direct its motion. Unfortunately, tracking each individual particle is infeasible[20]: we might have over 1×10^{10} particles per second, each moving at $1000\,\mathrm{m\,s^{-1}}$ over tens of millimeters, where each particle is less than 100 nm wide and has charge $q < 100e$ (not very far from single atoms), and tracking needs sub-1 µm precision with microsecond time resolution. These tracking system specifications are somewhat ridiculous to meet. We must make do without closed-loop control[21].

Instead, our solution is to add a damping force. In addition to time-invariant electric fields, add a force that slows down (dampens) particle motion in all directions[22]. Over time, each particle will lose both kinetic and potential energy until it has moved to the local minimum[23] of the the electrostatic potential energy field. This is like marbles rolling around in a round bowl (a potential energy field, albeit due to gravity). Without damping, like our previous ion optics, the marbles move forever, never stopping. With damping (air drag and friction) they slow down until they rest at the center of the bowl (the potential local minimum). Setting the shape of the electric potential lets us direct where the particles end up.

This damping approach is widely used in particle accelerators, mass spectrometers, and other trapped ion applications. It is simple, works well, and moves all particles to known positions without needing to track them individually. It is sometimes called "cooling" because slower organized movement generally means lower temperature[24]. Commensurate with its importance, many ways to create the damping force have been developed [316][318][319][320]:

- **Buffer gas cooling:** This is just air drag as discussed in chapter 4. Impacts from (ideally inert) gas atoms, here called buffer gas, slow down particles. This is fairly universal and common in mass spectrometry [321][322][323], particle accelerators [324], and elsewhere [325], but cools to a nonzero limit. Also called "collisional cooling" [326] or "collisional focusing" [327][328].

[20] Tracking and controlling only one particle (not many) is sometimes possible; see feedback cooling.
[21] Without per-particle closed-loop control. Control of total beam behavior (e.g., current) is possible.
[22] Damping a beam only in the radial direction would be preferable but we have no way to do so.
[23] Electric potentials have no local minima; we will address and fix this with ion traps and in appendix A.
[24] This is tricky as it requires a new definition of temperature for the (usually isolated) particles, e.g., [317].

- **Laser cooling:** A class of techniques that exploit the quantum behavior of particles to absorb and re-emit photons in specific ways, using photon momentum to slow down the particle [329] (Doppler cooling, for example, uses the fact that a particle traveling in one direction will see incoming photons blueshifted and, if those photons' frequencies were carefully chosen, will only absorb photons and their momentum from that direction). Usually only works for single atoms with certain quantum energy levels.
- **Cavity cooling:** Although standard laser cooling doesn't work on nanoparticles which have much messier band structures than single atoms, similar results can be achieved by clever arrangement of nanoparticles scattering a laser in an optical cavity. This might be able to cool nanoparticles to near their ground state but methods are still in development; it is not obvious how we would implement it[25] [332][333][330][334][335][336].
- **Sympathetic cooling:** Buffer gas cooling but improved by using laser cooling on the buffer gas (not nanoparticles) to reach lower temperatures [323][337].
- **Feedback cooling:** In well-controlled circumstances, it actually is sometimes possible to sense individual particles (either via their electric image charge when resonating [111][338][321] or optically via scattered light) and sometimes apply electrical or optical feedback to control their position [339][340][341][342][343]. This remains infeasible for our large number of particles. Currently investigated mainly for quantum experiments.
- **Stochastic cooling:** This is the one known way to make feedback cooling practical, used in particle accelerators: sensing average particle beam asymmetries and applying a correcting electrical pulse, many times over as the beam circulates [344][345]. Won the 1984 Physics Nobel [346]. Is not easily applied to our nanoparticles.
- **Radiation damping:** When sufficiently fast (near lightspeed) particles accelerate, they emit light with significant momentum, slowing the particle; this can be used to cool a particle accelerator beam [347][319][318]. Related to synchrotrons.
- **Electron cooling:** Like gas cooling, except the gas is replaced with a beam of electrons [348][349]. Used in particle accelerators.
- **Ionization cooling:** Like gas cooling, except the gas is solid matter (in which nuclei are ionized as the beam passes through). Shown for muon particle accelerators [350].
- **Evaporative cooling:** When multiple particles in a beam interact, they share energy (again like gas cooling) with some distribution; if the fastest are removed (evaporated) from the beam or trap, the remainder are slower on average [351][352][353].

Of all these methods, buffer gas cooling seems the only feasible option for our nanoparticle printer. Other methods don't work on nanoparticles (laser cooling), require much higher speeds and longer times (stochastic cooling), or lose nanoparticles (evaporative cooling). Fortunately, buffer gas cooling is also simple to implement: all we have to do is let some small amount of gas float near the nanoparticles (instead of using high vacuum), and the particles will be slowed as discussed in section 4.1.1. Ideally the gas should be inert (e.g., argon, not oxygen; see section 4.3.3) to avoid chemical reactions with the particles.

[25] There is some evidence cavity cooling might eventually work for particle beams [330][331].

How can we use this buffer gas cooling method to focus particles?

We must create an electric potential field such that an incoming beam of particles, when slowed by the buffer gas, falls into our desired beam shape. This potential must be lower at the center at the beam and higher elsewhere. As discussed in appendix A, this cannot be done with static electric fields due to Earnshaw's theorem. However, an oscillating field of the correct shape, generally formed by four parallel rods—a quadrupole—creates an average potential that pushes particles toward the center, focusing the beam like we want!

Specifically, as detailed in appendices A and B, the oscillating field causes particles to vibrate back and forth (micromotion), but asymmetry causes particles to feel a time-averaged force (the ponderomotive force) toward regions of lower electric field magnitude, which acts like the conservative force of a potential field (the pseudopotential).

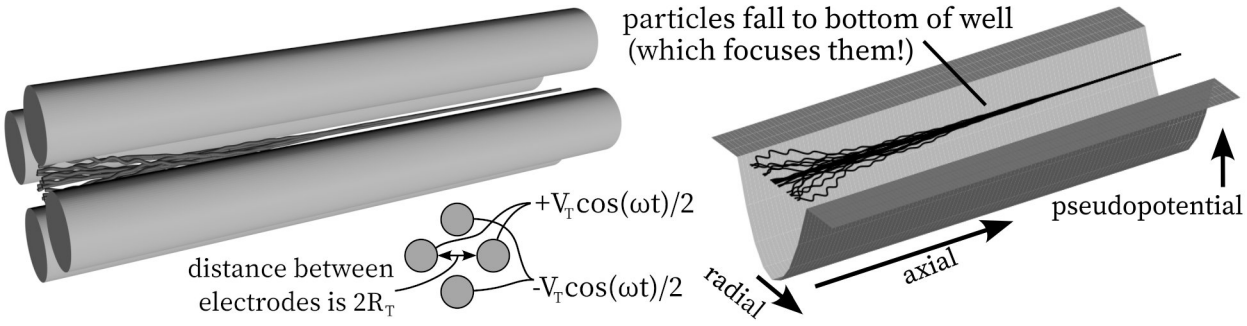

Figure 6.6: Particles moving left to right through a quadrupole ion trap with buffer gas, in the style of figures 6.3 and 6.4. Left: the trap consists of four electrode rods with oscillating voltages. Right: although the fields oscillate, particles experience an average force over time which forces them toward the center like a quadratic potential well (the pseudopotential); see appendix A. When air drag is applied, particles fall down the potential into the center of the well, focusing the particle beam in a completely different way from an Einzel lens.

This quadrupole setup is relatively easy to design and build reliably. This same configuration is common for focusing beams of heavy atoms or molecules, either in particle accelerators, where it is called a radio frequency quadrupole (RFQ) beam cooler [317][354][355][324][356][357], or in mass spectrometers, called a linear quadrupole ion trap [358][321][359][328].

There is one major problem with quadrupole focusing: because buffer gas is omnidirectional, it also slows down particles in the axial direction. Particles will slow down and eventually stop over time due to air drag (according to the stopping distance in chapter 4) [328], as shown in figure 6.7. This is unavoidable since particle motion is exponentially damped with the same time constant in all directions, so by the time a particle loses 95% of its radial velocity, for example, it has also lost 95% of its axial velocity. Particles cannot be fully focused without becoming stuck. A straightforward solution to this axial slowing problem is superimposing an additional axial electric field to keep particles moving. There are multiple ways to do this, so we address it in depth in section 6.4. For the remainder of this section, we assume this is a solvable problem and only consider particle radial motion.

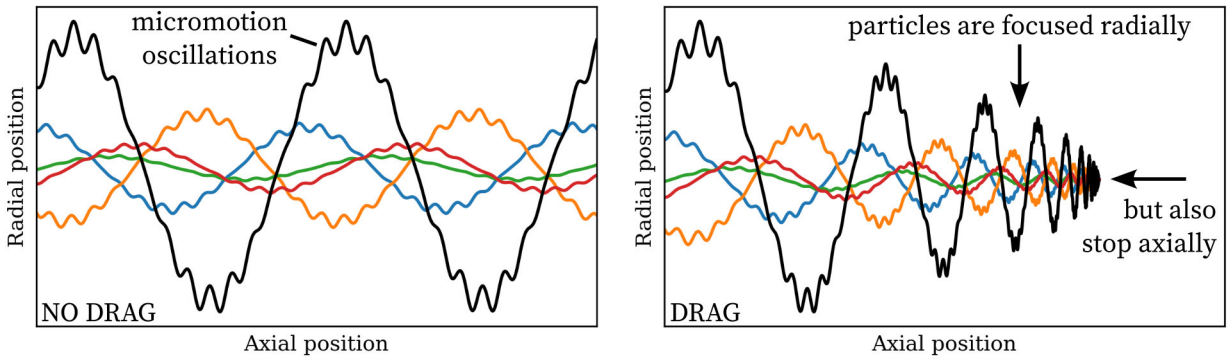

Figure 6.7: Trajectories of particles (different colors) moving left to right in a quadrupole trap. Left: with no air drag, particles move in simple harmonic motion plus an additional micromotion oscillation. The beam diameter stays the same size it was initially. Right: when air drag is added, particles move toward the center, falling down the potential shown in figure 6.6. The beam is focused! However, the particles slow down and eventually stop in the axial direction; they'd never make it to a substrate. We will fix this in section 6.4.

Assuming axial motion works, we are ready to consider how much we can focus particles.

Consider a single particle in a quadrupole trap. The pseudopotential is formed by electric fields with nearly infinite resolution, so if a particle were perfectly damped the particle could be centered nearly exactly. However, the buffer gas molecules continue to hit the nanoparticle and shift it off center. We've brought back Brownian motion! Brownian motion is our main limit to focusing; for several other considerations see section 6.3.3.

We can approximate the smallest beam diameter we can focus particles to by comparing the quadrupole pseudopotential, which narrows the beam, to Brownian motion, which expands it. In appendix A we found the quadrupole pseudopotential (equation A.9) has height

$$\widetilde{U}_T(r) \approx \frac{qV_T\, r^2}{8R_T^2} \cdot \frac{q}{q_0} \cdot \frac{m_0}{m} \tag{6.5}$$

where r is the distance of a particle from the trap center, R_T is the distance from trap center to closest quadrupole electrode, V_T is the peak-to-peak voltage amplitude between quadrupole electrodes, and the particle has mass/charge ratio m/q while the oscillation frequency is optimized[26] (equation A.6) for particles with slightly smaller ratio m_0/q_0.

Brownian motion is random, not a force in a single direction, but we can conveniently analyze it (as noted in chapter 4) by noting it gives particles some amount of kinetic energy. Particles can move in the 2D radial plane perpendicular to the beam and Brownian motion gives $\frac{1}{2}k_BT$ per dimension of movement, so on average particles have a total of $1k_BT$ of radial energy (in a random direction) when cooled to the temperature of the gas. Since this is only an average effect, some particles will have more kinetic energy and make the beam slightly wider, but here we use only $1k_BT$ in our calculations for simplicity.

[26]Increasing frequency by $\omega = s \cdot \omega_{min}$ gives $\widetilde{U}_T = \widetilde{U}_{Tmin}/s^2$ and (equation 6.6) $d_{Bquad} = s \cdot d_{Bquad,min}$.

If we set Brownian energy $1k_BT$ equal to $\widetilde{U}_T(r)$, we can find an expression for the average radius of displacement r, and the resulting particle beam diameter d_{Bquad} is twice that:

$$d_{Bquad} \approx 2R_T\sqrt{\frac{8k_BT}{qV_T}\cdot\frac{q_0}{q}\cdot\frac{m}{m_0}} \tag{6.6}$$

This equation gives the best resolution[27] (minimum beam diameter d_{Bquad}) a quadrupole particle focusing system can achieve. Let's compute some example beam diameters:

n	$R_T = 0.5\,\mu m$	$R_T = 5\,\mu m$	$R_T = 50\,\mu m$	$R_T = 500\,\mu m$	$R_T = 5\,mm$
1	45.3 nm	453 nm	4.53 µm	45.3 µm	453 µm
2	32.0 nm	320 nm	3.2 µm	32.0 µm	320 µm
5	20.3 nm	203 nm	2.03 µm	20.3 µm	203 µm
10	14.3 nm	143 nm	1.43 µm	14.3 µm	143 µm
20	10.1 nm	101 nm	1.01 µm	10.1 µm	101 µm
1	26.3 MHz	2.63 MHz	263 kHz	26.3 kHz	2.63 kHz

Table 6.4: The beam diameter d_{Bquad} nanoparticles of charge $q = n \cdot e$ can be focused to with a quadrupole built with electrodes of size R_T, calculated with equation 6.6 using $V_T = 100\,V$ and $T = 298\,K$. We can beat 1 µm resolution, perhaps even 100 nm! Eventually resolution is limited instead by the diameter of the nanoparticles themselves. These resolutions require the trap to have particular frequencies as described in appendices A and B; the last row computes these with equation A.6 for 10 nm Cu particles with $q = 1e$.

This is excellent: quadrupole ion traps with buffer gas theoretically allow us to focus particles to sub-1 µm resolutions, finally achieving our original goal from chapter 1! This entire idea of nanoparticle printing might yet work! However, it requires significant detail.

First, note that with $V_T = 100\,V$, $T = 298\,K$, and $q = 1e$, the beam diameter d_B is focused to $\approx 5\%$ of the space between the electrodes ($2R_T$). A beam starting at $d_B = 0.1\,mm$ to 1 mm as in table 6.3 wouldn't fit in a sub-100 µm quadrupole; we will instead need to focus the beam through multiple progressively smaller quadrupole stages to reach sub-micron dimensions. We comment on how to do this (and how to build tiny quadrupoles) in section 6.5.1.

We can improve focus by increasing the trap voltage V_T, but only to a point: sufficiently high voltage will cause electrical breakdown, making the buffer gas into a conductive plasma[28]. As described by the Paschen curve in figure 2.4, there is a maximum safe voltage below which breakdown never occurs. The exact voltage varies with gas, geometry, surface roughness and other conditions [138]; for this chapter we assume $V_T = 100\,V$ is always safe[29]. Alternatively, we can use a low gas pressure (and trap size), on the left of the Paschen minimum, to increase the allowed voltage. Many particle accelerator quadrupoles use 0.01 Torr to 0.1 Torr pressures to reach voltages as high as $V_T = 1\,kV$ to $10\,kV$ [360][355][357][361][362].

[27] Approximately. The beam is somewhat Gaussian and subject to some other effects (section 6.3.3).

[28] Which will distort the electric field, short-circuit electrodes, and generally stop focusing from working.

[29] We further assume 200 V ($V_T = 100\,V$ plus 100 V for axial acceleration) is safe in section 6.4.

What pressure should the buffer gas be? There is an optimal value. Besides electrical breakdown, at low pressures damping takes longer than necessary (as described by the damping time constant in chapter 4); high pressures give slower axial movement (section 6.4) and reduced micromotion for lower ponderomotive focusing force [355][317]. The gas specifics and exact damping equation can vary so long as the damping is predictable[30]. Our simulations generally use 0.01 Torr to 10 Torr argon in quadrupoles around 100 mm long.

Decreasing the temperature T improves resolution. Some particle accelerator RFQ beam coolers use liquid nitrogen to reach $T = 77\,\mathrm{K}$ (vs. $298\,\mathrm{K}$ room temperature) [363][362][364].

What about our wide range of particle sizes: 350% variation, according to table 6.3? It turns out we can probably focus everything at once without worrying about chromatic aberration! All particles will be damped to $1k_BT$ radial thermal motion[31] then stay at a constant minimum diameter which, according to equation 6.6, will only scale with $\sqrt{m}$ so the mass variation merely doubles the beam diameter.

Particle charge should be as high as possible for better focusing (and higher axial velocity in section 6.4), though this results in higher space charge effects (section 6.3.3). If we can vary particle charge based on size (thus mass), as chapter 5 suggests may occur when charging to a fixed ionization energy, we would reduce mass/charge ratio variation.

We should also note that while simulating quadrupole traps is straightforward, simulating Brownian motion (see chapter 4), while feasible via statistical methods [215][216][365], is not. We did not have time to verify a numerical Brownian simulation for our large nanoparticles at intermediate pressures and so did without. This should not change our conclusions.

6.3.3 Additional Limits to Quadrupole Radial Focusing

We now have a tractable approach to radially focus particles—quadrupoles with buffer gas—and are ready to tackle the final problem of axial velocity control. But before we switch discussion from radial to axial particle movement, there are several more[32] radial effects we should mention: space charge, RF heating, and beam expansion outside the trap due to thermal energy. These are all minor but will still affect the ultimate focusing performance.

Space Charge

A beam of nanoparticles contains many particles, and since all these particles have a positive charge, they will repel each other and make the beam wider, reducing printing resolution. This effect is called space charge and limits the number of particles in any given beam. Space charge limits are also a large concern in particle accelerators and electron and ion beam tools. In these systems, the Child-Langmuir law [296] gives the maximum density of charges that can be moved axially through a region with a given voltage. But we would like to consider radial forces for the moment, so we will need to make a different calculation.

[30] Small quadrupoles can be smaller than the gas mean free path, so quantization effects may appear.

[31] This is sometimes called thermalization and is roughly why any damping method is called cooling, though it would be heating if the particles started with a lower velocity.

[32] Even more effects exist (e.g., electrical noise). See [366] for a review in trapped-ion quantum computing.

Define the number flux N' as the number of nanoparticles per second moving through the beam cross-section (N' is fixed by the volumetric flux Q and particle diameter d_p). When N' is small (as an extreme, $N' = 1\,\mathrm{s}^{-1}$), particles are so far apart that space charge effects are negligible and we can achieve the high resolution of table 6.4 without trouble. But if N' is sufficiently large, space charge pushes particles out radially.

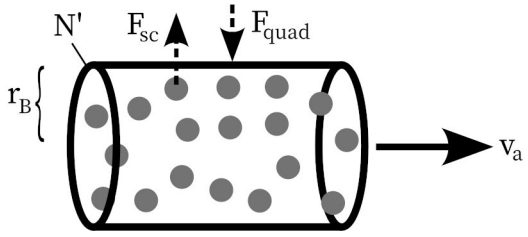

Figure 6.8: Cartoon of the space charge effect. Electrically charged nanoparticles in the same beam repel each other with force F_{SC} to make the beam wider (in addition to Brownian motion), opposing the quadrupole trap ponderomotive force F_{quad} that makes the beam more narrow. A total rate of N' particles, each with charge q, move through the beam cross-section (radius r_B or diameter $d_B = 2r_B$) at axial velocity v_a.

We can roughly approximate[33] the effect of space charge on radial focusing in a quadrupole as follows [367][360]: compare the quadrupole potential (equation 6.5) to a repulsive potential from the beam. Approximate the beam as uniform positive charge density within a cylinder of radius $r_B = d_B/2$. Since N' is the number of particles per time with charge q moving through the cylinder cross-section at velocity v_a, the linear charge density of the cylinder is qN'/v_a (units $\mathrm{C\,m}^{-1}$). The electric field $\vec{E}$ (pointing radially outward) of this cylinder and corresponding potential energy U_{SC} from $q\vec{E} = -\nabla U_{SC}$ (setting $U_{SC}(0) = 0$) are

$$|\vec{E}(r)| \approx \begin{cases} \dfrac{qN'r}{2\pi\epsilon_0 v_a r_B^2} & r \le r_B \\ \dfrac{qN'}{2\pi\epsilon_0 v_a r} & r > r_B \end{cases} \quad \text{and} \quad U_{SC}(r) \approx \begin{cases} -\dfrac{q^2N'r^2}{4\pi\epsilon_0 v_a r_B^2} & r \le r_B \\ -\dfrac{q^2N'}{2\pi\epsilon_0 v_a}\left(\ln\left(\dfrac{r}{r_B}\right) + \dfrac{1}{2}\right) & r > r_B \end{cases} \tag{6.7}$$

for radial distance r from the beam center. Particles are pushed away from the beam center via the electric field (i.e., they fall down the potential U_{SC}). The beam is stable when this potential U_{SC} is less than the quadrupole pseudopotential $\widetilde{U}_T(r)$ (equation 6.5) in the same way we derived equation 6.6 (but ignoring[34] Brownian motion).

$$\widetilde{U}_T(r) > U_{SC}(r) \quad \text{so} \quad \frac{qV_T\,r^2}{8R_T^2} > \frac{q^2N'r^2}{4\pi\epsilon_0 v_a r_B^2} \tag{6.8}$$

[33]More accuracy could be obtained via particle simulation, modeling the beam with Poisson's equation.

[34]This is valid when space charge is a larger effect than Brownian motion; the exact boundary for N' we find will be a slight overestimate of the maximum charge a beam can fit.

Rearranging this equation, we find the maximum number flux N' that fits in a beam (that also satisfies equation 6.6) of diameter $d_B = 2r_B$ with quadrupole trap voltage V_T, axial velocity v_a, particle charge q, quadrupole trap radius R_T, and vacuum permittivity ϵ_0:

$$N' < \frac{V_T \pi \epsilon_0 v_a d_B^2}{8 q R_T^2}. \tag{6.9}$$

For example, a beam of diameter $d_B = 1\,\mu\text{m}$ and $v_a = 1000\,\text{m}\,\text{s}^{-1}$ focused by a trap with $V_T = 100\,\text{V}$ and $R_T = 5\,\mu\text{m}$ can move a maximum of $N'_{max} \approx 8.7 \times 10^{10}$ singly-charged ($q = 1e$) particles s^{-1}, which is a current of about 14 nA. We discuss the ramifications of this space charge limit in section 6.5.3, where it is often the largest constraint on print speed at high resolutions giving an incentive to use particles of higher mass and lower charge.

RF Heating

Our approximation of a quadrupole as a quadratic potential well for particles has some limits, and these differences can affect particle motion, typically increasing the beam diameter.

Recall the quadrupole trap works (in appendices A and B) by creating an oscillating electric field. A particle experiences quick oscillations that we call micromotion, and asymmetry in the field during micromotion is what provides the average ponderomotive force that makes the particle act as if it were in a quadratic potential well. This micromotion itself slightly increases the beam diameter[35], but in addition to this, disturbing the particle from an ideal micromotion trajectory modifies the resulting ponderomotive force which can then be nonconservative and add kinetic energy. RF heating is any such effect[36].

RF heating can happen in many ways. See [323] for an excellent review, or [368][369][365][370][371]. Collisions with gas molecules, for example, disturb particle motion and adjust their micromotion. We can likely neglect single collisions as our nanoparticles are significantly heavier than the surrounding gas molecules, but the collective behavior (which produces the drag we use) is statistically nontrivial [365]. Another source of RF heating is multiple nanoparticles repelling each other[37]. This makes nanoparticles rest at a nonzero radial position, where they have nonzero micromotion. Finally, particles entering or leaving a quadrupole out of sync with its oscillations will be deflected in some direction (which is arguably RF heating); they might only experience half of a micromotion cycle. All these RF heating effects can be modeled with particle trajectory computer simulations.

Beam Expansion from Thermal Velocity

Our last consideration is what happens when a focused beam of particles leaves a quadrupole, because there must be some distance between the quadrupole and the substrate we wish to print particles onto. While in the quadrupole, particles stay within a constant beam diameter d_B but have radial energy $1k_BT$. As soon as the particles leave the trap at axial velocity v_a,

[35] Increase in beam diameter due to expected micromotion oscillations is not usually considered RF heating.

[36] This occurs in any RF ion trap (see appendix A), hence the name.

[37] This is what causes space charge repulsion, can also be called intra-beam scattering [372], and can distribute particles radially by mass/charge ratio [326].

the particles will also move outward radially, expanding the beam[38]. We assume L is small and v_a high so drag is negligible. The mean radial velocity v_r from $kT = \frac{1}{2}mv_r^2$ is

$$v_r = \sqrt{\frac{2k_BT}{m}} \tag{6.10}$$

so the beam forms half-angle $\theta \approx v_r/v_a$. If the beam had original diameter d_{B1} (perhaps d_{Bquad} from equation 6.6) and travels axial distance L, the final beam diameter d_{B2} is

$$d_{B2} \approx d_{B1} + 2\theta L \approx d_{B1} + 2v_r\frac{L}{v_a} \approx d_{B1} + 2\frac{L}{v_a}\sqrt{\frac{2k_BT}{m}}. \tag{6.11}$$

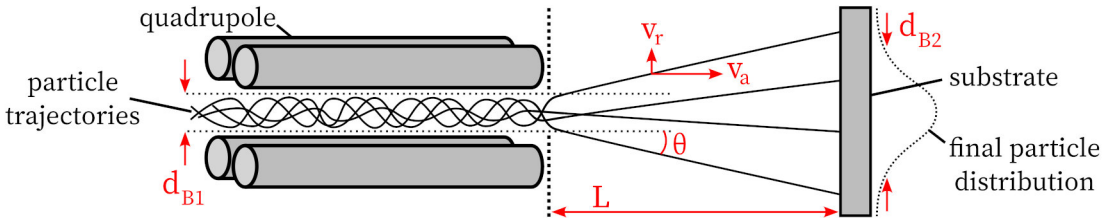

Figure 6.9: Illustration of beam expansion when particles (moving left to right) leave a quadrupole (or pinhole [214]). Particles have nonzero radial energy, so they move outward with no more quadrupole to confine them. The final beam distribution is roughly Gaussian.

	1 nm	10 nm	100 nm
v_r	$41.9\,\mathrm{m\,s^{-1}}$	$1.32\,\mathrm{m\,s^{-1}}$	$0.0419\,\mathrm{m\,s^{-1}}$
θ $(1000\,\mathrm{m\,s^{-1}})$	$2.4°$ $(41.9\,\mathrm{mrad})$	$0.0759°$ $(1.32\,\mathrm{mrad})$	$0.0024°$ $(0.0419\,\mathrm{mrad})$

Table 6.5: Mean radial velocity v_r of nanoparticles leaving a quadrupole at $298\,\mathrm{K} = 25\,°\mathrm{C}$ and corresponding beam half-angles for $v_a = 1000\,\mathrm{m\,s^{-1}}$, assuming density of copper. These tiny angles give low emittance so the ion optics of section 6.3.1 might actually be useful.

As a result of this effect, we may need to place the output of a quadrupole focusing mechanism close to the substrate (see section 6.5.1). For example: if 10 nm particles travel with an axial velocity $v_a = 100\,\mathrm{m\,s^{-1}}$, then printed spot diameter increases $2v_r/v_a * 1\,\mu\mathrm{m} = 26\,\mathrm{nm}$ for each micrometer of distance L from the substrate; at $1000\,\mathrm{m\,s^{-1}}$ this is only 2.6 nm. Achieving high resolution $< 1\,\mu\mathrm{m}$ probably requires putting the quadrupole exit within tens of microns of the substrate. Fortunately, this is feasible: machine tools and XYZ stages easily maintain position within $10\,\mu\mathrm{m}$. Quadrupole focusing, as in table 6.4, is the bigger limit.

Alternatively, note the beam exiting the quadrupole can have low emittance (see table 6.5), so we might allow the beam to travel a long L while expanding, then use standard ion optics (e.g., an Einzel lens) to focus it back over a similarly long[39] L if we can achieve sufficiently low chromatic aberration. We make some remarks in section 6.5.1.

[38]This derivation also appears (with experimental confirmation) in [214] for aerodynamic lenses and supersonic gas jets [325], and as an upper limit for brightness of electron sources at some temperature [296][373].

[39]This is how SEMs and FIBs can place their electron and ion optics far from a substrate.

6.4 Axial Acceleration

We are halfway to solving the particle focusing problem of section 6.1. We found a way to radially focus nanoparticles to small sub-1 µm areas by using quadrupole traps with buffer gas cooling, but also found we will need to somehow keep particles moving in the axial direction without being stopped by the buffer gas. Furthermore, in order to control printed material quality (see chapter 3), we want to set the axial speed of the particles when they impact the substrate to some adjustable value we can choose within $v_a = 100\,\mathrm{m\,s^{-1}}$ to $3000\,\mathrm{m\,s^{-1}}$.

A solution exists. We will be able to control particle axial speed, i.e., accelerate particles to a desired velocity. The fundamental trick we will use is that quadrupoles only control particle motion in the radial direction; axial movement is separate and can be controlled with its own electric field. We will first present a relatively simple approach (DC acceleration) and its limits then discuss a more advanced axial acceleration system (a linac).

6.4.1 DC Acceleration

The easiest method to make particles continue to move axially (instead of being slowed and stopped by gas damping) is to apply a DC[40] field in the axial direction, resulting in the basic 1D electrostatic movement discussed in section 6.2.

The most straightforward way to achieve this is to divide the quadrupole electrodes into axial segments onto which are applied the oscillating voltages required for the quadrupole plus a DC bias voltage that increases in the axial direction. The oscillating voltage component creates a quadrupole pseudopotential and the DC bias voltages create an axial field; they add together by superposition (the electric field is linear in voltage). Particles are now focused radially by the quadrupole with gas damping and also accelerated axially.

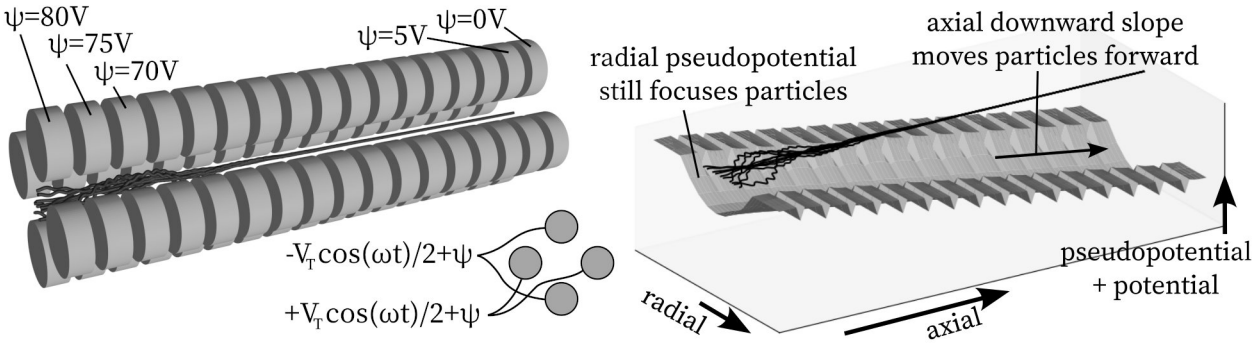

Figure 6.10: Left: we can take the quadrupole of section 6.3.2 and figure 6.6 and apply an axial electric field by segmenting the electrodes and applying an increasing DC bias ψ to each set (here, an additional 5 V per segment). Right: The resulting potential and pseudopotential field the particle moves in is a quadratic well that slopes down in the axial direction.

[40]By DC for "direct current" we mean an electric field or voltage is time-invariant, as in any ion optics in section 6.3.1, as opposed to, e.g., the oscillating-in-time electric field of a quadrupole trap.

Particle trajectory simulations show this works. Particles have damped radial motion but keep moving in the axial direction, eventually producing a narrow beam with the diameter d_{Bquad} we computed in equation 6.6. We have successfully made a highly focused beam!

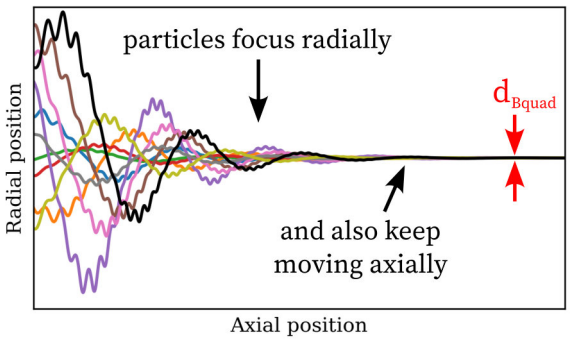

Figure 6.11: Trajectories of particles in a quadrupole with buffer gas, which focuses them radially, and DC acceleration, which keeps them moving in the axial direction. We have successfully made a focused beam! This continues figure 6.7 (and in fact uses an identical simulation save slightly higher pressure and more particles for visualization). The final beam diameter should be d_{Bquad} from equation 6.6 but, as briefly mentioned in section 6.3.2, the simulation results are slightly better than this since we only simulate drag and not Brownian motion. The general behavior is realistic.

This is not a new idea. Axial DC fields, both with and without a quadrupole, are common: they are the most basic way to move particles electrostatically (see section 6.2).

Any quadrupole using a buffer gas will run into the same axial slowing issue and solution. Using segmented electrodes to simultaneously create a radial quadrupole field and axial DC field is common practice in particle accelerator RFQ beam coolers [317][354][374][375][324][356][357][376] and mass spectrometry linear quadrupole traps [328][377]. There are also ways[41] to create the axial field without segmenting the quadrupole, reducing the number of electrodes: the quadrupole electrodes can be tapered and slanted [379][328][380] or crosscut and twisted [364], or additional DC-only electrodes added around or between the quadrupole electrodes [381][382][362][378], though this distorts the quadrupole field [328][378].

Axial fields are also used without a quadrupole when focusing is not required. Applications include (see also chapter 3) ionized cluster beam deposition (ICBD) [178][47] which prints nanoparticles over a wide area instead of in a focused beam, ion optics for SEMs, FIBs, and ion implantation, micrometeoroid impact studies [198][199], and electrostatic precipitators [102]. Axial electric fields have been proposed to further accelerate particles in cold spray and aerosol deposition[42] [98][383][384]. We should also mention ion mobility spectrometry [210][385][386] which moves molecules in an axial DC field in buffer gas (sometimes with a radial RF trap, but a simpler ring design, similar to the ion funnels we will mention in section 6.5.1, instead of a quadrupole as it does not need to minimize beam diameter).

[41] Confusingly, some of these nonsegmented geometries are sometimes called Linacs [328][378] with no relation to the generic linear accelerator linac as used in particle accelerators and section 6.4.2.

[42] This increases particle impact velocity but does not solve the Brownian focusing limit from chapter 4.

We can analyze DC axial acceleration as follows.

First, without gas drag, an axial field of total voltage V will accelerate a particle of mass m and charge q from zero to a speed of $v_a = \sqrt{2qV/m}$ (from KE $= qV = \frac{1}{2}mv_a^2$); it adds qV kinetic energy (this is why the volt is a joule per coulomb). This happens no matter how long the field is. If we made an axial field without a quadrupole by taking just two of the three rings of an Einzel lens (section 6.3.1)—an "immersion lens"—whether the two ring electrodes are 100 µm or 100 mm long does not matter (as long as gas drag is negligible); the particle will reach the same speed as it travels through.

This speed increase from a gas-drag-free axial field varies with the square root of particle mass and charge. The square root means this is less sensitive than radially focusing with other ion optics (which depends directly on the mass/charge ratio). This limited chromatic aberration means we might find DC axial acceleration useful (if still imperfect) for our wide range of particle parameters if there is ever low gas pressure and we can use a high enough voltage: a 10 nm $q = 10e$ copper particle needs a high 1460 V to reach 1000 m s^{-1}.

A particle with gas drag in an axial field acts slightly differently: it will try to increase its speed as before, but because the gas drag force increases with velocity, it turns out particles will accelerate up to some steady-state drift velocity[43], and this drift velocity depends on the electric field (the voltage per distance), not the voltage itself. If the particle has viscous damping coefficient β giving drag force $F_{drag} = -\beta v_a$ (see chapter 4) and is pulled forward by an axial electric field E as $F_{field} = qE$, it will slow down or speed up until reaching drift velocity $v_{a,drift}$ defined by

$$F_{field} = qE = \beta v_{a,drift} = -F_{drag} \quad \text{so} \quad v_{a,drift} = \frac{q}{\beta}E = K \cdot E \tag{6.12}$$

where we define the electrical mobility[44] $K = q/\beta$ [102][205][211]. We can expand β using our Epstein drag equation 4.7 to see

$$v_{a,drift} = \frac{q}{\beta}E = \frac{12}{8 + \pi\varphi}\sqrt{\frac{k_B T}{2\pi m_g}}\frac{q}{P d_p^2} \cdot E \tag{6.13}$$

where P is the pressure, m_g is the gas molecular mass, $\varphi \approx 0.9$, and d_p is particle diameter. Because the mass of the particle varies with diameter cubed ($m = \rho\pi d_p^3/6$ where ρ is density), this steady-state velocity scales with $m^{-2/3}$, which means there is slightly more chromatic aberration than the $\sqrt{1/m} = m^{-1/2}$ scaling of gas-free acceleration. Furthermore, a particle only reaches this velocity if the field E is sustained over a long enough distance (roughly the gas stopping distance, equation 4.14), which requires high voltage V over long distance L for $E = V/L$ (at shorter distances, the particle accelerates similar to the no-drag case).

Gas breakdown usually limits the maximum voltage we can use to around 100 V (see section 6.3.2), thus limiting maximum electric field and drift velocity. We can compute the resulting possible drift velocities for particles of our range of sizes to see what might be practical.

[43] This is similar to the terminal velocity of falling objects on Earth or electron drift velocity.

[44] Electrical mobility is a crucial parameter in ion mobility spectrometry, where it is used to precisely differentiate molecules in a different way than the mass/charge ratio in mass spectrometry [210][385].

	1 nm	10 nm	100 nm
100 V, 0 Torr	$2610\,\mathrm{m\,s^{-1}}$	$82.6\,\mathrm{m\,s^{-1}}$	$2.61\,\mathrm{m\,s^{-1}}$
100 V / 100 mm, 0.01 Torr	$(13\,200\,\mathrm{m\,s^{-1}})$	$(132\,\mathrm{m\,s^{-1}})$	$1.32\,\mathrm{m\,s^{-1}}$
100 V / 100 mm, 0.1 Torr	$1320\,\mathrm{m\,s^{-1}}$	$13.2\,\mathrm{m\,s^{-1}}$	$0.132\,\mathrm{m\,s^{-1}}$
100 V / 100 mm, 1 Torr	$132\,\mathrm{m\,s^{-1}}$	$1.32\,\mathrm{m\,s^{-1}}$	$0.0132\,\mathrm{m\,s^{-1}}$
100 V / 100 mm, 10 Torr	$13.2\,\mathrm{m\,s^{-1}}$	$0.132\,\mathrm{m\,s^{-1}}$	$0.001\,32\,\mathrm{m\,s^{-1}}$

Table 6.6: Top row: velocities of singly-charged Cu particles of the indicated diameters from a 100 V field (note this is similar to table 6.2). Bottom rows: drift velocities of the same particles in a field of 100 V applied over a 100 mm distance ($E = 1\,\mathrm{V\,mm^{-1}}$); parentheses note a longer distance (and thus higher voltage) is required for the particle to reach that drift velocity. Most velocities are below our desired $100\,\mathrm{m\,s^{-1}}$ to $3000\,\mathrm{m\,s^{-1}}$ velocities but particles with higher charge q have proportionally higher drift velocities. In the top row, velocities vary with $\sqrt{m} \propto d_p^{3/2}$, and in the bottom row by $m^{2/3} \propto d_p^2$.

As shown in table 6.6, axial DC acceleration in gas cannot quite reach the $100\,\mathrm{m\,s^{-1}}$ to $3000\,\mathrm{m\,s^{-1}}$ velocities we want for most particles when allowing only 100 V. Other applications that use axial fields in gas typically accept this: particle accelerator RFQ beam coolers [374][376][362][364] and ion mobility spectrometry[45] use small fields (1 V to 200 V per 100 mm), because they only need nonzero (if low) velocity. If we want high velocities, we must use higher voltages, probably in vacuum. SEMs or ICBD and similar [47][199] use high voltage ($> 1\,\mathrm{kV}$) by working in high vacuum and chromatic aberration is either minimal (if all particles, e.g., electrons, are the same mass and charge) or ignored.

So DC axial acceleration through a quadrupole as in figure 6.10 works but is limited to low axial speeds. We could achieve high-speed impact velocities by accelerating in vacuum. But if we want very precise impact velocities that do not vary with particle size at all, we will need to use something more than a single axial DC field.

6.4.2 Linacs and Controlled Motion

There is a trick that could let us solve two problems simultaneously. At the cost of extra complexity, we could accelerate particles of different masses to the same velocity, and we could also reach higher velocities in a gas than with a simple axial DC field.

The trick is to start with segmented electrodes as in figure 6.10 but instead of applying a simple voltage gradient, we sinusoidally vary the voltage in the axial direction, making a number of "buckets" in the electrostatic potential. Background gas damping makes particles fall into these buckets much as it works for the quadrupole (section 6.3.2). We move the buckets along the axial direction (making the sinusoid a traveling wave) by changing voltages on each of the segmented electrodes, and the particles move with them. If we construct this correctly, all particles move as "bunches" inside the buckets precisely at the speed of the linac with no chromatic aberration. This is a linear accelerator, or linac.

[45] Ion mobility spectrometry is interesting as it encourages chromatic aberration; that is how it works.

A linac can accelerate particles to higher velocities than a single DC field for the same voltage because as the field shifts, a particle that has already been accelerated by voltage V can be pushed again by the same voltage, even though that voltage didn't change in magnitude (only position). In high-energy physics, this is how particle accelerators can reach ridiculously high particle impact energies[46] (though our linac is different by including buffer gas).

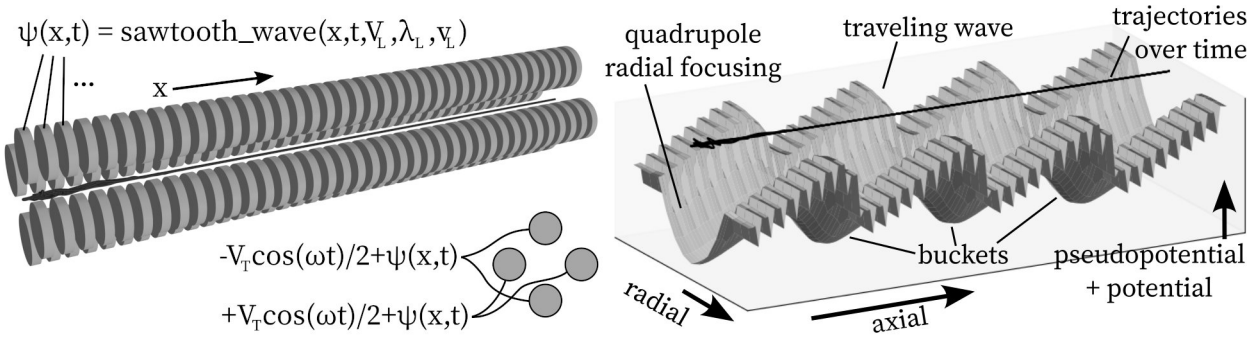

Figure 6.12: Beginning with a segmented quadrupole as in figure 6.10, instead of applying a smoothly increasing DC potential (in addition to quadrupole oscillations), use a wave of peak-to-peak amplitude V_L and wavelength λ_L (a sinusoid works, but a sawtooth wave with steeper slope is ideal) that travels in the axial direction at velocity v_L. This creates discrete buckets of electrostatic potential that particles fall into via buffer gas damping. As the buckets move at axial velocity v_L, the particles move with them at that velocity.

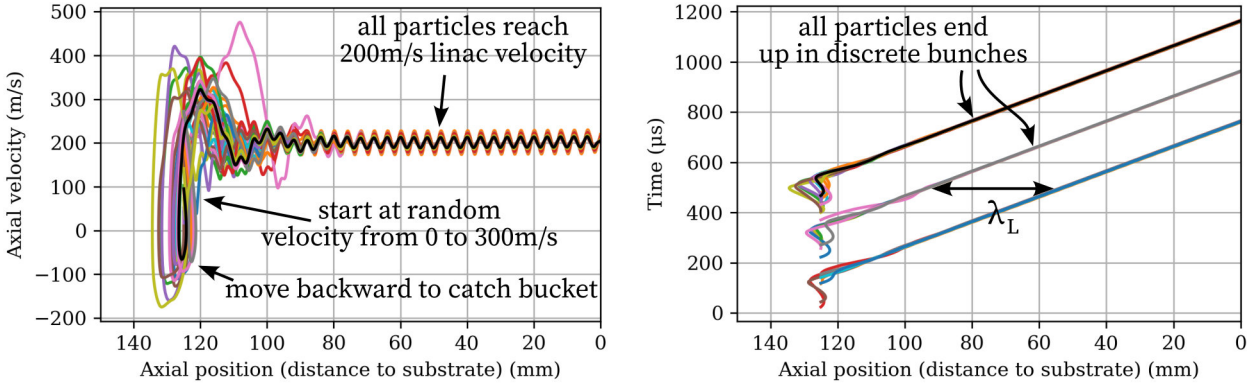

Figure 6.13: The linac works in simulation! These are trajectories of 4 nm to 6 nm Cu $q = 5e$ particles in a linac, beginning at axial position 125 mm with random velocities $0\,\mathrm{m\,s^{-1}}$ to $300\,\mathrm{m\,s^{-1}}$ and times (with respect to linac phase), and all eventually reach the steady-state $v_L = 200$ meter/s velocity of a linac with $V_L = 100$ V, $\lambda_L = 40$ mm, and 4 mm electrode pitch (and 100 Pa buffer gas) while forming bunches. The steady-state velocity oscillates due to the segmented electrodes. The particle drift velocity if the 100 V were applied over 100 mm is only $35\,\mathrm{m\,s^{-1}}$; this linac lets them achieve speeds over 5 times higher.

[46]These can reach TeV particle kinetic energies without a teravolt DC voltage, which is impractical.

To analyze the linac, consider the potential particles feel in the axial direction. Let the linac have peak-to-peak voltage V_L, wavelength λ_L, and velocity v_L. The linac creates the axial potential energy surface $U_L(x,t)$ where x is distance in the axial direction and t is time. Let p_L be the distance between linac electrodes (the pitch); we must have $p_L < \lambda_L/2$ by the Nyquist theorem, and preferably $p_L < \lambda_L/4$. Let E_{Lmax} be the maximum electric field (because the electrodes are discretized, E_{Lmax} varies between V_L/p_L and $V_L/2p_L$ throughout a linac cycle). Let the particles have some mass m, diameter d_p, and charge q, and let the background buffer gas have pressure P (and temperature T, gas molecule mass m_g).

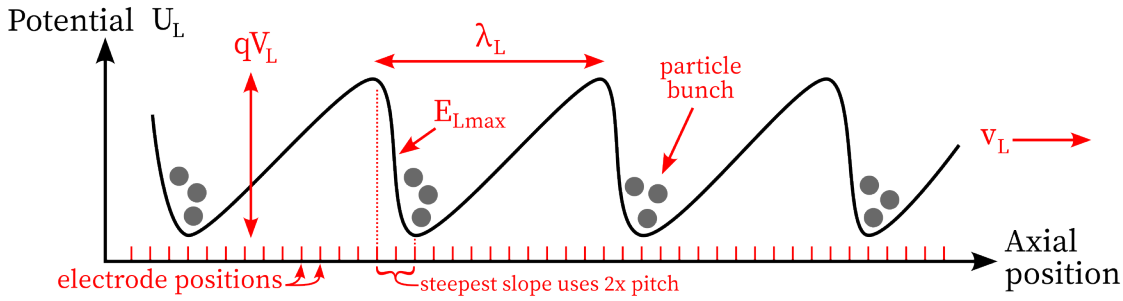

Figure 6.14: An annotated diagram of the linac potential waveform. This is a traveling wave of height $U_L = qV_L$, wavelength λ_L, and velocity v_L, created by electrodes at discrete positions. To maximize the force pushing particles to the right, we maximize the steepness of the left side of the well, which we do by making a sawtooth wave instead of simple sinusoid. Electrode discretization means it is more reliable to form the slope from twice the electrode pitch instead of over one. A beam separates into groups of particles, called bunches.

The behavior of our linac is somewhat complex and unique (particle accelerator linacs typically operate without buffer gas and with beam acceleration, not at constant velocity), but initial analysis and simulations lead us to hypothesize it can be roughly[47] described with the following three nondimensional parameters, which we name A_L, B_L, and C_L.

First, note that particles are pushed along by the linac with a maximum force of qE_{Lmax} and also experience gas drag; they will move as long as the former is greater than the latter. This is the same setup as drift velocity in section 6.4.1. We can express this with nondimensional parameter A_L, the ratio of maximum axial electrostatic force to gas drag at linac velocity v_L, and say that a linac and particle function as long as $A_L > 1$.

$$A_L > 1 \quad \text{where} \quad A_L = \frac{qE_{Lmax}}{\beta v_L} = \frac{qE_{Lmax}}{v_L} \cdot \left[\frac{8+\pi\varphi}{12} \sqrt{\frac{2\pi m_g}{k_B T}} P d_p^2 \right]^{-1} \tag{6.14}$$

If $A_L < 1$, then the linac force is insufficient to move the particle at the linac velocity, and the particle will never move with the linac. It will instead be briefly accelerated by one side of a linac well as it passes, then decelerated by the other, resulting in oscillatory movement and minimal net velocity. Fortunately, A_L can be made arbitrarily high by minimizing the

[47] We suspect this is close but not quite a complete parametrization; we leave confirmation to future work.

electrode pitch to maximize E_{Lmax} (though this requires more electrodes) and by minimizing pressure (though this increases C_L below and also quadrupole focusing time).

We can use A_L to see how fast a linac can be. From table 6.6, find a maximum particle drift velocity in an electric field of 100 V/100 mm, then note that increasing the field to E_{Lmax} in a linac will scale the velocity proportionally. For example, a singly-charged 10 nm particle has a drift velocity of only $13.2\,\mathrm{m\,s^{-1}}$ in a 100 V / 100 mm field at 0.1 Torr but can move 100x faster at $1320\,\mathrm{m\,s^{-1}}$ if the field is applied over only 1 mm. This is close to reaching the upper half of the $100\,\mathrm{m\,s^{-1}}$ to $3000\,\mathrm{m\,s^{-1}}$ impact velocity range we want.

However, there is a second more subtle requirement that applies to only a subset of particles. If a particle is already within the potential well of a linac at the correct velocity, the A_L parameter is sufficient to describe its behavior. But a particle at a different velocity, or not in phase with the linac, will skip between potential wells until it slows down and is kept within a bucket by gas damping, and careful analysis shows this is only possible if a single linac bucket has enough potential energy to accelerate the particle from zero to linac velocity[48]. We define the second nondimensional parameter B_L to be the ratio of potential energy of a single linac well (the particle charge times linac amplitude) to the kinetic energy of a particle traveling at linac velocity. This is often a stricter limit than A_L.

$$B_L > 1 \quad \text{where} \quad B_L = \frac{2qV_L}{mv_L^2}. \tag{6.15}$$

	$q = 1e$	$q = 2e$	$q = 5e$	$q = 10e$	$q = 20e$
1 nm	$2610\,\mathrm{m\,s^{-1}}$	$3700\,\mathrm{m\,s^{-1}}$	-	-	-
10 nm	$82.6\,\mathrm{m\,s^{-1}}$	$117\,\mathrm{m\,s^{-1}}$	$185\,\mathrm{m\,s^{-1}}$	$261\,\mathrm{m\,s^{-1}}$	$370\,\mathrm{m\,s^{-1}}$
100 nm	$2.61\,\mathrm{m\,s^{-1}}$	$3.7\,\mathrm{m\,s^{-1}}$	$5.84\,\mathrm{m\,s^{-1}}$	$8.26\,\mathrm{m\,s^{-1}}$	$11.7\,\mathrm{m\,s^{-1}}$

Table 6.7: The maximum velocities of linacs that accept all input particles of some mass and charge ($B_L > 1$) at $V_L = 100$ V, assuming copper. Small particles have a maximum charge; see chapter 5. This is one of the major restrictions to how good a linac can be: even if reaching higher velocities is possible according to the A_L parameter, such a linac would require incoming particles to be presorted into bunches, which is tricky to implement.

This parameter is somewhat optional for a linac depending on desired behavior. Assuming $A_L > 1$ (or else nothing works): when $B_L \gg 1$, all particles no matter their initial conditions will eventually travel with the linac (for gas drag will bring any particle to zero velocity, from where the potential well is strong enough to accelerate it). When $B_L < 1$, particles in an increasingly smaller window of initial parameters will travel with the linac (but, importantly, the well of a linac can still provide enough energy to speed a slightly slower particle up to

[48]This is approximately because gas drag will slow a particle of any initial velocity to between 0 and v_L, at which point if a particle isn't caught by the crest of one bucket, it slips to the next bucket where it is pushed backward an equal amount by the opposite side, making it oscillate back and forth with little net motion. It can be helpful to analyze this in a reference frame moving at velocity v_L.

linac velocity). This means it is possible to create a linac that moves at higher velocities ($B_L < 1$ and $A_L > 1$) if particles are pre-bunched and fed to the linac at the right time.

We define the final linac parameter C_L to be the ratio of total linac length L to the stopping distance S of a particle in buffer gas (equation 4.14) at linac velocity v_L.

$$C_L \gg 1 \quad \text{where} \quad C_L = \frac{L}{S} = \frac{L}{\tau v_L} = \frac{L\beta}{m v_L} \tag{6.16}$$

When C_L is high (perhaps $C_L > 3$), gas drag has time to make particles reach steady state equilibrium with the linac, making it work as desired according to A_L and B_L parameters. But when C_L is low (perhaps $C_L < 3$), gas drag will not have time to equilibrate particle motion to the linac, so final particle velocities will be far from steady-state (i.e., potentially an unexpected wide range of velocities). This mainly determines linac length.

What can we conclude from this?

It seems like a linac does what we want, allowing us to axially move particles with a range of mass/charge ratios to a very specific (possibly adjustable) velocity v_L we choose. This can reach higher velocities than simple DC acceleration, which is helpful since DC acceleration's drift velocity was a bit low for us. However, it is not a panacea: table 6.7 indicates that high-velocity linacs (perhaps $1000\,\mathrm{m\,s^{-1}}$ to $3000\,\mathrm{m\,s^{-1}}$) require careful particle control, and the requirement to separate a particle beam into bunches will also reduce the total particles throughput which we will see strongly limits printing speed (section 6.5.3). Whether a linac is worthwhile depends on the circumstance.

Although our linac differs from standard particle accelerator linacs[49] [296], it is not entirely dissimilar to existing ideas. Particle accelerator RFQ beam coolers can often apply configurable DC biases to their segmented quadrupole electrodes, and they use this (a "buncher") to make bunches of particles [357][364][362][356][387]. Traveling wave ion mobility spectrometry uses buffer gas with a very similar axial field to our linac [388][389] but operates in the $A_L < 1$ regime specifically so different size particles travel at different velocities (see [390] for experimental measurements showing the $A_L \approx 1$ boundary).

There is one more use for these techniques: a linac[50] can precisely move particles at slower speeds, possibly as a better-controlled alternative to the gas drag particle transport methods we studied in chapter 4. Using traveling waves to move charged particles has been suggested as an "electric curtain" [391][392][393] for purposes including cleaning dust off solar panels [394]. This (when more controlled) is also the standard approach to moving particles around trapped-ion quantum computers [395][396][397][398], and particles can be moved not only in a single line but through junctions [399][400][401][402][403], allowing particles to traverse a 2D (or 3D [404]) grid. This has also been used to move molecules for ion mobility spectrometry [390][405][406][407][408][409][169]. In other words, electrostatic manipulation can be used for general handling and sorting of particles[51], not just for focusing and acceleration.

[49] Though some similarities exist: linacs in vacuum still have phase stability; particles stay in buckets [296]. It is also possible to accelerate nanoparticles with such a high-vacuum linac [157].

[50] We could also use the ponderomotive force in the axial direction, but the complexity is unnecessary.

[51] This might be useful for switching between different materials while printing.

6.5 Complete Electrostatic Focusing Systems

At long last (over 20 pages later!) we finally have everything we need to solve the focusing problem posed in section 6.1. Recall our goal is to move charged nanoparticles, which begin with some initial positions and velocities, onto a substrate in a narrow beam (near 1 µm wide) and at high impact velocities ($100\,\mathrm{m\,s^{-1}}$ to $3000\,\mathrm{m\,s^{-1}}$), as quantified in tables 6.1 and 6.3. If we accomplish this, we will have found the last part of a printer hopefully capable of printing useful multimaterial nanoscale semiconductor devices.

In section 6.5.1, we will describe and simulate an example system capable of printing 10 nm particles with $< 5\,\mu\mathrm{m}$ resolution at $> 1000\,\mathrm{m\,s^{-1}}$ and make some notes on how it would be physically constructed and how resolution could be improved to $< 1\,\mu\mathrm{m}$ or better. We will follow this with more general remarks on printing particles electrostatically.

6.5.1 A Proof-of-Concept Focusing System and Beyond

There are multiple ways to combine our previously-discussed electrostatic manipulation components to solve the focusing problem, but to give a concrete working example we designed a particularly minimal and straightforward configuration. We focus particles in a quadrupole with buffer gas as per section 6.3.2, but since a single quadrupole is insufficient to focus all the way (see table 6.4), we add a second quadrupole to further focus the output of the first. To move particles axially, we choose to use segmented quadrupoles with DC fields (section 6.4.1) because a linac (section 6.4.2) is tricky to implement, then accelerate particles to high velocities right before impact with the substrate via an extremely high DC field.

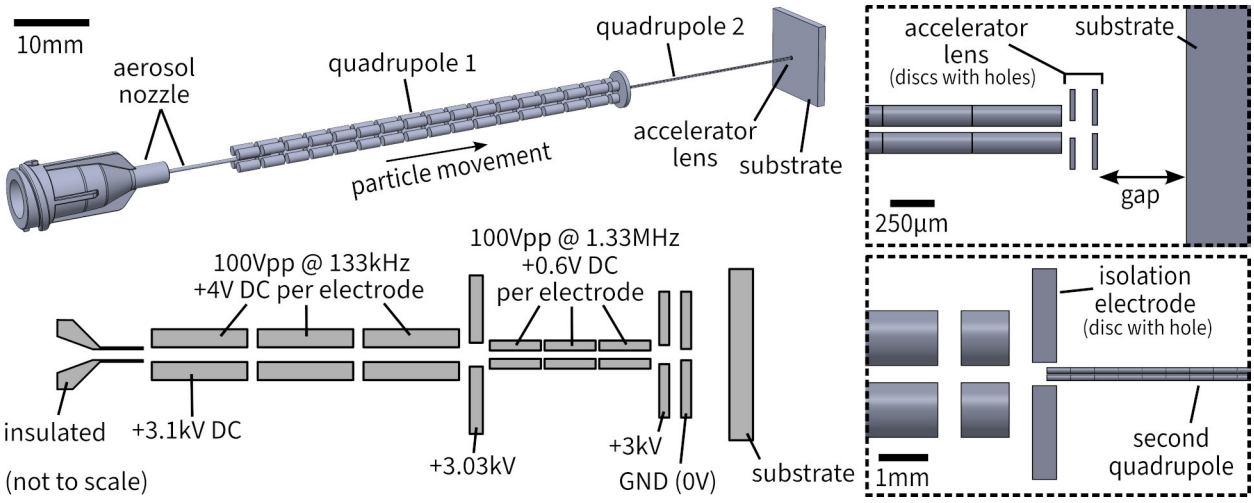

Figure 6.15: A (simulated) working electrostatic focusing system that prints 10 nm $q = +10e$ nanoparticles with $< 5\,\mu\mathrm{m}$ resolution at $> 1000\,\mathrm{m\,s^{-1}}$. If built, this could be inserted into an existing aerosol deposition system (figure 6.18). Bottom left: a schematic (not to scale) of the system, which has two quadrupoles and a DC accelerating lens just before the substrate. Top left: a 3D render (to scale) of the system. Top right: close-up cross-section of geometry near substrate. Bottom right: close-up of junction between quadrupoles.

The resulting structure is extremely compact: only 75 mm long and below 5 mm in diameter. Particles can be injected via aerosol nozzle (another 25 mm long). The main trick this design uses is allowing low particle velocities in the quadrupoles to maximize focusing time while minimizing pressure, then using high voltage (avoiding breakdown via low pressure and small size) to accelerate particles right before impact with a simple DC accelerator lens. This lens is subject to the emittance theorem but only accelerates axially without focus, avoiding issues. We accept the chromatic aberration (velocity variation). The particles travel 0.5 mm between the final lens and substrate (making resolution only 1.3 µm worse by equation 6.11).

We designed each quadrupole by choosing their voltage V_T and initial particle beam radius then making the trap radius R_T slightly larger. This combined with particle characteristics determines trap frequency (equation A.6) and minimum beam diameter (equation 6.6). We used a frequency 1.6 times minimum to allow a range of particles (8 nm to 12 nm) at some resolution cost. We chose buffer gas pressures[52] high enough to focus quickly yet low enough (< 1 Torr) to allow high voltage acceleration without breakdown. Segmented electrodes apply an axial field high enough such that the particle stopping distance is longer than the junction between quadrupoles. An isolation electrode between the two quadrupoles prevents their waveforms interfering with each other. We ended up with the following parameters:

	Quadrupole 1	Quadrupole 2
Quadrupole radius R_T	0.5 mm	50 µm
Quadrupole length L_T	50 mm	25 mm
Voltage V_T	100 V	100 V
Frequency $f = \omega/2\pi$	133 kHz	1.33 MHz
DC acceleration voltage V_{DC}	64 V (over 50 mm)	30 V (over 25 mm)
Buffer gas pressure P (argon)	0.5 Torr	0.4 Torr
Drift velocity $v_{a,drift}$	34 m s^{-1}	40 m s^{-1}
Stopping distance S	15.5 mm ($v_0 = 200$ m s^{-1})	3.3 mm ($v_0 = 34$ m s^{-1})
Input beam diameter d_B	0.21 mm	23 µm (quad 1 output)
Output beam diameter d_{Bquad}	23 µm	2.3 µm

Table 6.8: Operating parameters of the two segmented quadrupoles. Calculated for 10 nm $q = +10e$ copper particles (with $f = 1.6 f_{min}$ to allow 8 nm to 12 nm particles).

After focusing, the particles accelerate through two electrodes (an immersion lens) with a 3 kV DC voltage chosen to reach > 1000 m s^{-1} as approximated by $v_a = \sqrt{2qV/m}$ (section 6.4.1). Building this requires avoiding gas breakdown due to high voltage (section 6.3.2), but our 0.4 Torr pressure and the 100 µm electrode separation can probably suffice[53] (table 2.4). To avoid having to charge the substrate (section 6.3), the final electrode is grounded and the quadrupoles are raised to progressively higher voltages. The input aerosol nozzle can be electrically insulated, moving particles into the quadrupole via drag even when the main printer chamber is grounded. There would also be a cylindrical shield (not shown) around the entire focusing mechanism to prevent gas breakdown around its outside.

[52] The 0.5 vs. 0.4 Torr pressure difference is unnecessary but demos differential pumping (chapter 4).

[53] [355] confirmed 10 kV across a 150 µm gap between steel electrodes at < 0.5 Torr can avoid breakdown.

To demonstrate functionality, we used SIMION (section 6.3) to simulate motion of 8 nm to 12 nm particles through the focusing system (without Brownian motion; see section 6.3.2. Our conclusions should be unaffected). Due to software limitations, we simulated the two quadrupoles separately then merged the results to create the following graphs.

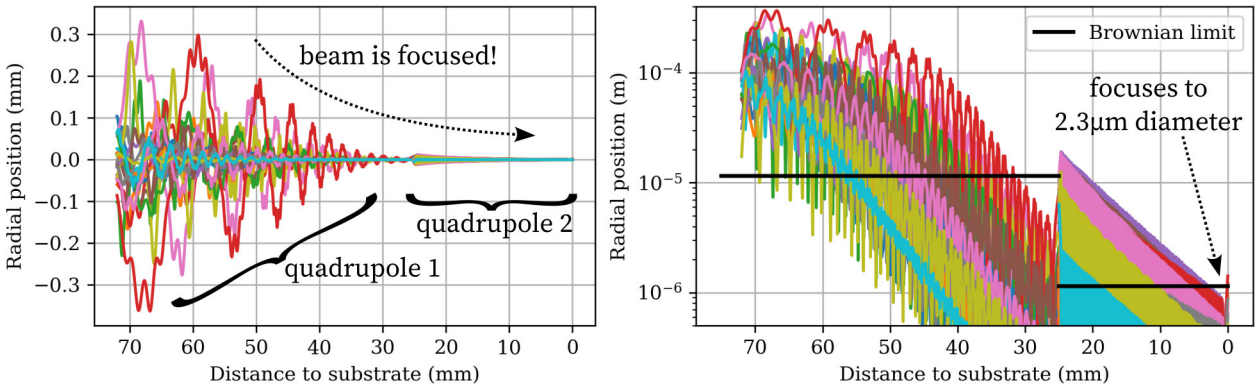

Figure 6.16: Left: nanoparticle radial positions as they are focused while moving toward the substrate. When entering a quadrupole and before focusing, note the beams briefly expand (beyond the simulation starting diameters of 0.21 mm and 23 µm from table 6.8) due to radial velocity and RF heating (section 6.3.3). Right: the same graph with a logarithmic scale. The Brownian limit is the realistic final beam diameter given by equation 6.6; our simulation unrealistically does better but would match this if simulating Brownian motion.

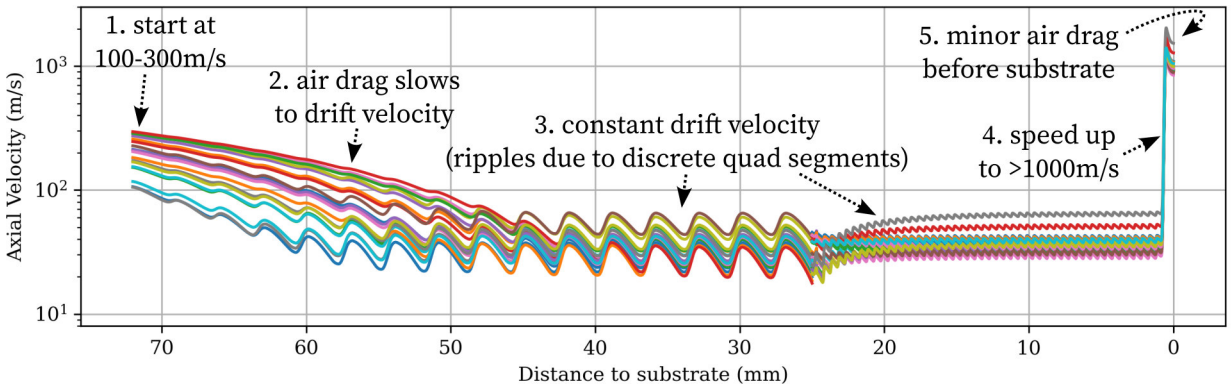

Figure 6.17: Axial velocity of particles as they move toward the substrate. They begin at the 100 m s^{-1} to 300 m s^{-1} we estimate our aerosol nozzle outputs (see chapter 4) but are quickly slowed down by air drag until DC acceleration plus drag (section 6.4.1) moves them at constant slow velocity through the quadrupoles. The final acceleration is nearly instantaneous and lets particles reach 1000 m s^{-1} to 2000 m s^{-1} (depending on mass/charge ratio—this is the chromatic aberration that a linac can improve upon). Finally, particles slow down slightly due to drag while traversing the gap before hitting the substrate (assuming 0.4 Torr). This could be reduced by minimizing the distance to or pressure at the substrate.

These simulations confirm the system works like we expect! In the radial direction, particles are focused by the first quadrupole, then focused further by the second. The final diameter of the particle beam is less than 5 µm wide. Axially, particles reach a slow 40 m s^{-1} drift velocity as they move through the quadrupoles then are accelerated to over 1000 m s^{-1}. Experimental confirmation will have to wait, as previously noted, until we have built a nanoparticle charger (see chapter 5). But a complete nanoparticle printing system should be straightforward to construct: we simply add our focusing system into our aerosol printer from chapter 4.

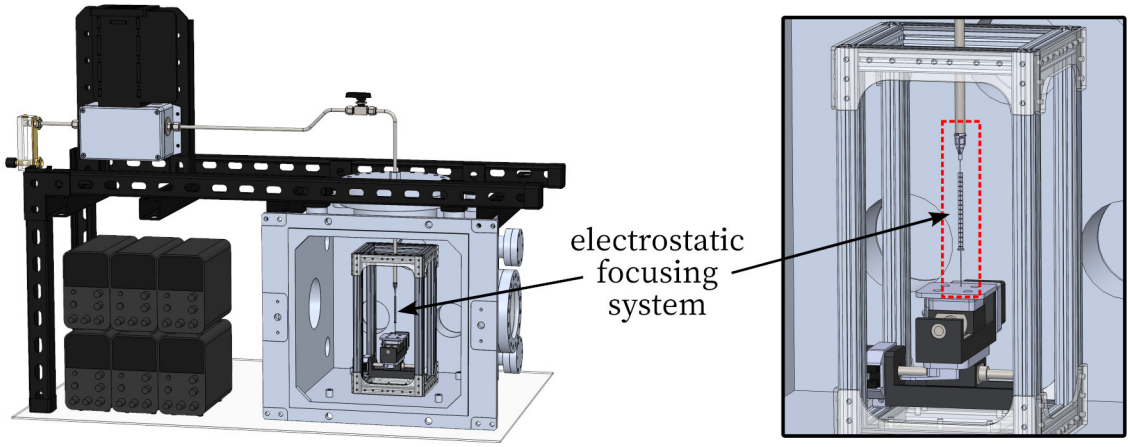

Figure 6.18: Left: render (not yet physically built) of what a complete nanoparticle printer with electrostatic focusing might look like. This is the aerosol printer of chapter 4, but as proposed in section 6.1, we have moved the aerosol nozzle away from the substrate to add our proof-of-concept focusing system. The only major missing component is a nanoparticle charger, which could be included as noted in chapter 5. Right: zoomed-in view.

Implementation Concerns

How can we manufacture the focusing system, given that it has extremely tiny electrodes and complex electrical waveforms (figure 6.15)? Regarding the mechanical construction, the smallest quadrupole has electrodes about 100 µm wide. If they are made rectangular instead of perfectly round (which can work; see appendix A), the electrodes could be traces on stacked printed circuit boards (PCBs); this works for other ion traps [410][411][408][409][412]. Alternatively, microfabrication MEMS techniques[54] can be used to build these electrodes; this too is somewhat common[55] [415][416][417][414][418][419]. A final (amazing) option is to realize the very device we are designing is capable of printing multimaterial structures at this size scale: we could use one nanoparticle printer to make parts [420] for another!

As for the electrical circuitry, our challenge is to apply hundred-volt waveforms to electrodes, which act as small capacitors (our quadrupole electrodes are low picofarads while significantly larger ion traps might have nanofarads of capacitance). The waveforms are

[54] I (the author) previously built a MEMS device of similar 100x10 mm size for an unrelated project [15].
[55] This is how the trapped ion quantum computers mentioned in appendix A are built [413][414].

sinusoids for the quadrupoles (where frequencies, typically 1 kHz to 10 MHz, depend on trap geometry and need to be adjusted further to suit different particle mass/charge ratios (section 6.3.2 and equation A.6), plus a DC potential (for DC acceleration, section 6.4.1) or possibly even a sawtooth wave for a linac (section 6.4.2). Many quadrupoles in the literature only require a single-frequency sinusoid ("RF" for radio frequency) with DC bias, which is most easily achieved with a resonant LC circuit to generate RF[56] while the DC bias is provided either by applying the RF to one pair of quadrupole electrodes and the DC to the other [424] or by combining the DC and RF with capacitive or inductive coupling [376][357][364][411]. An interesting alternative is to drive quadrupoles with a rectangular wave with precisely-controlled duty cycle [425][375][426][427]. This is called a digital ion trap. The electronics (fast high-voltage switches) can be simpler and easier to adjust than an LC resonator [428][429][430][431][432]. The performance can be comparable to a sinusoid-driven quadrupole [356][433] though the analysis is slightly more complicated [434][435][436].

For our electronics, because our analysis so far has used sinusoids, we made a preliminary investigation of circuits to generate adjustable-frequency sinusoids (via arbitrary waveform generation) in appendix C with promising results. It seems feasible to build cheap circuits that will generate arbitrary trap frequencies with DC offsets (or linac waveforms), which may be useful when printing nanoparticles of different sizes and charges. We also discussed the tens of electrodes that might be required[57]. See appendix C for more detail.

This is a point worth repeating: by adjusting the trap frequency and DC acceleration voltage, the same focusing system should be able to handle a range of particle mass/charge ratios (one at a time). The focusing (equation 6.6) is somewhat independent of particle mass/charge so long as the frequency (equation A.6) is set correctly. This means we should be able to print multiple materials sequentially (as we did in chapter 4) without major problems.

Further Improvements

Although we've shown a way to print particles at $< 5\,\mu m$ resolution with velocities spread between $1000\,m\,s^{-1}$ to $2000\,m\,s^{-1}$, this is not quite as good as the specifications we originally hoped for in tables 6.1 and 6.3 (namely, $< 1\,\mu m$ resolution and velocities with only $\pm 10\%$ variation). But we suspect reaching (and exceeding) these specifications is possible.

Improving resolution is most easily done by making a smaller quadrupole (perhaps a third stage) or raising quadrupole voltage, ultimately limited by equation 6.6 (table 6.4)—which suggests the theoretical possibility of sub-100 nm resolutions, at which point the finite size of the nanoparticles starts to be a limit to resolution! It is also possible that an Einzel lens, though not extremely effective due to chromatic aberration, still helps a small amount (perhaps we use the accelerating lens to focus slightly). Given how close we are already ($< 5\,\mu m$) and the lack of fundamental barriers, we suspect sub-1 µm can be obtained without

[56] Microfabrication plasma tools rely on similar resonant circuitry to generate RF signals, but typically at higher voltage and power specifically to generate a plasma via gas breakdown (unlike us) [421][422]. This is often at 13.56 MHz within an ISM frequency band so legal RF emission regulations are less strict, but some tools (e.g., pulsed DC sputtering) use lower kilohertz frequencies [423].

[57] Our example system of figure 6.15 has 256 separate quadrupole electrodes, though since the two diagonals of a quadrupole are symmetric only $256/2 = 128$ separate signals are required.

too much more effort (in fact, if layers are printed with a 10:1 width:height aspect ratio as in chapter 4, we can print sub-micron layer thicknesses already). Reaching 100 nm is more difficult but surprisingly not out of the question.

We might add other electrostatic manipulation methods. Velocity variance can be reduced[58] with a linac. It might be possible to combine the multiple quadrupoles by tapering them if their different frequencies can be reconciled; tapered non-quadrupole ring geometries exist as ion funnels [218][412][411][437][432]. We could consider reducing the buffer gas throughout the focusing system (via differential pumping) to allow higher voltages at its end.

Better computer simulation may help design these improved focusing systems. Our own simulation neglected Brownian motion, modeled each quadrupole separately, and ignored space charge. While we think our analysis, which instead relied on analytical approximations, is generally correct, a better simulation could model the Brownian-dependent output beam diameter to confirm printing resolution. Even more useful would be computer optimization of electrode geometry [305][403][401] which can find ways to deform electrodes to improve performance (tapered quadrupole ends might better capture incoming particles [364]). Finally, a boundary element method simulation may be more accurate than the finite difference method SIMION uses [438][439].

In conclusion: it seems likely electrostatic focusing will work well, which means a complete multimaterial nanoscale printer is feasible! Our proof-of-concept electrostatic focusing system already definitively beats aerosol deposition, which cannot simultaneously reach high resolutions and high speeds, especially for smaller nanoparticles (see section 4.2.1). We are ready to make some final notes on electrostatic printing in general.

6.5.2 Managing Deposited Charge

There is an issue with electrostatic particle printing we have neglected to mention so far. When a charged particle is printed on a substrate, because like charges repel, it will deflect additional particles from being printed there. This will decrease resolution or, in the extreme, might even prevent new particles from sticking at all, stopping the print.

We know this will be a problem because it occurs elsewhere. This has been studied directly [290], was used (to beneficial effect) to pattern charged nanoparticles with an insulating mask [63][68], might occur inside aerosol tubing (chapter 4), and is a known effect in scanning electron microscopy and lithography where electrons build up on insulating surfaces and repel further electrons [440], decreasing image resolution (or they attract positively-charged nanoparticles as xerography [69]). It is also known that in ion traps (like ours), charge tends to build up on any insulating surface and deflect particle trajectories, so we should build our focusing system with only conductive exposed surfaces [416][415][441].

The easiest solution would be for the substrate (and the part we are printing) to be conductive so electrons can move through it to neutralize built-up charge. However, we are very explicitly

[58] A simple mechanical mechanism [159][152] or electrostatic field (Wien filter) can filter particles by velocity, but this wastes particles just like an aperture does to improve position resolution.

hoping to print electrical circuits, which need insulation between conductors, and MOSFET transistors, which have charge-sensitive insulators[59]. We need a more general approach.

The ultimate solution may be to actively neutralize charges[60] as they are printed. Reviewing the charging methods listed in chapter 5, note electrons can be generated[61] with field or thermionic emission then impacted into nanoparticles after focusing and either before or after collision with the substrate. This is especially elegant as electrons are attracted to the positively-charged particles. This can occur in the gap between focusing system and substrate (0.5 mm long in our example system), which can be at sufficiently low pressure to allow electron travel. This may require careful engineering but seems physically feasible.

6.5.3 Printing Speed Limits

So far we have discussed almost exclusively the problem of moving nanoparticles with high resolution and velocity so we can make semiconductor devices. But there is another practical limit: how fast is printing? A slow fabrication process might be uneconomical even if it is otherwise easier than microfabrication. For example, focused ion beam induced deposition (FIBID, chapter 1 and section 6.5.4) is so slow that it is used only in rare circumstances.

It is easy to compute a maximum limit on printing speed that depends little on the other complexities we just discussed (or even electrostatic vs. aerosol focusing).

To calculate a maximum printing speed, the crucial realization is that particles can impact the substrate at up to a maximum velocity (as according to chapter 3, higher velocities will vaporize a particle and leave an impact crater instead of the desired deposition), and this applies a speed limit to everything else.

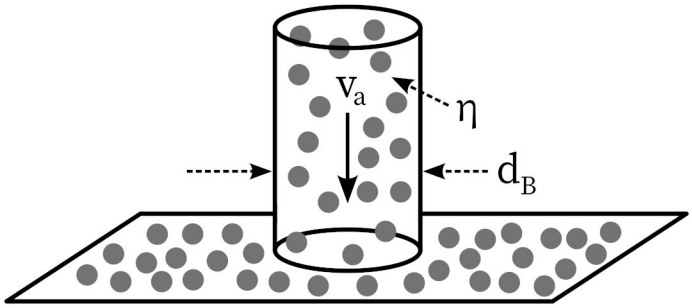

Figure 6.19: A cartoon illustrating a particles in a beam of diameter d_B being printed onto a substrate. The particles move at velocity v_a and fill a fraction η of the beam volume.

Consider a focused nanoparticle beam of diameter d_B impacting a substrate, which is scanned in the XY plane to produce a pattern. d_B is limited because we want the printer to have high resolution (for example, printing a 1 µm wide line requires $d_B \leq 1\,\mu m$). The particles

[59] Charges trapped in the gate oxide of a MOSFET during fabrication change its threshold voltage [1].
[60] For prior art, see [177] which neutralizes argon clusters via diffusion (dis)charging.
[61] We might use a MEMS electron source to fit in the small gap before the substrate [442][443].

travel at velocity v_a, which chapter 3 suggests is at most $1000\,\mathrm{m\,s^{-1}}$ to $3000\,\mathrm{m\,s^{-1}}$. Finally, particles in the beam[62] don't touch; they fill some fraction of the beam volume for which we use the variable η (an efficiency). The maximum ($\eta = 1 = 100\%$) means there is no space between particles and the beam is a solid cylinder, which doesn't work, of course. It is not immediately clear what a reasonable upper bound to η should be[63], but if we choose 0.1%, we can compute a possible upper value for print speed. Calculate the volume of material printed onto the substrate per unit time, the volumetric flux Q, to be

$$Q = \frac{\eta\, v_a\, \pi\, d_B^2}{4}. \tag{6.17}$$

For example, printing with $d_B = 1\,\mu\mathrm{m}$ resolution, $v_a = 1000\,\mathrm{m\,s^{-1}}$, and our hypothetical $\eta = 0.001$ deposits $Q = 7.9 \times 10^5\,\mu\mathrm{m}^3/\mathrm{s}$. If we tried to print an integrated circuit with 10x10x0.01 mm volume[64], the total print time is $1273\,\mathrm{s} = 21\,\mathrm{min}$. Printing with a smaller 100 nm beam is much slower: $Q = 7900\,\mu\mathrm{m}^3/\mathrm{s}$, so that chip would take 35 hours to print. Contemporary state-of-the-art CPU, GPU, and memory chips have 10 nm features requiring another 100x time increase and months per chip, which seems impractical.

But this used a hypothetical value for η. How close to this can we actually get?

We previously calculated two other speed limits we can compare against: the rate we can produce nanoparticles and the space charge limit to fitting particles in a beam.

In chapter 2 (and confirmed in chapter 4), we found we could make particles at $0.6\,\mathrm{mg\,h^{-1}}$ to $6\,\mathrm{mg\,h^{-1}}$, which is a volumetric flux (for copper) of $Q = 1.9 \times 10^4\,\mu\mathrm{m}^3/\mathrm{s}$ to $1.9 \times 10^5\,\mu\mathrm{m}^3/\mathrm{s}$, which is similar to Q with our hypothetical $\eta = 0.001 = 0.1\%$. We can make slightly faster nanoparticle sources (e.g., by combining multiple), so it seems nanoparticle generation will not be a strong limit to print speed[65], at least at these small resolutions.

Space charge limits (section 6.3.3) are stricter. Equation 6.9 approximates the number flux N' (particles per second) of particles with charge q that can be contained at velocity v_a in beam diameter d_B in a quadrupole of voltage V_T and radius R_T. We can use this to calculate the volumetric flux limit due to space charge Q_{SC} for particles with diameter d_p as

$$Q_{SC} = N' \cdot \frac{4}{3}\pi \left(\frac{d_p}{2}\right)^3 < \frac{V_T \pi \epsilon_0 v_a d_B^2}{8 q R_T^2} \cdot \frac{\pi d_p^3}{6}. \tag{6.18}$$

This volumetric flux scales with the cube of particle diameter, which is the quantitative explanation for why using large nanoparticles (and low charge) instead of single atoms as first described in chapter 2 makes printing faster: we print more atoms per unit charge

[62] Notice we're printing many small particles—billions per second—randomly inside a larger beam. This is because the nanoparticle size (1 nm to 50 nm diameter) is much smaller than the resolution we can place them with (perhaps 1 µm), but it is also convenient because it allows us to treat the entire process statistically. This helps when, for example, nanoparticles have some variance in diameter and charge.

[63] Randomly tightly packed spherical particles fill about $\eta = 64\%$ of a volume [444], but the movement of particles during focusing probably requires η to be much lower (say, $< 1\%$).

[64] As noted in chapter 2, this is typical. Chips made with the SkyWater SKY130 130 nm process are 12 µm of transistors and wiring atop a silicon substrate [139], and most chips are several millimeters on a side.

[65] This means we can afford to filter nanoparticles to reduce size variation as proposed in chapter 2.

(see table 2.1). For a specific value, our example focusing system in section 6.5.1 has (in the second quadrupole[66]) $d_B = 5\,\mu m$, $V_T = 100\,V$, $R_T = 50\,\mu m$, $v_a = 40\,m\,s^{-1}$, $q = 10e$, and $d_p = 10\,nm$, giving $Q_{SC} = 45\,\mu m^3/s$ (and $\eta = 5.8 \times 10^{-8}$). This is very slow: that 10x10x0.01 mm example chip would take two thirds of a year to print! A straight line 5 µm wide and 500 nm tall would be printed at only $20\,\mu m\,s^{-1}$. This is on the edge of impracticality. It is immediately apparent that space charge is likely the greatest limit to print speed.

We can increase the speed to reach reasonable rates as follows. First, we could consider using larger nanoparticles. Since $Q_{SC} \propto d_p^3$, doubling nanoparticle diameter to 20 nm gets us 8x faster speed (though we need to carefully consider drift velocity and the final acceleration voltage); reducing particle charge q helps but not as much and makes focusing worse. We can also consider increasing particle velocity through the quadrupoles (perhaps with a linac, though this makes space charge worse; in a linac particles occupy the same radial distance as a continuous beam but only in discrete axial bunches), or optimizing quadrupole electrode radius R_T and increasing voltage V_T.

(We could also consider neutralizing the space charge (though the complexity means we will leave it to future work) [445][446][447][448][449] by engineering a situation where free negative charges coexist in the same area as our positive nanoparticles. This is most common in particle accelerators where an oppositely-charged background plasma offsets the space charge of a beam [296]. Alternatively, there has also been work on trapping (appendix A) and focusing neutral atoms [450][451][452].)

Another promising method is to actively vary the beam diameter d_B to print small features with high resolution but larger features more quickly with lower resolution, much like the front-end-of-line (FEOL) vs. back-end-of-line (BEOL) divide in microfabricated chips.

Finally, we could consider having multiple focusing systems printing particles in parallel[67]. We could fit an array of tens of our example focusing system over a 10x10 mm chip, although this proportionally increases engineering complexity.

Each of these methods—larger particles, resolution variation, and parallelism—can add an order of magnitude improvement in speed. Together, we think it is possible to bring the total realistic volumetric flux back up to at least $5 \times 10^4\,\mu m^3/s$, which prints our test chip in 6 hours. This is reasonable and comparable to how long macroscale plastic and metal 3D printers take to make objects. Still, speed issues will always be significant, and slower speeds at higher resolutions might limit us to large-feature-size chips (see also section 7.2.2).

Again: speed limits mean we can probably only print simple low-resolution chips, and each will take hours to days.

[66]The Child-Langmuir law [296] says particles of mass m and charge q accelerated from rest by a voltage V across distance L can create a maximum current density J (units A/m^2) of $J = 4/9 \cdot \sqrt{2q/m} \cdot \epsilon_0 V^{3/2}/L^2$. In our proposed system, this applies to the final accelerating lens but is less strict than radial space charge. It does not apply to drift motion in the quadrupoles, for which future work should derive a similar relation.

[67]Massively parallel electron beam lithography systems do exist and are used commercially to make EUV lithography masks (IMS sells a tool with 262144 separate beams [453]); the company Multibeam is commercializing a multi-column e-beam tool [454]. Multi-beam FIB has been considered but is tricky [455].

6.5.4 Is it Possible to Do Better?

Before finishing this chapter, we can check our work against existing electrostatic particle manipulation systems to help determine whether even faster and higher-resolution printing might be possible (or to confirm we have started to run against fundamental limits).

First we should compare our methods to focused beam tools, which work on similar principles. As briefly mentioned in chapter 1, this includes scanning electron microscopes (SEMs), which use beams of electrons, and focused ion beam (FIB) tools, which use positively-charged single atoms. Much like we do, these tools create charged particles than focus them with emittance-limited ion optics to affect a surface. Thorough study has found their resolutions are limited[68] usually around 1 nm to 10 nm by emittance, geometrical aberrations (including spherical aberration and astigmatism), chromatic aberrations, space charge effects, diffraction[69], and system imperfections [296][304][457]. We have already accounted for these for nanoparticles; our previous analyses appear to be sufficiently complete and we cannot do much better.

To achieve their highest resolutions, FIBs and SEMs use bright (equation 6.3) particle sources [458][459][456], preferably with low temperature[70] (equation 6.11). The majority of FIBs are somewhat limited in the materials their sources provide: most use a liquid metal ion source (LMIS) [304][464][465][466] that typically makes a high-velocity beam of gallium ions (Ga^+). This Ga^+ beam can etch material or its impact energy can induce material deposition from a precursor gas that floats around the substrate [457][75][467] ("focused ion beam induced depsition", "FIBID" [75] or "FIB-CVD" [467]). This can only print limited materials (mainly Pt, W, and SiO_2, but with Ga and C impurities [75]; not semiconductors). Our quadrupole setup could be called a high-brightness low-velocity multimaterial nanoparticle source.

Though uncommon, a FIB system can print its ions directly on a surface [468][469], like our printing but with atoms instead of nanoparticles. This needs a different ion source (e.g., Au instead of Ga) and the relatively slow impact velocity[71] makes it hard to focus [445][470][471]. Several prototypes printed lines of material [471][472][473] (including sub-micron resolution [470][472] and multimaterial printing [474]) and were explicitly proposed[72] for direct-write microfabrication [473][472][470], but it was concluded that space charge limits meant the process would be impractically slow [445][475][473] ([473][445][476] suggest print rates of $Q = 1\,\mu m^3/s$ and below). Today, this exists with wide beams as ion beam deposition (IBD) [477][478], while simpler FIBID (with Ga^+) found a niche for sample analysis despite similar slow speeds [476]. Our nanoparticle printing process is extremely similar to these approaches but, as shown in section 6.5.3, the use of nanoparticles instead of single atoms lets us print orders of magnitude faster, which is just barely enough to make the method practical.

We can now place our electrostatic nanoparticle printing method relative to other particle methods, FIB and aerosol deposition, to find it averages out the pros and cons of both. We may have found the Pareto-optimal regime for semiconductor device manufacturing.

[68] These limits can be elegantly graphed as curves on a beam angle vs. area (emittance) plot [313][456].
[69] Negligible for us; the deBroglie wavelength of a $1000\,m\,s^{-1}$ 10 nm Cu particle is only 1.4×10^{-16} m.
[70] Recent work studied laser-cooled ion sources [460][456] or cooled single atoms [80][461][462][463].
[71] Below about $50\,eV \approx 10\,000\,m\,s^{-1}$, since higher velocities etch instead of deposit (see chapter 3).
[72] First proposed perhaps by Feynman [16], who also explicitly called out space charge as a possible issue.

	Direct FIB	Nanoparticle printing	Aerosol deposition
Resolution d_B	$< 100\,\text{nm}$	$1\,\mu\text{m}$	$> 10\,\mu\text{m}$
Particle impact velocity v_a	$> 10\,000\,\text{m}\,\text{s}^{-1}$	$1000\,\text{m}\,\text{s}^{-1}$	$< 500\,\text{m}\,\text{s}^{-1}$
Volumetric print speed Q	$< 1\,\mu\text{m}^3/\text{s}$	$1 \times 10^5\,\mu\text{m}^3/\text{s}$	$\gg 1 \times 10^5\,\mu\text{m}^3/\text{s}$

Table 6.9: The (very approximate) specifications of our proposed electrostatic nanoparticle printing method compared to direct FIB deposition and aerosol deposition. Of the three, nanoparticle printing is the only one with resolution, impact velocity (chapter 3), and print speed (section 6.5.3) simultaneously suitable for semiconductor device fabrication.

This implies we may be close to the limits of not only electrostatic beam focusing but of any method that prints a beam of particles. And there are other reasons to suspect we can't do much better: for example, small particles (adatoms) can move around on the surface after impact (see chapter 3), making resolution likely at best on the order of 10 nm [43][171]. The fundamental limit becomes surface chemical reactions[73] (driven by kT thermal energy). We might hypothesize that manufacturing with even smaller resolutions approaching the atomic scale starts to require either lower temperatures or materials with more precisely arranged chemical (covalent) bonds, as done in synthetic chemistry and DNA nanotechnology.

To achieve higher manufacturing performance, future work might consider totally different approaches than particle beams. Standard microfabrication technically counts (though it has its own limits), or we could combine techniques ([480][481] propose aerosol deposition followed by FIB milling to increase resolution). More universally, recall that when discussing nanoparticle manipulation methods in chapter 3, we disregarded direct mechanical/chemical atomic-scale manipulation due to its complexity which makes engineering difficult. But this still holds promise[74], and if any system eventually supersedes both nanoparticle printing and microfabrication, this is likely where we would find it.

That is the end of this chapter and our analysis of electrostatic particle manipulation.

It seems electrostatic nanoparticle printing is likely to work. We proposed a concrete design and are ready to build a working implementation given a nanoparticle charger (chapter 5), after which many iterative improvements are available to increase performance (particularly resolution and speed)—and if there's one thing the microfabrication industry is good at, it's progressively improving a technology to its theoretical limits[75].

So we now finally have a nanoscale printer as proposed in chapter 1. But is it good enough to matter? Would this printing process achieve our goals of improving on microfabrication's speed, cost, or complexity? We will answer this at last in chapter 7.

[73] Photolithography also starts hitting limits near 10 nm due to photoresist molecular structure [479].

[74] This is roughly how biology works (in addition to all chemistry, of course).

[75] Keeping Moore's law [6] alive for sixty years by consistently improving photolithography and other microfabrication tooling to astounding levels is one of humanity's greatest technical accomplishments.

Chapter 7

Future Work and Implications

We've proposed a solution to our original problem: how to manufacture electrical devices more easily than with microfabrication. We found a new way to print multiple semiconductor materials by manipulating nanoparticles, and we know how to achieve nanoscale resolution via electrostatics. But did it work? Did we actually improve upon microfabrication?

7.1 Remaining Steps to Print a Transistor

We should first ask if nanoparticle printing can compare with microfabrication at all, and to do so we can consider the quintessential microfabricated device: the transistor. Can we print a transistor? We weren't quite able to in this dissertation, but we're probably close.

Recall this dissertation covered many subtopics, each progressing toward our ultimate goal. To understand this progress, we can draw out what we accomplished and what future steps are required to make a transistor.

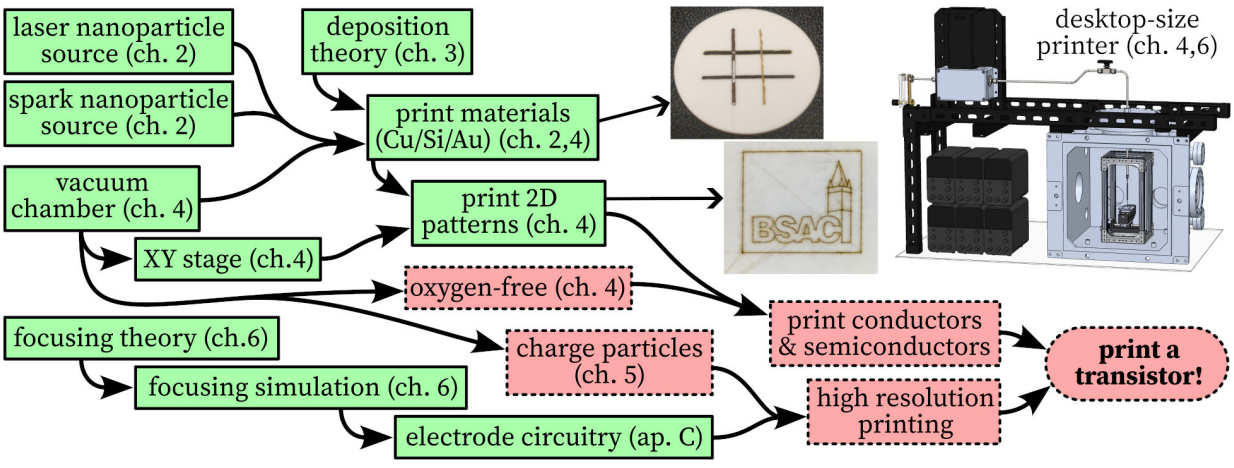

Figure 7.1: A dependency graph of what was accomplished in this dissertation (green, solid) and what tasks remain (red, dashed) before manufacturing standard semiconductor devices.

In the end, we made a number of important nontrivial advances but there are still several (small) steps left before we can print a transistor, though we think it is achievable.

In chapter 1, we made the simplification that transistors and other devices require multiple materials, each of precise atomic composition, combined with high 1 µm resolution. With the hypothesis that printing nanoparticles might achieve these requirements, we experimentally demonstrated multimaterial printing in chapters 2 and 4. Our use of aerosol focusing limited both resolution and material properties—chapter 3 suggested higher impact velocities were needed for materials to have electrically-useful crystalline structures. This inspired chapters 5 and 6, where we proposed an electrostatic focusing mechanism capable of both high $< 5\,\mu m$ printing resolution and also the high $1000\,m\,s^{-1}$ velocity we required with the theoretical possibility of future improvement. But along the way, we ran into two roadblocks:

- **Oxygen:** Residual oxygen inside the vacuum chamber stuck to nanoparticles, reacting with conductors and semiconductors to instead make insulators (e.g., Si became SiO_2). As discussed in section 4.3.3, this is a well-known effect easily solved with a better (albeit expensive) vacuum chamber.
- **Charging:** The methods of electrostatically moving particles to high resolution and velocity that we found in chapter 6 required the particles to be electrically charged. We were unable to build a UV charger in chapter 5, but it seems likely a future attempt can succeed; prior art already exists (section 5.4).

These two problems should be solvable with engineering effort. They are not fundamental limits, merely temporary slowdowns we did not have the time or funding to pursue within this dissertation. However, as a result of these problems, the most interesting electronic device we experimentally demonstrated was merely a barely conductive gold trace in section 4.3.3. Printing other conductive metals or semiconductors requires solving the oxidation issue, and printing materials with useful atomic structures and thus electrical properties requires solving charging to get high particle impact velocities.

But once these problems are solved, building a transistor might be as simple as printing layers of doped silicon, insulators, and metal wiring as in figure 1.1. In reality, since the atomic structure of printed materials varies with deposition conditions, experimentation is likely required to find what particle velocities and other conditions result in electrical properties suitable for a transistor—but this seems feasible, given prior art in chapter 3 was able to build semiconductor ohmic contacts and PN junctions [171][172][47].

We can now put this entire dissertation into perspective: we proposed a single tool, a desktop-size printer, to (sometimes) replace microfabrication. We are not the first to discuss such a paradigm—direct-write printing of semiconductors [19] has been proposed many times via aerosol deposition [60] or FIB [445][473]—but no other method has worked. Our approach might become the first to simultaneously achieve the high resolution, print speed, and material capability needed to make many semiconductor devices. This may be the first complete roadmap to general-purpose[1] nanoscale device manufacturing using similar materials but methods separate from standard microfabrication. But is this new method useful?

[1]Not including niche applications such as wide-area printing of polymer solar cells [482].

7.2 What if it Works?

Suppose future work follows through with the above roadmap and we obtain a functional nanoparticle printer that can make semiconductor devices. Does this matter?

Our original motivation for this project was improving on the high difficulty, cost, and time of microfabrication. While quantifying difficulty is somewhat subjective (though we posit using only a single tool removes much of the complexity of normal microfabrication), cost and time are quite computable as follows.

We will find nanoparticle printing might make prototyping of simple semiconductor devices significantly faster and cheaper, though microfabrication is still easily superior for mass production or high performance applications (such as computer CPUs and memory).

7.2.1 Cost Comparison

Although money is a very noisy metric, it can give a useful approximation of the overall difficulty of a manufacturing process, accounting for all materials, equipment, time, energy, labor, space, and other resources involved. How might the monetary cost of nanoparticle printing compare to microfabrication?

Item	Cost	Note
vacuum pump	\$3k	prices vary widely
vacuum chamber	\$15k	often custom-made
pulsed laser	\$3k	have recently decreased in price
tubing & fittings	\$3k	expensive to meet high-vacuum requirements
gas flow (MFCs, filters)	\$3k	
XY stage	\$5k	a DIY stage can fall below \$1000 [483]
electrode circuitry	\$1k	custom (e.g., appendix C)
material targets	\$1k	at most
computer	\$1k	for XY stage and system control
miscellaneous	\$5k	to reach a round number
Total	\$40k	approximately; can vary significantly

Table 7.1: Rough estimates for the components of a nanoparticle printer if purchased new. Actual price may vary significantly. The components in this dissertation were obtained used for perhaps 10x less, and certain additional components (e.g., a turbopump, loadlock, and integrated metrology equipment), if added, might increase the price up to 10x.

Both microfabrication and nanoparticle printing have two main costs: the manufacturing equipment (which is typically very expensive) and the materials the equipment makes chips out of. The materials are relatively cheap since chips and other semiconductor devices are physically very small, so in both cases the capital cost of the manufacturing equipment, amortized over all chips it builds, would be the majority of a single chip's cost.

Nanoparticle printing, unlike microfabrication, uses only a single vacuum chamber and may be able to do without a cleanroom or postprocessing steps[2]. The equipment cost is relatively low: merely the cost of a single printer, which we can estimate by summing its individual components in table 7.1 as below $100k.

Microfabrication equipment (as per section 1.1) consists of tens of separate tools, kept in a dust-free cleanroom, and the infrastructure to power them and safely handle large quantities of chemicals. This is much more complex to set up than a single printer. We can graph the historical cost of microfabrication fabs to find even minimal fabs[3] are multimillion dollar investments, one or two orders of magnitude more than a nanoparticle printer.

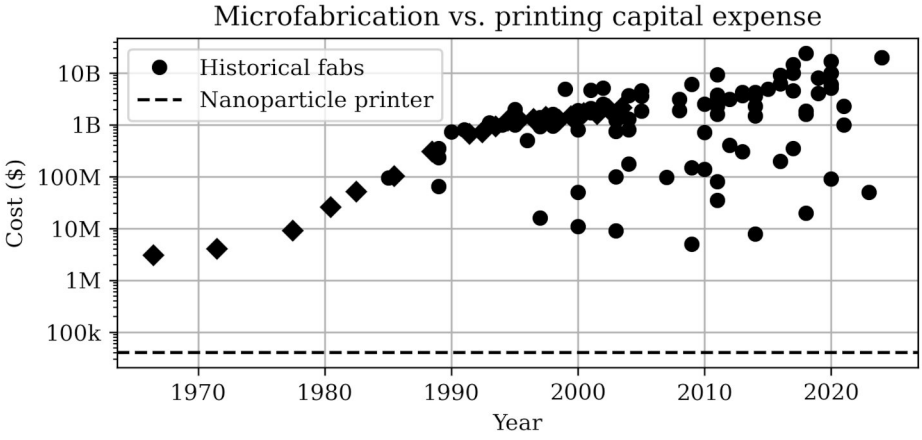

Figure 7.2: Some historical microfabrication fab costs from [9] (diamonds) and [484] (circles). Higher end fabs became more expensive over time to include tooling for higher perfomance chips, though they also increased throughput (via larger wafers [9]) so total cost per chip would not increase too much. The best comparison for nanoparticle printing are the cheapest earliest fabs at several million dollars—which we have still beat handily.

So if we want a minimal system capable of any semiconductor manufacturing whatsoever, a nanoparticle printer would be by far the cheapest option to build. But if our goal is to mass produce large numbers of chips, these results change.

Once the manufacturing equipment exists, we estimated a nanoparticle printer would take hours to days to print single chips (section 6.5.3), which is hundreds to thousands of chips per year. A $40k printer cost amortized over several years might result in a cost per chip of $100 or similar. This only works for chips that are simple or printed with relatively low resolution; modern CPUs are likely infeasible (see section 7.2.2).

Microfabrication, on the other hand, regularly makes sub-$1 integrated circuits (as well as hundred-dollar CPUs). Even though a large fab is more expensive, it can make such high

[2]Annealing or release etch steps may be useful, but we'll ignore those for simplicity.

[3]The data of figure 7.2 is subject to selection bias: cheaper fabs are less likely to be tracked. However, we can estimate the cost of cheap fabs by noting each needs tens of pieces of equipment, each of which is often in the same $10k–$100k price range as our nanoparticle printer, and thereby reach the same conclusion.

quantities of chips that, when amortized, the cost per chip is lower than printing—but only with a certain extremely important caveat. Microfabrication can only mass produce identical chips. It makes thousands or millions of copies of the same thing.

Specifically, whenever a microfabrication fab receives a blueprint for a new chip, it must prepare the fab for that specific design (including making photolithography masks), which takes nontrivial time and cost (masks can be thousands to millions of dollars, and the first wafers might be done in weeks to months). It runs the planar fabrication process on hundreds or thousands of silicon wafers, each of which contains hundreds of chips (see section 1.1). Each new chip design must pay for the fab preparation plus hundred-chip wafers, so getting a fab to make only a single chip from that design is inefficient and expensive even if the original fab equipment costs were already amortized out (compared to printing, which can easily make each chip unique).

How much are these per-design microfabrication costs? Definitive minimum prices are hard to come by. Commercial fabs tend to keep information private (fabs often require customers to sign a nondisclosure agreement covering fab details, for example [485]). Some information is publicly available from multi-project wafer (MPW) services, which are middleman companies that combine multiple smaller chip designs together before sending the result to a fab, which reduces the cost per design and is intended for prototyping. These are generally the cheapest ways to manufacture a chip in low volumes.

Fab	Min. cost	Min. qty.	Lead time	Tapeouts per year
GlobalFoundries 130nm	$44900	50 chips	5 months	2
TSMC 65nm	$4700		3 months	6–10
TSMC 28nm	$11100		3 months	4
UMC 40N (40nm)	$103000	90 chips	4.5 months	5
UMC L180 (180nm)	$19900	50 chips		2
IHP SG13S (130nm)	$5300	40 chips	6 months	3
X-Fab XT018 (180nm)	$6100	50 chips	7 months	2–5
SkyWater SKY130 (130nm)	$3500	25 chips	5 months	4

Table 7.2: Approximate minimum cost, time, and availability of some microfabrication fab processes via MPW services. These numbers are not accurate enough to compare fabs and are only intended to indicate order-of-magnitude similarities. Each fab process accepts new designs ("tapeouts") only several times per year and returns a minimum number of chips at some cost after some lead time. Data is combined from [486][487][488][489][490] using the cheapest advertised prices among all MPW services. This does not account for the additional cost of EDA chip design software, which often far exceeds $100k per year.

We can see the minimum cost to get chips of a new design is in the thousands of dollars, though this typically provides 10–100 chips, nearing the $100 per chip cost of nanoparticle printing (making these chips in larger volumes would lower the price further). Note this does not include difficulties communicating with the fabs (nondisclosure agreements and expensive design software) or the long lead time required to make chips (discussed in section 7.2.2), but

chips are fabricated with minimum feature sizes of 180 nm or below, much better than the 1 µm resolution nanoparticle printing might easily reach, which means the microfabricated transistors will generally be faster and draw less power.

Using this data and assuming microfabricated chips can cost as little as $1 each when a million or more are made, we can draw the following approximate graph of the cost required to make a given number of chips of a new design.

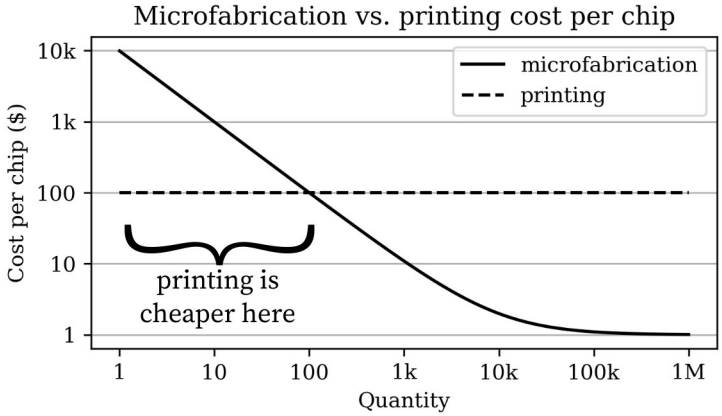

Figure 7.3: Very approximate cost per chip to produce a given quantity of a new chip design, including amortized equipment capital expenses. The decrease in microfabrication costs is due to amortizing additional design-specific costs such as mask making. From this figure we see that nanoparticle printing may be most useful for small quantities of chips (below about 100). Many more advanced fab processes (say, for CPUs) are much more expensive.

It appears nanoparticle printing will likely be cheaper whenever only a low quantity of some chip design (below about 100) is required; microfabrication becomes cheaper (with higher chip quality) for higher quantities[4]. This suggests printing might be suitable for research and prototyping applications, which typically use only these low chip volumes (and in section 7.2.2 we will see printing lead time is much faster, which is also helpful for prototyping), as opposed to more generic integrated circuits which are built millions at a time and sold worldwide over multiple years.

We can also consider different kinds of chips.

Most of our discussion in this section applies to integrated circuits (ICs), which are purely electrical circuits. Most chips are ICs, and fabs specialize in these by standardizing a certain sequence of fabrication steps, after which customer designs simply change the arrangement of transistors made with that standardized process on a chip. But as stated in Chapter 1, integrated circuits are not the only thing microfabrication makes. Another (albeit smaller) category is microelectromechanical systems (MEMS), which are small mechanical devices and sensors (including inkjet printheads, cell phone RF filters, microphones, and more).

[4]This is the same effect observed between plastic 3D printing, which makes single parts one at a time, and plastic injection molding, which has significant setup (mold making) costs but can then produce thousands of parts more cheaply on average.

Although MEMS devices are generally mass-produced and roughly follow the same economics as ICs, the development of a new MEMS device is much more painful. Microfabrication fabs that make ICs with a standardized process are reliable, so a chip designer can often simulate a design then have it made successfully by a fab on only the first or second attempt. On the other hand, each MEMS device typically uses a different fabrication process (to make different material layers or make them different thicknesses, for example), so fabs cannot standardize processes[5]. Developing a new MEMS device requires both designing the chip and also completely changing the sequence of microfabrication steps, which can take a dedicated engineer months of testing due to microfabrication's complexity (so this also requires physical access to a fab). The excellent book [491] on MEMS development estimates the cost of a new MEMS device as follows, and we see nanoparticle printing might again be useful for prototyping.

Development stage	Minimum cost	Time
Proof-of-concept prototype	\$500k	1 year
Advanced prototypes	\$1.5M	1.2 years
Foundry feasibility	\$1M	0.8 years
Foundry pilot production	\$1M	1 year
Total	\$4M	4 years

Table 7.3: Total cost (tools and labor) and time for developing a MEMS device with standard microfabrication, copied from [491]. This includes not only the MEMS fabrication but also chip characterization and testing, and is significantly higher than building an IC. Nanoparticle printing might be able to replace the proof-of-concept prototype stage.

Finally, we should mention several other ongoing attempts to make microfabrication easier, cheaper, and faster. Pragmatic Semiconductor [492], InchFab (MEMS) [493], Atomic Semi [494], and Minimal Fab [495] are all small organizations that appear[6] to be building microfabrication fabs while attempting to reduce the equipment capital cost by making smaller tools[7] and reduce the per-design cost and time by using smaller wafers and fewer microfabrication steps. We applaud these efforts and look forward to their hopeful success, but it it is possible that since they still rely on the multiple-tool planar process microfabrication paradigm, their total improvements will be limited (compared to, for example, the large turnaround time improvements from nanoparticle printing we discuss in section 7.2.2).

In conclusion, there do indeed seem to be situations in which nanoparticle printing can be cheaper than microfabrication. This is mainly the case when only a small number of chips (1–100) of some new design are required, and we should also stress that printed chips will likely be lower quality than microfabrication, unable to make certain complex chips (e.g., computer CPUs). All this suggests printing may be useful for research and prototyping.

[5]With the notable historic exception of the PolyMUMPs standardized MEMS process, which to the best of our knowledge was never responsible for a significant fraction of worldwide MEMS fabrication.

[6]As best as we can determine from publicly available information. These organizations are all relatively new and might not have settled on a particular commercial strategy yet.

[7]Several excellent custom-built microfabrication tools proposed for InchFab are [421][422][496].

7.2.2 Time Comparison

Besides cost, another important parameter of a manufacturing process is how long it takes. Here, too, nanoparticle printing and microfabrication differ greatly.

Consider the time after a new chip design has begun manufacturing. Some number of chips will be made after a certain amount of time (in manufacturing, the number of things made is typically called the "volume" as in "high volume manufacturing").

A nanoparticle printer should be straightforward. In section 6.5.3, we calculated one can probably make several simple chips per day. This can continue indefinitely.

Microfabrication is more complicated: it takes several months to prepare a fab for a new design and complete the first batch of wafers (from section 7.2.1 and especially table 7.2, which adds the additional constraint that new designs are only accepted every few months). Afterward, more wafers can be produced extremely quickly. As noted in section 1.1, a wafer actually takes weeks to months to be manufactured, but making multiple chips per wafer and running multiple wafers at different steps in parallel allows a very high total rate. A large modern fab can produce thousands of wafers per month, each with hundreds of chips.

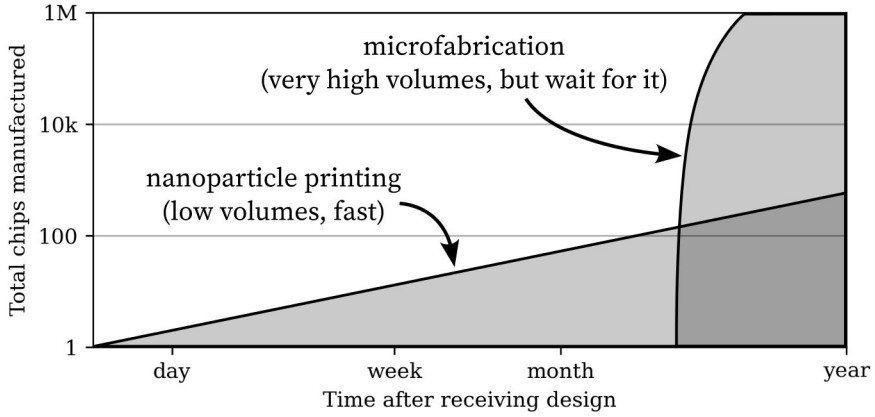

Figure 7.4: Another way nanoparticle printing significantly differs from microfabrication. Printing can make a single chip within a day and continue producing chips at a constant rate. Microfabrication requires several months to get started, but then (if desired) can produce large numbers of chips very quickly.

We see a nanoparticle printer might be useful whenever turnaround times of a month or less are required: in other words, research and prototyping applications[8]—again! By sheer fortunate coincidence, nanoparticle printing is doubly beneficial (cost and turnaround time) for research applications, and the break-even point with microfabrication is once again near the 100-chip mark. By analogy to macroscopic manufacturing methods (such as 3D printing and laser cutting, which similarly produce low volumes of parts quickly), this might justify calling nanoparticle printing a rapid prototyping technique.

[8] A chip might be manufactured, tested, tweaked, and a new version manufactured, repeating as desired.

There is another speed-related effect worth consideration. We have claimed several times (e.g., section 6.5.3) that nanoparticle printing can only make "simple" chips, not large modern chips like CPUs, GPUs, and memory. What does that mean, and why is that?

Although all semiconductor devices are made by arranging materials in different 3D patterns (see chapter 1), some patterns are much more complicated and thus harder to make than others. A solar cell or LED is just several uniform layers of material, while a computer CPU has thousands to billions of tiny transistors. Call these "simple" and "complex".

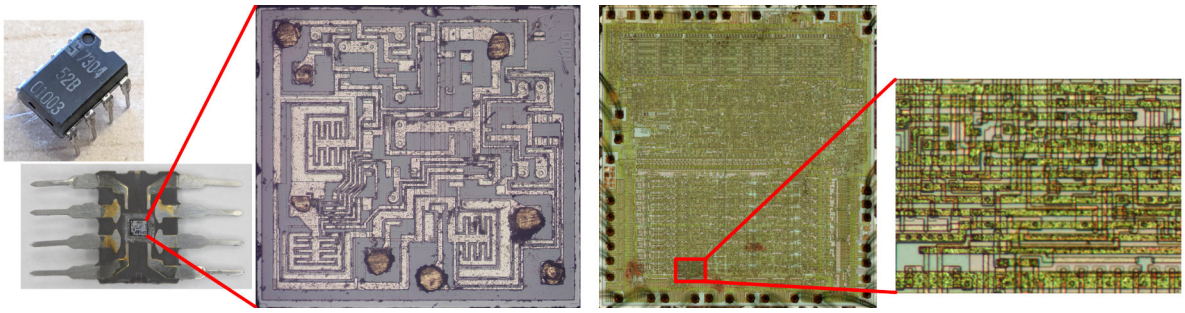

Figure 7.5: Examples of chip complexity. Top-down images of chips (see figure 1.1) are from the excellent [497][498][499]. Left: a simple 1.2 mm wide chip with about 25 transistors and other components (an early 555 timer IC). Right: a complex 10 mm wide chip with about 4500 transistors (the MOS 6502, the CPU of the the Atari 2600, Apple II, Commodore 64, and other historical computers). The right chip has significantly higher complexity (and modern computer CPUs, with billions of transistors in the same space, have vastly more).

We might quantify complexity by taking a digital picture (a square grid of pixels) of the chip and counting how many pixels we needed to accurately describe it. A blank square needs only one pixel. We could pixelate the left chip of figure 7.5 to a 250x250 pixel grid without losing fundamental details, but the right chip needs at least 5000x5000 pixels or its tiny wires blur together. Because chips are actually several layers stacked in 3D, we use the term voxel (a 3D pixel). The number of voxels in a chip is a way to measure its complexity[9].

This finally lets us describe what we mean. Microfabrication cares little about complexity[10] because photolithography (section 1.1) makes all features of a 2D layer on a chip at once in parallel, but nanoparticle printing has to put down each voxel one at a time. In section 6.5.3 we hypothesized a fast nanoparticle printer might print material at up to 5×10^4 µm^3/s (varying with resolution) with 1 µm resolution, which is (very approximately) 5×10^4 voxels/s. This cannot print the trillions of voxels required for a modern CPU in a reasonable amount of time. Nanoparticle printing is best suited for printing simple chips.

[9] An improved metric accounting for varying feature sizes might use the size in bits of a compressed image, i.e., the information entropy. The corresponding manufacturing metric is the information transfer rate to the substrate. [500][501][502][503][504][505] compare resolution vs. speed of other manufacturing methods.

[10] As long as photolithography resolution and yield suffice. Incidentally, Moore's law [6], which is typically explained as photolithography improvements making more complex chips possible, does not describe simpler things like solar cells (for which smaller size isn't an improvement as they need the area to collect sunlight), or even MEMS, for which more general microfabrication improvements (materials, etc.) matter more.

7.2.3 Efficiency and Environmental Impact

Nanoparticle printing might have an additional significant advantage over microfabrication: extreme space, material, and energy efficiency. For example, a microfabrication fab needs a warehouse-sized cleanroom with tens of tools while a printer could fit on a desktop.

The nanoparticle printing process requires as input only electricity, an inert gas for particle flow, and the target materials, and only outputs printed chips, exhaust gas[11], and waste heat. Contrast this to microfabrication [7][8], which in addition to a high power draw requires photoresist, wet developing and removal chemicals [506][507], hazardous process gases, and water for wafer cleaning between steps; the output is additional hazardous liquid and gas byproducts that must be properly cared for[12]. Of a chip's entire lifetime, its manufacturing has the greatest impact to assorted worldwide systems and environments [509][510][511][512], so improving manufacturing efficiency[13] and reducing byproducts is useful.

We quantified printer power consumption by measuring electricity use of our chapter 4 printer and adding the hypothetical power draw of a nanoparticle charger UV lamp (chapter 5) and a drive circuit (appendix C) for an electrostatic focusing system.

Component	Power draw (W)
Edwards R8 vacuum pump	800
Edwards APG-M-NW16 vacuum gauge	1
xTool 1064nm laser	10
XY stage (custom)	24
UV lamp	4
40-output electrode drive circuit	400
Laptop computer	20
Total	1300

Table 7.4: Electrical power draw of assorted parts of a nanoparticle printer. The vacuum pump (high vacuum not included here) draws 60% of the power and the electrode circuitry is known to be inefficient; future work can likely reduce power use much further.

The total 1300 W power draw of the printer is small enough it can be supplied by a single standard 120 V 15 A North American NEMA 5-15 mains outlet. It appears we can bring fabrication energy requirements[14] (at least for simple chips) down from the industrial scale to a desktop tool capable of running in any standard workshop[15].

This suggests nanoparticle printing is ideal for distributed onsite manufacturing of chips—which (yet again!) may make it an excellent fit for research and prototyping.

[11] Possibly with some nanoparticles, which can be filtered out and the gas fed back to the input.

[12] Insufficient chemical containment at early Silicon Valley fabs created groundwater contamination and human health hazards that had to be cleaned up decades later [508].

[13] An interesting calculation for future work is the theoretical minimum energy required to assemble a chip.

[14] Though average energy use per chip may be similar to microfabrication, for chips made by which [513] found a surprisingly constant 1.5 kWh/cm^2, about what printing needs for an hour-long print job.

[15] Or perhaps a space station? Sending a fragile microfabrication fab to orbit would be much harder.

7.3 What Printing Can't Do

We should emphasize: **printing will not replace microfabrication** (save in very limited circumstances). If we took our results from this dissertation, built a full nanoparticle printer (section 7.1) and improved it to its theoretical limits (section 6.5.3), it would not change the majority of the microfabrication industry, instead assisting only simple and low-volume research applications. But that does not mean these improvements are unimportant.

Throughout this dissertation, the new nanoparticle printing method we proposed does indeed seem to be easier, cheaper, and faster than microfabrication in some ways, achieving the goals we set out to reach in chapter 1. It is easier as measured by complexity and equipment cost, cheaper in low volumes, and has faster turnaround times.

On the other hand, printing is worse than microfabrication in that it cannot make complex chips (modern CPUs) and is slower and more expensive for mass production. The majority of the microfabrication industry is exactly these chips (precisely because mass production lets this part of the industry scale to high volumes) and would be unchanged by printing.

Printing may be useful in circumstances when low volumes, fast turnaround times, and simplicity are more important than chip complexity or mass production. Examples include research and prototyping of new MEMS devices, small analog circuits, and sensors—most university research, for example, only needs several copies of a given chip. Another promising possibility is making minimal chips affordable, easy, and fast enough for education: creating simple chips may be the best way to teach students semiconductor device design.

There may also be times when printing and microfabrication are used together. A printed chip might be subsequently postprocessed with a microfabrication-style anneal or release etch (for MEMS), or even combined with techniques like spatial ALD (section 1.2.4) to print more uniform thin films than nanoparticles can manage by themselves. Likewise, microfabrication prototyping fabs, where many engineers constantly develop new semiconductor devices, may benefit from the addition of a nanoparticle printer.

So, while microfabrication will remain the only practical method to make computers in the forseeable decades, nanoparticle printing may open new avenues of rapid prototyping, finally increasing the accessibility of semiconductor manufacturing to match its ubiquitous use in our contemporary world. We think that's a future worth aiming for.

Bibliography

[1] Richard C. Jaeger. *Introduction to Microelectronic Fabrication*. 2nd ed. Modular Series on Solid State Devices, Volume V. Prentice Hall, 2002. ISBN: 978-0-20-144494-0 (cited on pages 2, 3, 29, 53, 101).

[2] Chenming C. Hu. *Modern Semiconductor Devices for Integrated Circuits*. Pearson, 2009. ISBN: 978-0-13-608525-6 (cited on page 2).

[3] *Self Assembling Chips*. Phys.org. 2007. URL: https://phys.org/news/2007-05-chips.html (cited on page 2).

[4] *Integrated Circuits*. SparkFun. 2015. URL: https://learn.sparkfun.com/tutorials/integrated-circuits/all (cited on page 2).

[5] C. J. Frosch and L. Derick. "Surface Protection and Selective Masking during Diffusion in Silicon". In: *Journal of The Electrochemical Society* 104.9 (1957), p. 547. ISSN: 1945-7111. DOI: 10.1149/1.2428650 (cited on page 3).

[6] R.R. Schaller. "Moore's law: past, present and future". In: *IEEE Spectrum* 34.6 (1997), pp. 52–59. ISSN: 1939-9340. DOI: 10.1109/6.591665 (cited on pages 3, 4, 105, 114).

[7] Sami Franssila. *Introduction to Microfabrication*. 1st ed. Wiley, 2010. ISBN: 978-0-470-74983-8. DOI: 10.1002/9781119990413 (cited on pages 3, 115).

[8] Yoshio Nishi and Robert Doering. *Handbook of Semiconductor Manufacturing Technology*. CRC Press, 2017. ISBN: 978-1-4200-1766-3 (cited on pages 3, 115).

[9] Paolo Gargini et al. *2023 International Roadmap for Devices and Systems Chairman's Editorial*. Tech. rep. IEEE, 2023 (cited on pages 4, 109).

[10] Kader Ibrahim, Chik Ma, and U Hashim. "Semiconductor Fabrication Strategy for Cycle Time and Capacity Optimization: Past and Present". In: *International Conference on Industrial Engineering and Operations Management*. Malaysia, 2016 (cited on page 4).

[11] Wassen Mohammad, Adel Elomri, and Laoucine Kerbache. "The Global Semiconductor Chip Shortage: Causes, Implications, and Potential Remedies". In: *IFAC-PapersOnLine*. 10th IFAC Conference on Manufacturing Modelling, Management and Control MIM 2022 55.10 (2022), pp. 476–483. ISSN: 2405-8963. DOI: 10.1016/j.ifacol.2022.09.439 (cited on page 4).

[12] Lars Mönch, Reha Uzsoy, and John W. Fowler. "A survey of semiconductor supply chain models part I: semiconductor supply chains, strategic network design, and supply chain simulation". In: *International Journal of Production Research* 56.13 (2018), pp. 4524–4545. ISSN: 0020-7543, 1366-588X. DOI: 10.1080/00207543.2017.1401233 (cited on page 5).

[13] C.J. McDonald. "Copy EXACTLY! A paradigm shift in technology transfer method". In: *1997 IEEE/SEMI Advanced Semiconductor Manufacturing Conference and Workshop ASMC 97 Proceedings*. ISSN: 1078-8743. 1997, pp. 414–417. DOI: 10.1109/ASMC.1997.630771 (cited on page 5).

[14] 117th US Congress. *CHIPS and Science Act*. Pub. L. 117–167. 2022 (cited on page 5).

[15] Daniel Teal, Hani C. Gomez, Craig B. Schindler, and Kristofer S. J. Pister. "Robust Electrostatic Inchworm Motors for Macroscopic Manipulation and Movement". In: *2021 21st International Conference on Solid-State Sensors, Actuators and Microsystems (Transducers)*. 2021, pp. 635–638. DOI: 10.1109/Transducers50396.2021.9495446 (cited on pages 5, 98).

[16] Richard Feynman. *There's Plenty of Room at the Bottom*. Caltech, 1959 (cited on pages 5, 104).

[17] Eric Drexler. *Engines of Creation: The Coming Era of Nanotechnology*. Doubleday, 1986. ISBN: 0-385-19973-2 (cited on page 5).

[18] K. K. B. Hon, L. Li, and I. M. Hutchings. "Direct writing technology—Advances and developments". In: *CIRP Annals* 57.2 (2008), pp. 601–620. ISSN: 0007-8506. DOI: 10.1016/j.cirp.2008.09.006 (cited on page 5).

[19] Alberto Piqué and Douglas B. Chrisey. *Direct-Write Technologies for Rapid Prototyping: Sensors, Electronics, and Integrated Power Sources*. Ed. by Alberto Piqué. San Diego: Academic Press, 2002. ISBN: 978-0-12-174231-7. DOI: 10.1016/B978-012174231-7/50049-X (cited on pages 5, 107).

[20] *Product Lineup — Inkjet Printheads*. Kyocera. 2024. URL: https://global.kyocera.com/prdct/inkjet-printheads/application/detail/index.html (cited on page 6).

[21] *"10n World": Kyocera's Piezoelectric Inkjet Printhead Advancing the Evolution of Digital Printing - YouTube*. Kyocera. 2024. URL: https://www.youtube.com/watch?v=NsNFuVYSFa8 (cited on page 6).

[22] *PolyJet Technology for 3D Printing*. Stratasys. 2024. URL: https://www.stratasys.com/en/guide-to-3d-printing/technologies-and-materials/polyjet-technology/ (cited on page 6).

[23] *DragonFly IV - A new era in 3D electronics printing*. Nano Dimension. 2024. URL: https://www.nano-di.com/dragonfly-iv (cited on page 6).

[24] Jimin Kwon, Yasunori Takeda, Kenjiro Fukuda, Kilwon Cho, Shizuo Tokito, and Sungjune Jung. "Three-Dimensional, Inkjet-Printed Organic Transistors and Integrated Circuits with 100% Yield, High Uniformity, and Long-Term Stability". In: *ACS Nano* 10.11 (2016), pp. 10324–10330. ISSN: 1936-0851. DOI: 10.1021/acsnano.6b06041 (cited on page 6).

[25] Patrizia Richner, Patrick Galliker, Tobias Lendenmann, Stephan J. P. Kress, David K. Kim, David J. Norris, and Dimos Poulikakos. "Full-Spectrum Flexible Color Printing at the Diffraction Limit". In: *ACS Photonics* 3.5 (2016), pp. 754–757. DOI: 10.1021/acsphotonics.6b00131 (cited on page 6).

[26] Giorgio Mattana, Alberto Loi, Marion Woytasik, Massimo Barbaro, Vincent Noël, and Benoît Piro. "Inkjet-Printing: A New Fabrication Technology for Organic Transistors". In: *Advanced Materials Technologies* 2.10 (2017), p. 1700063. ISSN: 2365-709X. DOI: 10.1002/admt.201700063 (cited on page 6).

[27] *NANO PARTICLE JETTING — XJET*. XJet. 2024. URL: https://xjet3d.com/npj-technology/direct-material-jetting/ (cited on page 6).

[28] Seungjun Chung, Kyungjune Cho, and Takhee Lee. "Recent Progress in Inkjet-Printed Thin-Film Transistors". In: *Advanced Science* 6.6 (2019), p. 1801445. ISSN: 2198-3844. DOI: 10.1002/advs.201801445 (cited on page 6).

[29] Peter Mack Grubb, Harish Subbaraman, Saungeun Park, Deji Akinwande, and Ray T. Chen. "Inkjet Printing of High Performance Transistors with Micron Order Chemically Set Gaps". In: *Scientific Reports* 7.1 (2017), p. 1202. ISSN: 2045-2322. DOI: 10.1038/s41598-017-01391-2 (cited on page 6).

[30] Jang-Ung Park, Matt Hardy, Seong Jun Kang, Kira Barton, Kurt Adair, Deep kishore Mukhopadhyay, Chang Young Lee, Michael S. Strano, Andrew G. Alleyne, John G. Georgiadis, Placid M. Ferreira, and John A. Rogers. "High-resolution electrohydrodynamic jet printing". In: *Nature Materials* 6.10 (2007), pp. 782–789. ISSN: 1476-4660. DOI: 10.1038/nmat1974 (cited on pages 6, 14, 73).

[31] P. Galliker, J. Schneider, H. Eghlidi, S. Kress, V. Sandoghdar, and D. Poulikakos. "Direct printing of nanostructures by electrostatic autofocussing of ink nanodroplets". In: *Nature Communications* 3.1 (2012), p. 890. ISSN: 2041-1723. DOI: 10.1038/ncomms1891 (cited on page 6).

[32] *Scrona - Electrostatic Multi-Nozzle Printing*. Scrona. 2024. URL: https://www.scrona.com/ (cited on page 6).

[33] *Advanced Additive Manufacturing Solutions - Micro 3D Printers : BMF*. Boston Micro Fabrication. 2024. URL: https://bmf3d.com/ (cited on page 7).

[34] Ryan Hensleigh, Huachen Cui, Zhenpeng Xu, Jeffrey Massman, Desheng Yao, John Berrigan, and Xiaoyu Zheng. "Charge-programmed three-dimensional printing for multi-material electronic devices". In: *Nature Electronics* 3.4 (2020), pp. 216–224. ISSN: 2520-1131. DOI: 10.1038/s41928-020-0391-2 (cited on page 7).

[35] J. Bauer, A. Schroer, R. Schwaiger, and O. Kraft. "Approaching theoretical strength in glassy carbon nanolattices". In: *Nature Materials* 15.4 (2016), pp. 438–443. ISSN: 1476-4660. DOI: 10.1038/nmat4561 (cited on page 7).

[36] Huachen Cui, Ryan Hensleigh, Desheng Yao, Deepam Maurya, Prashant Kumar, Min Gyu Kang, Shashank Priya, and Xiaoyu (Rayne) Zheng. "Three-dimensional printing of piezoelectric materials

with designed anisotropy and directional response". In: *Nature Materials* 18.3 (2019), pp. 234–241. ISSN: 1476-4660. DOI: 10.1038/s41563-018-0268-1 (cited on page 7).

[37] V. Harinarayana and Y. C. Shin. "Two-photon lithography for three-dimensional fabrication in micro/nanoscale regime: A comprehensive review". In: *Optics & Laser Technology* 142 (2021), p. 107180. ISSN: 0030-3992. DOI: 10.1016/j.optlastec.2021.107180 (cited on page 7).

[38] *Highest precision microfabrication technologies*. Nanoscribe. 2024. URL: https://www.nanoscribe.com/en/microfabrication-technologies/ (cited on page 7).

[39] Sukjun Kim, Regan Kubicek, and Sarah Bergbreiter. "3D-Printed Electrostatic Microactuators for Flexible Microsystems". In: *Advanced Functional Materials* 33.47 (2023), p. 2304991. ISSN: 1616-3028. DOI: 10.1002/adfm.202304991 (cited on page 7).

[40] *Microfabrica - Technology*. Microfabrica. 2024. URL: https://microfabrica.com/technology.html (cited on page 7).

[41] Armelle Vardelle, Christian Moreau, Jun Akedo, Hossein Ashrafizadeh, Christopher C. Berndt, Jörg Oberste Berghaus, Maher Boulos, Jeffrey Brogan, Athanasios C. Bourtsalas, Ali Dolatabadi, Mitchell Dorfman, Timothy J. Eden, Pierre Fauchais, Gary Fisher, Frank Gaertner, Malko Gindrat, Rudolf Henne, Margaret Hyland, Eric Irissou, Eric H. Jordan, Khiam Aik Khor, Andreas Killinger, Yuk-Chiu Lau, Chang-Jiu Li, Li Li, Jon Longtin, Nicolaie Markocsan, Patrick J. Masset, Jiri Matejicek, Georg Mauer, André McDonald, Javad Mostaghimi, Sanjay Sampath, Günter Schiller, Kentaro Shinoda, Mark F. Smith, Asif Ansar Syed, Nickolas J. Themelis, Filofteia-Laura Toma, Juan Pablo Trelles, Robert Vassen, and Petri Vuoristo. "The 2016 Thermal Spray Roadmap". In: *Journal of Thermal Spray Technology* 25.8 (2016), pp. 1376–1440. ISSN: 1059-9630, 1544-1016. DOI: 10.1007/s11666-016-0473-x (cited on pages 8, 30).

[42] Jun Akedo. "Room Temperature Impact Consolidation (RTIC) of Fine Ceramic Powder by Aerosol Deposition Method and Applications to Microdevices". In: *Journal of Thermal Spray Technology* 17.2 (2008), pp. 181–198. ISSN: 1059-9630, 1544-1016. DOI: 10.1007/s11666-008-9163-7 (cited on pages 8, 29–31).

[43] Paolo Milani and Salvatore Iannotta. *Cluster beam synthesis of nanostructured materials*. Springer series in cluster physics. Berlin Heidelberg New York Barcelona Budapest Hong Kong London Milan Paris Singapore Tokyo: Springer, 1999. ISBN: 978-3-642-64173-2 (cited on pages 8, 15, 16, 29, 30, 105).

[44] *Technology - SPEE3D 3D Metal Printing*. Spee3D. 2024. URL: https://www.spee3d.com/technology/ (cited on page 8).

[45] M. Maiwald, C. Werner, V. Zoellmer, and M. Busse. "INKtelligent printed strain gauges". In: *Sensors and Actuators A: Physical*. Eurosensors XXIII, 2009 162.2 (2010), pp. 198–201. ISSN: 0924-4247. DOI: 10.1016/j.sna.2010.02.019 (cited on page 8).

[46] Heechul Lee, Sukbeom You, Peter V. Pikhitsa, Junhoi Kim, Sunghoon Kwon, Chang Gyu Woo, and Mansoo Choi. "Three-Dimensional Assembly of Nanoparticles from Charged Aerosols". In: *Nano Letters* 11.1 (2011), pp. 119–124. ISSN: 1530-6984. DOI: 10.1021/nl103787k (cited on pages 8, 73).

[47] Isao Yamada and Toshinori Takagi. "Vaporized-metal cluster formation and ionized-cluster beam deposition and epitaxy". In: *Thin Solid Films* 80.1 (1981), pp. 105–115. ISSN: 0040-6090. DOI: 10.1016/0040-6090(81)90212-1 (cited on pages 8, 15, 30, 32, 33, 56, 88, 90, 107).

[48] Isao Yamada. "Advances in Ion and Laser Beam Technology: Achievements of Japanese Government and University Projects". In: *MRS Online Proceedings Library* 504.1 (1997), pp. 69–79. ISSN: 1946-4274. DOI: 10.1557/PROC-504-69 (cited on pages 8, 30).

[49] *3D Printed Electronics - Aerosol Jet Technology*. Optomec. 2024. URL: https://optomec.com/printed-electronics/aerosol-jet-technology/ (cited on page 8).

[50] Justin M. Hoey, Artur Lutfurakhmanov, Douglas L. Schulz, and Iskander S. Akhatov. "A Review on Aerosol-Based Direct-Write and Its Applications for Microelectronics". In: *Journal of Nanotechnology* 2012 (2012), pp. 1–22. ISSN: 1687-9503, 1687-9511. DOI: 10.1155/2012/324380 (cited on pages 8, 39).

[51] *Nanoporous Printer, VSP-P1 Nanoporous Printer*. VSPARTICLE. 2024. URL: https://vsparticle.com/products/research-tools/vsp-p1-nanoprinter (cited on pages 8, 16, 27).

[52] Gaurav Prashar and Hitesh Vasudev. "A comprehensive review on sustainable cold spray additive manufacturing: State of the art, challenges and future challenges". In: *Journal of Cleaner Production*

310 (2021), p. 127606. ISSN: 0959-6526. DOI: 10.1016/j.jclepro.2021.127606 (cited on pages 8, 30).

[53] Minxiang Zeng, Yipu Du, Qiang Jiang, Nicholas Kempf, Chen Wei, Miles V. Bimrose, A. N. M. Tanvir, Hengrui Xu, Jiahao Chen, Dylan J. Kirsch, Joshua Martin, Brian C. Wyatt, Tatsunori Hayashi, Mortaza Saeidi-Javash, Hirotaka Sakaue, Babak Anasori, Lihua Jin, Michael D. McMurtrey, and Yanliang Zhang. "High-throughput printing of combinatorial materials from aerosols". In: *Nature* 617.7960 (2023), pp. 292–298. ISSN: 0028-0836, 1476-4687. DOI: 10.1038/s41586-023-05898-9 (cited on page 8).

[54] Kihyon Hong, Se Hyun Kim, Ankit Mahajan, and C. Daniel Frisbie. "Aerosol Jet Printed p- and n-type Electrolyte-Gated Transistors with a Variety of Electrode Materials: Exploring Practical Routes to Printed Electronics". In: *ACS Applied Materials & Interfaces* 6.21 (2014), pp. 18704–18711. ISSN: 1944-8244. DOI: 10.1021/am504171u (cited on page 8).

[55] Carissa S. Jones, Xuejun Lu, Mike Renn, Mike Stroder, and Wu-Sheng Shih. "Aerosol-jet-printed, high-speed, flexible thin-film transistor made using single-walled carbon nanotube solution". In: *Microelectronic Engineering*. Materials for Advanced Metallization 2009 87.3 (2010), pp. 434–437. ISSN: 0167-9317. DOI: 10.1016/j.mee.2009.05.034 (cited on page 8).

[56] Changyong Cao, Joseph B. Andrews, and Aaron D. Franklin. "Completely Printed, Flexible, Stable, and Hysteresis-Free Carbon Nanotube Thin-Film Transistors via Aerosol Jet Printing". In: *Advanced Electronic Materials* 3.5 (2017), p. 1700057. ISSN: 2199-160X. DOI: 10.1002/aelm.201700057 (cited on page 8).

[57] Shiheng Lu, Jorge A. Cardenas, Robyn Worsley, Nicholas X. Williams, Joseph B. Andrews, Cinzia Casiraghi, and Aaron D. Franklin. "Flexible, Print-in-Place 1D–2D Thin-Film Transistors Using Aerosol Jet Printing". In: *ACS Nano* 13.10 (2019), pp. 11263–11272. ISSN: 1936-0851. DOI: 10.1021/acsnano.9b04337 (cited on page 8).

[58] Vincent A. Vons, Louis C. P. M. de Smet, David Munao, Alper Evirgen, Erik M. Kelder, and Andreas Schmidt-Ott. "Silicon nanoparticles produced by spark discharge". In: *Journal of Nanoparticle Research* 13.10 (2011), p. 4867. ISSN: 1572-896X. DOI: 10.1007/s11051-011-0466-0 (cited on pages 8, 16, 20, 54).

[59] N. P Rao, N Tymiak, J Blum, A Neuman, H. J Lee, S. L Girshick, P. H McMurry, and J Heberlein. "Hypersonic plasma particle deposition of nanostructured silicon and silicon carbide". In: *Journal of Aerosol Science* 29.5 (1998), pp. 707–720. ISSN: 0021-8502. DOI: 10.1016/S0021-8502(97)10015-5 (cited on pages 8, 31, 45).

[60] Steven L. Girshick. "Aerosol processing for nanomanufacturing". In: *Journal of Nanoparticle Research* 10.6 (2008), pp. 935–945. ISSN: 1572-896X. DOI: 10.1007/s11051-007-9331-6 (cited on pages 8, 11, 15, 31, 107).

[61] Xiaoliang Wang and Peter H. McMurry. "A Design Tool for Aerodynamic Lens Systems". In: *Aerosol Science and Technology* 40.5 (2006), pp. 320–334. ISSN: 0278-6826. DOI: 10.1080/02786820600615063 (cited on pages 8, 45).

[62] D L Schulz, J M Hoey, D Thompson, O F Swenson, S Han, J Lovaasen, X Dai, C Braun, K Keller, and I S Akhatov. "Collimated Aerosol Beam Deposition: Sub-5-µm Resolution of Printed Actives and Passives". In: *IEEE Transactions on Advanced Packaging* 33.2 (2010), pp. 421–427. ISSN: 1521-3323, 1557-9980. DOI: 10.1109/TADVP.2009.2038615 (cited on page 8).

[63] Wooik Jung, Peter V. Pikhitsa, Yoon-Ho Jung, Jooyeon Shin, Minsung Han, and Mansoo Choi. "3D Nanoprinting with Charged Aerosol Particles-An Overview". In: *Accounts of Materials Research* 2.11 (2021), pp. 1117–1128. DOI: 10.1021/accountsmr.1c00187 (cited on pages 8, 11, 73, 100).

[64] Hyoungchul Kim, Jaehyun Kim, Hongjoo Yang, Jeongsoo Suh, Taeyoung Kim, Bangwoo Han, Sungwon Kim, Dae Seong Kim, Peter V. Pikhitsa, and Mansoo Choi. "Parallel patterning of nanoparticles via electrodynamic focusing of charged aerosols". In: *Nature Nanotechnology* 1.2 (2006), pp. 117–121. ISSN: 1748-3387, 1748-3395. DOI: 10.1038/nnano.2006.94 (cited on pages 8, 11).

[65] Kiwoong Lee, Hoseop Choi, Dae Seong Kim, Min Seok Jang, and Mansoo Choi. "Vertical stacking of three-dimensional nanostructures via an aerosol lithography for advanced optical applications". In: *Nanotechnology* 28.47 (2017), p. 475302. ISSN: 0957-4484, 1361-6528. DOI: 10.1088/1361-6528/aa900d (cited on page 8).

[66] Wooik Jung, Yoon-Ho Jung, Peter V. Pikhitsa, Jicheng Feng, Younghwan Yang, Minkyung Kim, Hao-Yuan Tsai, Takuo Tanaka, Jooyeon Shin, Kwang-Yeong Kim, Hoseop Choi, Junsuk Rho, and Mansoo Choi. "Three-dimensional nanoprinting via charged aerosol jets". In: *Nature* 592.7852 (2021), pp. 54–59. ISSN: 0028-0836, 1476-4687. DOI: 10.1038/s41586-021-03353-1 (cited on page 8).

[67] Jooyeon Shin, Yoon-Ho Jung, Peter V. Pikhitsa, Changnyeong Hur, Wonjin Cho, Wooik Jung, and Mansoo Choi. "Three-dimensional nanoprinting with charged aerosol focusing via an electrified mask". en. In: *Additive Manufacturing* 60 (2022), p. 103206. ISSN: 22148604. DOI: 10.1016/j.addma.2022.103206 (cited on page 8).

[68] En-Chiang Lin, Jesse J. Cole, and Heiko O. Jacobs. "Gas Phase Electrodeposition: A Programmable Multimaterial Deposition Method for Combinatorial Nanostructured Device Discovery". In: *Nano Letters* 10.11 (2010), pp. 4494–4500. ISSN: 1530-6984. DOI: 10.1021/nl102344r (cited on pages 8, 16, 73, 100).

[69] Chad R. Barry, Michael G. Steward, Nyein Z. Lwin, and Heiko O. Jacobs. "Printing nanoparticles from the liquid and gas phases using nanoxerography". In: *Nanotechnology* 14.10 (2003), p. 1057. ISSN: 0957-4484. DOI: 10.1088/0957-4484/14/10/301 (cited on pages 8, 73, 100).

[70] Mohammad Vaezi, Hermann Seitz, and Shoufeng Yang. "A review on 3D micro-additive manufacturing technologies". In: *The International Journal of Advanced Manufacturing Technology* 67.5 (2013), pp. 1721–1754. ISSN: 1433-3015. DOI: 10.1007/s00170-012-4605-2 (cited on page 9).

[71] M. J. Martínez-Pérez, J. Sesé, R. Córdoba, F. Luis, D. Drung, and T. Schurig. "Circuit edit of superconducting microcircuits". In: *Superconductor Science and Technology* 22.12 (2009), p. 125020. ISSN: 0953-2048. DOI: 10.1088/0953-2048/22/12/125020 (cited on page 9).

[72] Giorgio Ercolano, Cathelijn van Nisselroy, Thibaut Merle, János Vörös, Dmitry Momotenko, Wabe W. Koelmans, and Tomaso Zambelli. "Additive Manufacturing of Sub-Micron to Sub-mm Metal Structures with Hollow AFM Cantilevers". In: *Micromachines* 11.1 (2020), p. 6. ISSN: 2072-666X. DOI: 10.3390/mi11010006 (cited on page 9).

[73] Paul W. K. Rothemund. "Folding DNA to create nanoscale shapes and patterns". In: *Nature* 440.7082 (2006), pp. 297–302. ISSN: 1476-4687. DOI: 10.1038/nature04586 (cited on pages 9, 10).

[74] G. Binnig and H. Rohrer. "In touch with atoms". In: *Reviews of Modern Physics* 71.2 (1999), S324–S330. DOI: 10.1103/RevModPhys.71.S324 (cited on pages 9, 10, 13).

[75] Lucille A. Giannuzzi, ed. *Introduction to focused ion beams: instrumentation, theory, techniques and practice*. New York, NY: Springer, 2005. ISBN: 978-0-387-23116-7 (cited on pages 9, 29, 104).

[76] Katja Höflich, Gerhard Hobler, Frances I. Allen, Tom Wirtz, Gemma Rius, Lisa McElwee-White, Arkady V. Krasheninnikov, Matthias Schmidt, Ivo Utke, Nico Klingner, Markus Osenberg, Rosa Córdoba, Flyura Djurabekova, Ingo Manke, Philip Moll, Mariachiara Manoccio, José María De Teresa, Lothar Bischoff, Johann Michler, Olivier De Castro, Anne Delobbe, Peter Dunne, Oleksandr V. Dobrovolskiy, Natalie Frese, Armin Gölzhäuser, Paul Mazarov, Dieter Koelle, Wolfhard Möller, Francesc Pérez-Murano, Patrick Philipp, Florian Vollnhals, and Gregor Hlawacek. "Roadmap for focused ion beam technologies". In: *Applied Physics Reviews* 10.4 (2023), p. 041311. ISSN: 1931-9401. DOI: 10.1063/5.0162597 (cited on pages 9, 55, 56).

[77] Harald Plank, Robert Winkler, Christian H. Schwalb, Johanna Hütner, Jason D. Fowlkes, Philip D. Rack, Ivo Utke, and Michael Huth. "Focused Electron Beam-Based 3D Nanoprinting for Scanning Probe Microscopy: A Review". In: *Micromachines* 11.1 (2020), p. 48. ISSN: 2072-666X. DOI: 10.3390/mi11010048 (cited on page 9).

[78] *Focused Ion Beams*. Raith. 2024. URL: https://raith.com/products/focused-ion-beams/ (cited on page 9).

[79] *Circuit Edit Systems*. Thermo Fisher Scientific. 2024. URL: https://www.thermofisher.com/us/en/home/electron-microscopy/products/circuit-edit-systems.html (cited on page 9).

[80] Karin Groot-Berning, Thomas Kornher, Georg Jacob, Felix Stopp, Samuel T. Dawkins, Roman Kolesov, Jörg Wrachtrup, Kilian Singer, and Ferdinand Schmidt-Kaler. "Deterministic Single-Ion Implantation of Rare-Earth Ions for Nanometer-Resolution Color-Center Generation". In: *Physical Review Letters* 123.10 (2019), p. 106802. DOI: 10.1103/PhysRevLett.123.106802 (cited on pages 9, 13, 104).

[81] Paul Poodt, David C. Cameron, Eric Dickey, Steven M. George, Vladimir Kuznetsov, Gregory N. Parsons, Fred Roozeboom, Ganesh Sundaram, and Ad Vermeer. "Spatial atomic layer deposition: A

route towards further industrialization of atomic layer deposition". In: *Journal of Vacuum Science & Technology A* 30.1 (2011), p. 010802. ISSN: 0734-2101. DOI: 10.1116/1.3670745 (cited on page 9).

[82] Cesar Arturo Masse de la Huerta, Viet H. Nguyen, Abderrahime Sekkat, Chiara Crivello, Fidel Toldra-Reig, Pedro Brandao Veiga, Serge Quessada, Carmen Jimenez, and David Muñoz-Rojas. "Gas-Phase 3D Printing of Functional Materials". In: *Advanced Materials Technologies* 5.12 (2020), p. 2000657. ISSN: 2365-709X. DOI: 10.1002/admt.202000657 (cited on page 9).

[83] Ivan Kundrata, Maïssa Barr, Sarah Tymek, Dirk Döhler, Boris Hudec, Philipp Brüner, Gabriel Vanko, Marian Precner, Tadahiro Yokosawa, Erdmann Spiecker, Maksym Plakhotnyuk, Karol Fröhlich, and Julien Bachmann. "Additive Manufacturing in Atomic Layer Processing Mode". In: *Small Methods* 6.5 (2022), p. 2101546. ISSN: 2366-9608. DOI: 10.1002/smtd.202101546 (cited on page 9).

[84] *Driving advanced technology innovation. Atom by Atom.* ATLANT 3D. 2024. URL: https://atlant3d.com/ (cited on page 9).

[85] I. W. Rangelow, J. Voigt, and K. Edinger. ""NANOJET": Tool for the nanofabrication". In: *Journal of Vacuum Science & Technology B: Microelectronics and Nanometer Structures Processing, Measurement, and Phenomena* 19.6 (2001), pp. 2723–2726. ISSN: 1071-1023. DOI: 10.1116/1.1415504 (cited on page 9).

[86] M. Shtein, P. Peumans, J. B. Benziger, and S. R. Forrest. "Direct, Mask- and Solvent-Free Printing of Molecular Organic Semiconductors". In: *Advanced Materials* 16.18 (2004), pp. 1615–1620. ISSN: 1521-4095. DOI: 10.1002/adma.200400260 (cited on page 9).

[87] Julian Hengsteler, Karuna Aurel Kanes, Liaisan Khasanova, and Dmitry Momotenko. "Beginner's Guide to Micro- and Nanoscale Electrochemical Additive Manufacturing". In: *Annual Review of Analytical Chemistry* 16.Volume 16, 2023 (2023), pp. 71–91. ISSN: 1936-1327, 1936-1335. DOI: 10.1146/annurev-anchem-091522-122334 (cited on page 9).

[88] *Metal 3D Printing of Microscale Objects.* Exaddon. 2024. URL: https://www.exaddon.com/ (cited on page 9).

[89] *Electrochemical Additive Manufacturing.* Fabric8Labs. 2024. URL: https://www.fabric8labs.com/technology/ (cited on page 9).

[90] M. Stuke, K. Mueller, T. Mueller, K. Williams, R. Oliver, D.A.A. Ohlberg, G. Fuhr, and R. S. Williams. "Direct-Writing of Three-Dimensional Structures Using Laser-Based Processes". In: *MRS Bulletin* 32.1 (2007), pp. 32–39. ISSN: 1938-1425. DOI: 10.1557/mrs2007.12 (cited on page 10).

[91] Alberto Piqué, Raymond C. Y. Auyeung, Heungsoo Kim, Nicholas A. Charipar, and Scott A. Mathews. "Laser 3D micro-manufacturing". In: *Journal of Physics D: Applied Physics* 49.22 (2016), p. 223001. ISSN: 0022-3727. DOI: 10.1088/0022-3727/49/22/223001 (cited on pages 10, 23).

[92] Pere Serra and Alberto Piqué. "Laser-Induced Forward Transfer: Fundamentals and Applications". In: *Advanced Materials Technologies* 4.1 (2019), p. 1800099. ISSN: 2365-709X. DOI: 10.1002/admt.201800099 (cited on page 10).

[93] Andre V. Pinheiro, Dongran Han, William M. Shih, and Hao Yan. "Challenges and opportunities for structural DNA nanotechnology". In: *Nature Nanotechnology* 6.12 (2011), pp. 763–772. ISSN: 1748-3395. DOI: 10.1038/nnano.2011.187 (cited on page 10).

[94] Nadrian C. Seeman and Hanadi F. Sleiman. "DNA nanotechnology". In: *Nature Reviews Materials* 3.1 (2017), pp. 1–23. ISSN: 2058-8437. DOI: 10.1038/natrevmats.2017.68 (cited on page 10).

[95] Pengfei Fan, Jian Gao, Hui Mao, Yanquan Geng, Yongda Yan, Yuzhang Wang, Saurav Goel, and Xichun Luo. "Scanning Probe Lithography: State-of-the-Art and Future Perspectives". In: *Micromachines* 13.2 (2022), p. 228. ISSN: 2072-666X. DOI: 10.3390/mi13020228 (cited on page 10).

[96] D. M. Eigler and E. K. Schweizer. "Positioning single atoms with a scanning tunnelling microscope". In: *Nature* 344.6266 (1990), pp. 524–526. ISSN: 1476-4687. DOI: 10.1038/344524a0 (cited on page 10).

[97] Martin Fuechsle, Jill A. Miwa, Suddhasatta Mahapatra, Hoon Ryu, Sunhee Lee, Oliver Warschkow, Lloyd C. L. Hollenberg, Gerhard Klimeck, and Michelle Y. Simmons. "A single-atom transistor". In: *Nature Nanotechnology* 7.4 (2012), pp. 242–246. ISSN: 1748-3395. DOI: 10.1038/nnano.2012.21 (cited on page 10).

[98] Tien-Chien Jen, Liangming Pan, Longjian Li, Qinghua Chen, and Wenzhi Cui. "The acceleration of charged nano-particles in gas stream of supersonic de-Laval-type nozzle coupled with static electric field". In: *Applied Thermal Engineering* 26.5 (2006), pp. 613–621. ISSN: 1359-4311. DOI: w (cited on pages 11, 88).

[99] Rayhan Ahmed and Ranganathan Gopalakrishnan. "Computational study of electrostatic focusing of aerosol nanoparticles using an einzel lens". In: *Journal of Aerosol Science* 137 (2019), p. 105443. ISSN: 0021-8502. DOI: 10.1016/j.jaerosci.2019.105443 (cited on pages 11, 74).

[100] Rayhan Ahmed. "Electrostatic Focusing and Impact Consolidation of Aerosol Particles". Thesis. University of Memphis, 2020. URL: https://digitalcommons.memphis.edu/etd/2394/ (cited on pages 11, 74).

[101] E. R. Buckle, P. Tsakiropoulos, and K. C. Pointon. "Preparation and properties of metallic aerosol particles". In: *International Metals Reviews* 31.1 (1986), pp. 258–288. ISSN: 0308-4590. DOI: 10.1179/imtr.1986.31.1.258 (cited on pages 12, 15).

[102] William C. Hinds. *Aerosol technology: properties, behavior, and measurement of airborne particles*. 2nd ed. New York: Wiley, 1999. ISBN: 978-0-471-19410-1 (cited on pages 12, 15, 19, 20, 27, 30, 35, 38–41, 43, 44, 55, 57, 88, 89).

[103] John Rumble, ed. *CRC Handbook of Chemistry and Physics*. 105th ed. CRC Press, Taylor & Francis, 2023 (cited on pages 13, 29, 36, 59, 63).

[104] C. Suryanarayana. "Mechanical alloying and milling". In: *Progress in Materials Science* 46.1 (2001), pp. 1–184. ISSN: 0079-6425. DOI: 10.1016/S0079-6425(99)00010-9 (cited on page 13).

[105] D. L. Zhang. "Processing of advanced materials using high-energy mechanical milling". In: *Progress in Materials Science*. A Festschrift in Honor of T. B. Massalski 49.3 (2004), pp. 537–560. ISSN: 0079-6425. DOI: 10.1016/S0079-6425(03)00034-3 (cited on page 13).

[106] Arthur H. Lefebvre and Vincent G. McDonell. *Atomization and sprays*. Second edition. Boca Raton: CRC Press, Taylor & Francis Group, CRC Press is an imprint of the Taylor & Francis Group, an informa business, 2017. ISBN: 978-1-4987-3625-1 (cited on page 13).

[107] Leo V. M. Antony and Ramana G. Reddy. "Processes for production of high-purity metal powders". en. In: *JOM* 55.3 (2003), pp. 14–18. ISSN: 1543-1851. DOI: 10.1007/s11837-003-0153-4 (cited on page 13).

[108] Simon J. Gaskell. "Electrospray: Principles and Practice". In: *Journal of Mass Spectrometry* 32.7 (1997), pp. 677–688. ISSN: 1096-9888. DOI: 10.1002/(SICI)1096-9888(199707)32:7<677::AID-JMS536>3.0.CO;2-G (cited on pages 14, 56).

[109] Matthias Wilm. "Principles of Electrospray Ionization". In: *Molecular & Cellular Proteomics* 10.7 (2011). ISSN: 1535-9476, 1535-9484. DOI: 10.1074/mcp.M111.009407 (cited on pages 14, 56).

[110] Brian D. Adamson, Morgan E. C. Miller, and Robert E. Continetti. "The aerosol impact spectrometer: a versatile platform for studying the velocity dependence of nanoparticle-surface impact phenomena". In: *EPJ Techniques and Instrumentation* 4.1 (2017), p. 2. ISSN: 2195-7045. DOI: 10.1140/epjti/s40485-017-0037-6 (cited on page 14).

[111] Conner C. Harper, Zachary M. Miller, Matthew S. McPartlan, Jacob S. Jordan, Randall E. Pedder, and Evan R. Williams. "Accurate Sizing of Nanoparticles Using a High-Throughput Charge Detection Mass Spectrometer without Energy Selection". In: *ACS Nano* 17.8 (2023). Publisher: American Chemical Society, pp. 7765–7774. ISSN: 1936-0851. DOI: 10.1021/acsnano.3c00539 (cited on pages 14, 27, 79).

[112] Peter J. Gallimore and Markus Kalberer. "Characterizing an Extractive Electrospray Ionization (EESI) Source for the Online Mass Spectrometry Analysis of Organic Aerosols". In: *Environmental Science & Technology* 47.13 (2013), pp. 7324–7331. ISSN: 0013-936X. DOI: 10.1021/es305199h (cited on pages 14, 56).

[113] Nguyen T. K. Thanh, N. Maclean, and S. Mahiddine. "Mechanisms of Nucleation and Growth of Nanoparticles in Solution". In: *Chemical Reviews* 114.15 (2014), pp. 7610–7630. ISSN: 0009-2665. DOI: 10.1021/cr400544s (cited on page 14).

[114] *nanoComposix*. nanoComposix. 2024. URL: https://nanocomposix.com/ (cited on page 14).

[115] M. Kulmala, H. Vehkamäki, T. Petäjä, M. Dal Maso, A. Lauri, V. -M. Kerminen, W. Birmili, and P. H. McMurry. "Formation and growth rates of ultrafine atmospheric particles: a review of observations". In: *Journal of Aerosol Science* 35.2 (2004), pp. 143–176. ISSN: 0021-8502. DOI: 10.1016/j.jaerosci.2003.10.003 (cited on page 14).

[116] Renyi Zhang, Alexei Khalizov, Lin Wang, Min Hu, and Wen Xu. "Nucleation and Growth of Nanoparticles in the Atmosphere". In: *Chemical Reviews* 112.3 (2012). Publisher: American Chemical Society, pp. 1957–2011. ISSN: 0009-2665. DOI: 10.1021/cr2001756 (cited on page 14).

[117] S. L. Girshick, M. T. Swihart, S.-M. Suh, M. R. Mahajan, and S. Nijhawan. "Numerical Modeling of Gas-Phase Nucleation and Particle Growth during Chemical Vapor Deposition of Silicon". en. In: *Journal of The Electrochemical Society* 147.6 (2000). Publisher: IOP Publishing, p. 2303. ISSN: 1945-7111. DOI: 10.1149/1.1393525 (cited on page 14).

[118] D. M. Mattox. *Handbook of physical vapor deposition (PVD) processing*. 2nd ed. Oxford, UK: William Andrew, 2010. ISBN: 978-0-8155-2037-5 (cited on pages 14, 29, 32, 33, 54).

[119] K. K. Nanda, A. Maisels, F. E. Kruis, H. Fissan, and S. Stappert. "Higher Surface Energy of Free Nanoparticles". In: *Physical Review Letters* 91.10 (2003), p. 106102. DOI: 10.1103/PhysRevLett.91.106102 (cited on page 14).

[120] Nilabh K. Roy, Dipankar Behera, Obehi G. Dibua, Chee S. Foong, and Michael A. Cullinan. "A novel microscale selective laser sintering (μ-SLS) process for the fabrication of microelectronic parts". In: *Microsystems & Nanoengineering* 5.1 (2019), pp. 1–14. ISSN: 2055-7434. DOI: 10.1038/s41378-019-0116-8 (cited on page 15).

[121] Steven L. Girshick. *Nucleation of Particles from the Gas Phase*. Cambridge: Cambridge University Press, 2024. ISBN: 978-0-521-82053-0. DOI: 10.1017/9781139028851 (cited on page 15).

[122] F. Einar Kruis, Heinz Fissan, and Aaron Peled. "Synthesis of nanoparticles in the gas phase for electronic, optical and magnetic applications—a review". In: *Journal of Aerosol Science* 29.5 (1998), pp. 511–535. ISSN: 0021-8502. DOI: 10.1016/S0021-8502(97)10032-5 (cited on page 15).

[123] Mark T Swihart. "Vapor-phase synthesis of nanoparticles". In: *Current Opinion in Colloid & Interface Science* 8.1 (2003), pp. 127–133. ISSN: 1359-0294. DOI: 10.1016/S1359-0294(03)00007-4 (cited on page 15).

[124] Uwe R. Kortshagen, R. Mohan Sankaran, Rui N. Pereira, Steven L. Girshick, Jeslin J. Wu, and Eray S. Aydil. "Nonthermal Plasma Synthesis of Nanocrystals: Fundamental Principles, Materials, and Applications". In: *Chemical Reviews* 116.18 (2016), pp. 11061–11127. ISSN: 0009-2665. DOI: 10.1021/acs.chemrev.6b00039 (cited on page 15).

[125] K Wegner, P Piseri, H Vahedi Tafreshi, and P Milani. "Cluster beam deposition: a tool for nanoscale science and technology". In: *Journal of Physics D: Applied Physics* 39.22 (2006), R439–R459. ISSN: 0022-3727, 1361-6463. DOI: 10.1088/0022-3727/39/22/R02 (cited on pages 15, 30, 33, 45).

[126] Claes Granqvist, Laszlo Kish, and William Marlow, eds. *Gas Phase Nanoparticle Synthesis*. Dordrecht: Springer Netherlands, 2004. ISBN: 978-90-481-6657-2. DOI: 10.1007/978-1-4020-2444-3 (cited on pages 15, 43).

[127] Steven L. Girshick and Chia-Pin Chiu. "Kinetic nucleation theory: A new expression for the rate of homogeneous nucleation from an ideal supersaturated vapor". In: *The Journal of Chemical Physics* 93.2 (1990), pp. 1273–1277. ISSN: 0021-9606. DOI: 10.1063/1.459191 (cited on page 15).

[128] Andreas Schmidt-Ott, ed. *Spark Ablation: Building Blocks for Nanotechnology*. New York: Jenny Stanford Publishing, 2020. ISBN: 978-0-367-81709-1. DOI: 10.1201/9780367817091 (cited on pages 15, 16, 22, 27, 56).

[129] Michele L. Ostraat, Jan W. De Blauwe, Martin L. Green, L. Douglas Bell, Harry A. Atwater, and Richard C. Flagan. "Ultraclean Two-Stage Aerosol Reactor for Production of Oxide-Passivated Silicon Nanoparticles for Novel Memory Devices". In: *Journal of The Electrochemical Society* 148.5 (2001), G265. ISSN: 1945-7111. DOI: 10.1149/1.1360210 (cited on page 15).

[130] Giuseppe Sanzone, Jinlong Yin, and Hailin Sun. "Scaling up of cluster beam deposition technology for catalysis application". In: *Frontiers of Chemical Science and Engineering* 15.6 (2021), pp. 1360–1379. ISSN: 2095-0187. DOI: 10.1007/s11705-021-2101-7 (cited on page 15).

[131] Shigeki Yatsuya, Susumu Kasukabe, and Ryozi Uyeda. "Formation of Ultrafine Metal Particles by Gas Evaporation Technique. I. Aluminium in Helium". In: *Japanese Journal of Applied Physics* 12.11 (1973), p. 1675. ISSN: 1347-4065. DOI: 10.1143/JJAP.12.1675 (cited on page 15).

[132] Panagiotis Grammatikopoulos, Stephan Steinhauer, Jerome Vernieres, Vidyadhar Singh, and Mukhles Sowwan. "Nanoparticle design by gas-phase synthesis". In: *Advances in Physics: X* 1.1 (2016), pp. 81–100. DOI: 10.1080/23746149.2016.1142829 (cited on pages 15, 27).

[133] S Schwyn, E Garwin, and A Schmidt-Ott. "Aerosol generation by spark discharge". In: *Journal of Aerosol Science* 19.5 (1988), pp. 639–642. ISSN: 0021-8502. DOI: 10.1016/0021-8502(88)90215-7 (cited on page 16).

[134] Bengt O. Meuller, Maria E. Messing, David L. J. Engberg, Anna M. Jansson, Linda I. M. Johansson, Susanne M. Norlén, Nina Tureson, and Knut Deppert. "Review of Spark Discharge Generators for Production of Nanoparticle Aerosols". In: *Aerosol Science and Technology* 46.11 (2012), pp. 1256–1270. ISSN: 0278-6826, 1521-7388. DOI: 10.1080/02786826.2012.705448 (cited on pages 16, 19).

[135] *Durable Resin*. Formlabs. URL: https://formlabs.com/store/materials/durable-resin/ (cited on page 16).

[136] N. S. Tabrizi, M. Ullmann, V. A. Vons, U. Lafont, and A. Schmidt-Ott. "Generation of nanoparticles by spark discharge". In: *Journal of Nanoparticle Research* 11.2 (2009), pp. 315–332. ISSN: 1572-896X. DOI: 10.1007/s11051-008-9407-y (cited on pages 18–20, 22, 27).

[137] K. T. a. L. Burm. "Calculation of the Townsend Discharge Coefficients and the Paschen Curve Coefficients". In: *Contributions to Plasma Physics* 47.3 (2007), pp. 177–182. ISSN: 1521-3986. DOI: 10.1002/ctpp.200710025 (cited on page 18).

[138] Yangyang Fu, Peng Zhang, John P. Verboncoeur, and Xinxin Wang. "Electrical breakdown from macro to micro/nano scales: a tutorial and a review of the state of the art". In: *Plasma Research Express* 2.1 (2020). Publisher: IOP Publishing, p. 013001. ISSN: 2516-1067. DOI: 10.1088/2516-1067/ab6c84 (cited on pages 18, 82).

[139] *Criteria & Assumptions*. SkyWater SKY130 PDK Documentation. 2024. URL: https://skywater-pdk.readthedocs.io/en/main/rules/assumptions.html#process-stack-diagram (cited on pages 22, 102).

[140] Marc Ullmann, Sheldon K Friedlander, and Andreas Schmidt-Ott. "Nanoparticle Formation by Laser Ablation". en. In: *Journal of Nanoparticle Research* 4 (2002), pp. 499–509 (cited on pages 23, 25).

[141] T. G. Dietz, M. A. Duncan, D. E. Powers, and R. E. Smalley. "Laser production of supersonic metal cluster beams". In: *The Journal of Chemical Physics* 74.11 (1981), pp. 6511–6512. ISSN: 0021-9606. DOI: 10.1063/1.440991 (cited on page 23).

[142] R. E. Smalley. "Laser Studies of Metal Cluster Beams". In: *Laser Chemistry* 2.3-4 (1983). ISSN: 1476-3516. DOI: 10.1155/LC.2.167 (cited on pages 23, 25, 30, 60).

[143] John C. Miller, U. Gonser, R. M. Osgood, M. B. Panish, H. Sakaki, and Helmut K. V. Lotsch, eds. *Laser Ablation: Principles and Applications*. Vol. 28. Springer Series in Materials Science. Berlin, Heidelberg: Springer Berlin Heidelberg, 1994. ISBN: 978-3-642-78722-5. DOI: 10.1007/978-3-642-78720-1 (cited on page 23).

[144] Katherine C. Phillips, Hemi H. Gandhi, Eric Mazur, and S. K. Sundaram. "Ultrafast laser processing of materials: a review". In: *Advances in Optics and Photonics* 7.4 (2015), p. 684. ISSN: 1943-8206. DOI: 10.1364/AOP.7.000684 (cited on page 23).

[145] Shuchang Li, Suyu Li, Fangjian Zhang, Dan Tian, He Li, Dunli Liu, Yuanfei Jiang, Anmin Chen, and Mingxing Jin. "Possible evidence of Coulomb explosion in the femtosecond laser ablation of metal at low laser fluence". In: *Applied Surface Science* 355 (2015), pp. 681–685. ISSN: 0169-4332. DOI: 10.1016/j.apsusc.2015.07.136 (cited on page 23).

[146] Nick A. Shepelin, Zahra P. Tehrani, Natacha Ohannessian, Christof W. Schneider, Daniele Pergolesi, and Thomas Lippert. "A practical guide to pulsed laser deposition". In: *Chemical Society Reviews* 52.7 (2023), pp. 2294–2321. DOI: 10.1039/D2CS00938B (cited on pages 23, 62).

[147] H. Cai, N. Chaudhary, J. Lee, M. F. Becker, J. R. Brock, and J. W. Keto. "Generation of metal nanoparticles by laser ablation of microspheres". In: *Journal of Aerosol Science* 29.5 (1998), pp. 627–636. ISSN: 0021-8502. DOI: 10.1016/S0021-8502(97)00465-5 (cited on page 23).

[148] William T. Nichols, Gokul Malyavanatham, Dale E. Henneke, James R. Brock, Michael F. Becker, John W. Keto, and Howard D. Glicksman. "Gas and Pressure Dependence for the Mean Size of Nanoparticles Produced by Laser Ablation of Flowing Aerosols". In: *Journal of Nanoparticle Research* 2.2 (2000), pp. 141–145. ISSN: 1572-896X. DOI: 10.1023/A:1010014004508 (cited on page 23).

[149] J. Ma, M. F. Becker, J. W. Keto, and D. Kovar. "Laser ablation of nanoparticles and nanoparticulate, thick Fe1.92Tb0.3Dy0.7 films". In: *Journal of Materials Research* 25.9 (2010), pp. 1733–1740. ISSN: 2044-5326. DOI: 10.1557/JMR.2010.0234 (cited on pages 23, 27, 54).

[150] George Chryssolouris. *Laser Machining*. Ed. by Frederick F. Ling. Mechanical Engineering Series. New York, NY: Springer New York, 1991. ISBN: 978-1-4757-4086-8. DOI: 10.1007/978-1-4757-4084-4 (cited on page 23).

[151] *xTool 1064nm Infrared Laser Module*. xTool. 2024. URL: https://www.xtool.com/products/xtool-1064nm-infrared-laser-module (cited on page 23).

[152] M. Ehbrecht, B. Kohn, F. Huisken, M. A. Laguna, and V. Paillard. "Photoluminescence and resonant Raman spectra of silicon films produced by size-selected cluster beam deposition". In: *Physical Review B* 56.11 (1997). Publisher: American Physical Society, pp. 6958–6964. DOI: 10.1103/PhysRevB.56.6958 (cited on pages 27, 100).

[153] M. Ganeva, T. Peter, S. Bornholdt, H. Kersten, T. Strunskus, V. Zaporojtchenko, F. Faupel, and R. Hippler. "Mass Spectrometric Investigations of Nano-Size Cluster Ions Produced by High Pressure Magnetron Sputtering". In: *Contributions to Plasma Physics* 52.10 (2012), pp. 881–889. ISSN: 1521-3986. DOI: 10.1002/ctpp.201200046 (cited on page 27).

[154] Yang Lu, Jian Yu Huang, Chao Wang, Shouheng Sun, and Jun Lou. "Cold welding of ultrathin gold nanowires". In: *Nature Nanotechnology* 5.3 (2010). Publisher: Nature Publishing Group, pp. 218–224. ISSN: 1748-3395. DOI: 10.1038/nnano.2010.4 (cited on page 28).

[155] Richard Feynman, Robert Leighton, and Matthew Sands. *The Feynman Lectures on Physics, New Millennium Edition*. New York, NY: Basic Books, 2011 (cited on page 28).

[156] Bernd Rauschenbach. *Low-Energy Ion Irradiation of Materials: Fundamentals and Application*. Springer Series in Materials Science. Springer International Publishing, 2022. ISBN: 978-3-030-97276-9. DOI: 10.1007/978-3-030-97277-6 (cited on page 29).

[157] Sally E. Burke and Robert E. Continetti. "Submicrometer Particle Impact Dynamics and Chemistry". In: *Annual Review of Physical Chemistry* 75.Volume 75, 2024 (2024), pp. 67–88. ISSN: 0066-426X, 1545-1593. DOI: 10.1146/annurev-physchem-083122-122157 (cited on pages 29–31, 94).

[158] Sergei Vladimirovich Klinkov, Vladimir Fedorovich Kosarev, and Martin Rein. "Cold spray deposition: Significance of particle impact phenomena". In: *Aerospace Science and Technology* 9.7 (2005), pp. 582–591. ISSN: 1270-9638. DOI: 10.1016/j.ast.2005.03.005 (cited on pages 29, 30).

[159] H. Fuchs and H. Gleiter. "The Significance of the Impact Velocity of Vacuum-Deposited Atoms for the Structure of thin Films". In: *MRS Online Proceedings Library* 47.1 (1985), pp. 41–44. ISSN: 1946-4274. DOI: 10.1557/PROC-47-41 (cited on pages 29, 100).

[160] J A Thornton. "High Rate Thick Film Growth". In: *Annual Review of Materials Science* 7.1 (1977), pp. 239–260. ISSN: 0084-6600. DOI: 10.1146/annurev.ms.07.080177.001323 (cited on page 29).

[161] R. Messier, A. P. Giri, and R. A. Roy. "Revised structure zone model for thin film physical structure". In: *Journal of Vacuum Science & Technology A* 2.2 (1984), pp. 500–503. ISSN: 0734-2101. DOI: 10.1116/1.572604 (cited on pages 29, 32).

[162] Henry Windischmann. "Intrinsic stress in sputter-deposited thin films". In: *Critical Reviews in Solid State and Materials Sciences* 17.6 (1992), pp. 547–596. ISSN: 1040-8436. DOI: 10.1080/10408439208244586 (cited on page 29).

[163] D. W. Hoffman and M. R. Gaerttner. "Modification of evaporated chromium by concurrent ion bombardment". In: *Journal of Vacuum Science and Technology* 17.1 (1980), pp. 425–428. ISSN: 0022-5355. DOI: 10.1116/1.570473 (cited on page 29).

[164] H. Oechsner. "Sputtering—a review of some recent experimental and theoretical aspects". In: *Applied physics* 8.3 (1975), pp. 185–198. ISSN: 1432-0630. DOI: 10.1007/BF00896610 (cited on page 29).

[165] V. Franchetti, B. H. Solka, W. E. Baitinger, J. W. Amy, and R. G. Cooks. "Soft landing of ions as a means of surface modification". In: *International Journal of Mass Spectrometry and Ion Physics* 23.1 (1977), pp. 29–35. ISSN: 0020-7381. DOI: 10.1016/0020-7381(77)80004-1 (cited on pages 30, 32).

[166] Grant E. Johnson, Don Gunaratne, and Julia Laskin. "Soft- and reactive landing of ions onto surfaces: Concepts and applications". In: *Mass Spectrometry Reviews* 35.3 (2016), pp. 439–479. ISSN: 1098-2787. DOI: 10.1002/mas.21451 (cited on pages 30, 32).

[167] Alessandra Tata, Chiara Salvitti, and Federico Pepi. "From vacuum to atmospheric pressure: A review of ambient ion soft landing". In: *International Journal of Mass Spectrometry* 450 (2020), p. 116309. ISSN: 1387-3806. DOI: 10.1016/j.ijms.2020.116309 (cited on pages 30, 32).

[168] Andreas Walz, Karolina Stoiber, Annette Huettig, Hartmut Schlichting, and Johannes V. Barth. "Navigate Flying Molecular Elephants Safely to the Ground: Mass-Selective Soft Landing up to the Mega-Dalton Range by Electrospray Controlled Ion-Beam Deposition". In: *Analytical Chemistry* 94.22 (2022), p. 7767. DOI: 10.1021/acs.analchem.1c04495 (cited on pages 30, 32).

[169] Jung Y. Lee, Ailin Li, Venkateshkumar Prabhakaran, Xin Zhang, Christopher P. P. Harrilal, Libor Kovarik, Yehia M. Ibrahim, Richard D. Smith, and Sandilya V. B. Garimella. "Mobility Selective Ion Soft-Landing and Characterization Enabled Using Structures for Lossless Ion Manipulation". In: *Analytical Chemistry* 96.8 (2024), pp. 3373–3381. ISSN: 0003-2700. DOI: 10.1021/acs.analchem.3c04328 (cited on pages 30, 32, 94).

[170] Hellmut Haberland, Vitalii I. Goldanskii, Fritz Peter Schäfer, J. Peter Toennies, and Helmut K. V. Lotsch, eds. *Clusters of Atoms and Molecules*. Vol. 52. Springer Series in Chemical Physics. Berlin, Heidelberg: Springer, 1994. ISBN: 978-3-642-84331-0. DOI: 10.1007/978-3-642-84329-7 (cited on pages 30, 60).

[171] Toshinori Takagi, Isao Yamada, and Akio Sasaki. "An evaluation of metal and semiconductor films formed by ionized-cluster beam deposition". In: *Thin Solid Films* 39 (1976), pp. 207–217. ISSN: 0040-6090. DOI: 10.1016/0040-6090(76)90638-6 (cited on pages 30, 32, 105, 107).

[172] Toshinori Takagi, Isao Yamada, and Akio Sasaki. "Ionized-cluster beam deposition and epitaxy as fabrication techniques for electron devices". In: *Thin Solid Films* 45.3 (1977), pp. 569–576. ISSN: 0040-6090. DOI: 10.1016/0040-6090(77)90248-6 (cited on pages 30, 107).

[173] Toshinori Takagi. "Ionized-Cluster Beam Deposition and Epitaxy". In: *Emergent Process Methods for High-Technology Ceramics*. Ed. by Robert F. Davis, Hayne Palmour, and Richard L. Porter. Boston, MA: Springer US, 1984, pp. 425–446. ISBN: 978-1-4684-8205-8. DOI: 10.1007/978-1-4684-8205-8_32 (cited on page 30).

[174] I Yamada, H Inokawa, and T Takagi. "Aluminium epitaxy on Si(111) and Si(100) using an ionized cluster beam". In: *Thin Solid Films* 124.3 (1985), pp. 179–184. ISSN: 0040-6090. DOI: 10.1016/0040-6090(85)90263-9 (cited on page 30).

[175] Bernd Rauschenbach. "Ion Beam Figuring and Smoothing". In: *Low-Energy Ion Irradiation of Materials: Fundamentals and Application*. Ed. by Bernd Rauschenbach. Cham: Springer International Publishing, 2022, pp. 265–304. ISBN: 978-3-030-97277-6. DOI: 10.1007/978-3-030-97277-6_7 (cited on page 30).

[176] Noriaki Toyoda and Isao Yamada. "Gas Cluster Ion Beam Equipment and Applications for Surface Processing". In: *IEEE Transactions on Plasma Science* 36.4 (2008). Conference Name: IEEE Transactions on Plasma Science, pp. 1471–1488. ISSN: 1939-9375. DOI: 10.1109/TPS.2008.927266 (cited on page 30).

[177] Sean Kirkpatrick, Michael Walsh, Richard Svrluga, and Joseph Khoury. "Accelerated neutral atom beam (ANAB) technology for nanoscale surface processing". In: *2016 IEEE 16th International Conference on Nanotechnology (IEEE-NANO)*. 2016, pp. 710–713. DOI: 10.1109/NANO.2016.7751397 (cited on pages 30, 101).

[178] T. Takagi, I. Yamada, and A. Sasaki. "Ionized-cluster beam deposition". In: *Journal of Vacuum Science and Technology* 12.6 (1975), pp. 1128–1134. ISSN: 0022-5355. DOI: 10.1116/1.568474 (cited on pages 30, 56, 88).

[179] K. Yamanishi, Y. Hashimoto, and H. Tsukazaki. "Industrial applications of ICB deposition for the fabrication of electronic devices". In: *Nuclear Instruments and Methods in Physics Research Section B: Beam Interactions with Materials and Atoms*. Application of Accelerators in Research and Industry '94 99.1 (1995), pp. 233–236. ISSN: 0168-583X. DOI: 10.1016/0168-583X(95)00048-8 (cited on page 30).

[180] Morgan E. C. Miller, Michelle Mezher, Silvia De Dea, and Robert E. Continetti. "Size-Dependent Phenomena in Angle-Resolved Measurements of Submicron Sn Particle Scattering from a Molybdenum Surface". In: *The Journal of Physical Chemistry C* 126.1 (2022), pp. 356–364. ISSN: 1932-7447. DOI: 10.1021/acs.jpcc.1c07603 (cited on page 30).

[181] T. Miyakawa, R. Matsuzawa, M. Katayama, and N. Takegawa. "Reconsidering Adhesion and Bounce of Submicron Particles Upon High-Velocity Impact". In: *Aerosol Science and Technology* 47.5 (2013), pp. 472–481. ISSN: 0278-6826. DOI: 10.1080/02786826.2013.763895 (cited on page 30).

[182] Barton Dahneke. "The capture of aerosol particles by surfaces". In: *Journal of Colloid and Interface Science* 37.2 (1971), pp. 342–353. ISSN: 0021-9797. DOI: 10.1016/0021-9797(71)90302-X (cited on page 30).

[183] Raymond M. Brach and Patrick F. Dunn. "A Mathematical Model of the Impact and Adhesion of Microsphers". In: *Aerosol Science and Technology* 16.1 (1992), pp. 51–64. ISSN: 0278-6826. DOI: 10.1080/02786829208959537 (cited on page 30).

[184] Changran Liu and Hai Wang. "Nanoparticles in dilute gases: Fundamental equivalence between momentum accommodation and surface adsorption". In: *Physical Review E* 99.4 (2019). Publisher: American Physical Society, p. 042127. DOI: 10.1103/PhysRevE.99.042127 (cited on pages 30, 34, 39).

[185] D. Hanft, J. Exner, M. Schubert, T. Stöcker, P. Fuierer, and R. Moos. "An Overview of the Aerosol Deposition Method: Process Fundamentals and New Trends in Materials Applications". In: *Journal of Ceramic Science and Technology* 03 (2015). DOI: 10.4416/JCST2015-00018 (cited on pages 30, 31, 44).

[186] Tobias Schmidt, Frank Gärtner, Hamid Assadi, and Heinrich Kreye. "Development of a generalized parameter window for cold spray deposition". In: *Acta Materialia* 54.3 (2006), pp. 729–742. ISSN: 1359-6454. DOI: 10.1016/j.actamat.2005.10.005 (cited on pages 30, 32).

[187] Austin J. Andrews, Devin A. J. McGee, Ioannis Pothos, Nathan A. Bellefeuille, Kaleb A. Siekmeier, Bernard A. Olson, Thomas E. Schwartzentruber, and Christopher J. Hogan. "Characterization of surface cratering and particle deformation during high speed microparticle impact events". In: *International Journal of Impact Engineering* 180 (2023), p. 104682. ISSN: 0734-743X. DOI: 10.1016/j.ijimpeng.2023.104682 (cited on page 30).

[188] Tobias Schmidt, Hamid Assadi, Frank Gärtner, Horst Richter, Thorsten Stoltenhoff, Heinrich Kreye, and Thomas Klassen. "From Particle Acceleration to Impact and Bonding in Cold Spraying". In: *Journal of Thermal Spray Technology* 18.5-6 (2009), p. 794. ISSN: 1059-9630, 1544-1016. DOI: 10.1007/s11666-009-9357-7 (cited on pages 30, 32).

[189] Hiroaki Ashizawa, Kiyohara Masakatsu, and Katsumi Yoshida. "Microstructure and plasma corrosion behavior of yttria coatings prepared by the aerosol deposition method". In: *Journal of the American Ceramic Society* 103.12 (2020), pp. 7031–7040. ISSN: 1551-2916. DOI: 10.1111/jace.17193 (cited on page 31).

[190] Sourin Bhattacharya, Artur Lutfurakhmanov, Justin M. Hoey, Orven F. Swenson, and Rob Sailer. "Micro Cold Spray Direct Write Process". en. In: *ASME 2012 International Mechanical Engineering Congress and Exposition*. 2012, pp. 907–911. DOI: 10.1115/IMECE2012-86601 (cited on page 31).

[191] N. P. Rao, H. J. Lee, M. Kelkar, D. J. Hansen, J. V. R. Heberlein, P. H. McMurry, and S. L. Girshick. "Nanostructured materials production by hypersonic plasma particle deposition". In: *Nanostructured Materials* 9.1 (1997), pp. 129–132. ISSN: 0965-9773. DOI: 10.1016/S0965-9773(97)00035-4 (cited on page 31).

[192] J. Blum, N. Tymiak, A. Neuman, Z. Wong, N.P. Rao, S.L. Girshick, W.W. Gerberich, P.H. McMurry, and J.V.R. Heberlein. "The Effect of Substrate Temperature on the Properties of Nanostructured Silicon Carbide Films Deposited by Hypersonic Plasma Particle Deposition". In: *Journal of Nanoparticle Research* 1.1 (1999), pp. 31–42. ISSN: 1572-896X. DOI: 10.1023/A:1010033413357 (cited on pages 31, 32).

[193] F. Di Fonzo, A. Gidwani, M. H. Fan, D. Neumann, D. I. Iordanoglou, J. V. R. Heberlein, P. H. McMurry, S. L. Girshick, N. Tymiak, W. W. Gerberich, and N. P. Rao. "Focused nanoparticle-beam deposition of patterned microstructures". In: *Applied Physics Letters* 77.6 (2000), pp. 910–912. ISSN: 0003-6951. DOI: 10.1063/1.1306638 (cited on page 31).

[194] J. Hafiz, R. Mukherjee, X. Wang, P. H. McMurry, J. V. R. Heberlein, and S. L. Girshick. "Hypersonic plasma particle deposition—A hybrid between plasma spraying and vapor deposition". In: *Journal of Thermal Spray Technology* 15.4 (2006), pp. 822–826. ISSN: 1544-1016. DOI: 10.1361/105996306X146802 (cited on page 31).

[195] Hansol Kwon, Yeonju Kim, Hyungkwon Park, and Changhee Lee. "Impact Behavior for Successful Particle–Particle Bonding in Vacuum Kinetic Spraying". In: *Journal of Thermal Spray Technology* 30.3 (2021), pp. 542–557. ISSN: 1544-1016. DOI: 10.1007/s11666-020-01078-7 (cited on page 31).

[196] Doo-Man Chun and Sung-Hoon Ahn. "Deposition mechanism of dry sprayed ceramic particles at room temperature using a nano-particle deposition system". In: *Acta Materialia* 59.7 (2011), pp. 2693–2703. ISSN: 1359-6454. DOI: 10.1016/j.actamat.2011.01.007 (cited on page 31).

[197] Burton G. Cour-Palais. "Hypervelocity impact in metals, glass and composites". In: *International Journal of Impact Engineering*. Hypervelocity Impact Proceedings of the 1986 Symposium 5.1 (1987), pp. 221–237. ISSN: 0734-743X. DOI: 10.1016/0734-743X(87)90040-6 (cited on page 31).

[198] H. Shelton, C. D. Hendricks, and R. F. Wuerker. "Electrostatic Acceleration of Microparticles to Hypervelocities". In: *Journal of Applied Physics* 31.7 (1960), pp. 1243–1246. ISSN: 0021-8979, 1089-7550. DOI: 10.1063/1.1735813 (cited on pages 31, 33, 88).

[199] H. Dietzel, G. Neukum, and P. Rauser. "Micrometeoroid simulation studies on metal targets". In: *Journal of Geophysical Research (1896-1977)* 77.8 (1972), pp. 1375–1395. ISSN: 2156-2202. DOI: 10.1029/JB077i008p01375 (cited on pages 31, 88, 90).

[200] Hellmut Haberland, Zinetulla Insepov, and Michael Moseler. "Molecular-dynamics simulation of thin-film growth by energetic cluster impact". In: *Physical Review B* 51.16 (1995), pp. 11061–11067. ISSN: 0163-1829, 1095-3795. DOI: 10.1103/PhysRevB.51.11061 (cited on page 31).

[201] Pau Mestres, Johann Berthelot, Marko Spasenović, Jan Gieseler, Lukas Novotny, and Romain Quidant. "Cooling and manipulation of a levitated nanoparticle with an optical fiber trap". In: *Applied Physics Letters* 107.15 (2015), p. 151102. ISSN: 0003-6951. DOI: 10.1063/1.4933180 (cited on page 33).

[202] M. Calamai, A. Ranfagni, and F. Marin. "Transfer of a levitating nanoparticle between optical tweezers". In: *AIP Advances* 11.2 (2021), p. 025246. ISSN: 2158-3226. DOI: 10.1063/5.0024432 (cited on page 33).

[203] Jiangwei Yan, Xudong Yu, Zheng Vitto Han, Tongcang Li, and Jing Zhang. "On-demand assembly of optically levitated nanoparticle arrays in vacuum". In: *Photonics Research* 11.4 (2023). Publisher: Optica Publishing Group, pp. 600–608. ISSN: 2327-9125. DOI: 10.1364/PRJ.471547 (cited on page 33).

[204] A. V. Krasheninnikov and K. Nordlund. "Ion and electron irradiation-induced effects in nanostructured materials". In: *Journal of Applied Physics* 107.7 (2010), p. 071301. ISSN: 0021-8979. DOI: 10.1063/1.3318261 (cited on page 34).

[205] Zhigang Li and Hai Wang. "Drag force, diffusion coefficient, and electric mobility of small particles. I. Theory applicable to the free-molecule regime". In: *Physical Review E* 68.6 (2003). Publisher: American Physical Society, p. 061206. DOI: 10.1103/PhysRevE.68.061206 (cited on pages 34, 38–40, 89).

[206] Jun Wang, Junjie Su, and Guodong Xia. "Drag forces on nanoparticles in the free-molecule regime: Effect of the particle temperature". In: *Physical Review E* 101.1 (2020). Publisher: American Physical Society, p. 013103. DOI: 10.1103/PhysRevE.101.013103 (cited on pages 34, 39).

[207] John F. O'Hanlon and Timothy A. Gessert. *A Users Guide to Vacuum Technology*. en. 1st ed. Wiley, 2023. ISBN: 978-1-394-17413-3. DOI: 10.1002/9781394174232 (cited on pages 38, 42, 48, 54).

[208] R. A. Millikan. "On the Elementary Electrical Charge and the Avogadro Constant". In: *Physical Review* 2.2 (1913). Publisher: American Physical Society, pp. 109–143. DOI: 10.1103/PhysRev.2.109 (cited on page 38).

[209] Carlos Larriba-Andaluz and James S. Prell. "Fundamentals of ion mobility in the free molecular regime. Interlacing the past, present and future of ion mobility calculations". In: *International Reviews in Physical Chemistry* 39.4 (2020), pp. 569–623. ISSN: 0144-235X. DOI: 10.1080/0144235X.2020.1826708 (cited on page 39).

[210] G. A. Eiceman and Z. Karpas. *Ion Mobility Spectrometry*. 2nd ed. Boca Raton: CRC Press, 2005. ISBN: 978-0-429-19589-1. DOI: 10.1201/9781420038972 (cited on pages 39, 88, 89).

[211] Valérie Gabelica, Alexandre A. Shvartsburg, Carlos Afonso, Perdita Barran, Justin L.P. Benesch, Christian Bleiholder, Michael T. Bowers, Aivett Bilbao, Matthew F. Bush, J. Larry Campbell, Iain D.G. Campuzano, Tim Causon, Brian H. Clowers, Colin S. Creaser, Edwin De Pauw, Johann Far, Francisco Fernandez-Lima, John C. Fjeldsted, Kevin Giles, Michael Groessl, Christopher J. Hogan Jr, Stephan Hann, Hugh I. Kim, Ruwan T. Kurulugama, Jody C. May, John A. McLean, Kevin Pagel, Keith Richardson, Mark E. Ridgeway, Frédéric Rosu, Frank Sobott, Konstantinos Thalassinos, Stephen J. Valentine, and Thomas Wyttenbach. "Recommendations for reporting ion mobility Mass Spectrometry measurements". In: *Mass Spectrometry Reviews* 38.3 (2019), pp. 291–320. ISSN: 1098-2787. DOI: 10.1002/mas.21585 (cited on pages 39, 89).

[212] H. E. Revercomb and E. A. Mason. "Theory of plasma chromatography/gaseous electrophoresis. Review". In: *Analytical Chemistry* 47.7 (1975), pp. 970–983. ISSN: 0003-2700, 1520-6882. DOI: 10.1021/ac60357a043 (cited on page 39).

[213] Zhigang Li and Hai Wang. "Drag force, diffusion coefficient, and electric mobility of small particles. II. Application". In: *Physical Review E* 68.6 (2003). Publisher: American Physical Society, p. 061207. DOI: 10.1103/PhysRevE.68.061207 (cited on page 39).

[214] Peng Liu, Paul J. Ziemann, David B. Kittelson, and Peter H. McMurry. "Generating Particle Beams of Controlled Dimensions and Divergence: I. Theory of Particle Motion in Aerodynamic Lenses and Nozzle Expansions". In: *Aerosol Science and Technology* 22.3 (1995), pp. 293–313. ISSN: 0278-6826, 1521-7388. DOI: 10.1080/02786829408959748 (cited on pages 39, 45, 86).

[215] Anthony D. Appelhans and David A. Dahl. "SIMION ion optics simulations at atmospheric pressure". In: *International Journal of Mass Spectrometry* 244.1 (2005), pp. 1–14. ISSN: 1387-3806. DOI: 10.1016/j.ijms.2005.03.010 (cited on pages 40, 83).

[216] David A. Dahl, Timothy R. McJunkin, and Jill R. Scott. "Comparison of ion trajectories in vacuum and viscous environments using SIMION: Insights for instrument design". In: *International Journal of Mass Spectrometry* 266.1 (2007), pp. 156–165. ISSN: 1387-3806. DOI: 10.1016/j.ijms.2007.07.008 (cited on pages 40, 83).

[217] Vikram Suresh and Ranganathan Gopalakrishnan. "Tutorial: Langevin Dynamics methods for aerosol particle trajectory simulations and collision rate constant modeling". In: *Journal of Aerosol Science* 155 (2021), p. 105746. ISSN: 0021-8502. DOI: 10.1016/j.jaerosci.2021.105746 (cited on page 40).

[218] Ryan T. Kelly, Aleksey V. Tolmachev, Jason S. Page, Keqi Tang, and Richard D. Smith. "The ion funnel: Theory, implementations, and applications". In: *Mass Spectrometry Reviews* 29.2 (2010), pp. 294–312. ISSN: 1098-2787. DOI: 10.1002/mas.20232 (cited on pages 42, 100).

[219] Sandilya Garimella, Xiaoyu Zhou, and Zheng Ouyang. "Simulation of Rarefied Gas Flows in Atmospheric Pressure Interfaces for Mass Spectrometry Systems". In: *Journal of the American Society for Mass Spectrometry* 24.12 (2013), pp. 1890–1899. DOI: 10.1007/s13361-013-0736-4 (cited on pages 42, 44, 48).

[220] Walter Wißdorf, David Müller, Yessica Brachthäuser, Markus Langner, Valerie Derpmann, Sebastian Klopotowski, Christine Polaczek, Hendrik Kersten, Klaus Brockmann, and Thorsten Benter. "Gas Flow Dynamics in Inlet Capillaries: Evidence for non Laminar Conditions". In: *Journal of the American Society for Mass Spectrometry* 27.9 (2016), pp. 1550–1563. DOI: 10.1007/s13361-016-1415-z (cited on pages 42, 48).

[221] Nicholas Taylor and Paul B. Farnsworth. "Experimental characterization of the effect of skimmer cone design on shock formation and ion transmission efficiency in the vacuum interface of an inductively coupled plasma mass spectrometer". In: *Spectrochimica Acta Part B: Atomic Spectroscopy* 69 (2012), pp. 2–8. ISSN: 0584-8547. DOI: 10.1016/j.sab.2012.02.003 (cited on page 42).

[222] Li Li, Sudarshan K. Loyalka, Tomoya Tamadate, Deepak Sapkota, Hui Ouyang, and Christopher J. Hogan. "Measurements of the thermophoretic force on submicrometer particles in gas mixtures". In: *Journal of Aerosol Science* 178 (2024), p. 106337. ISSN: 0021-8502. DOI: 10.1016/j.jaerosci.2024.106337 (cited on page 43).

[223] Francisco J. Romay, Sho S. Takagaki, David Y. H. Pui, and Benjamin Y. H. Liu. "Thermophoretic deposition of aerosol particles in turbulent pipe flow". In: *Journal of Aerosol Science* 29.8 (1998), pp. 943–959. ISSN: 0021-8502. DOI: 10.1016/S0021-8502(98)00004-4 (cited on page 43).

[224] B. Y. H. LIU, D. Y. H. PUI, K. L. RUBOW, and W. W. SZYMANSKI. "Electrostatic Effects In Aerosol Sampling and Filtration". In: *The Annals of Occupational Hygiene* 29.2 (1985), pp. 251–269. ISSN: 0003-4878. DOI: 10.1093/annhyg/29.2.251 (cited on page 43).

[225] Kuang-Nan Chang, Yu-Kang Chen, Sheng-Hsiu Huang, Chun-Wan Chen, Chane-Yu Lai, and Chih-Chieh Chen. "Penetration of charged particles through metallic tubes". In: *Journal of Aerosol Science* 48 (2012), pp. 10–17. ISSN: 0021-8502. DOI: 10.1016/j.jaerosci.2012.01.006 (cited on page 43).

[226] K. R. May. "The Cascade Impactor: An Instrument for Sampling Coarse Aerosols". In: *Journal of Scientific Instruments* 22.10 (1945), p. 187. ISSN: 0950-7671. DOI: 10.1088/0950-7671/22/10/303 (cited on page 44).

[227] G. J. Newton, O. G. Raabe, and B. V. Mokler. "Cascade impactor design and performance". In: *Journal of Aerosol Science* 8.5 (1977), pp. 339–347. ISSN: 0021-8502. DOI: 10.1016/0021-8502(77)90021-0 (cited on page 44).

[228] Virgil A. Marple, Benjamin Y. H. Liu, and Kenneth T. Whitby. "Fluid mechanics of the laminar flow aerosol impactor". In: *Journal of Aerosol Science* 5.1 (1974), pp. 1–16. ISSN: 0021-8502. DOI: 10.1016/0021-8502(74)90002-0 (cited on page 44).

[229] Seiichiro Kashu, Eiji Fuchita, Takeshi Manabe, and Chikara Hayashi. "Deposition of Ultra Fine Particles Using a Gas Jet". In: *Japanese Journal of Applied Physics* 23.12A (1984), p. L910. ISSN: 1347-4065. DOI: 10.1143/JJAP.23.L910 (cited on page 44).

[230] J. Akedo, M. Ichiki, K. Kikuchi, and R. Maeda. "Jet molding system for realization of three-dimensional micro-structures". In: *Sensors and Actuators A: Physical* 69.1 (1998), pp. 106–112. ISSN: 0924-4247. DOI: 10.1016/S0924-4247(98)00059-4 (cited on page 44).

[231] J. Fernández De La Mora and P. Riesco-Chueca. "Aerodynamic focusing of particles in a carrier gas". In: *Journal of Fluid Mechanics* 195 (1988), pp. 1–21. ISSN: 1469-7645, 0022-1120. DOI: 10.1017/S0022112088002307 (cited on page 44).

[232] J. Fernandez de la Mora and J. Rosell-Llompart. "Aerodynamic focusing of heavy molecules in seeded supersonic jets". In: *The Journal of Chemical Physics* 91.4 (1989), pp. 2603–2615. ISSN: 0021-9606. DOI: 10.1063/1.456969 (cited on page 44).

[233] Gerhard W Israel and S. K Friedlander. "High-speed beams of small particles". In: *Journal of Colloid and Interface Science* 24 (1967), pp. 330–337. ISSN: 0021-9797. DOI: 10.1016/0021-9797(67)90258-5 (cited on page 44).

[234] A. P. Alkhimov, V. F. Kosarev, and S. V. Klinkov. "The features of cold spray nozzle design". In: *Journal of Thermal Spray Technology* 10.2 (2001), pp. 375–381. ISSN: 1544-1016. DOI: 10.1361/105996301770349466 (cited on page 45).

[235] Stephen G. Bierschenk and Desiderio Kovar. "A nozzle design for mitigating particle slowing in the bow shock region during micro-cold spray of 8 YSZ films". In: *Journal of Aerosol Science* 179 (2024), p. 106360. ISSN: 0021-8502. DOI: 10.1016/j.jaerosci.2024.106360 (cited on page 45).

[236] Tien-Chien Jen, Longjian Li, Wenzhi Cui, Qinghua Chen, and Xinming Zhang. "Numerical investigations on cold gas dynamic spray process with nano- and microsize particles". In: *International Journal of Heat and Mass Transfer* 48.21 (2005), pp. 4384–4396. ISSN: 0017-9310. DOI: 10.1016/j.ijheatmasstransfer.2005.05.008 (cited on page 45).

[237] Stephen G. Bierschenk, Michael F. Becker, and Desiderio Kovar. "Gas and ceramic particle velocities for micro-cold spray". In: *Journal of Aerosol Science* 169 (2023), p. 106113. ISSN: 0021-8502. DOI: 10.1016/j.jaerosci.2022.106113 (cited on page 45).

[238] Chenxi Li, Narendra Singh, Austin Andrews, Bernard A. Olson, Thomas E. Schwartzentruber, and Christopher J. Hogan. "Mass, momentum, and energy transfer in supersonic aerosol deposition processes". In: *International Journal of Heat and Mass Transfer* 129 (2019), pp. 1161–1171. ISSN: 0017-9310. DOI: 10.1016/j.ijheatmasstransfer.2018.10.028 (cited on page 45).

[239] Ethan B. Secor. "Principles of aerosol jet printing". In: *Flexible and Printed Electronics* 3.3 (2018). Publisher: IOP Publishing, p. 035002. ISSN: 2058-8585. DOI: 10.1088/2058-8585/aace28 (cited on page 45).

[240] A. Mette, P. L. Richter, M. Hörteis, and S. W. Glunz. "Metal aerosol jet printing for solar cell metallization". In: *Progress in Photovoltaics: Research and Applications* 15.7 (2007), pp. 621–627. ISSN: 1099-159X. DOI: 10.1002/pip.759 (cited on page 45).

[241] D. L. Schulz, J. M. Hoey, D. Thompson, O. F. Swenson, S. Han, J. Lovaasen, X. Dai, C. Braun, K. Keller, and I. S. Akhatov. "Collimated Aerosol Beam Deposition: Sub-5-um Resolution of Printed Actives and Passives". In: *IEEE Transactions on Advanced Packaging* 33.2 (2010), pp. 421–427. ISSN: 1557-9980. DOI: 10.1109/TADVP.2009.2038615 (cited on page 45).

[242] I. S. Akhatov, J. M. Hoey, O. F. Swenson, and D. L. Schulz. "Aerosol flow through a long microcapillary: collimated aerosol beam". In: *Microfluidics and Nanofluidics* 5.2 (2008), pp. 215–224. ISSN: 1613-4990. DOI: 10.1007/s10404-007-0239-3 (cited on page 45).

[243] Peng Liu, Paul J. Ziemann, David B. Kittelson, and Peter H. McMurry. "Generating Particle Beams of Controlled Dimensions and Divergence: II. Experimental Evaluation of Particle Motion in Aerody-

namic Lenses and Nozzle Expansions". In: *Aerosol Science and Technology* 22.3 (1995), pp. 314–324. ISSN: 0278-6826. DOI: 10.1080/02786829408959749 (cited on page 45).

[244] Xiaoliang Wang, Frank Einar Kruis, and Peter H. McMurry. "Aerodynamic Focusing of Nanoparticles: I. Guidelines for Designing Aerodynamic Lenses for Nanoparticles". In: *Aerosol Science and Technology* 39.7 (2005), pp. 611–623. ISSN: 0278-6826. DOI: 10.1080/02786820500181901 (cited on page 45).

[245] Xiaoliang Wang, Ashok Gidwani, Steven L. Girshick, and Peter H. McMurry. "Aerodynamic Focusing of Nanoparticles: II. Numerical Simulation of Particle Motion Through Aerodynamic Lenses". In: *Aerosol Science and Technology* 39.7 (2005), pp. 624–636. ISSN: 0278-6826. DOI: 10.1080/02786820500181950 (cited on page 45).

[246] Xuefeng Zhang, Kenneth A. Smith, Douglas R. Worsnop, Jose Jimenez, John T. Jayne, and Charles E. Kolb. "A Numerical Characterization of Particle Beam Collimation by an Aerodynamic Lens-Nozzle System: Part I. An Individual Lens or Nozzle". In: *Aerosol Science and Technology* 36.5 (2002), pp. 617–631. ISSN: 0278-6826. DOI: 10.1080/02786820252883856 (cited on page 45).

[247] Xuefeng Zhang, Kenneth A. Smith, Douglas R. Worsnop, Jose L. Jimenez, John T. Jayne, Charles E. Kolb, James Morris, and Paul Davidovits. "Numerical Characterization of Particle Beam Collimation: Part II Integrated Aerodynamic-Lens–Nozzle System". In: *Aerosol Science and Technology* 38.6 (2004), pp. 619–638. ISSN: 0278-6826. DOI: 10.1080/02786820490479833 (cited on page 45).

[248] Xiaoliang Wang and Peter H. McMurry. "Instruction Manual for the Aerodynamic Lens Calculator". In: *Aerosol Science and Technology* 40.5 (2006), pp. 1–10. ISSN: 0278-6826. DOI: 10.1080/02786820600616764 (cited on page 45).

[249] Lejun Qi, Peter H. McMurry, David J. Norris, and Steven L. Girshick. "Micropattern Deposition of Colloidal Semiconductor Nanocrystals by Aerodynamic Focusing". en. In: *Aerosol Science and Technology* 44.1 (2010), pp. 55–60. ISSN: 0278-6826, 1521-7388. DOI: 10.1080/02786820903376876 (cited on page 45).

[250] *PI (Physik Instrumente) - Solutions for Precise Motion and Positioning*. Physik Instrumente. 2024. URL: https://www.physikinstrumente.com/en/ (cited on page 49).

[251] *Xeryon: Piezo Stages & Actuators*. Xeryon. 2024. URL: https://xeryon.com/ (cited on page 49).

[252] *Precision Motion and Automation Company*. Aerotech. 2024. URL: https://www.aerotech.com/ (cited on page 49).

[253] O. Vazquez-Mena, L. Gross, S. Xie, L. G. Villanueva, and J. Brugger. "Resistless nanofabrication by stencil lithography: A review". In: *Microelectronic Engineering*. Micro and Nanofabrication Breakthroughs for Electronics, MEMS and Life Sciences 132 (2015), pp. 236–254. ISSN: 0167-9317. DOI: 10.1016/j.mee.2014.08.003 (cited on page 51).

[254] Ke Du, Junjun Ding, Yuyang Liu, Ishan Wathuthanthri, and Chang-Hwan Choi. "Stencil Lithography for Scalable Micro- and Nanomanufacturing". In: *Micromachines* 8.4 (2017), p. 131. ISSN: 2072-666X. DOI: 10.3390/mi8040131 (cited on page 51).

[255] Richard Lally, Matthias Imboden, Alexander Stange, Lawrence K. Barrett, Diego J. Perez-Morelo, and David J. Bishop. "A Fully Integrated, MEMS Based, Micro-Scale Printer for Cryogenic Thin Film Structures". In: *Journal of Microelectromechanical Systems* 32 (2023), pp. 126–135. ISSN: 1941-0158. DOI: 10.1109/JMEMS.2022.3224476 (cited on page 51).

[256] Stephen G. Bierschenk, Michael F. Becker, and Desiderio Kovar. "Effect of an oxide layer on high velocity impact of tantalum particles characterized using molecular dynamics". In: *Applied Surface Science* 640 (2023), p. 158394. ISSN: 0169-4332. DOI: 10.1016/j.apsusc.2023.158394 (cited on page 54).

[257] Xu-dong Wang and Otto S. Wolfbeis. "Optical methods for sensing and imaging oxygen: materials, spectroscopies and applications". In: *Chemical Society Reviews* 43.10 (2014), pp. 3666–3761. DOI: 10.1039/C4CS00039K (cited on page 54).

[258] Panich Intra and Nakorn Tippayawong. "An Overview of Unipolar Charger Developments for Nanoparticle Charging". In: *Aerosol and Air Quality Research* 11.2 (2011), pp. 187–209. ISSN: 2071-1409. DOI: 10.4209/aaqr.2010.10.0082 (cited on pages 56, 64–67).

[259] Hiroshi Kimura. "On the photoelectric quantum yield of small dust particles". In: *Monthly Notices of the Royal Astronomical Society* 459.3 (2016), pp. 2751–2761. ISSN: 0035-8711. DOI: 10.1093/mnras/stw820 (cited on pages 56, 60).

[260] Paul J. Ziemann, Peng Liu, David B. Kittelson, and Peter H. McMurry. "Electron Impact Charging Properties of Size-Selected, Submicrometer Organic Particles". In: *The Journal of Physical Chemistry* 99.14 (1995). Publisher: American Chemical Society, pp. 5126–5138. ISSN: 0022-3654. DOI: 10.1021/j100014a037 (cited on page 56).

[261] Paul J. Ziemann, Peng Liu, Nagaraja P. Rao, David B. Kittelson, and Peter H. McMurry. "Particle beam mass spectrometry of submicron particles charged to saturation in an electron beam". In: *Journal of Aerosol Science* 26.5 (1995), pp. 745–756. ISSN: 0021-8502. DOI: 10.1016/0021-8502(95)00009-2 (cited on page 56).

[262] M. M. Abbas, D. Tankosic, P. D. Craven, A. C. LeClair, and J. F. Spann. "Lunar dust grain charging by electron impact: complex role of secondary electron emissions in space environments". In: *The Astrophysical Journal* 718.2 (2010). Publisher: The American Astronomical Society, p. 795. ISSN: 0004-637X. DOI: 10.1088/0004-637X/718/2/795 (cited on page 56).

[263] G. Mainfray and G. Manus. "Multiphoton ionization of atoms". In: *Reports on Progress in Physics* 54.10 (1991), p. 1333. ISSN: 0034-4885. DOI: 10.1088/0034-4885/54/10/002 (cited on page 58).

[264] David M. Wood. "Classical Size Dependence of the Work Function of Small Metallic Spheres". In: *Physical Review Letters* 46.11 (1981). Publisher: American Physical Society, pp. 749–749. DOI: 10.1103/PhysRevLett.46.749 (cited on page 58).

[265] A. Schmidt-Ott, P. Schurtenberger, and H. C. Siegmann. "Enormous Yield of Photoelectrons from Small Particles". In: *Physical Review Letters* 45.15 (1980). Publisher: American Physical Society, pp. 1284–1287. DOI: 10.1103/PhysRevLett.45.1284 (cited on pages 58, 60).

[266] Walt A. de Heer. "The physics of simple metal clusters: experimental aspects and simple models". In: *Reviews of Modern Physics* 65.3 (1993). Publisher: American Physical Society, pp. 611–676. DOI: 10.1103/RevModPhys.65.611 (cited on page 60).

[267] U. Müller, A. Schmidt-Ott, and H. Burtscher. "Photoelectric quantum yield of free silver particles near threshold". In: *Zeitschrift für Physik B Condensed Matter* 73.1 (1988), pp. 103–106. ISSN: 1431-584X. DOI: 10.1007/BF01312160 (cited on pages 60, 64).

[268] Tsung-Chi Hsu, Yu-Tsai Teng, Yen-Wei Yeh, Xiaotong Fan, Kuo-Hsiung Chu, Su-Hui Lin, Kuo-Kuang Yeh, Po-Tsung Lee, Yue Lin, Zhong Chen, Tingzhu Wu, and Hao-Chung Kuo. "Perspectives on UVC LED: Its Progress and Application". In: *Photonics* 8.6 (2021), p. 196. ISSN: 2304-6732. DOI: 10.3390/photonics8060196 (cited on pages 61, 62).

[269] E. A. Sosnin and D. A. Sorokin. "Current Sources of Vacuum Ultraviolet Radiation: State and Prospects (A Review)". In: *Plasma Physics Reports* 50.7 (2024), pp. 880–893. ISSN: 1562-6938. DOI: 10.1134/S1063780X24601068 (cited on pages 61, 62).

[270] Melanie Johnson, Andras Bodi, Lothar Schulz, and Thomas Gerber. "Vacuum ultraviolet beamline at the Swiss Light Source for chemical dynamics studies". In: *Nuclear Instruments and Methods in Physics Research Section A: Accelerators, Spectrometers, Detectors and Associated Equipment* 610.2 (2009), pp. 597–603. ISSN: 0168-9002. DOI: 10.1016/j.nima.2009.08.069 (cited on page 62).

[271] W. R. Hunter and S. A. Malo. "The temperature dependence of the short wavelength transmittance limit of vacuum ultraviolet window materials—I. Experiment". In: *Journal of Physics and Chemistry of Solids* 30.12 (1969), pp. 2739–2745. ISSN: 0022-3697. DOI: 10.1016/0022-3697(69)90047-X (cited on page 62).

[272] James E. Whitten. "Ultraviolet photoelectron spectroscopy: Practical aspects and best practices". In: *Applied Surface Science Advances* 13 (2023), p. 100384. ISSN: 2666-5239. DOI: 10.1016/j.apsadv.2023.100384 (cited on page 62).

[273] Dirk Basting and Gerd Marowsky, eds. *Excimer Laser Technology*. Berlin, Heidelberg: Springer, 2005. ISBN: 978-3-540-20056-7. DOI: 10.1007/b137894 (cited on page 62).

[274] Ian W. Boyd, Jun-Ying Zhang, and Ulrich Kogelschatz. "Development and Applications of UV Excimer Lamps". In: *Photo-Excited Processes, Diagnostics and Applications: Fundamentals and Advanced Topics*. Ed. by A. Peled. Boston, MA: Springer US, 2003, pp. 161–199. ISBN: 978-1-4020-2610-2. DOI: 10.1007/1-4020-2610-2_6 (cited on page 62).

[275] Mikhail I. Lomaev, V. S. Skakun, E. A. Sosnin, Viktor F. Tarasenko, D. V. Shitts, and M. V. Erofeev. "Excilamps: efficient sources of spontaneous UV and VUV radiation". In: *Physics-Uspekhi* 46.2 (2003). Publisher: IOP Publishing, p. 193. ISSN: 1063-7869. DOI: 10.1070/PU2003v046n02ABEH001308 (cited on page 62).

[276] E. A. Sosnin and D. A. Sorokin. "Current Sources of Vacuum Ultraviolet Radiation: State and Prospects (A Review)". In: *Plasma Physics Reports* 50.7 (2024), pp. 880–893. ISSN: 1562-6938. DOI: 10.1134/S1063780X24601068 (cited on page 62).

[277] Michael Meißer. "Resonant Behaviour of Pulse Generators for the Efficient Drive of Optical Radiation Sources Based on Dielectric Barrier Discharges". PhD thesis. Karlsruher Institut für Technologie, 2013 (cited on pages 62, 63, 67).

[278] John M. Gray, Jason Bossert, Yomay Shyur, Ben Saarel, Travis C. Briles, and H. J. Lewandowski. "Characterization of a vacuum ultraviolet light source at 118 nm". In: *The Journal of Chemical Physics* 154.2 (2021), p. 024201. ISSN: 0021-9606. DOI: 10.1063/5.0033135 (cited on page 62).

[279] Michael Kneissl, Tae-Yeon Seong, Jung Han, and Hiroshi Amano. "The emergence and prospects of deep-ultraviolet light-emitting diode technologies". In: *Nature Photonics* 13.4 (2019), pp. 233–244. ISSN: 1749-4893. DOI: 10.1038/s41566-019-0359-9 (cited on page 62).

[280] Hiroshi Amano, Ramón Collazo, Carlo De Santi, Sven Einfeldt, Mitsuru Funato, Johannes Glaab, Sylvia Hagedorn, Akira Hirano, Hideki Hirayama, Ryota Ishii, Yukio Kashima, Yoichi Kawakami, Ronny Kirste, Michael Kneissl, Robert Martin, Frank Mehnke, Matteo Meneghini, Abdallah Ougazzaden, Peter J. Parbrook, Siddharth Rajan, Pramod Reddy, Friedhard Römer, Jan Ruschel, Biplab Sarkar, Ferdinand Scholz, Leo J. Schowalter, Philip Shields, Zlatko Sitar, Luca Sulmoni, Tao Wang, Tim Wernicke, Markus Weyers, Bernd Witzigmann, Yuh-Renn Wu, Thomas Wunderer, and Yuewei Zhang. "The 2020 UV emitter roadmap". In: *Journal of Physics D: Applied Physics* 53.50 (2020), p. 503001. ISSN: 0022-3727. DOI: 10.1088/1361-6463/aba64c (cited on page 62).

[281] *UV LEDs*. Marktech Optoelectronics. URL: https://marktechopto.com/led-emitters/uv-leds/ (cited on page 62).

[282] P. A. Heimann, M. Koike, C. W. Hsu, D. Blank, X. M. Yang, A. G. Suits, Y. T. Lee, M. Evans, C. Y. Ng, C. Flaim, and H. A. Padmore. "Performance of the vacuum ultraviolet high-resolution and high-flux beamline for chemical dynamics studies at the Advanced Light Source". In: *Review of Scientific Instruments* 68.5 (1997), pp. 1945–1951. ISSN: 0034-6748. DOI: 10.1063/1.1148082 (cited on page 62).

[283] Tomas Baer. "Vacuum UV Photophysics and Photoionization Spectroscopy". In: *Annual Review of Physical Chemistry* 40.Volume 40, (1989). Publisher: Annual Reviews, pp. 637–669. ISSN: 0066-426X, 1545-1593. DOI: 10.1146/annurev.pc.40.100189.003225 (cited on page 62).

[284] *XERADEX - excimer lamps made by Radium*. Radium. URL: https://www.radium.de/en/products/xeradexr (cited on page 63).

[285] Jinhong Kim, Andrey E. Mironov, Jin H. Cho, Dane S. Sievers, Cyrus M. Herring, Sehyun Park, Peter P. Sun, Zhihu Liang, Wenyuan Chen, Sung-Jin Park, and J. Gary Eden. "Commercialization of microcavity plasma devices and arrays: Systems for VUV photolithography and nanopatterning, disinfection of drinking water and air, and biofilm deactivation for medical therapeutics". In: *Plasma Processes and Polymers* 19.10 (2022), p. 2200075. ISSN: 1612-8869. DOI: 10.1002/ppap.202200075 (cited on page 63).

[286] H. Burtscher, L. Scherrer, H. C. Siegmann, A. Schmidt-Ott, and B. Federer. "Probing aerosols by photoelectric charging". In: *Journal of Applied Physics* 53.5 (1982), pp. 3787–3791. ISSN: 0021-8979. DOI: 10.1063/1.331120 (cited on pages 63, 64).

[287] Alex G. Harrison. *Chemical Ionization Mass Spectrometry*. 2nd ed. New York: Routledge, 2017. ISBN: 978-1-315-13912-8. DOI: 10.1201/9781315139128 (cited on page 63).

[288] D. M. P. Holland, K. Codling, G. V. Marr, and J. B. West. "Multiple photoionisation in the rare gases from threshold to 280 eV". In: *Journal of Physics B: Atomic and Molecular Physics* 12.15 (1979), p. 2465. ISSN: 0022-3700. DOI: 10.1088/0022-3700/12/15/008 (cited on page 63).

[289] L. J. Kieffer and Gordon H. Dunn. "Electron Impact Ionization Cross-Section Data for Atoms, Atomic Ions, and Diatomic Molecules: I. Experimental Data". In: *Reviews of Modern Physics* 38.1 (1966), pp. 1–35. DOI: 10.1103/RevModPhys.38.1 (cited on page 63).

[290] Thomas J Krinke, Knut Deppert, Martin H Magnusson, Frank Schmidt, and Heinz Fissan. "Microscopic aspects of the deposition of nanoparticles from the gas phase". In: *Journal of Aerosol Science* 33.10 (2002), pp. 1341–1359. ISSN: 0021-8502. DOI: 10.1016/S0021-8502(02)00074-5 (cited on pages 64, 100).

[291] D. Matter, M. Mohr, W. Fendel, A. Schmidt-Ott, and H. Burtscher. "Multiple wavelength aerosol photoemission by excimer lamps". In: *Journal of Aerosol Science* 26.7 (1995), pp. 1101–1115. ISSN: 0021-8502. DOI: 10.1016/0021-8502(95)00040-J (cited on page 64).

[292] D. A. Gobeli, J. J. Yang, and M. A. El-Sayed. "Laser multiphoton ionization-dissociation mass spectrometry". In: *Chemical Reviews* 85.6 (1985), pp. 529–554. DOI: 10.1021/cr00070a002 (cited on page 64).

[293] Dieter Gerlich. "Inhomogeneous RF Fields: A Versatile Tool for the Study of Processes with Slow Ions". In: *Advances in Chemical Physics*. John Wiley & Sons, Ltd, 1992, pp. 1–176. ISBN: 978-0-470-14139-7. DOI: 10.1002/9780470141397.ch1 (cited on pages 64, 151–153, 157, 161).

[294] Martin Hessling, Robin Haag, Nicole Sieber, and Petra Vatter. "The impact of far-UVC radiation (200–230 nm) on pathogens, cells, skin, and eyes – a collection and analysis of a hundred years of data". In: *GMS Hygiene and Infection Control* 16 (2021), Doc07. DOI: 10.3205/dgkh000378 (cited on page 64).

[295] *Nukit Torch Far-UVC Lights (Set of Four)*. Nukit 222. 2024. URL: https://www.nukit222.com/products/torch-far-uvc-lights-set (cited on page 64).

[296] Martin Reiser. *Theory and Design of Charged Particle Beams*. Wiley, 2008 (cited on pages 69, 73, 75, 76, 83, 86, 94, 103, 104).

[297] *SIMION Ion and Electron Optics Simulator*. Adaptas Solutions. 2024. URL: https://simion.com/ (cited on page 72).

[298] *Python (programming language)*. Python Software Foundation. 2024. URL: https://www.python.org/ (cited on page 72).

[299] *blender.org - Home of the Blender project - Free and Open 3D Creation Software*. Blender Foundation. 2024. URL: https://www.blender.org/ (cited on page 72).

[300] Hector Rusinque, Elena Fedianina, Alfred Weber, and Gunther Brenner. "Numerical study of the controlled electrodeposition of charged nanoparticles in an electric field". In: *Journal of Aerosol Science* 129 (2019), pp. 28–39. ISSN: 0021-8502. DOI: 10.1016/j.jaerosci.2018.11.005 (cited on page 73).

[301] J.-W. Kim, Y. Yamagata, B. J. Kim, and T. Higuchi. "Direct and dry micro-patterning of nanoparticles by electrospray deposition through a micro-stencil mask". In: *Journal of Micromechanics and Microengineering* 19.2 (2009), p. 025021. ISSN: 0960-1317. DOI: 10.1088/0960-1317/19/2/025021 (cited on page 73).

[302] Wei-Cheng Yan, Jingwei Xie, and Chi-Hwa Wang. "Electrical Field Guided Electrospray Deposition for Production of Gradient Particle Patterns". In: *ACS Applied Materials & Interfaces* 10.22 (2018), pp. 18499–18506. ISSN: 1944-8244. DOI: 10.1021/acsami.8b02914 (cited on page 73).

[303] Huihui Xia, Boyang Yu, Kai Chang, Xinyan Zhao, and Weiwei Deng. "Shaping electrospray deposition profile by a quadrupole: From circular to elliptical patterns". In: *Journal of Aerosol Science* 154 (2021), p. 105739. ISSN: 0021-8502. DOI: 10.1016/j.jaerosci.2020.105739 (cited on page 73).

[304] Jon Orloff, ed. *Handbook of Charged Particle Optics*. 2nd ed. Boca Raton: CRC Press, 2017. ISBN: 978-1-315-21988-2. DOI: 10.1201/9781420045550 (cited on pages 73, 76, 104).

[305] Miklos Szilagyi. *Electron and Ion Optics*. Boston, MA: Springer US, 1988. ISBN: 978-1-4612-8247-1. DOI: 10.1007/978-1-4613-0923-9 (cited on pages 73, 74, 100).

[306] Hermann Wollnik. "Ion optics in mass spectrometers". In: *Journal of Mass Spectrometry* 34.10 (1999), pp. 991–1006. ISSN: 1096-9888. DOI: 10.1002/(SICI)1096-9888(199910)34:10<991::AID-JMS870>3.0.CO;2-1 (cited on page 73).

[307] Christoph Weißbäcker and Harald Rose. "Electrostatic correction of the chromatic and of the spherical aberration of charged-particle lenses". In: *Journal of Electron Microscopy* 50.5 (2001), pp. 383–390. ISSN: 0022-0744. DOI: 10.1093/jmicro/50.5.383 (cited on page 74).

[308] Robert Saf, Marian Goriup, Thomas Steindl, Thomas E. Hamedinger, Daniel Sandholzer, and Gertraude Hayn. "Thin organic films by atmospheric-pressure ion deposition". In: *Nature Materials* 3.5 (2004), pp. 323–329. ISSN: 1476-4660. DOI: 10.1038/nmat1117 (cited on page 74).

[309] Elham Vakil Asadollahei and Manuel Gamero-Castaño. "Investigation of the electrostatic focusing of beams of electrosprayed nanodroplets for microfabrication applications". In: *AIP Advances* 9.12 (2019), p. 125006. ISSN: 2158-3226. DOI: 10.1063/1.5128113 (cited on page 74).

[310] Klaus Floettmann. "Some basic features of the beam emittance". In: *Physical Review Special Topics - Accelerators and Beams* 6.3 (2003). Publisher: American Physical Society, p. 034202. DOI: 10.1103/PhysRevSTAB.6.034202 (cited on page 76).

[311] C. A. Brau. "What brightness means". In: *The Physics and Applications of High Brightness Electron Beams*. World Scientific, 2003, pp. 20–27. ISBN: 978-981-238-726-4. DOI: 10.1142/9789812705235_0002 (cited on page 76).

[312] P. Kruit, M. Bezuijen, and J. E. Barth. "Source brightness and useful beam current of carbon nanotubes and other very small emitters". In: *Journal of Applied Physics* 99.2 (2006), p. 024315. ISSN: 0021-8979. DOI: 10.1063/1.2162270 (cited on page 76).

[313] IW Drummond. "The ion optics of low-energy ion beams". In: *Vacuum*. Vacuum Special Issue: Proceedings of the 3rd International Conference on Low Energy Ion Beams Loughborough University of Technology, UK 34.1 (1984), pp. 51–61. ISSN: 0042-207X. DOI: 10.1016/0042-207X(84)90107-6 (cited on pages 76, 104).

[314] Julio Chaves. *Introduction to nonimaging optics*. Second edition. Boca Raton: CRC Press/Taylor & Francis, 2016. ISBN: 978-1-4822-0673-9 (cited on pages 76, 77).

[315] W. H. Steel. "Luminosity, Throughput, or Etendue?" In: *Applied Optics* 13.4 (1974), pp. 704–705. ISSN: 2155-3165. DOI: 10.1364/AO.13.000704 (cited on page 76).

[316] A G Ruggiero. "Are We Beating Liouville's Theorem?" In: *Proceedings of the Workshop on Producing High Luminosity High Energy Proton-Antiproton Collisions*. Berkeley, 1978, p. 123 (cited on page 78).

[317] Taeman Kim. "Buffer gas cooling of ions in a radio frequency quadrupole ion guide : a study of the cooling process and cooled beam properties". Thesis. McGill University, 1997. URL: https://escholarship.mcgill.ca/concern/theses/p5547t229 (cited on pages 78, 80, 83, 88).

[318] A. N. Skrinskii and V. V. Parkhomchuk. "Methods of cooling beams of charged particles". In: *Soviet journal of particles and nuclei* 12.3 (1981) (cited on pages 78, 79).

[319] Dieter Möhl and Andrew M. Sessler. "Beam cooling: principles and achievements". In: *Nuclear Instruments and Methods in Physics Research Section A: Accelerators, Spectrometers, Detectors and Associated Equipment*. International Workshop on Beam Cooling and Related Topics 532.1 (2004), pp. 1–10. ISSN: 0168-9002. DOI: 10.1016/j.nima.2004.06.102 (cited on pages 78, 79).

[320] Wayne M. Itano, J. C. Bergquist, J. J. Bollinger, and D. J. Wineland. "Cooling methods in ion traps". In: *Physica Scripta* 1995.T59 (1995), p. 106. ISSN: 1402-4896. DOI: 10.1088/0031-8949/1995/T59/013 (cited on page 78).

[321] Wolfgang Paul. "Electromagnetic traps for charged and neutral particles". In: *Reviews of Modern Physics* 62.3 (1990), pp. 531–540. DOI: 10.1103/RevModPhys.62.531 (cited on pages 78–80, 152, 153, 157).

[322] D. Gerlich. "Molecular Ions and Nanoparticles in RF and AC Traps". In: *Hyperfine Interactions* 146.1 (2003), pp. 293–306. ISSN: 1572-9540. DOI: 10.1023/B:HYPE.0000004210.79490.b1 (cited on page 78).

[323] Eric R. Hudson. "Sympathetic cooling of molecular ions with ultracold atoms". In: *EPJ Techniques and Instrumentation* 3.1 (2016), p. 8. ISSN: 2195-7045. DOI: 10.1140/epjti/s40485-016-0035-0 (cited on pages 78, 79, 85).

[324] David Lunney, Cyril Bachelet, Céline Guénaut, Sylvain Henry, and Michael Sewtz. "COLETTE: A linear Paul-trap beam cooler for the on-line mass spectrometer MISTRAL". In: *Nuclear Instruments and Methods in Physics Research Section A: Accelerators, Spectrometers, Detectors and Associated Equipment* 598.2 (2009), pp. 379–387. ISSN: 0168-9002. DOI: 10.1016/j.nima.2008.09.050 (cited on pages 78, 80, 88).

[325] Nicholas R. Hutzler, Hsin-I Lu, and John M. Doyle. "The Buffer Gas Beam: An Intense, Cold, and Slow Source for Atoms and Molecules". In: *Chemical Reviews* 112.9 (2012), pp. 4803–4827. ISSN: 0009-2665. DOI: 10.1021/cr200362u (cited on pages 78, 86).

[326] Aleksey V. Tolmachev, Harold R. Udseth, and Richard D. Smith. "Radial stratification of ions as a function of mass to charge ratio in collisional cooling radio frequency multipoles used as ion guides or ion traps". In: *Rapid Communications in Mass Spectrometry* 14.20 (2000), pp. 1907–1913. ISSN: 1097-0231. DOI: 10.1002/1097-0231(20001030)14:20<1907::AID-RCM111>3.0.CO;2-M (cited on pages 78, 85).

[327] D. J. Douglas and J. B. French. "Collisional focusing effects in radio frequency quadrupoles". In: *Journal of the American Society for Mass Spectrometry* 3.4 (1992), pp. 398–408. ISSN: 1044-0305. DOI: 10.1016/1044-0305(92)87067-9 (cited on page 78).

[328] Bruce A Thomson. "1997 McBryde Medal Award Lecture Radio frequency quadrupole ion guides in modern mass spectrometry". In: *Canadian Journal of Chemistry* 76.5 (1998). Publisher: NRC Research Press, pp. 499–505. ISSN: 0008-4042. DOI: 10.1139/v98-073 (cited on pages 78, 80, 88).

[329] Harold J. Metcalf and Peter Van Der Straten. *Laser Cooling and Trapping*. Ed. by R. Stephen Berry, Joseph L. Birman, Jeffrey W. Lynn, Mark P. Silverman, H. Eugene Stanley, and Mikhail Voloshin. Graduate Texts in Contemporary Physics. New York, NY: Springer, 1999. ISBN: 978-0-387-98728-6. DOI: 10.1007/978-1-4612-1470-0 (cited on page 79).

[330] Peter Asenbaum, Stefan Kuhn, Stefan Nimmrichter, Ugur Sezer, and Markus Arndt. "Cavity cooling of free silicon nanoparticles in high vacuum". In: *Nature Communications* 4.1 (2013), p. 2743. ISSN: 2041-1723. DOI: 10.1038/ncomms3743 (cited on page 79).

[331] Thomas Salzburger and Helmut Ritsch. "Collective transverse cavity cooling of a dense molecular beam". In: *New Journal of Physics* 11.5 (2009), p. 055025. ISSN: 1367-2630. DOI: 10.1088/1367-2630/11/5/055025 (cited on page 79).

[332] Markus Aspelmeyer, Tobias J. Kippenberg, and Florian Marquardt. "Cavity optomechanics". In: *Reviews of Modern Physics* 86.4 (2014), pp. 1391–1452. DOI: 10.1103/RevModPhys.86.1391 (cited on page 79).

[333] P. F. Barker and M. N. Shneider. "Cavity cooling of an optically trapped nanoparticle". In: *Physical Review A* 81.2 (2010), p. 023826. DOI: 10.1103/PhysRevA.81.023826 (cited on page 79).

[334] J. Millen, P. Z. G. Fonseca, T. Mavrogordatos, T. S. Monteiro, and P. F. Barker. "Cavity Cooling a Single Charged Levitated Nanosphere". In: *Physical Review Letters* 114.12 (2015), p. 123602. DOI: 10.1103/PhysRevLett.114.123602 (cited on page 79).

[335] J. Millen, S. Kuhn, F. Patolsky, A. Kosloff, and M. Arndt. "Cooling and manipulation of nanoparticles in high vacuum". In: *Optical Trapping and Optical Micromanipulation XIII*. Vol. 9922. SPIE, 2016, pp. 41–48. DOI: 10.1117/12.2238753 (cited on page 79).

[336] A. Pontin, H. Fu, M. Toroš, T. S. Monteiro, and P. F. Barker. "Simultaneous cavity cooling of all six degrees of freedom of a levitated nanoparticle". In: *Nature Physics* 19.7 (2023), pp. 1003–1008. ISSN: 1745-2481. DOI: 10.1038/s41567-023-02006-6 (cited on page 79).

[337] Christian Schneider, Steven J. Schowalter, Kuang Chen, Scott T. Sullivan, and Eric R. Hudson. "Laser-Cooling-Assisted Mass Spectrometry". In: *Physical Review Applied* 2.3 (2014), p. 034013. DOI: 10.1103/PhysRevApplied.2.034013 (cited on page 79).

[338] Lowell S. Brown and Gerald Gabrielse. "Geonium theory: Physics of a single electron or ion in a Penning trap". In: *Reviews of Modern Physics* 58.1 (1986), pp. 233–311. DOI: 10.1103/RevModPhys.58.233 (cited on page 79).

[339] Jan Gieseler, Bradley Deutsch, Romain Quidant, and Lukas Novotny. "Subkelvin Parametric Feedback Cooling of a Laser-Trapped Nanoparticle". In: *Physical Review Letters* 109.10 (2012). Publisher: American Physical Society, p. 103603. DOI: 10.1103/PhysRevLett.109.103603 (cited on page 79).

[340] Felix Tebbenjohanns, Martin Frimmer, Andrei Militaru, Vijay Jain, and Lukas Novotny. "Cold Damping of an Optically Levitated Nanoparticle to Microkelvin Temperatures". In: *Physical Review Letters* 122.22 (2019), p. 223601. ISSN: 0031-9007, 1079-7114. DOI: 10.1103/PhysRevLett.122.223601 (cited on page 79).

[341] Gerard P. Conangla, Francesco Ricci, Marc T. Cuairan, Andreas W. Schell, Nadine Meyer, and Romain Quidant. "Optimal Feedback Cooling of a Charged Levitated Nanoparticle with Adaptive Control". In: *Physical Review Letters* 122.22 (2019), p. 223602. ISSN: 0031-9007, 1079-7114. DOI: 10.1103/PhysRevLett.122.223602 (cited on page 79).

[342] Lorenzo Dania, Dmitry S. Bykov, Matthias Knoll, Pau Mestres, and Tracy E. Northup. "Optical and electrical feedback cooling of a silica nanoparticle levitated in a Paul trap". In: *Physical Review Research* 3.1 (2021), p. 013018. DOI: 10.1103/PhysRevResearch.3.013018 (cited on page 79).

[343] Y. Minowa, K. Kato, S. Ueno, T. W. Penny, A. Pontin, M. Ashida, and P. F. Barker. "Imaging-based feedback cooling of a levitated nanoparticle". In: *Review of Scientific Instruments* 93.7 (2022), p. 075109. ISSN: 0034-6748. DOI: 10.1063/5.0095614 (cited on page 79).

[344] D. Möhl, G. Petrucci, L. Thorndahl, and S. van der Meer. "Physics and technique of stochastic cooling". In: *Physics Reports* 58.2 (1980), pp. 73–102. ISSN: 0370-1573. DOI: 10.1016/0370-1573(80)90140-4 (cited on page 79).

[345] John Marriner. "Stochastic cooling overview". In: *Nuclear Instruments and Methods in Physics Research Section A: Accelerators, Spectrometers, Detectors and Associated Equipment*. International Workshop on Beam Cooling and Related Topics 532.1 (2004), pp. 11–18. ISSN: 0168-9002. DOI: 10.1016/j.nima.2004.06.025 (cited on page 79).

[346] S. van der Meer. "Stochastic cooling and the accumulation of antiprotons". In: *Reviews of Modern Physics* 57.3 (1985), pp. 689–697. DOI: 10.1103/RevModPhys.57.689 (cited on page 79).

[347] Paul Emma and Tor Raubenhemier. "Systematic approach to damping ring design". In: *Physical Review Special Topics - Accelerators and Beams* 4.2 (2001). Publisher: American Physical Society, p. 021001. DOI: 10.1103/PhysRevSTAB.4.021001 (cited on page 79).

[348] V. V. Parkhomchuk and Aleksandr N. Skrinskiĭ. "Electron cooling: 35 years of development". In: *Physics-Uspekhi* 43.5 (2000), p. 433. ISSN: 1063-7869. DOI: 10.1070/PU2000v043n05ABEH000741 (cited on page 79).

[349] Helmut Poth. "Electron cooling: Theory, experiment, application". In: *Physics Reports* 196.3 (1990), pp. 135–297. ISSN: 0370-1573. DOI: 10.1016/0370-1573(90)90040-9 (cited on page 79).

[350] M. Bogomilov et al. "Demonstration of cooling by the Muon Ionization Cooling Experiment". In: *Nature* 578.7793 (2020), pp. 53–59. ISSN: 1476-4687. DOI: 10.1038/s41586-020-1958-9 (cited on page 79).

[351] B. M. Penetrante, J. N. Bardsley, M. A. Levine, D. A. Knapp, and R. E. Marrs. "Evaporative cooling of highly charged dysprosium ions in an enhanced electron-beam ion trap". In: *Physical Review A* 43.9 (1991), pp. 4873–4882. DOI: 10.1103/PhysRevA.43.4873 (cited on page 79).

[352] E. Mandonnet, A. Minguzzi, R. Dum, I. Carusotto, Y. Castin, and J. Dalibard. "Evaporative cooling of an atomic beam". In: *The European Physical Journal D - Atomic, Molecular, Optical and Plasma Physics* 10.1 (2000), pp. 9–18. ISSN: 1434-6079. DOI: 10.1007/s100530050521 (cited on page 79).

[353] M. Hobein, A. Solders, M. Suhonen, Y. Liu, and R. Schuch. "Evaporative Cooling and Coherent Axial Oscillations of Highly Charged Ions in a Penning Trap". In: *Physical Review Letters* 106.1 (2011), p. 013002. DOI: 10.1103/PhysRevLett.106.013002 (cited on page 79).

[354] F Herfurth, J Dilling, A Kellerbauer, G Bollen, S Henry, H. -J Kluge, E Lamour, D Lunney, R. B Moore, C Scheidenberger, S Schwarz, G Sikler, and J Szerypo. "A linear radiofrequency ion trap for accumulation, bunching, and emittance improvement of radioactive ion beams". In: *Nuclear Instruments and Methods in Physics Research Section A: Accelerators, Spectrometers, Detectors and Associated Equipment* 469.2 (2001), pp. 254–275. ISSN: 0168-9002. DOI: 10.1016/S0168-9002(01)00168-1 (cited on pages 80, 88).

[355] Omar Gianfrancesco. "Design principles of a high field RFQ device for ion cooling and confinement". Thesis. McGill University, 2002. URL: https://escholarship.mcgill.ca/concern/theses/p5547s06q (cited on pages 80, 82, 83, 96, 157).

[356] T. Brunner, M. J. Smith, M. Brodeur, S. Ettenauer, A. T. Gallant, V. V. Simon, A. Chaudhuri, A. Lapierre, E. Mané, R. Ringle, M. C. Simon, J. A. Vaz, P. Delheij, M. Good, M. R. Pearson, and J. Dilling. "TITAN's digital RFQ ion beam cooler and buncher, operation and performance". In: *Nuclear Instruments and Methods in Physics Research Section A: Accelerators, Spectrometers, Detectors and Associated Equipment* 676 (2012), pp. 32–43. ISSN: 0168-9002. DOI: 10.1016/j.nima.2012.02.004 (cited on pages 80, 88, 94, 99).

[357] Ramzi Boussaid, Young-Ho Park, and Sergey Kondrashev. "Technical design of RISP RFQ Cooler buncher". In: *Journal of the Korean Physical Society* 71.11 (2017), pp. 848–854. ISSN: 1976-8524. DOI: 10.3938/jkps.71.848 (cited on pages 80, 82, 88, 94, 99).

[358] Peter H. Dawson, ed. *Quadrupole Mass Spectrometry and its Applications*. Elsevier, 1976. ISBN: 978-0-444-41345-1. DOI: 10.1016/B978-0-444-41345-1.50001-0 (cited on pages 80, 154, 157).

[359] Raymond E. March. "An Introduction to Quadrupole Ion Trap Mass Spectrometry". In: *Journal of Mass Spectrometry* 32.4 (1997), pp. 351–369. ISSN: 1096-9888. DOI: 10.1002/(SICI)1096-9888(199704)32:4<351::AID-JMS512>3.0.CO;2-Y (cited on pages 80, 154, 155).

[360] R. B. Moore, O. Gianfrancesco, R. Lumbo, and S. Schwarz. "The use of high RFQ fields to manipulate ions". In: *International Journal of Mass Spectrometry* 251.2 (2006), pp. 190–197. ISSN: 1387-3806. DOI: 10.1016/j.ijms.2006.01.039 (cited on pages 82, 84).

[361] Ramzi Boussaid, G. Ban, G. Quéméner, Y. Merrer, and J. Lorry. "Development of a radio-frequency quadrupole cooler for high beam currents". In: *Physical Review Accelerators and Beams* 20.12 (2017), p. 124701. DOI: 10.1103/PhysRevAccelBeams.20.124701 (cited on page 82).

[362] S. Schwarz, G. Bollen, R. Ringle, J. Savory, and P. Schury. "The LEBIT ion cooler and buncher". In: *Nuclear Instruments and Methods in Physics Research Section A: Accelerators, Spectrometers, Detectors and Associated Equipment* 816 (2016), pp. 131–141. ISSN: 0168-9002. DOI: 10.1016/j.nima.2016.01.078 (cited on pages 82, 83, 88, 90, 94).

[363] G. Bollen, S. Schwarz, D. Davies, P. Lofy, D. Morrissey, R. Ringle, P. Schury, T. Sun, and L. Weissman. "Beam cooling at the low-energy-beam and ion-trap facility at NSCL/MSU". In: *Nuclear Instruments and Methods in Physics Research Section A: Accelerators, Spectrometers, Detectors and Associated Equipment*. International Workshop on Beam Cooling and Related Topics 532.1 (2004), pp. 203–209. ISSN: 0168-9002. DOI: 10.1016/j.nima.2004.06.046 (cited on page 83).

[364] B. R. Barquest, G. Bollen, P. F. Mantica, K. Minamisono, R. Ringle, S. Schwarz, and C. S. Sumithrarachchi. "RFQ beam cooler and buncher for collinear laser spectroscopy of rare isotopes". In: *Nuclear Instruments and Methods in Physics Research Section A: Accelerators, Spectrometers, Detectors and Associated Equipment* 866 (2017), pp. 18–28. ISSN: 0168-9002. DOI: 10.1016/j.nima.2017.05.036 (cited on pages 83, 88, 90, 94, 99, 100).

[365] Ralph G. DeVoe. "Power-Law Distributions for a Trapped Ion Interacting with a Classical Buffer Gas". In: *Physical Review Letters* 102.6 (2009), p. 063001. DOI: 10.1103/PhysRevLett.102.063001 (cited on pages 83, 85).

[366] M. Brownnutt, M. Kumph, P. Rabl, and R. Blatt. "Ion-trap measurements of electric-field noise near surfaces". In: *Reviews of Modern Physics* 87.4 (2015), pp. 1419–1482. DOI: 10.1103/RevModPhys.87.1419 (cited on pages 83, 157).

[367] R. Boussaid, G. Ban, J. F. Cam, and C. Vandamme. "Simulations of high intensity ion beam RFQ cooler for DESIR/SPIRAL 2: SHIRaC". In: *Journal of Instrumentation* 9.07 (2014), P07009. ISSN: 1748-0221. DOI: 10.1088/1748-0221/9/07/P07009 (cited on page 84).

[368] F. G. Major and H. G. Dehmelt. "Exchange-Collision Technique for the rf Spectroscopy of Stored Ions". In: *Physical Review* 170.1 (1968), pp. 91–107. DOI: 10.1103/PhysRev.170.91 (cited on page 85).

[369] Yoshiki Moriwaki, Maki Tachikawa, Yoshiharu Maeno Yoshiharu Maeno, and Tadao Shimizu Tadao Shimizu. "Collision Cooling of Ions Stored in Quadrupole Radio-Frequency Trap". In: *Japanese Journal of Applied Physics* 31.11B (1992). Publisher: IOP Publishing, p. L1640. ISSN: 1347-4065. DOI: 10.1143/JJAP.31.L1640 (cited on page 85).

[370] Kuang Chen, Scott T. Sullivan, and Eric R. Hudson. "Neutral Gas Sympathetic Cooling of an Ion in a Paul Trap". In: *Physical Review Letters* 112.14 (2014), p. 143009. DOI: 10.1103/PhysRevLett.112.143009 (cited on page 85).

[371] M.D.N. Lunney, F. Buchinger, and R.B. Moore. "The Temperature of Buffer-gas Cooled Ions in a Paul Trap". In: *Journal of Modern Optics* 39.2 (1992), pp. 349–360. ISSN: 0950-0340. DOI: 10.1080/09500349214550341 (cited on page 85).

[372] Sai-Ke Tian, Jiu-Qing Wang, Gang Xu, and Yi Jiao. "Intra-beam scattering studies for low emittance at BAPS". In: *Chinese Physics C* 39.6 (2015), p. 067001. ISSN: 1674-1137. DOI: 10.1088/1674-1137/39/6/067001 (cited on page 85).

[373] Ivan V. Bazarov, Bruce M. Dunham, and Charles K. Sinclair. "Maximum Achievable Beam Brightness from Photoinjectors". In: *Physical Review Letters* 102.10 (2009), p. 104801. DOI: 10.1103/PhysRevLett.102.104801 (cited on page 86).

[374] A. Nieminen, P. Campbell, J. Billowes, D. H. Forest, J. A. R. Griffith, J. Huikari, A. Jokinen, I. D. Moore, R. Moore, G. Tungate, and J. Äystö. "On-Line Ion Cooling and Bunching for Collinear Laser Spectroscopy". In: *Physical Review Letters* 88.9 (2002), p. 094801. DOI: 10.1103/PhysRevLett.88.094801 (cited on pages 88, 90).

[375] Mathew Smith. "A square-wave-driven radiofrequency quadrupole cooler and buncher for TITAN". Thesis. University of British Columbia, 2005. DOI: 10.14288/1.0085163. URL: https://open.library.ubc.ca/soa/cIRcle/collections/ubctheses/831/items/1.0085163 (cited on pages 88, 99).

[376] M. Cavenago, L. Bellan, M. Comunian, G. Maero, M. Maggiore, N. Panzeri, L. Pranovi, and M. Romé. "A RFQ Cooler Development". In: *9th International Particle Accelerator Conference*. 2018. DOI: 10.18429/jacow-ipac2018-thpal008 (cited on pages 88, 90, 99).

[377] Chris M. Lock and Edward Dyer. "Characterisation of high pressure quadrupole collision cells possessing direct current axial fields". In: *Rapid Communications in Mass Spectrometry* 13.5 (1999), pp. 432–448. ISSN: 1097-0231. DOI: 10.1002/(SICI)1097-0231(19990315)13:5<432::AID-RCM504>3.0.CO;2-I (cited on page 88).

[378] Alexander Loboda, Andrew Krutchinsky, Olga Loboda, James McNabb, Victor Spicer, Werner Ens, and Kenneth Standing. "Novel Linac II Electrode Geometry for Creating An Axial Field in a Multipole Ion Guide". In: *European Journal of Mass Spectrometry* 6.6 (2000), pp. 531–536. ISSN: 1469-0667. DOI: 10.1255/ejms.383 (cited on page 88).

[379] Bashir A Mansoori, Edward W Dyer, Christopher M Lock, Kevin Bateman, Robert K Boyd, and Bruce A Thomson. "Analytical performance of a high-pressure radio frequency-only quadrupole collision cell with an axial field applied by using conical rods". In: *Journal of the American Society for Mass Spectrometry* 9.8 (1998), pp. 775–788. ISSN: 1044-0305. DOI: 10.1016/S1044-0305(98)00042-7 (cited on page 88).

[380] Y. Ito, P. Schury, M. Wada, S. Naimi, C. Smorra, T. Sonoda, H. Mita, A. Takamine, K. Okada, A. Ozawa, and H. Wollnik. "A novel ion cooling trap for multi-reflection time-of-flight mass spectrograph". In: *Nuclear Instruments and Methods in Physics Research Section B: Beam Interactions with Materials and Atoms*. XVIth International Conference on ElectroMagnetic Isotope Separators and Techniques Related to their Applications, December 2–7, 2012 at Matsue, Japan 317 (2013), pp. 544–549. ISSN: 0168-583X. DOI: 10.1016/j.nimb.2013.07.069 (cited on page 88).

[381] Y. Liu, J. F. Liang, G. D. Alton, J. R. Beene, Z. Zhou, and H. Wollnik. "Collisional cooling of negative-ion beams". In: *Nuclear Instruments and Methods in Physics Research Section B: Beam Interactions with Materials and Atoms* 187.1 (2002), pp. 117–131. ISSN: 0168-583X. DOI: 10.1016/S0168-583X(01)00844-8 (cited on page 88).

[382] Martin Martschini, Johanna Pitters, Tobias Moreau, Pontus Andersson, Oliver Forstner, Dag Hanstorp, Johannes Lachner, Yuan Liu, Alfred Priller, Peter Steier, and Robin Golser. "Selective laser photodetachment of intense atomic and molecular negative ion beams with the ILIAS RFQ ion beam cooler". In: *International Journal of Mass Spectrometry* 415 (2017), pp. 9–17. ISSN: 1387-3806. DOI: 10.1016/j.ijms.2016.12.015 (cited on page 88).

[383] Hidemasa Takana, Kazuhiro Ogawa, Tetsuo Shoji, and Hideya Nishiyama. "Computational simulation of cold spray process assisted by electrostatic force". In: *Powder Technology* 185.2 (2008), pp. 116–123. ISSN: 0032-5910. DOI: 10.1016/j.powtec.2007.10.005 (cited on page 88).

[384] Jaehong Park, Jimin Jeong, Chul Kim, and Jungho Hwang. "Deposition of Charged Aerosol Particles on a Substrate by Collimating Through an Electric Field Assisted Coaxial Flow Nozzle". In: *Aerosol Science and Technology* 47.5 (2013), pp. 512–519. ISSN: 0278-6826. DOI: 10.1080/02786826.2013.767981 (cited on page 88).

[385] Abu B. Kanu, Prabha Dwivedi, Maggie Tam, Laura Matz, and Herbert H. Hill Jr. "Ion mobility–mass spectrometry". In: *Journal of Mass Spectrometry* 43.1 (2008), pp. 1–22. ISSN: 1096-9888. DOI: 10.1002/jms.1383 (cited on pages 88, 89).

[386] James N. Dodds and Erin S. Baker. "Ion Mobility Spectrometry: Fundamental Concepts, Instrumentation, Applications, and the Road Ahead". In: *Journal of the American Society for Mass Spectrometry* 30.11 (2019), pp. 2185–2195. DOI: 10.1007/s13361-019-02288-2 (cited on page 88).

[387] A. Nieminen, P. Campbell, J. Billowes, D. H. Forest, J. A. R. Griffith, J. Huikari, A. Jokinen, I. D. Moore, R. Moore, G. Tungate, and J. Äystö. "On-Line Ion Cooling and Bunching for Collinear Laser Spectroscopy". In: *Physical Review Letters* 88.9 (2002), p. 094801. DOI: 10.1103/PhysRevLett.88.094801 (cited on page 94).

[388] Kevin Giles, Steven D. Pringle, Kenneth R. Worthington, David Little, Jason L. Wildgoose, and Robert H. Bateman. "Applications of a travelling wave-based radio-frequency-only stacked ring ion

guide". In: *Rapid Communications in Mass Spectrometry* 18.20 (2004), pp. 2401–2414. ISSN: 1097-0231. DOI: 10.1002/rcm.1641 (cited on page 94).

[389] Alexandre A. Shvartsburg and Richard D. Smith. "Fundamentals of Traveling Wave Ion Mobility Spectrometry". In: *Analytical Chemistry* 80.24 (2008), pp. 9689–9699. ISSN: 0003-2700. DOI: 10.1021/ac8016295 (cited on page 94).

[390] Ahmed M. Hamid, Yehia M. Ibrahim, Sandilya V. B. Garimella, Ian K. Webb, Liulin Deng, Tsung-Chi Chen, Gordon A. Anderson, Spencer A. Prost, Randolph V. Norheim, Aleksey V. Tolmachev, and Richard D. Smith. "Characterization of Traveling Wave Ion Mobility Separations in Structures for Lossless Ion Manipulations". In: *Analytical Chemistry* 87.22 (2015), pp. 11301–11308. ISSN: 0003-2700. DOI: 10.1021/acs.analchem.5b02481 (cited on page 94).

[391] S. Masuda, K. Fujibayashi, K. Ishida, and H. Inaba. "Confinement and transportation of charged aerosol clouds via electric curtain". In: *Electrical Engineering in Japan* 92.1 (1972), pp. 43–52. ISSN: 1520-6416. DOI: 10.1002/eej.4390920106 (cited on page 94).

[392] S. Masuda and Y. Matsumoto. "Theoretical characteristics of standing-wave electric curtains". In: *Electrical Engineering in Japan* 93.1 (1973), pp. 71–77. ISSN: 1520-6416. DOI: 10.1002/eej.4390930110 (cited on page 94).

[393] D. K. Hutchins, J. Holm, and S. R. Addison. "Electrodynamic Focusing of Charged Aerosol Particles". In: *Aerosol Science and Technology* 14.4 (1991), pp. 389–405. ISSN: 0278-6826. DOI: 10.1080/02786829108959501 (cited on page 94).

[394] Yue Yu, Jan Cilliers, Kathryn Hadler, Stanley Starr, and Yanghua Wang. "A review of particle transport and separation by electrostatic traveling wave methods". In: *Journal of Electrostatics* 119 (2022), p. 103735. ISSN: 0304-3886. DOI: 10.1016/j.elstat.2022.103735 (cited on page 94).

[395] D. Kielpinski, C. Monroe, and D. J. Wineland. "Architecture for a large-scale ion-trap quantum computer". In: *Nature* 417.6890 (2002), pp. 709–711. ISSN: 1476-4687. DOI: 10.1038/nature00784 (cited on pages 94, 157).

[396] J. M. Amini, H. Uys, J. H. Wesenberg, S. Seidelin, J. Britton, J. J. Bollinger, D. Leibfried, C. Ospelkaus, A. P. VanDevender, and D. J. Wineland. "Toward scalable ion traps for quantum information processing". In: *New Journal of Physics* 12.3 (2010), p. 033031. ISSN: 1367-2630. DOI: 10.1088/1367-2630/12/3/033031 (cited on pages 94, 157).

[397] V. Kaushal, B. Lekitsch, A. Stahl, J. Hilder, D. Pijn, C. Schmiegelow, A. Bermudez, M. Müller, F. Schmidt-Kaler, and U. Poschinger. "Shuttling-based trapped-ion quantum information processing". In: *AVS Quantum Science* 2.1 (2020), p. 014101. ISSN: 2639-0213. DOI: 10.1116/1.5126186 (cited on page 94).

[398] S. A. Moses, C. H. Baldwin, M. S. Allman, R. Ancona, L. Ascarrunz, C. Barnes, J. Bartolotta, B. Bjork, P. Blanchard, M. Bohn, J. G. Bohnet, N. C. Brown, N. Q. Burdick, W. C. Burton, S. L. Campbell, J. P. Campora, C. Carron, J. Chambers, J. W. Chan, Y. H. Chen, A. Chernoguzov, E. Chertkov, J. Colina, J. P. Curtis, R. Daniel, M. DeCross, D. Deen, C. Delaney, J. M. Dreiling, C. T. Ertsgaard, J. Esposito, B. Estey, M. Fabrikant, C. Figgatt, C. Foltz, M. Foss-Feig, D. Francois, J. P. Gaebler, T. M. Gatterman, C. N. Gilbreth, J. Giles, E. Glynn, A. Hall, A. M. Hankin, A. Hansen, D. Hayes, B. Higashi, I. M. Hoffman, B. Horning, J. J. Hout, R. Jacobs, J. Johansen, L. Jones, J. Karcz, T. Klein, P. Lauria, P. Lee, D. Liefer, S. T. Lu, D. Lucchetti, C. Lytle, A. Malm, M. Matheny, B. Mathewson, K. Mayer, D. B. Miller, M. Mills, B. Neyenhuis, L. Nugent, S. Olson, J. Parks, G. N. Price, Z. Price, M. Pugh, A. Ransford, A. P. Reed, C. Roman, M. Rowe, C. Ryan-Anderson, S. Sanders, J. Sedlacek, P. Shevchuk, P. Siegfried, T. Skripka, B. Spaun, R. T. Sprenkle, R. P. Stutz, M. Swallows, R. I. Tobey, A. Tran, T. Tran, E. Vogt, C. Volin, J. Walker, A. M. Zolot, and J. M. Pino. "A Race-Track Trapped-Ion Quantum Processor". In: *Physical Review X* 13.4 (2023), p. 041052. DOI: 10.1103/PhysRevX.13.041052 (cited on page 94).

[399] J. H. Wesenberg. "Ideal intersections for radio-frequency trap networks". In: *Physical Review A* 79.1 (2009), p. 013416. DOI: 10.1103/PhysRevA.79.013416 (cited on page 94).

[400] W. K. Hensinger, S. Olmschenk, D. Stick, D. Hucul, M. Yeo, M. Acton, L. Deslauriers, C. Monroe, and J. Rabchuk. "T-junction ion trap array for two-dimensional ion shuttling, storage, and manipulation". In: *Applied Physics Letters* 88.3 (2006), p. 034101. ISSN: 0003-6951. DOI: 10.1063/1.2164910 (cited on page 94).

[401] Kenneth Wright, Jason M. Amini, Daniel L. Faircloth, Curtis Volin, S. Charles Doret, Harley Hayden, C.-S. Pai, David W. Landgren, Douglas Denison, Tyler Killian, Richart E. Slusher, and Alexa W. Harter. "Reliable transport through a microfabricatedX-junction surface-electrode ion trap". In: *New Journal of Physics* 15.3 (2013), p. 033004. ISSN: 1367-2630. DOI: 10.1088/1367-2630/15/3/033004 (cited on pages 94, 100).

[402] T. Karin, I. Le Bras, A. Kehlberger, K. Singer, N. Daniilidis, and H. Häffner. "Transport of charged particles by adjusting rf voltage amplitudes". In: *Applied Physics B* 106.1 (2012), pp. 117–125. ISSN: 1432-0649. DOI: 10.1007/s00340-011-4738-2 (cited on page 94).

[403] D. L. Moehring, C. Highstrete, D. Stick, K. M. Fortier, R. Haltli, C. Tigges, and M. G. Blain. "Design, fabrication and experimental demonstration of junction surface ion traps". In: *New Journal of Physics* 13.7 (2011), p. 075018. ISSN: 1367-2630. DOI: 10.1088/1367-2630/13/7/075018 (cited on pages 94, 100).

[404] D. Hucul, M. Yeo, S. Olmschenk, C. Monroe, W. K. Hensinger, and J. Rabchuk. "On the transport of atomic ions in linear and multidimensional ion trap arrays". In: *Quantum Info. Comput.* 8.6 (2008), pp. 501–578. ISSN: 1533-7146 (cited on page 94).

[405] Aleksey V. Tolmachev, Ian K. Webb, Yehia M. Ibrahim, Sandilya V.B. Garimella, Xinyu Zhang, Gordon A. Anderson, and Richard D. Smith. "Characterization of Ion Dynamics in Structures for Lossless Ion Manipulations". In: *Analytical Chemistry* 86.18 (2014), pp. 9162–9168. ISSN: 0003-2700. DOI: 10.1021/ac502054p (cited on page 94).

[406] Ian K. Webb, Sandilya V. B. Garimella, Aleksey V. Tolmachev, Tsung-Chi Chen, Xinyu Zhang, Randolph V. Norheim, Spencer A. Prost, Brian LaMarche, Gordon A. Anderson, Yehia M. Ibrahim, and Richard D. Smith. "Experimental Evaluation and Optimization of Structures for Lossless Ion Manipulations for Ion Mobility Spectrometry with Time-of-Flight Mass Spectrometry". In: *Analytical Chemistry* 86.18 (2014), pp. 9169–9176. ISSN: 0003-2700. DOI: 10.1021/ac502055e (cited on page 94).

[407] Sandilya V. B. Garimella, Yehia M. Ibrahim, Ian K. Webb, Aleksey V. Tolmachev, Xinyu Zhang, Spencer A. Prost, Gordon A. Anderson, and Richard D. Smith. "Simulation of Electric Potentials and Ion Motion in Planar Electrode Structures for Lossless Ion Manipulations (SLIM)". In: *Journal of the American Society for Mass Spectrometry* 25.11 (2014), pp. 1890–1896. DOI: 10.1007/s13361-014-0976-y (cited on page 94).

[408] Xinyu Zhang, Sandilya V. B. Garimella, Spencer A. Prost, Ian K. Webb, Tsung-Chi Chen, Keqi Tang, Aleksey V. Tolmachev, Randolph V. Norheim, Erin S. Baker, Gordon A. Anderson, Yehia M. Ibrahim, and Richard D. Smith. "Ion Trapping, Storage, and Ejection in Structures for Lossless Ion Manipulations". In: *Analytical Chemistry* 87.12 (2015), pp. 6010–6016. ISSN: 0003-2700. DOI: 10.1021/acs.analchem.5b00214 (cited on pages 94, 98).

[409] Yehia M. Ibrahim, Ahmed M. Hamid, Liulin Deng, Sandilya V. B. Garimella, Ian K. Webb, Erin S. Baker, and Richard D. Smith. "New frontiers for mass spectrometry based upon structures for lossless ion manipulations". In: *Analyst* 142.7 (2017), pp. 1010–1021. DOI: 10.1039/C7AN00031F (cited on pages 94, 98, 157).

[410] Dan Jiang, Gong-Yu Jiang, Xiao-Xu Li, Fu-xing Xu, Liang Wang, Li Ding, and Chuan-Fan Ding. "Printed Circuit Board Ion Trap Mass Analyzer: Its Structure and Performance". In: *Analytical Chemistry* 85.12 (2013), pp. 6041–6046. ISSN: 0003-2700. DOI: 10.1021/ac400864k (cited on page 98).

[411] Florian Schlottmann, Maria Allers, Ansgar T. Kirk, Alexander Bohnhorst, and Stefan Zimmermann. "A Simple Printed Circuit Board–Based Ion Funnel for Focusing Low m/z Ratio Ions with High Kinetic Energies at Elevated Pressure". In: *Journal of the American Society for Mass Spectrometry* 30.9 (2019), pp. 1813–1823. DOI: 10.1007/s13361-019-02241-3 (cited on pages 98–100).

[412] Tsung-Chi Chen, Ian K. Webb, Spencer A. Prost, Marques B. Harrer, Randolph V. Norheim, Keqi Tang, Yehia M. Ibrahim, and Richard D. Smith. "Rectangular Ion Funnel: A New Ion Funnel Interface for Structures for Lossless Ion Manipulations". In: *Analytical Chemistry* 87.1 (2015), pp. 716–722. ISSN: 0003-2700. DOI: 10.1021/ac503564c (cited on pages 98, 100).

[413] Colin D. Bruzewicz, John Chiaverini, Robert McConnell, and Jeremy M. Sage. "Trapped-Ion Quantum Computing: Progress and Challenges". In: *Applied Physics Reviews* 6.2 (2019), p. 021314. ISSN: 1931-9401. DOI: 10.1063/1.5088164 (cited on pages 98, 157).

[414] Dong-Il "Dan" Cho, Seokjun Hong, Minjae Lee, and Taehyun Kim. "A review of silicon microfabricated ion traps for quantum information processing". In: *Micro and Nano Systems Letters* 3.1 (2015), p. 2. ISSN: 2213-9621. DOI: 10.1186/s40486-015-0013-3 (cited on page 98).

[415] Zak David Romaszko, Seokjun Hong, Martin Siegele, Reuben Kahan Puddy, Foni Raphaël Lebrun-Gallagher, Sebastian Weidt, and Winfried Karl Hensinger. "Engineering of microfabricated ion traps and integration of advanced on-chip features". In: *Nature Reviews Physics* 2.6 (2020), pp. 285–299. ISSN: 2522-5820. DOI: 10.1038/s42254-020-0182-8 (cited on pages 98, 100).

[416] Marcus D. Hughes, Bjoern Lekitsch, Jiddu A. Broersma, and Winfried K. Hensinger. "Microfabricated ion traps". In: *Contemporary Physics* 52.6 (2011), pp. 505–529. ISSN: 0010-7514, 1366-5812. DOI: 10.1080/00107514.2011.601918 (cited on pages 98, 100, 157).

[417] J. M. Amini, J. Britton, D. Leibfried, and D. J. Wineland. "Micro-Fabricated Chip Traps for Ions". In: *Atom Chips*. John Wiley & Sons, Ltd, 2011, pp. 395–420. ISBN: 978-3-527-63335-7. DOI: 10.1002/9783527633357.ch13 (cited on page 98).

[418] R. R. A. Syms, L. Michelutti, and M. M. Ahmad. "Two-dimensional microfabricated electrostatic einzel lens". In: *Sensors and Actuators A: Physical* 107.3 (2003), pp. 285–295. ISSN: 0924-4247. DOI: 10.1016/j.sna.2003.08.001 (cited on page 98).

[419] K. K. Mehta, A. M. Eltony, C. D. Bruzewicz, I. L. Chuang, R. J. Ram, J. M. Sage, and J. Chiaverini. "Ion traps fabricated in a CMOS foundry". In: *Applied Physics Letters* 105.4 (2014), p. 044103. ISSN: 0003-6951. DOI: 10.1063/1.4892061 (cited on page 98).

[420] Rhys Jones, Patrick Haufe, Edward Sells, Pejman Iravani, Vik Olliver, Chris Palmer, and Adrian Bowyer. "RepRap – the replicating rapid prototyper". In: *Robotica* 29.1 (2011), pp. 177–191. ISSN: 1469-8668, 0263-5747. DOI: 10.1017/S026357471000069X (cited on page 98).

[421] Parker Andrew Gould and Mitchell David Hsing. "Design, fabrication, and characterization of a compact deep reactive ion etching system for MEMS processing". Thesis. Massachusetts Institute of Technology, 2014. URL: https://dspace.mit.edu/handle/1721.1/93835 (cited on pages 99, 112).

[422] Parker Andrew Gould. "Design, fabrication, and characterization of an ultra-low cost inductively-coupled plasma chemical vapor deposition tool for micro- and nanofabrication". Thesis. Massachusetts Institute of Technology, 2019. URL: https://dspace.mit.edu/handle/1721.1/122561 (cited on pages 99, 112).

[423] W. D. Sproul, D. J. Christie, and D. C. Carter. "Control of reactive sputtering processes". In: *Thin Solid Films* 491.1 (2005), pp. 1–17. ISSN: 0040-6090. DOI: 10.1016/j.tsf.2005.05.022 (cited on page 99).

[424] Nicholas D. Guise, Spencer D. Fallek, Harley Hayden, C.-S. Pai, Curtis Volin, K. R. Brown, J. True Merrill, Alexa W. Harter, Jason M. Amini, Lisa M. Lust, Kelly Muldoon, Doug Carlson, and Jerry Budach. "In-Vacuum Active Electronics for Microfabricated Ion Traps". In: *Review of Scientific Instruments* 85.6 (2014), p. 063101. ISSN: 0034-6748, 1089-7623. DOI: 10.1063/1.4879136 (cited on pages 99, 165).

[425] M. J. Barnes, G. D. Wait, J. Dilling, J. V. Vaz, L. Blomeley, O. Hadary, and M. J. Smith. "A High Frequency Mosfet Driver for the Titan Facility at TRIUMF". In: *2005 IEEE Pulsed Power Conference*. 2005, pp. 178–181. DOI: 10.1109/PPC.2005.300554 (cited on page 99).

[426] L. Ding and S. Kumashiro. "Ion motion in the rectangular wave quadrupole field and digital operation mode of a quadrupole ion trap mass spectrometer". In: *Rapid Communications in Mass Spectrometry* 20.1 (2006), pp. 3–8. ISSN: 1097-0231. DOI: 10.1002/rcm.2253 (cited on page 99).

[427] Jeonghoon Lee, Maxwell A. Marino, Hideya Koizumi, and Peter T. A. Reilly. "Simulation of duty cycle-based trapping and ejection of massive ions using linear digital quadrupoles: The enabling technology for high resolution time-of-flight mass spectrometry in the ultra high mass range". In: *International Journal of Mass Spectrometry* 304.1 (2011), pp. 36–40. ISSN: 1387-3806. DOI: 10.1016/j.ijms.2011.03.011 (cited on page 99).

[428] Nathan M. Hoffman, Bojana Opačić, and Peter T. A. Reilly. "Note: An inexpensive square waveform ion funnel driver". In: *Review of Scientific Instruments* 88.1 (2017), p. 016104. ISSN: 0034-6748. DOI: 10.1063/1.4974345 (cited on page 99).

[429] Nathan M. Hoffman, Zachary P. Gotlib, Bojana Opačić, Brian H. Clowers, and Peter T. A. Reilly. "A comparison based digital waveform generator for high resolution duty cycle". In: *Review of Scientific Instruments* 89.8 (2018), p. 084101. ISSN: 0034-6748. DOI: 10.1063/1.5004798 (cited on page 99).

[430] J. A. Richards, R. M. Huey, and J. Hiller. "A new operating mode for the quadrupole mass filter". In: *International Journal of Mass Spectrometry and Ion Physics* 12.4 (1973), pp. 317–339. ISSN: 0020-7381. DOI: 10.1016/0020-7381(73)80102-0 (cited on page 99).

[431] Li Ding, Michael Sudakov, and Sumio Kumashiro. "A simulation study of the digital ion trap mass spectrometer". In: *International Journal of Mass Spectrometry* 221.2 (2002), pp. 117–138. ISSN: 1387-3806. DOI: 10.1016/S1387-3806(02)00921-1 (cited on page 99).

[432] Taeman Kim, Aleksey V. Tolmachev, Richard Harkewicz, David C. Prior, Gordon Anderson, Harold R. Udseth, Richard D. Smith, Thomas H. Bailey, Sergey Rakov, and Jean H. Futrell. "Design and Implementation of a New Electrodynamic Ion Funnel". In: *Analytical Chemistry* 72.10 (2000), pp. 2247–2255. ISSN: 0003-2700. DOI: 10.1021/ac991412x (cited on pages 99, 100).

[433] Peter T. A. Reilly, Sumeet Chakravorty, Conner F. Bailey, Fatima O. Obe, and Adam P. Huntley. "Will the Digital Mass Filter Be the Next High-Resolution High-Mass Analyzer?" In: *Journal of the American Society for Mass Spectrometry* 32.10 (2021), pp. 2615–2620. ISSN: 1044-0305. DOI: 10.1021/jasms.1c00234 (cited on page 99).

[434] Gregory F. Brabeck and Peter T. A. Reilly. "Mapping ion stability in digitally driven ion traps and guides". In: *International Journal of Mass Spectrometry* 364 (2014), pp. 1–8. ISSN: 1387-3806. DOI: 10.1016/j.ijms.2014.03.008 (cited on page 99).

[435] N. V. Konenkov, M. Sudakov, and D. J. Douglas. "Matrix methods for the calculation of stability diagrams in quadrupole mass spectrometry". In: *Journal of the American Society for Mass Spectrometry* 13.6 (2002), pp. 597–613. ISSN: 1879-1123. DOI: 10.1016/S1044-0305(02)00365-3 (cited on page 99).

[436] Adam P. Huntley and Peter T.A. Reilly. "New tools for theoretical comparison of rectangular and sine wave operation of ion traps, guides and mass filters". In: *Journal of Mass Spectrometry* 55.12 (2020), e4661. ISSN: 1096-9888. DOI: 10.1002/jms.4661 (cited on page 99).

[437] Shunxiang Li, Anqi Hu, Yingchao Liu, Xiaohui Liu, Kai Liu, Chenxin Zhu, Hongxiu Yu, Weiqian Cao, Huali Shen, Quanqing Zhang, and Pengyuan Yang. "Design and implementation of MIR F-Disc: An electrodynamic ion manipulation device". In: *International Journal of Mass Spectrometry* (2022), p. 116901. ISSN: 1387-3806. DOI: 10.1016/j.ijms.2022.116901 (cited on page 100).

[438] Boris Brkić, Stephen Taylor, Jason F. Ralph, and Neil France. "High-fidelity simulations of ion trajectories in miniature ion traps using the boundary-element method". In: *Physical Review A* 73.1 (2006), p. 012326. DOI: 10.1103/PhysRevA.73.012326 (cited on page 100).

[439] J. Raymond Gibson, Kenneth G. Evans, and Stephen Taylor. "Modelling mass analyzer performance with fields determined using the boundary element method". In: *Journal of Mass Spectrometry* 45.4 (2010), pp. 364–371. ISSN: 1096-9888. DOI: 10.1002/jms.1720 (cited on page 100).

[440] Kerim T. Arat, Thomas Klimpel, Aernout C. Zonnevylle, Wilhelmus S. M. M. Ketelaars, Carel Th. H. Heerkens, and Cornelis W. Hagen. "Charge-induced pattern displacement in E-beam lithography". In: *Journal of Vacuum Science & Technology B* 37.5 (2019), p. 051603. ISSN: 2166-2746. DOI: 10.1116/1.5120631 (cited on page 100).

[441] M. Harlander, M. Brownnutt, W. Hänsel, and R. Blatt. "Trapped-ion probing of light-induced charging effects on dielectrics". In: *New Journal of Physics* 12.9 (2010), p. 093035. ISSN: 1367-2630. DOI: 10.1088/1367-2630/12/9/093035 (cited on page 100).

[442] F. Santagata, C.K. Yang, J.F. Creemer, P. J. French, and P. M. Sarro. "Single Wafer Surface Micromachined Field Emission Electron Source". In: *2009 IEEE 22nd International Conference on Micro Electro Mechanical Systems*. 2009, pp. 848–851. DOI: 10.1109/MEMSYS.2009.4805516 (cited on page 101).

[443] Nishita Deka and Vivek Subramanian. "On-Chip Fully Integrated Field Emission Arrays for High-Voltage MEMS Applications". In: *IEEE Transactions on Electron Devices* 67.9 (2020), pp. 3753–3760. ISSN: 1557-9646. DOI: 10.1109/TED.2020.3006167 (cited on page 101).

[444] Yugong Wu, Zhigang Fan, and Yuzhu Lu. "Bulk and interior packing densities of random close packing of hard spheres". In: *Journal of Materials Science* 38.9 (2003), pp. 2019–2025. ISSN: 1573-4803. DOI: 10.1023/A:1023597707363 (cited on page 102).

[445] B. A. Probyn. "A low-energy ion source for the deposition of chromium". In: *Journal of Physics D: Applied Physics* 1.4 (1968), p. 457. ISSN: 0022-3727. DOI: 10.1088/0022-3727/1/4/307 (cited on pages 103, 104, 107).

[446] S. V. Dudin, A. V. Zykov, and V. I. Farenik. "Low-energy ion beam space-charge neutralization". In: *Review of Scientific Instruments* 65.4 (1994), pp. 1451–1453. ISSN: 0034-6748. DOI: 10.1063/1.1144941 (cited on page 103).

[447] K. H. Kingdon. "A Method for the Neutralization of Electron Space Charge by Positive Ionization at Very Low Gas Pressures". In: *Physical Review* 21.4 (1923), pp. 408–418. DOI: 10.1103/PhysRev.21.408 (cited on page 103).

[448] R. H. Plumlee. "Space Charge Neutralization in the Ionizing Beam of a Mass Spectrometer". In: *Review of Scientific Instruments* 28.10 (1957), pp. 830–832. ISSN: 0034-6748. DOI: 10.1063/1.1715734 (cited on page 103).

[449] G. Mladenov and S. Sabchevski. "Potential distribution and space-charge neutralization in technological intense electron beams — an overview". In: *Vacuum* 62.2 (2001), pp. 113–122. ISSN: 0042-207X. DOI: 10.1016/S0042-207X(00)00418-8 (cited on page 103).

[450] M. Koch, S. Rehbein, G. Schmahl, T. Reisinger, G. Bracco, W. E. Ernst, and B. Holst. "Imaging with neutral atoms—a new matter-wave microscope". In: *Journal of Microscopy* 229.1 (2008), pp. 1–5. ISSN: 1365-2818. DOI: 10.1111/j.1365-2818.2007.01874.x (cited on page 103).

[451] S. D. Eder, T. Reisinger, M. M. Greve, G. Bracco, and B. Holst. "Focusing of a neutral helium beam below one micron". In: *New Journal of Physics* 14.7 (2012), p. 073014. ISSN: 1367-2630. DOI: 10.1088/1367-2630/14/7/073014 (cited on page 103).

[452] Alexander D. Cronin, Jörg Schmiedmayer, and David E. Pritchard. "Optics and interferometry with atoms and molecules". In: *Reviews of Modern Physics* 81 (2009), pp. 1051–1129. DOI: 10.1103/RevModPhys.81.1051 (cited on page 103).

[453] *Products - MBMW-101 - IMS Nanofabrication GmbH*. IMS. 2024. URL: https://www.ims.co.at/en/products/ (cited on page 103).

[454] *World's First High-Productivity Multicolum E-Beam Lithography Platform*. Multibeam. 2024. URL: https://multibeamcorp.com/ (cited on page 103).

[455] Ryo Yoshida, Motoaki Hara, Hiroyuki Oguchi, and Hiroki Kuwano. "Micromachined multiple focused-ion-beam devices". In: *Journal of Vacuum Science & Technology B* 34.2 (2016), p. 022001. ISSN: 2166-2746. DOI: 10.1116/1.4943561 (cited on page 103).

[456] J. J. McClelland, A. V. Steele, B. Knuffman, K. A. Twedt, A. Schwarzkopf, and T. M. Wilson. "Bright focused ion beam sources based on laser-cooled atoms". In: *Applied Physics Reviews* 3.1 (2016), p. 011302. ISSN: 1931-9401. DOI: 10.1063/1.4944491 (cited on page 104).

[457] Jon Orloff, Mark Utlaut, and Lynwood Swanson. *High Resolution Focused Ion Beams: FIB and its Applications*. Boston, MA: Springer US, 2003. ISBN: 978-1-4613-5229-7. DOI: 10.1007/978-1-4615-0765-9 (cited on page 104).

[458] P. Musumeci, J. Giner Navarro, J. B. Rosenzweig, L. Cultrera, I. Bazarov, J. Maxson, S. Karkare, and H. Padmore. "Advances in bright electron sources". In: *Nuclear Instruments and Methods in Physics Research Section A: Accelerators, Spectrometers, Detectors and Associated Equipment*. Advances in Instrumentation and Experimental Methods (Special Issue in Honour of Kai Siegbahn) 907 (2018), pp. 209–220. ISSN: 0168-9002. DOI: 10.1016/j.nima.2018.03.019 (cited on page 104).

[459] Ranjini Menon and P. Y. Nabhiraj. "Development of a compact high current low emittance RF ion source". In: *Nuclear Instruments and Methods in Physics Research Section B: Beam Interactions with Materials and Atoms*. XVIth International Conference on ElectroMagnetic Isotope Separators and Techniques Related to their Applications, December 2–7, 2012 at Matsue, Japan 317 (2013), pp. 442–445. ISSN: 0168-583X. DOI: 10.1016/j.nimb.2013.07.057 (cited on page 104).

[460] B. Knuffman, A. V. Steele, J. Orloff, and J. J. McClelland. "Nanoscale focused ion beam from laser-cooled lithium atoms". In: *New Journal of Physics* 13.10 (2011), p. 103035. ISSN: 1367-2630. DOI: 10.1088/1367-2630/13/10/103035 (cited on page 104).

[461] J. Meijer, S. Pezzagna, T. Vogel, B. Burchard, H.H. Bukow, I.W. Rangelow, Y. Sarov, H. Wiggers, I. Plümel, F. Jelezko, J. Wrachtrup, F. Schmidt-Kaler, W. Schnitzler, and K. Singer. "Towards the implanting of ions and positioning of nanoparticles with nm spatial resolution". In: *Applied Physics A* 91.4 (2008), pp. 567–571. ISSN: 1432-0630. DOI: 10.1007/s00339-008-4515-1 (cited on page 104).

[462] W. Schnitzler, N. M. Linke, R. Fickler, J. Meijer, F. Schmidt-Kaler, and K. Singer. "Deterministic Ultracold Ion Source Targeting the Heisenberg Limit". In: *Physical Review Letters* 102.7 (2009), p. 070501. DOI: 10.1103/PhysRevLett.102.070501 (cited on page 104).

[463] K Ito, H Higaki, K Izawa, and H Okamoto. "Coulomb Crystal Extraction from an Ion Trap for Application to Nano-beam Source". In: *1st International Particle Accelerator Conference*. Kyoto, Japan, 2010 (cited on page 104).

[464] Bernhard H. Wolf and Chemical Rubber Company, eds. *Handbook of ion sources*. Boca Raton, Fla.: CRC Press, 1995. ISBN: 978-0-8493-2502-1 (cited on page 104).

[465] Ampere A. Tseng. "Recent Developments in Nanofabrication Using Focused Ion Beams". In: *Small* 1.10 (2005), pp. 924–939. ISSN: 1613-6829. DOI: 10.1002/smll.200500113 (cited on page 104).

[466] Ping Li, Siyu Chen, Houfu Dai, Zhengmei Yang, Zhiquan Chen, Yasi Wang, Yiqin Chen, Wenqiang Peng, Wubin Shan, and Huigao Duan. "Recent advances in focused ion beam nanofabrication for nanostructures and devices: fundamentals and applications". In: *Nanoscale* 13.3 (2021), pp. 1529–1565. DOI: 10.1039/D0NR07539F (cited on page 104).

[467] Shinji Matsui, Takashi Kaito, Jun-ichi Fujita, Masanori Komuro, Kazuhiro Kanda, and Yuichi Haruyama. "Three-dimensional nanostructure fabrication by focused-ion-beam chemical vapor deposition". In: *Journal of Vacuum Science & Technology B: Microelectronics and Nanometer Structures Processing, Measurement, and Phenomena* 18.6 (2000), pp. 3181–3184. ISSN: 1071-1023. DOI: 10.1116/1.1319689 (cited on page 104).

[468] Richard B. Fair. "Analysis and Design of Ion-Beam Deposition Apparatus". In: *Journal of Applied Physics* 42.8 (1971), pp. 3176–3181. ISSN: 0021-8979. DOI: 10.1063/1.1660703 (cited on page 104).

[469] J. Amano, P. Bryce, and R. P. W. Lawson. "Thin film deposition using low-energy ion beams. I. System specification and design". In: *Journal of Vacuum Science and Technology* 13.2 (1976), pp. 591–595. ISSN: 0022-5355. DOI: 10.1116/1.569040 (cited on page 104).

[470] D. H. Narum and R. F. W. Pease. "A variable energy focused ion beam system for in-situ microfabrication". In: *Journal of Vacuum Science & Technology B: Microelectronics Processing and Phenomena* 6.3 (1988), pp. 966–973. ISSN: 0734-211X. DOI: 10.1116/1.584289 (cited on page 104).

[471] Shinji Nagamachi, Yasuhiro Yamakage, Hiromasa Maruno, Masahiro Ueda, Seiji Sugimoto, Masatoshi Asari, and Junzo Ishikawa. "Focused ion beam direct deposition of gold". In: *Applied Physics Letters* 62.17 (1993), pp. 2143–2145. ISSN: 0003-6951. DOI: 10.1063/1.109453 (cited on page 104).

[472] D. H. Narum and R. F. W. Pease. "Applications of a variable energy focused ion beam system". In: *Journal of Vacuum Science & Technology B: Microelectronics Processing and Phenomena* 6.6 (1988), pp. 2115–2119. ISSN: 0734-211X. DOI: 10.1116/1.584096 (cited on page 104).

[473] Shinji Nagamachi, Masahiro Ueda, and Junzo Ishikawa. "Focused ion beam direct deposition and its applications". In: *Journal of Vacuum Science & Technology B: Microelectronics and Nanometer Structures Processing, Measurement, and Phenomena* 16.4 (1998), pp. 2515–2521. ISSN: 1071-1023. DOI: 10.1116/1.590201 (cited on pages 104, 107).

[474] J. Ahn, R. P. W. Lawson, K. M. Yoo, K. A. Stromsmoe, and M. J. Brett. "Deposition of metastable binary alloy thin films using sequential ion beams from a single ion source". In: *Nuclear Instruments and Methods in Physics Research Section B: Beam Interactions with Materials and Atoms* 17.1 (1986), pp. 37–45. ISSN: 0168-583X. DOI: 10.1016/0168-583X(86)90449-0 (cited on page 104).

[475] James M. E. Harper. "II-5 - Ion Beam Deposition". In: *Thin Film Processes*. Ed. by John L. Vossen and Werner Kern. San Diego: Academic Press, 1978, pp. 175–206. ISBN: 978-0-12-728250-3. DOI: 10.1016/B978-0-12-728250-3.50010-6 (cited on page 104).

[476] Robert L. Gerlach and Mark Utlaut. "Focused ion beam methods of nanofabrication: room at the bottom". In: *Charged Particle Detection, Diagnostics, and Imaging*. Vol. 4510. SPIE, 2001, pp. 96–106. DOI: 10.1117/12.451270 (cited on page 104).

[477] Wuxia Li and Changzhi Gu. "Ion Beam Instruments Used for Nanomanufacturing". In: *Handbook of Manufacturing Engineering and Technology*. Ed. by Andrew Nee. London: Springer, 2013, pp. 1–22. ISBN: 978-1-4471-4976-7. DOI: 10.1007/978-1-4471-4976-7_63-4 (cited on page 104).

[478] B. R. Appleton, S. J. Pennycook, R. A. Zuhr, N. Herbots, and T. S. Noggle. "Low-temperature epitaxial growth of Si and Ge and fabrication of isotopic heterostructures by direct ion beam deposition". In: *Nuclear Instruments and Methods in Physics Research Section B: Beam Interactions with Materials and Atoms*. Proceedings of the Fifth International Conference on Ion Beam Modification of Materials 19-20 (1987), pp. 975–982. ISSN: 0168-583X. DOI: 10.1016/S0168-583X(87)80195-7 (cited on page 104).

[479] Andrew Grenville, Jeremy T. Anderson, Benjamin L. Clark, Peter De Schepper, Joseph Edson, Michael Greer, Kai Jiang, Michael Kocsis, Stephen T. Meyers, Jason K. Stowers, Alan J. Telecky, Danilo De Simone, and Geert Vandenberghe. "Integrated fab process for metal oxide EUV photoresist". In: *Advances in Patterning Materials and Processes XXXII*. Vol. 9425. SPIE, 2015, pp. 225–232. DOI: 10.1117/12.2086006 (cited on page 105).

[480] Chung-Soo Kim. "Nanoscale 3D printing process using nano particle deposition system and focused ion beam". Thesis. Seoul National University, 2013. URL: https://s-space.snu.ac.kr/handle/10371/118318 (cited on page 105).

[481] Sung-Hoon Ahn, Hae-Sung Yoon, Ki-Hwan Jang, Eun-Seob Kim, Hyun-Taek Lee, Gil-Yong Lee, Chung-Soo Kim, and Suk-Won Cha. "Nanoscale 3D printing process using aerodynamically focused nanoparticle (AFN) printing, micro-machining, and focused ion beam (FIB)". In: *CIRP Annals* 64.1 (2015), pp. 523–526. ISSN: 0007-8506. DOI: 10.1016/j.cirp.2015.03.007 (cited on page 105).

[482] Roar Søndergaard, Markus Hösel, Dechan Angmo, Thue T. Larsen-Olsen, and Frederik C. Krebs. "Roll-to-roll fabrication of polymer solar cells". In: *Materials Today* 15.1 (2012), pp. 36–49. ISSN: 1369-7021. DOI: 10.1016/S1369-7021(12)70019-6 (cited on page 107).

[483] Hsien-Shun Liao, Christian Werner, Roman Slipets, Peter Emil Larsen, Ing-Shouh Hwang, Tien-Jen Chang, Hans Ulrich Danzebrink, Kuang-Yuh Huang, and En-Te Hwu. "Low-cost, open-source *XYZ* nanopositioner for high-precision analytical applications". In: *HardwareX* 11 (2022), e00317. ISSN: 2468-0672. DOI: 10.1016/j.ohx.2022.e00317 (cited on page 108).

[484] *List of semiconductor fabrication plants*. en. Page Version ID: 1261623827. 2024. URL: https://en.wikipedia.org/w/index.php?title=List_of_semiconductor_fabrication_plants (visited on 12/10/2024) (cited on page 109).

[485] *Frequently asked questions*. Muse Semiconductor. 2024. URL: https://www.musesemi.com/faq (cited on page 110).

[486] *Schedules & Prices, 2024*. Europractice. 2024. URL: https://europractice-ic.com/schedules-prices-2024/ (cited on page 110).

[487] *TSMC MPW SHARED TAPEOUT SCHEDULE*. Muse Semiconductor. 2024. URL: https://www.musesemi.com/shared-block-tapeout-schedule (cited on page 110).

[488] *MPW Schedule 2024 & 2025 and Price Information 2024*. IHP. 2024. URL: https://www.ihp-microelectronics.com/services/research-and-prototyping-service/mpw-prototyping-service/schedule-price-list (cited on page 110).

[489] *Prototyping Support*. X-Fab. 2024. URL: https://www.xfab.com/manufacturing/prototyping (cited on page 110).

[490] *chipignite Mini: Prototype Custom ICs on a Mini Budget*. efabless. 2024. URL: https://efabless.com/chipignite-mini (cited on page 110).

[491] Alissa M. Fitzgerald, Carolyn D. White, and Charles C. Chung. *MEMS Product Development: From Concept to Commercialization*. Microsystems and Nanosystems. Springer, 2021. ISBN: 978-3-030-61709-7. DOI: 10.1007/978-3-030-61709-7 (cited on page 112).

[492] *Pragmatic Semiconductor*. Pragmatic Semiconductor. 2024. URL: https://www.pragmaticsemi.com/ (cited on page 112).

[493] *Rapid, Cost Efficient Microfabrication*. InchFab. 2024. URL: https://www.inchfab.com/ (cited on page 112).

[494] *Atomic Semi - The Make Anything Company*. Atomic Semi. 2024. URL: https://atomicsemi.com/ (cited on page 112).

[495] *Minimal Fab Promoting Organization*. Minmimal Fab. 2024. URL: https://www.minimalfab.com/en/ (cited on page 112).

[496] Mitchell David Hsing. "Design, fabrication, and characterization of a compact magnetron sputtering system for micro/nano fabrication". Thesis. Massachusetts Institute of Technology, 2019. URL: https://dspace.mit.edu/handle/1721.1/122559 (cited on page 112).

[497] Ken Shirriff. *Silicon die teardown: a look inside an early 555 timer chip*. 2022. URL: https://www.righto.com/2022/01/silicon-die-teardown-look-inside-early.html (cited on page 114).

[498] Ken Shirriff. *The 6502 CPU's overflow flag explained at the silicon level*. 2013. URL: https://www.righto.com/2013/01/a-small-part-of-6502-chip-explained.html (cited on page 114).

[499] *Images of the 6502*. Visual6502.org. 2024. URL: http://visual6502.org/images/6502/index.html (cited on page 114).
[500] Christie R. K. Marrian and Donald M. Tennant. "Nanofabrication". In: *Journal of Vacuum Science & Technology A* 21.5 (2003), S207–S215. ISSN: 0734-2101. DOI: 10.1116/1.1600446 (cited on page 114).
[501] J. Alexander Liddle and Gregg M. Gallatin. "Lithography, metrology and nanomanufacturing". In: *Nanoscale* 3.7 (2011), pp. 2679–2688. ISSN: 2040-3372. DOI: 10.1039/C1NR10046G (cited on page 114).
[502] Sourabh K. Saha, Dien Wang, Vu H. Nguyen, Yina Chang, James S. Oakdale, and Shih-Chi Chen. "Scalable submicrometer additive manufacturing". In: *Science* 366.6461 (2019), pp. 105–109. DOI: 10.1126/science.aax8760 (cited on page 114).
[503] Vincent Hahn, Pascal Kiefer, Tobias Frenzel, Jingyuan Qu, Eva Blasco, Christopher Barner-Kowollik, and Martin Wegener. "Rapid Assembly of Small Materials Building Blocks (Voxels) into Large Functional 3D Metamaterials". In: *Advanced Functional Materials* 30.26 (2020), p. 1907795. ISSN: 1616-3028. DOI: 10.1002/adfm.201907795 (cited on page 114).
[504] Dipankar Behera, Samira Chizari, Lucas A. Shaw, Michael Porter, Ryan Hensleigh, Zhenpeng Xu, Ximeng Zheng, Liam G. Connolly, Nilabh K. Roy, Robert M. Panas, Sourabh K. Saha, Xiaoyu (Rayne) Zheng, Jonathan B. Hopkins, Shih-Chi Chen, and Michael A. Cullinan. "Current challenges and potential directions towards precision microscale additive manufacturing – Part IV: Future perspectives". In: *Precision Engineering* 68 (2021), pp. 197–205. ISSN: 0141-6359. DOI: 10.1016/j.precisioneng.2020.12.014 (cited on page 114).
[505] David M. Wirth, Chi Chung Li, Jonathan K. Pokorski, Hayden K. Taylor, and Maxim Shusteff. "Fundamental scaling relationships in additive manufacturing and their implications for future manufacturing and bio-manufacturing systems". In: *Additive Manufacturing* 84 (2024), p. 104081. ISSN: 2214-8604. DOI: 10.1016/j.addma.2024.104081 (cited on page 114).
[506] K.R. Williams and R.S. Muller. "Etch rates for micromachining processing". In: *Journal of Microelectromechanical Systems* 5.4 (1996), pp. 256–269. ISSN: 1941-0158. DOI: 10.1109/84.546406 (cited on page 115).
[507] K.R. Williams, K. Gupta, and M. Wasilik. "Etch rates for micromachining processing-Part II". In: *Journal of Microelectromechanical Systems* 12.6 (2003), pp. 761–778. ISSN: 1941-0158. DOI: 10.1109/JMEMS.2003.820936 (cited on page 115).
[508] Christophe Lécuyer. "From Clean Rooms to Dirty Water: Labor, Semiconductor Firms, and the Struggle over Pollution and Workplace Hazards in Silicon Valley". In: *Information & Culture* 52.3 (2017), pp. 304–333. ISSN: 2164-8034 (cited on page 115).
[509] Eric D Williams. "Environmental impacts of microchip manufacture". In: *Thin Solid Films*. Proceedings of Symposium on Semiconducting Silicides: Science and Future Technology of the 8th IUMRS International Conference on Advanced Materials 461.1 (2004), pp. 2–6. ISSN: 0040-6090. DOI: 10.1016/j.tsf.2004.02.049 (cited on page 115).
[510] Shih-Cheng Hu, Angus Shiue, Hsien-Chou Chuang, and Tengfang Xu. "Life cycle assessment of high-technology buildings: Energy consumption and associated environmental impacts of wafer fabrication plants". In: *Energy and Buildings* 56 (2013), pp. 126–133. ISSN: 0378-7788. DOI: 10.1016/j.enbuild.2012.09.023 (cited on page 115).
[511] Chetan Choppali Sudarshan, Nikhil Matkar, Sarma Vrudhula, Sachin S. Sapatnekar, and Vidya A. Chhabria. "ECO-CHIP: Estimation of Carbon Footprint of Chiplet-based Architectures for Sustainable VLSI". In: *2024 IEEE International Symposium on High-Performance Computer Architecture (HPCA)*. 2024, pp. 671–685. DOI: 10.1109/HPCA57654.2024.00058 (cited on page 115).
[512] Aurélie Villard, Alan Lelah, and Daniel Brissaud. "Drawing a chip environmental profile: environmental indicators for the semiconductor industry". In: *Journal of Cleaner Production* 86 (2015), pp. 98–109. ISSN: 0959-6526. DOI: 10.1016/j.jclepro.2014.08.061 (cited on page 115).
[513] Liqiu Deng and Eric Williams. "Measures and trends in energy use of semiconductor manufacturing". In: *2008 IEEE International Symposium on Electronics and the Environment*. ISSN: 2378-7260. 2008, pp. 1–6. DOI: 10.1109/ISEE.2008.4562888 (cited on page 115).
[514] Robert Weinstock. "On a fallacious proof of Earnshaw's theorem". In: *American Journal of Physics* 44.4 (1976), pp. 392–393. ISSN: 0002-9505. DOI: 10.1119/1.10449 (cited on page 151).

[515] H. G. Dehmelt. "Radiofrequency Spectroscopy of Stored Ions I: Storage*". In: *Advances in Atomic and Molecular Physics*. Ed. by D. R. Bates and Immanuel Estermann. Vol. 3. Academic Press, 1968, pp. 53–72. DOI: 10.1016/S0065-2199(08)60170-0 (cited on pages 152, 153, 161).

[516] P. V. Bugrov, A. A. Sysoev, A. N. Konenkov, and N. V. Konenkov. "Properties of the multipole fields formed by round electrodes". In: *International Journal of Mass Spectrometry* 490 (2023), p. 117081. ISSN: 1387-3806. DOI: 10.1016/j.ijms.2023.117081 (cited on page 153).

[517] D. R. Denison. "Operating Parameters of a Quadrupole in a Grounded Cylindrical Housing". In: *Journal of Vacuum Science and Technology* 8.1 (1971), pp. 266–269. ISSN: 0022-5355. DOI: 10.1116/1.1316304 (cited on page 153).

[518] I. E. Dayton, F. C. Shoemaker, and R. F. Mozley. "The Measurement of Two-Dimensional Fields. Part II: Study of a Quadrupole Magnet". In: *Review of Scientific Instruments* 25.5 (1954), pp. 485–489. ISSN: 0034-6748. DOI: 10.1063/1.1771107 (cited on page 153).

[519] Eugene I. Butikov. "Analytical expressions for stability regions in the Ince–Strutt diagram of Mathieu equation". In: *American Journal of Physics* 86.4 (2018), pp. 257–267. ISSN: 0002-9505. DOI: 10.1119/1.5021895 (cited on pages 154, 155).

[520] Frank W. J. Olver, Daniel W. Lozier, Ronald F. Boisvert, and Charles W. Clark. *NIST Handbook of Mathematical Functions*. Cambridge University Press, 2010. ISBN: 978-0-521-19225-5 (cited on pages 154, 155).

[521] Milton Abramowitz and Irene Stegun. *Handbook of Mathematical Functions*. Tenth Printing. Applied Mathematics Series 55. National Bureau of Standards, 1972 (cited on page 154).

[522] Raymond E. March and John F. J. Todd. *Practical aspects of ion trap mass spectrometry, Volume IV: Theory and Instrumentation*. Boca Raton, Fla: CRC Press, 2010. ISBN: 978-1-4200-8372-9 (cited on page 157).

[523] C. Monroe and J. Kim. "Scaling the Ion Trap Quantum Processor". In: *Science* 339.6124 (2013), pp. 1164–1169. DOI: 10.1126/science.1231298 (cited on page 157).

[524] J. Chiaverini, R. B. Blakestad, J. Britton, J. Jost, C. Langer, D. Leibfried, R. Ozeri, and D. Wineland. "Surface-electrode architecture for ion-trap quantum information processing". In: *Quantum Inf. Comput.* 5.6 (2005), pp. 419–439. ISSN: 1533-7146 (cited on page 157).

[525] C. E. Pearson, D. R. Leibrandt, W. S. Bakr, W. J. Mallard, K. R. Brown, and I. L. Chuang. "Experimental investigation of planar ion traps". In: *Physical Review A* 73.3 (2006), p. 032307. DOI: 10.1103/PhysRevA.73.032307 (cited on page 157).

[526] József Fortágh and Claus Zimmermann. "Magnetic microtraps for ultracold atoms". In: *Reviews of Modern Physics* 79.1 (2007), pp. 235–289. DOI: 10.1103/RevModPhys.79.235 (cited on page 157).

[527] G. B. Andresen, M. D. Ashkezari, M. Baquero-Ruiz, W. Bertsche, P. D. Bowe, E. Butler, C. L. Cesar, S. Chapman, M. Charlton, A. Deller, S. Eriksson, J. Fajans, T. Friesen, M. C. Fujiwara, D. R. Gill, A. Gutierrez, J. S. Hangst, W. N. Hardy, M. E. Hayden, A. J. Humphries, R. Hydomako, M. J. Jenkins, S. Jonsell, L. V. Jørgensen, L. Kurchaninov, N. Madsen, S. Menary, P. Nolan, K. Olchanski, A. Olin, A. Povilus, P. Pusa, F. Robicheaux, E. Sarid, S. Seif el Nasr, D. M. Silveira, C. So, J. W. Storey, R. I. Thompson, D. P. van der Werf, J. S. Wurtele, and Y. Yamazaki. "Trapped antihydrogen". In: *Nature* 468.7324 (2010), pp. 673–676. ISSN: 1476-4687. DOI: 10.1038/nature09610 (cited on page 157).

[528] G. B. Andresen, M. D. Ashkezari, M. Baquero-Ruiz, W. Bertsche, P. D. Bowe, E. Butler, C. L. Cesar, M. Charlton, A. Deller, S. Eriksson, J. Fajans, T. Friesen, M. C. Fujiwara, D. R. Gill, A. Gutierrez, J. S. Hangst, W. N. Hardy, R. S. Hayano, M. E. Hayden, A. J. Humphries, R. Hydomako, S. Jonsell, S. L. Kemp, L. Kurchaninov, N. Madsen, S. Menary, P. Nolan, K. Olchanski, A. Olin, P. Pusa, C. Ø. Rasmussen, F. Robicheaux, E. Sarid, D. M. Silveira, C. So, J. W. Storey, R. I. Thompson, D. P. van der Werf, J. S. Wurtele, Y. Yamazaki, and The ALPHA Collaboration. "Confinement of antihydrogen for 1,000 seconds". In: *Nature Physics* 7.7 (2011), pp. 558–564. ISSN: 1745-2481. DOI: 10.1038/nphys2025 (cited on page 157).

[529] J. R. Danielson, D. H. E. Dubin, R. G. Greaves, and C. M. Surko. "Plasma and trap-based techniques for science with positrons". In: *Reviews of Modern Physics* 87.1 (2015), pp. 247–306. DOI: 10.1103/RevModPhys.87.247 (cited on page 157).

[530] Landau and Lifshitz. *Mechanics*. 3rd ed. Vol. 1. Course of Theoretical Physics. Butterworth-Heinenam, 1976. ISBN: 978-0-7506-2896-9 (cited on page 161).

[531] *ADHV4702-1 24 V to 220 V Precision Operational Amplifier*. Analog Devices. 2024. URL: https://www.analog.com/en/products/adhv4702-1.html#part-details (cited on page 163).

[532] *OPA462 180-V, wide bandwidth (6.5 MHz), high-slew rate (25 V/µs) unity-gain stable op amp*. Texas Instruments. 2024. URL: https://www.ti.com/product/OPA462 (cited on page 163).

[533] *HV264 QUAD, High Voltage, Amplifier Array*. Microchip. 2024. URL: https://www.microchip.com/en-us/product/HV264 (cited on page 163).

[534] M. S. Colclough. "A fast high-voltage amplifier for driving piezoelectric positioners". In: *Review of Scientific Instruments* 71.11 (2000), pp. 4323–4324. ISSN: 0034-6748, 1089-7623. DOI: 10.1063/1.1319984 (cited on page 163).

[535] Carsten Wallenhauer, Bernhard Gottlieb, Roland Zeichfusl, and Andreas Kappel. "Efficiency-Improved High-Voltage Analog Power Amplifier for Driving Piezoelectric Actuators". In: *IEEE Transactions on Circuits and Systems I: Regular Papers* 57.1 (2010), pp. 291–298. ISSN: 1558-0806. DOI: 10.1109/TCSI.2009.2018938 (cited on page 163).

[536] Michael Karpelson, Gu-Yeon Wei, and Robert J. Wood. "Driving high voltage piezoelectric actuators in microrobotic applications". In: *Sensors and Actuators A: Physical* 176 (2012), pp. 78–89. ISSN: 0924-4247. DOI: 10.1016/j.sna.2011.11.035 (cited on page 163).

[537] W. Saito, T. Domon, I. Omura, M. Kuraguchi, Y. Takada, K. Tsuda, and M. Yamaguchi. "Demonstration of 13.56-MHz class-E amplifier using a high-Voltage GaN power-HEMT". In: *IEEE Electron Device Letters* 27.5 (2006), pp. 326–328. ISSN: 1558-0563. DOI: 10.1109/LED.2006.873756 (cited on page 163).

[538] Davide Ghisu, Andrea Gambero, Marco Terenzi, Giulio Ricotti, Anna Moroni, and Sandro Rossi. "180Vpp output voltage, 24MHz bandwidth, low power class AB current-feedback high voltage amplifier for ultrasound transmitters". In: *2018 IEEE Custom Integrated Circuits Conference (CICC)*. 2018, pp. 1–4. DOI: 10.1109/CICC.2018.8357014 (cited on page 163).

[539] Holger Müller. "Fast high-voltage amplifiers for driving electro-optic modulators". In: *Review of Scientific Instruments* 76.8 (2005), p. 084701. ISSN: 0034-6748. DOI: 10.1063/1.1988272 (cited on page 163).

[540] C. Koçum. "Digitally gain controlled linear high voltage amplifier for laboratory applications". In: *Review of Scientific Instruments* 82.8 (2011), p. 084702. ISSN: 0034-6748. DOI: 10.1063/1.3622750 (cited on page 163).

[541] *WMA-300 High speed high voltage amplifier*. Falco Systems. 2024. URL: https://www.falco-systems.com/High_voltage_amplifier_WMA-300.html (cited on pages 163, 165).

[542] J. Stuart, R. Panock, C.D. Bruzewicz, J.A. Sedlacek, R. McConnell, I.L. Chuang, J.M. Sage, and J. Chiaverini. "Chip-Integrated Voltage Sources for Control of Trapped Ions". In: *Physical Review Applied* 11.2 (2019), p. 024010. DOI: 10.1103/PhysRevApplied.11.024010 (cited on page 165).

Appendix A

Ion Traps and Quadrupoles

In chapter 6 we discussed the motion of charged nanoparticles in electric fields in vacuum then introduced certain static electric fields with useful properties (e.g., Einzel lenses focus particle beams). But something was missing at first: there was no way[1] to force (or "trap") a particle to stay still (levitate), even though it sounds like an easy thing to do.

It turns out trapping particles is fundamentally impossible with electric fields that do not change over time. This is called Earnshaw's theorem [514]. But as we will shortly discover, trapping is possible if we allowing electric fields to oscillate with time, and this is widely used in multiple areas of study [293]. We will introduce these ideas, especially linear quadrupole traps, so that we can use them in chapter 6 (specifically starting in section 6.3.2).

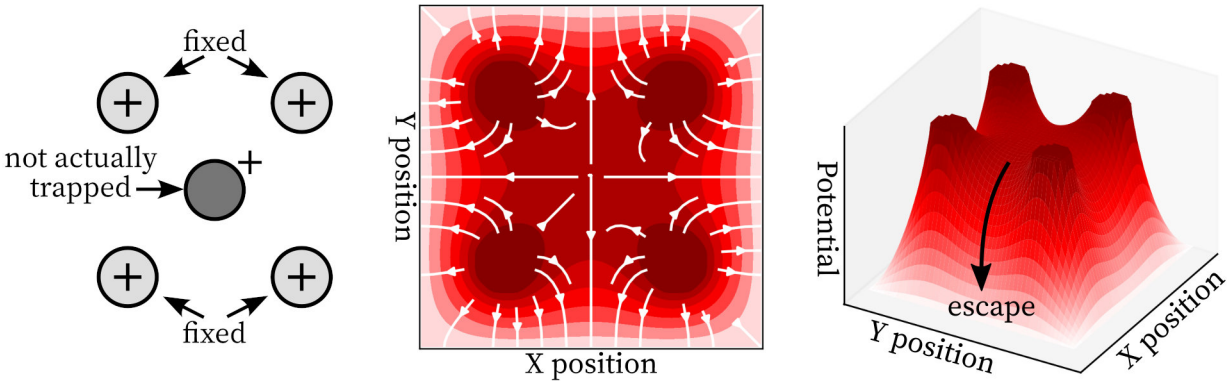

Figure A.1: An example of Earnshaw's theorem. Left: consider a positively charged particle between four infinitely long positively charged circular rods in a 2D plane. Charges repel each other, so one's intuition might expect the particle would be trapped in the middle, but in fact there is always a direction the particle is pushed in until it is far away (middle and right figures); when centered between the rods it is only in unstable equilibrium. The same occurs in any arrangement of electrodes/fixed charges (e.g., at the vertices of a tetrahedron).

[1] At least without tracking the particle and changing the field to compensate, which is often impractical.

Earnshaw's theorem can be quickly proved as follows: consider a time-invariant electric field. At any location the field satisfies Gauss's law by having zero divergence (Laplace's equation), which means the field is either perfectly flat or has decreasing potential in some direction.

We can avoid Earnshaw's theorem and levitate particles by allowing the electric field to change with time[2] in a way that uses a particle's inertia to prevent its escape. To do this we use the ponderomotive force, which we describe and prove in detail in appendix B.

The ponderomotive force (appendix B) is an emergent effect that occurs as follows. Suppose a point particle of mass m and charge q at position $\vec{x}$ placed in a time-oscillating electric field of the form $\vec{E}(t, \vec{x}) = \vec{E}_0(\vec{x}) \cdot \cos(\omega t)$. The particle will vibrate back and forth slightly ("micromotion") but, on average, will feel a net force

$$\vec{F}(\vec{x}) = -\frac{q^2}{4m\omega^2} \nabla \left(|\vec{E}_0(\vec{x})|^2 \right) \tag{A.1}$$

as long as the oscillation angular frequency ω is sufficiently large (as noted in appendix B, ω has units $\mathrm{rad\,s^{-1}}$; most applications use frequency $f = \omega/2\pi$). That is, the particle will be moved toward regions of lower electric field magnitude, which is always away from any electrodes (with varying voltages generating the oscillating field). Furthermore, this average behavior is conservative, meaning the particle moves as if it is in a potential just like a static electric field—this is extremely elegant.

Given this trick, our setup of figure A.1 can actually work as we intuitively expect if, instead of putting each of our four fixed electrodes at a single charge or voltage, we apply the correct oscillating voltages. Specifically, the lower left and upper right (diagonal) electrodes should have the same voltage changing sinusoidally with time, and the lower right and upper left (the other diagonal) need the same voltage but offset 180° in time—that is, if one diagonal electrode set has a positive voltage, the other diagonal has a negative, and vice-versa. The only remaining requirement is the oscillation frequency is above a certain minimum. A charged particle now experiences a force toward the center of the electrode array.

These sorts of structures are called "ion traps" as they confine charged particles (including atomic ions) to a fixed location. Sometimes they are called "RF traps" due to the oscillation at radio frequencies (kilohertz to megahertz), and sometimes "Paul traps" after Wolfgang Paul who won the 1989 Physics Nobel [321] with Dehmelt [515] for developing them.

It is easy to make ion traps in many shapes; almost any electrode arrangement can work. However, the most common [293] ion trap shape is the "quadrupole", which has four electrodes like we previously considered (albeit ideally hyperbolas instead of circles). Quadrupole traps are the only ion trap geometry with a tractable exact particle motion equation [293], are the simplest to build, and also provide the strongest trapping force[3].

We will review the full analytical theory of quadrupole traps—which are also what we use in chapter 6—then make some remarks about other trap geometries.

[2] Or by other methods, e.g., adding magnetic fields, which we briefly discuss at the end of this appendix.

[3] See our notes on multipole traps also at the end of this appendix.

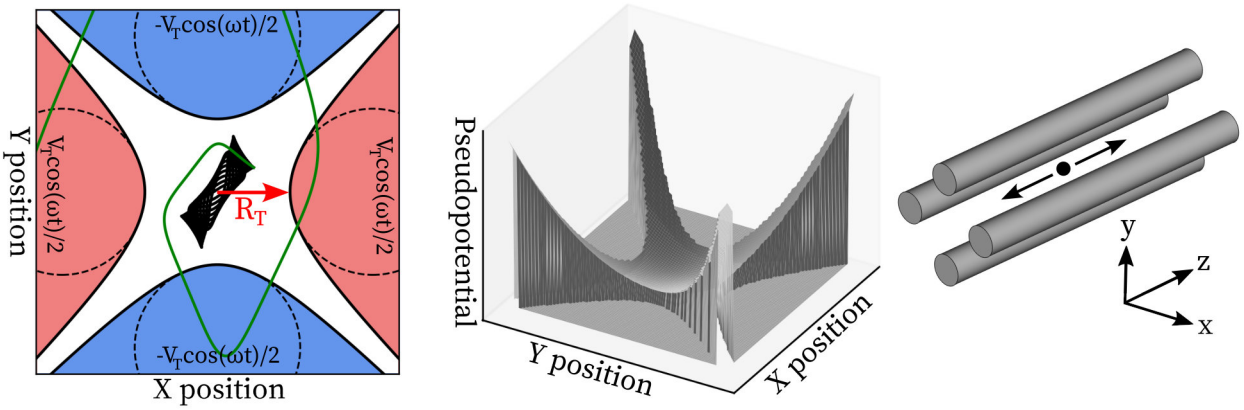

Figure A.2: Left: a 2D quadrupole ion trap made by four electrodes (two red, two blue) with corresponding oscillating voltages. At any one time, two are positive and the other two are negative. The electrodes are hyperbolas for an ideal quadrupole but can be approximated by circles [516][517]. We call the distance from trap center to the nearest electrode R_T. Some particles (black line) oscillate but are trapped between the electrodes; others (green line) move sufficiently far that they hit an electrode and are lost. Center: the average force stably trapped particles feel is a 2D quadratic potential well; we derive this in equation A.9. Right: extending this into 3D traps a particle between rod electrodes. The particle can move back and forth freely with no force or friction.

An ideal 2D quadrupole trap [293][515][321] is made from four hyperbolic electrodes[4] placed together as in figure A.2, fairly similar to figure A.1. Put two electrodes on the x axis and two on the y; the two x electrodes will always have the same voltage and similar for y. The distance from the trap center (the coordinate system origin) is R_T, and the electrodes are defined by $R_T^2 = \pm(x^2 - y^2)$.

To operate the trap, apply oscillating voltage $V_T \cos(\omega t)/2$ to one pair of electrodes (where V_T is a voltage, ω is an angular frequency, and t is time) and $-V_T \cos(\omega t)/2$ to the other (note this means the maximum total voltage difference between electrodes is V_T)[5]. This generates an electric field $\vec{E}$ inside the trap (between the electrodes) of

$$\vec{E}(x,y) = -\frac{V_T}{R_T^2}\cos(\omega t)\begin{bmatrix} x \\ -y \end{bmatrix} \tag{A.2}$$

which has electric potential energy U_T (with $q\vec{E} = -\nabla U_T$) of

$$U_T(x,y) = \frac{qV_T}{2R_T^2}(x^2 - y^2)\cos(\omega t). \tag{A.3}$$

[4]Since hyperbolas are hard to manufacture, the electrodes can be approximated well with circular electrodes of radius $1.14r_0$ [516][517][518] with centers at coordinates $(R_0 + 1.14r_0, 0)$, etc.

[5]Analysis of quadrupoles sometimes instead uses $V_0 = V_T/2$.

To analyze particle motion inside the trap, we could directly apply our ponderomotive force analysis (equation A.1) to equation A.2. We will do so momentarily. However, of all ion traps the quadrupole is notable in that it is possible to analyze exact particle trajectories without the ponderomotive approximation [358], so we will do that first.

So consider a particle of mass m and charge q moving $x(t)$ according to the simplified Lorentz force $\vec{F} = q\vec{E}$ (see section 6.2) and $\vec{F} = m\vec{a}$. An examination of equation A.2 reveals the electric field is independent in the x and y directions—this is why the quadrupole is simple enough to analyze—so we only have to write the equation of motion in the x direction; the particle will independently move in the y direction similarly:

$$\frac{d^2x}{dt^2} = -\frac{qV_T}{mR_T^2}\cos(\omega t)\, x. \tag{A.4}$$

This is a Mathieu differential equation; these occur in many areas of physics[6]. The solution trajectories (which are generally periodic oscillations) are known [520] but too complex to write here. But there is another useful way to analyze a Mathieu system: it turns out trajectories have one of two behaviors. Either trajectories will remain within some finite value (are "stable", i.e., our trapped particle will always stay trapped, close to the origin), or trajectories will grow until particles exit the trap (as in figure A.2).

To see this stability behavior, we need to rewrite equation A.4 in a standard form. To help, we will modify our conditions by adding a DC bias V_T' to the electrodes (the two x electrode voltages increase by $V_T'/2$ and the y decrease by $V_T'/2$). We don't usually want this save in quadrupole mass spectrometry [359], but it's useful for illustration. Equation A.4 becomes $\frac{d^2x}{dt^2} = -q/(mR_T^2)\left[V_T' + V_T\cos(\omega t)\right]\cdot x$. This matches the standard [520][521] Mathieu form

$$\frac{d^2w}{du^2} + \left[a_m - 2q_m\cos(2u)\right] w = 0 \tag{A.5}$$

when $w = x$, $u = t\cdot\omega/2$, $a_m = (4qV_T')/(mR_T^2\omega^2)$, and $q_m = (2qV_T)/(mR_T^2\omega^2)$. A thorough analysis of Mathieu equations [520] shows trajectories are either stable or unstable depending on the nondimensional parameters a_m and q_m in a surprisingly complex way, which we graph in figure A.3 (an Ince-Strutt diagram). For our purposes, we mainly care about the case when $V_T' = 0$ and thus $a_m = 0$, at which point the particle trajectory is stable when $q_m < 0.91$ (approximately), with little regard for its initial conditions.

Ion traps (and the ponderomotive force in general) only work when the voltage oscillation frequency ω is sufficiently high (as noted in appendix B); that is the case here. We can rewrite the Mathieu stability criterion $q_m < 0.91$ to get the minimum angular frequency ω:

$$\omega > \sqrt{\frac{2qV_T}{0.91mR_T^2}} \approx \sqrt{\frac{2qV_T}{mR_T^2}}. \tag{A.6}$$

[6]For example, the Mathieu equation describes Kapitza's pendulum, the effect that an inverted pendulum can be stable when oscillated vertically [519].

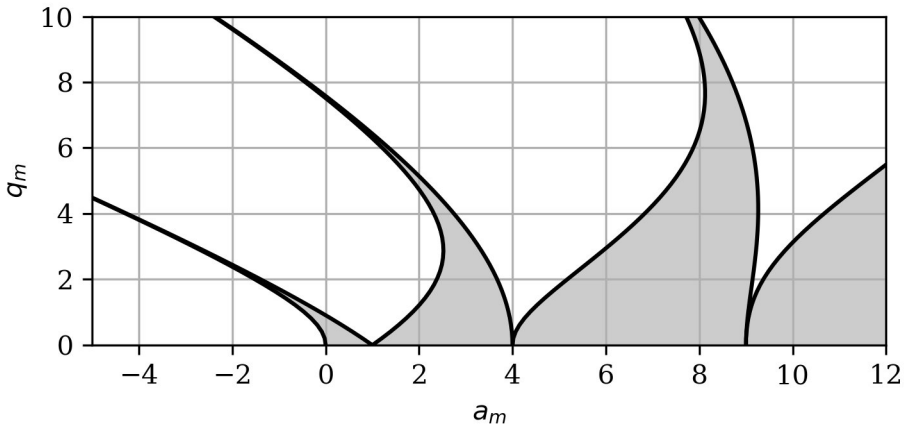

Figure A.3: The Ince-Strutt diagram [520][519][359]. The solutions to a Mathieu equation with parameters a_m and q_m are stable inside the regions shaded gray; otherwise, trajectories grow to infinity over time. The graph is symmetric about $q_m = 0$. We are mainly concerned with the region $a_m = 0$, for which stability occurs when $q_m < 0.91$ (approximately). This complexity of this graph is why finding the minimum frequency ω for an ion trap is hard.

This is about as much useful information as we're going to get out of the Mathieu equation. Equation A.6 describing the minimum frequency will be very useful (and is more accurate than our approximation of equation B.14 in appendix B), however, so we will briefly try to wrap more intuition around it. The frequency is important because, again, once trap geometry and voltage are fixed, the relationship between frequency ω and particle mass/charge ratio m/q determines whether the particle is stably trapped, and how strongly.

To build intuition, consider the relationship between the minimum frequency ω and the mass m of the particle (keeping charge q constant for illustration). In the normal case when the quadrupole electrodes have no DC bias ($V_T' = 0$ and $a_m = 0$), another way of stating $q_m < 0.91$ is that all particles above a certain mass will be trapped. Smaller particles will accelerate too quickly and leave the trap before voltages can oscillate to pull them back.

On the other hand, if some DC bias V_T' is applied to the electrodes, figure A.3 suggests there are regions ($a_m < 0$)[7] where larger particles are unstable. This is because, as particle size increases for fixed ω, the trap force is weaker and eventually small enough that the Earnshaw's theorem effect from the DC bias will move the particle out of the trap.

Quadrupole mass spectrometers work by taking advantage of this Mathieu stability criterion with combined lowpass and highpass effects [359]. Careful selection of voltages V_T and V_T' and frequency ω means particles within only a small (adjustable!) range of mass/charge ratios will be trapped and can be measured[8].

[7]This is asymmetrical because we're only considering one direction of motion (x or y). When the DC bias V_T' is applied to the electrodes, Earnshaw escapes are only in one of these directions; the other is stable.

[8]In chapter 6 we will want to use parameters (e.g., $V_T' = 0$) that trap a wider range of particles, though we might consider using this effect to filter nanoparticles by size; see chapter 2 for other filter methods.

It is probably clear that this exact Mathieu approach to analyzing quadrupole motion is complicated. Fortunately, we have a much easier way to understand and approximate the behavior of a quadrupole trap (or any other ion trap, even when the exact solution is unavailable): we apply the aforementioned ponderomotive force (still from appendix B).

Again, the ponderomotive effect is that a particle feels an average force away from strong oscillating electric fields. We can apply equation A.1 to equation A.2 to find the ponderomotive force $\vec{F}$ felt by a particle in a quadrupole trap:

$$\vec{F} = -\frac{q^2 V_T^2}{2m\omega^2 R_T^4} \begin{bmatrix} x \\ y \end{bmatrix}. \tag{A.7}$$

That is, a particle will feel an average force toward the center of the trap (which is why the trap works). This force is conservative, i.e., it is as if the particle were trapped in a potential field—the "pseudopotential"—with potential energy $\widetilde{U}_T$ (as $\vec{F} = q\vec{E} = -\nabla\widetilde{U}_T$)

$$\widetilde{U}_T(r) = \frac{q^2 V_T^2 r^2}{4m\omega^2 R_T^4} \tag{A.8}$$

where we have defined $r = \sqrt{x^2 + y^2}$ as the distance of the particle from the trap center. This is a radially symmetric 2D quadratic potential well, as shown in figure A.2! The behavior of a particle is now easy to reason about: if its initial position and kinetic energy are enough to stay within the well, it will stay trapped, merely oscillating within it over time (with angular frequency $\omega q_m/\sqrt{8}$ and amplitude X_P). Of course, ponderomotive micromotion is overlaid on top with frequency ω and, via equation B.5, amplitude $q_m X_P/2$.

Finally, suppose we have particles with a range of mass/charge ratios. These can be captured in the same trap if the frequency is sufficiently high. Find this frequency using equation A.6 for the lightest particles (smallest mass/charge ratio m_0/q_0). We can combine this with equation A.8 to rewrite the pseudopotential energy (at that optimal frequency) for any particle with mass/charge ratio m/q as

$$\widetilde{U}_T(r) \approx \frac{qV_T\, r^2}{8R_T^2} \cdot \frac{q}{q_0} \cdot \frac{m_0}{m}. \tag{A.9}$$

which now acts just like a normal electrostatic potential that scales with charge and voltage. Particles with $m/q > m_0/q_0$ will see proportionally smaller potential energies, and particles with $m/q < m_0/q_0$ escape the trap and are lost (by construction). This equation will be useful for us given the wide range of nanoparticle sizes we expect to use.

All this is enough to design the ion optics we use in chapter 6. We are done with analysis, though there are other minor effects we will discuss when relevant (e.g., the micromotion of the ponderomotive force can make it difficult to bring particle positions and velocities to exactly zero at the trap center, an effect called RF heating we bring up in section 6.3.3).

However, we think it is worth briefly mentioning alternative traps beyond quadrupoles.

RF ion traps are easy to design: simply place an oscillating[9] electric field between electrodes, and particles are trapped at regions of minimum electric field ("RF nulls"). This simplicity has allowed ion traps to find use in many subjects. Besides their use in mass spectrometry as quadrupoles [358] and related shapes (e.g., Kingdon trap geometries [522]), ion traps can be used in particle accelerators (see section 6.3.2) or trapped-ion quantum computing, in which ions are cooled to their quantum ground state (which requires careful study of noise [366]). This also uses a clever trick: the trap electrodes can all be placed on the same surface (a planar ion trap [395][396][523][413][409]), making it easy to microfabricate complex traps with multiple sections that particles can be moved between [416], though the trap depth is about 100x lower than a quadrupole of similar dimensions and voltage [524][525].

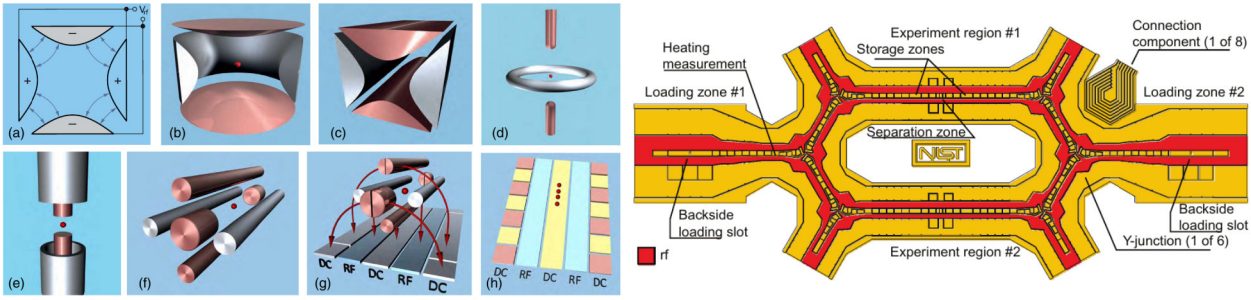

Figure A.4: Left: some other RF ion trap geometries, from [366]. The same quadrupole potential can be rotated to trap a particle at a point, or the electrodes can be a different shape. The electrodes can even be placed on a single planar surface, forming a particle trap just above it. Right: top view of a 5 mm wide planar ion trap separated into many segments demonstrating techniques for future trapped-ion quantum computers. Atomic ions could be levitated and moved around these tracks or through the three-way junctions [396].

Given the huge design space, it is worthwhile to ask if there are optimal trap shapes. One way to analyze this is to realize that no matter the electrode geometry, the potential at the center of a trap can be written as a multipole expansion: a linear combination of dipole, quadrupole, hexapole, and higher-order fields. The quadrupole field has the steepest center (which is what we want in chapter 6, so we use quadrupole electrodes[10]). Higher-order "multipoles", made with 6, 8, or other even numbers of electrodes, have a steeper edges and a flatter trap center, which can be useful if low RF heating is preferable at the expense of position resolution or for trapping multiple ions of significantly different masses [293].

It is also possible to build traps with magnetic fields. A "Penning trap" confines charged particles with only a DC electrostatic and magnetic field [321]. If a particle has a magnetic moment it can be trapped by certain magnetic fields even if it has no electric charge [321]. Microfabricated magnetic traps exist [526], and sufficiently good magnetic traps are used to store antimatter [527][528][529].

In short: electromagnetic particle traps have significant variety.

[9] It is also possible to use square waves instead of sinusoids; see digital ion traps in section 6.5.1.

[10] Using concave arc electrodes instead of convex hyperbolas or circular rods can give a slightly higher quadrupole component plus higher-order multipole factors with the same trap radius and voltage [355].

Appendix B

The Ponderomotive Force

In this appendix we derive and explain the ponderomotive force, which is the effect that a charged mass placed into an oscillating electric field feels an average force in the direction of lower electric field magnitude. This is a fundamental part of RF ion traps.

Specifically, we will see that a point particle of mass m and charge q at position $\vec{x}$ placed in a time-oscillating electric field of the form $\vec{E}(t, \vec{x}) = \vec{E}_0(\vec{x}) \cdot \cos(\omega t)$ experiences the time-averaged (for time periods much larger than $1/\omega$) net force

$$\vec{F}(\vec{x}) = -\frac{q^2}{4m\omega^2} \nabla \left(|\vec{E}_0(\vec{x})|^2 \right). \tag{B.1}$$

This effect is elegant and notable as follows:

- Because this force is the gradient of a continuous function (namely, $\frac{q^2}{4m\omega^2}|\vec{E}_0(\vec{x})|^2$), it is conservative, and that function acts like a potential energy function, exactly analogous to the regular Lorentz force being conservative for a static electric potential. Incidentally, we call this potential of the ponderomotive force the "pseudopotential". The behavior of particles under a ponderomotive force is easily intuited by imagining classical motion through the potential energy landscape of the pseudopotential.
- By electric field superposition, this oscillating electric field may be combined with additional DC and AC fields and their effect on particle motion evaluated separately as if there were no difference between an electrostatic potential and pseudopotential.
- The ponderomotive force acts equally (as a time-averaged force) on negatively and positively charged particles.
- The ponderomotive force is not subject to Earnshaw's theorem and thus allows simple stable electrostatic levitation (as used in ion traps).
- The ponderomotive force is stronger at slower oscillation frequencies ω. However, this also causes stronger unwanted particle movements (which we call "micromotion") and for any given application there is a limit beyond which the micromotion becomes too large. Thus there is usually a finite optimal value for ω.

We will first attempt to build an intuition for how the ponderomotive force works by considering one-dimensional motion of a particle in an electric field as in the following figure:

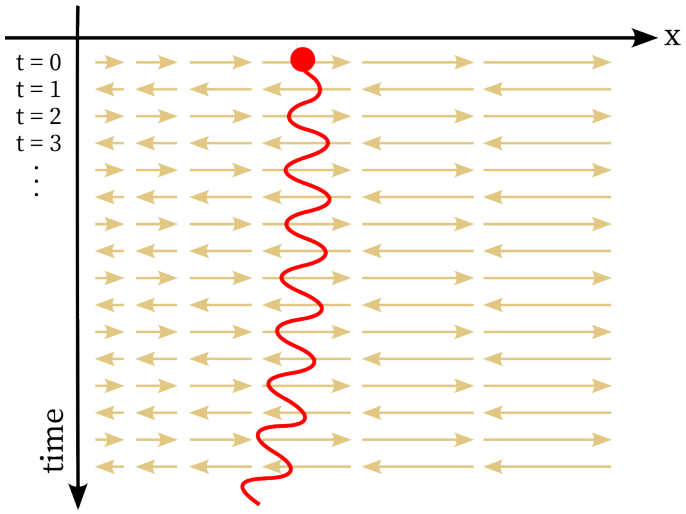

Figure B.1: A figure to guide ponderomotive force intuition.

The electric field, shown in yellow, oscillates sinusoidally with time and always has increasing magnitude toward the right-hand side of this one-dimensional world.

Consider the motion of a positively charged particle (the red circle) in this field. At time $t = 0$, the electric field points to the right, and so the particle begins to move in that direction. At $t = 1$, this is reversed, so the particle slows and then starts moving to the left instead. Repeat over time, and the particle oscillates around its average position. This is the "micromotion" mentioned earlier.

If the electric field had constant magnitude everywhere, this is all that would happen. However, the electric field is stronger to the right and, importantly, the particle oscillation is in phase with the electric field. In the 50% of the time the particle is further to the right of its average position, the stronger electric field there is pointing toward the left, and in the half of the time the particle is to the left, the electric field points to the right but is weaker. As a result, there is a force imbalance: the particle experiences slightly more force toward the left, and slowly moves, on average, in that direction. This is the ponderomotive force.

Now let's formalize this.

Consider a particle of mass m in a 1D rapidly oscillating force field $qE_0(x)\cos(\omega t)$, where $qE_0(x)$ is the force on the particle at position x, t is time, and ω is angular frequency (note many engineering applications prefer a frequency f with $\omega = 2\pi f$).

Assume the particle motion $x(t)$ has slow/large (ponderomotive, also called "secular", movement) and fast/small (micromotion) components $x_s(t)$ and $x_f(t)$, respectively:

$$x(t) = x_s(t) + x_f(t). \tag{B.2}$$

Our goal is to find $x_s(t)$. From $F = qE_0(x)\cos(\omega t) = ma$, we can find $a = \frac{d^2x}{dt^2}$:

$$\frac{d^2x}{dt^2} = \frac{d^2x_s}{dt^2} + \frac{d^2x_f}{dt^2} = \frac{qE_0(x_s + x_f)}{m}\cos(\omega t). \tag{B.3}$$

We will first approximate $x_f(t)$ as follows. Assume $qE_0(x_s + x_f) \approx qE_0(x_s)$, i.e., the micromotion oscillation amplitude is small compared to the distance over which the electric field varies, and further assume the micromotion is significantly faster than ponderomotive movement so we can consider a short amount of time in which $\frac{d^2x_s}{dt^2} \approx 0$ but $\frac{d^2x_f}{dt^2} > 0$. Then at any given such moment,

$$\frac{d^2x_f}{dt^2} \approx \frac{qE_0(x_s)\cos(\omega t)}{m} \tag{B.4}$$

and

$$x_f(t) \approx -\frac{qE_0(x_s)\cos(\omega t)}{m\omega^2}. \tag{B.5}$$

We see the fast micromotion $x_f(t)$ is periodic with amplitude proportional to force, as we would intuitively expect. Calculation of $x_s(t)$, the net movement due to ponderomotive force, is more involved because we now have to consider variation in $E_0(x)$ combined with $x_f(t)$. Start again from equation B.3, but this time approximate the electric field $E_0(x)$ as varying linearly around x_s:

$$\frac{d^2x_s}{dt^2} + \frac{d^2x_f}{dt^2} \approx \frac{1}{m}\left(qE_0(x_s) + x_f \cdot q\frac{dE_0}{dx}(x_s)\right)\cos(\omega t). \tag{B.6}$$

Substituting in our approximation B.5 for $x_f(t)$:

$$\frac{d^2x_s}{dt^2} + \frac{qE_0(x_s)\cos(\omega t)}{m} \approx \frac{1}{m}\left(qE_0(x_s) - \frac{qE_0(x_s)\cos(\omega t)}{m\omega^2} \cdot q\frac{dE_0}{dx}(x_s)\right)\cos(\omega t) \tag{B.7}$$

which simplifies to

$$\frac{d^2x_s}{dt^2} \approx -\frac{qE_0(x_s)}{m^2\omega^2} \cdot q\frac{dE_0}{dx}(x_s) \cdot \cos^2(\omega t). \tag{B.8}$$

Note we were able to combine the $\cos(\omega t)$ frequency of micromotion with the $\cos(\omega t)$ frequency of electric field variation to get a factor of $\cos^2(\omega t)$. We can average this out over time ($\cos^2(\omega t) \to 1/2$) to find

$$\frac{d^2x_s}{dt^2} \approx -\frac{qE_0(x_s)}{2m^2\omega^2} \cdot q\frac{dE_0}{dx}(x_s) = -\frac{q^2}{4m^2\omega^2} \cdot \frac{d}{dx}\left(|E_0(x_s)|^2\right). \tag{B.9}$$

Using $F = ma$ where $a = \frac{d^2x_s}{dt^2}$, we then obtain the expected 1D ponderomotive force

$$F(x_s) \approx -\frac{q^2}{4m\omega^2} \cdot \frac{d}{dx}\left(|E_0(x_s)|^2\right). \tag{B.10}$$

This derivation is now complete. This same derivation is straightforward to repeat in the multidimensional case, giving the promised result

$$\vec{F}(\vec{x}_s) \approx -\frac{q^2}{4m\omega^2}\nabla\left(|\vec{E}_0(\vec{x}_s)|^2\right). \tag{B.11}$$

This force, as previously mentioned, is the gradient of a scalar function which can be treated as a potential energy U where $\vec{F} = -\nabla U$. This pseudopotential is

$$U(\vec{x}_s) \approx \frac{q^2}{4m\omega^2}|\vec{E}_0(\vec{x}_s)|^2. \tag{B.12}$$

Now recall our derivation assumed the micromotion is small, which holds so long as the field oscillation frequency ω is sufficiently high. What is the minimum value of ω that works?

A general calculation of the precise minimum frequency ω_{min} is nontrivial [293] (for an example, see the Mathieu stability criterion for quadrupole electrodes in Appendix A), but we can approximate it[1] as follows. Suppose we want the peak-to-peak micromotion amplitude to be less than some distance L (for example, the distance between electrodes generating the electric field). Then, using equation B.5, we can write

$$L \approx \frac{2qE_0}{m\omega_{min}^2}, \tag{B.13}$$

or

$$\omega_{min} \approx \sqrt{\frac{2qE_0}{mL}}. \tag{B.14}$$

This equation is limited because it assumes a constant electric field magnitude E_0 when, by premise, the electric field will have varying magnitude. However, setting E_0 to the average or maximum electric field observed over the area of L should suffice for approximating micromotion amplitude to within an order of magnitude, and this can be refined later with numerical simulation. Defining $f_{min} = \omega_{min}/2\pi$, our nanoparticle ion traps typically[2] have $1\,\text{kHz} < f_{min} < 1\,\text{MHz}$.

Finally, a historical note: the basic derivation here is well-known and was used while developing the first ion traps and mass spectrometers, e.g., by Dehmelt [515]. Also, the fundamental physics holds not just for electric fields but for any force field [530].

[1] For discussion and comparison of several other methods to approximate where motion is stable, see [293], which prefers the conservative criterion $\omega_{min} \approx \text{sqrt}((2q|\nabla\vec{E}_0|)/(0.3m))$ with the same dimensions as ours.

[2] Example: +10 charge 10 nm dia. Cu particles in a 100 V and 1 mm field have $f_{min} = 42\,\text{kHz}$.

Appendix C

High Voltage Waveform Generator

In chapter 6, we discovered that some methods of electrostatically focusing nanoparticles need a complicated voltage waveform applied to each of tens of electrodes (a segmented quadrupole). Although there were some alternative electrode geometries with simpler waveform requirements, these complex setups were easier to analyze and might sometimes give superior results. In this appendix, we build a proof-of-concept circuit to show creating these waveforms (and thus our complicated focusing mechanisms) would be feasible[1].

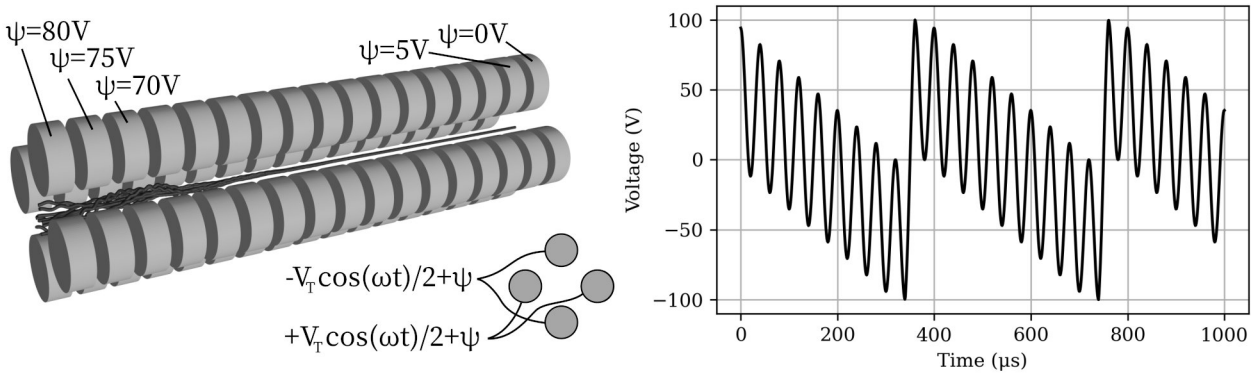

Figure C.1: Left: an example 17-segment quadrupole (section 6.4.1), where each of $17*2 = 34$ electrode pairs needs a waveform consisting of a sine wave (with adjustable frequency ω) plus DC bias ψ. Right: one of the more extreme possibilities is to replace the DC bias with a sawtooth wave to make this into a linac (section 6.4.2), giving the displayed waveform.

We require a circuit that can achieve the following:

- Create a time-varying voltage with up to 200 V amplitude (limited by gas breakdown), preferably ±100 V centered around zero (so particles don't feel a net force toward the outer vacuum chamber, which is grounded).

[1]As noted in chapter 6, we didn't physically build a complete electrostatic particle manipulation system because we lacked a working nanoparticle charger from chapter 5, but we should be able to in the future.

- This voltage needs to have a sinusoidal component to drive a quadrupole with a frequency 1 kHz to at least 1 MHz (table 6.4) adjustable in real time to handle particles of different mass/charge ratios. It should also be able to add a DC bias (again adjustable) and, if we need to build a linac, also superimpose a sawtooth wave (with maximum frequency component 1 kHz to 1 MHz defining the linac velocity).
- The voltage needs to be applied to metal electrodes in a vacuum chamber, which generally act as small capacitors probably in the 10 pF range. The possibility of gas breakdown suggests the circuit should tolerate temporary output short circuits.
- And since the waveforms on any two electrodes may not correlate (especially with both quadrupole and linac), we need an individual waveform for each of tens of electrodes.

This circuit is rather difficult to build due to the combination of high 1 MHz frequency and high 200 V voltage, let alone the requirement it be adjustable in real time with nonsinusoidal components (a DC bias or sawtooth wave) or the need to create tens of similar waveforms. The only simplifying factors are that the load is very small (10 pF) and simulations suggested high voltage output resolution is not necessary (5 bits = 32 voltage levels is more than enough; see also digital ion traps in section 6.5.1).

Again, there may be simpler ways to build a particle focusing system (see section 6.5.1 for thoughts on different electrodes, waveforms, and circuits), but if we can build a circuit that satisfies our complex requirements here, it would also suffice to power any simpler mechanism we want, so we decided to proceed.

This circuit is a high voltage and frequency arbitrary waveform generator. These do already exist for several purposes, but no existing solution is perfect for us. Available opamps cannot simultaneously output the high voltages and frequencies we require. Examples include the ADHV4702 [531], OPA462 [532], and HV264 [533], which can respectively reach ±110 V, ±90 V, and 215 V, but only up to about 10 kHz to 30 kHz. Driver circuits for piezoelectric or ultrasound actuators (which are also small capacitive loads) also achieve our voltage specifications but only up to low kilohertz frequencies [534][535][536]. Speeds > 10 MHz are possible when constructed via custom integrated circuits [537][538], but this is generally not feasible given the cost of custom ICs (see chapter 7)[2]. Other amplifiers built from discrete components can reach 500 V at 5 MHz [539][540], but the required circuits are fairly complicated and sometimes use specialized components (e.g., vacuum tubes [539]). Off-the-shelf amplifiers capable of ±150 V signals from DC to 5 MHz are available from [541], but at $2500 each, tens of these cost more than the rest of a nanoparticle printer combined.

This prior art suggests our circuit is possible but difficult to build. To demonstrate it could be cheap enough while driving tens of electrodes, we will have to design our own.

Safety note: These circuits can use somewhat high voltages and somewhat high power, enough to potentially cause electrical injuries. Caution was taken during assembling and testing. We ran only minimal experiments with loose cables to show basic functionality; further development would warrant building a robust enclosure for the system.

[2]The point of this dissertation is making such custom integrated circuits feasible; it might someday be.

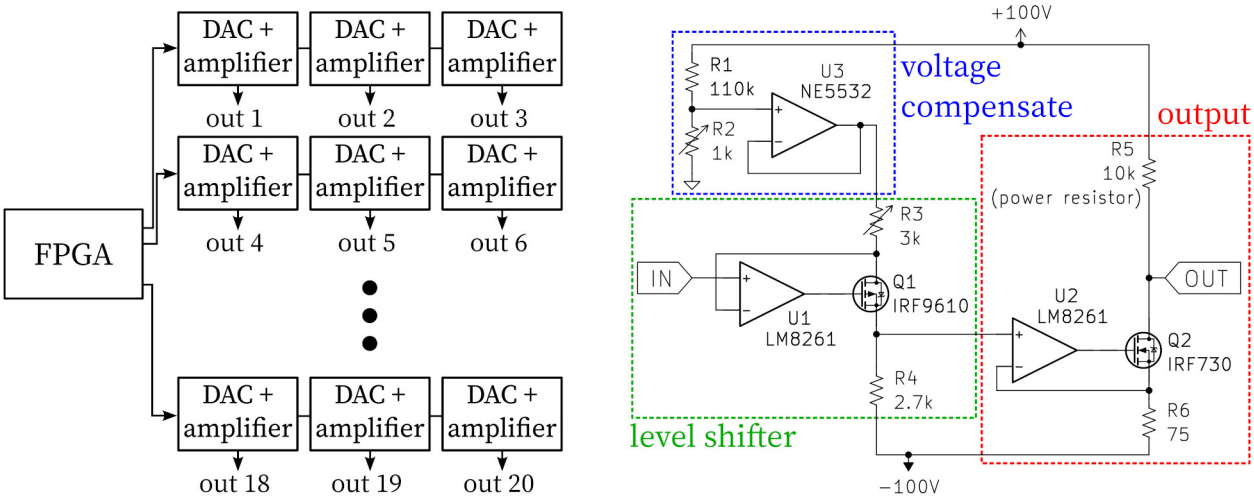

Figure C.2: Left: proposed system architecture. An FPGA sends digital signals to multiple boards, each with DAC and high voltage amplifier. Right: (simplified) high voltage amplifier. A class-A amplifier ("output") amplifies an incoming signal shifted to the low supply rail ("level shifter"). A "voltage compensate" circuit allows the high supply rail voltage to vary without affecting output gain. Resistors R2 and R3 calibrate the output DC bias and gain.

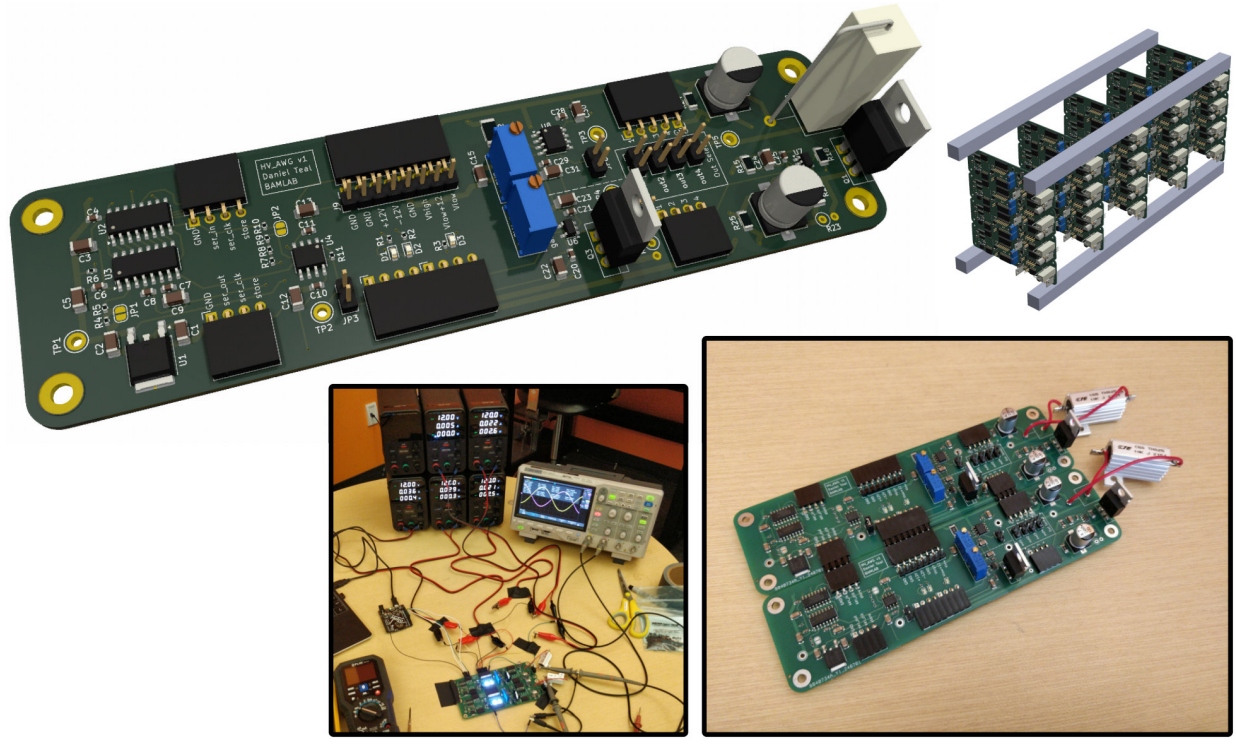

Figure C.3: Clockwise from top left: a 3D render of the DAC + amplifier board, a concept render of a multiboard array, two assembled and daisy-chained boards, and the daisy-chained boards generating ±120 V (240 Vpp) 20 Hz sinusoids, confirming basic functionality.

To demonstrate how a system with tens of output waveforms might be built, we chose an architecture where a single FPGA would provide signals to drive tens of boards (figure C.2), each containing a DAC and high voltage amplifier. The amplifier circuit was as shown in figure C.2. We chose a class A amplifier circuit topology as (though inefficient[3]) it is simple, predictable, and can be built from a single off-the-shelf high voltage NMOS MOSFET. To create a bipolar signal, we floated the class A amplifier to a negative voltage supply rail ($< -100\,\mathrm{V}$), then used current to transfer the input signal from near ground to the negative voltage rail[4]. Finally, a voltage compensation circuit adjusted the bias and gain to make the output independent to the high rail voltage. All power rails were provided from external supplies and shared between boards to reduce size, cost, and inefficiency.

We designed a PCB with a serial data circuit, DAC, and the high voltage amplifier[5]. These boards were designed to be daisy-chained together and arrayed en masse in a single enclosure (see figure C.3), where the class-A amplifier MOSFETs and power resistors could be attached to a heatsink if desired. We built and tested two of these PCBs (figure C.3) and confirmed their basic functionality. All circuit components are off-the-shelf, cheap, and have high availability. The total part and assembly cost of a single board is about $25 (two orders of magnitude less than the previously-mentioned off-the-shelf amplifier [541]), making an array of tens of electrodes economically feasible. Finally, we confirmed our system could generate high voltage high frequency[6] signals by connecting an Agilent 33210A signal generator (providing a $\pm 1\,\mathrm{V}$ ($2\,\mathrm{Vpp}$) wave) to a high voltage amplifier (bypassing the DAC for simplicity) and generating the frequency response plot in figure C.4.

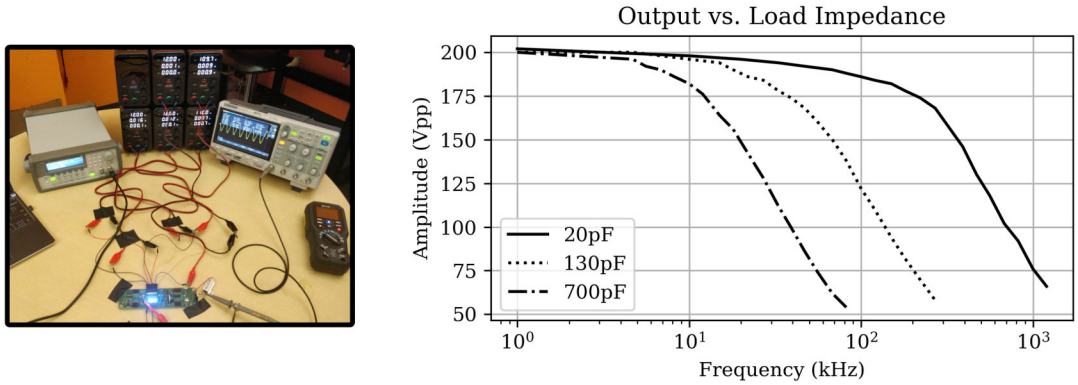

Figure C.4: Left: high frequency test setup with external signal input to amplifier. Right: Frequency response of the high voltage amplifier circuit with several capacitive loads.

We can conclude it seems possible to affordably construct a high voltage, high frequency, multi-output signal generator that meets our requirements, and constructing the full system can be done when ready for experimental tests. Driving circuitry is likely not the limit to nanoparticle printer feasibility.

[3]A single amplifier drew up to 10 W; efficiency (vs. CV^2f capacitor power draw) varied $\approx 0.01\%$ to 10%.

[4]We chose not to use feedback from the amplifier output to input to avoid phase delay problems.

[5]This could be simplified by putting all electronics on a smaller board, possibly inside the vacuum chamber to minimize parasitic capacitive load [424], or ultimately on a custom integrated circuit [542].

[6]Higher frequencies are achievable by decreasing the value of power resistor R5 in figure C.2.